

DOCTORAL THESIS

Closed-Loop Droplet Size Control in Microfluidics

Nafisat Gyimah

TALLINN UNIVERSITY OF TECHNOLOGY
DOCTORAL THESIS
47/2024

Closed-Loop Droplet Size Control in Microfluidics

NAFISAT GYIMAH



TALLINN UNIVERSITY OF TECHNOLOGY
School of Information Technologies
Thomas Johann Seebeck department of Electronics

The dissertation was accepted for the defence of the degree of Doctor of Philosophy (Information and Communication Technology) on 21 August 2024

Supervisor: Dr. Tamás Pardy, Ph.D.
Department of Chemistry and Biotechnology
Tallinn University of Technology
Tallinn, Estonia

Co-supervisor: Associate Professor Ott Scheler, Ph.D.
Department of Chemistry and Biotechnology
Tallinn University of Technology
Tallinn, Estonia

Opponents: Dr. Péter Fürjes, Ph.D.
Head of Microsystems Lab at HUN-REN Centre for Energy Research
Budapest, Hungary

Assistant Professor Ladislav Derzsi, Ph.D.
Laboratory of Microfluidics and Complex Fluids, Institute of Physical Chemistry
Polish Academy of Sciences
Warsaw, Poland

Defence of the thesis: 13 September 2024, Tallinn

Declaration:

Hereby I declare that this doctoral thesis, my original investigation and achievement, submitted for the doctoral degree at Tallinn University of Technology, has not been submitted for any academic degree elsewhere.

Nafisat Gyimah

signature

Copyright: Nafisat Gyimah, 2024
ISSN 2585-6898 (publication)
ISBN 978-9916-80-188-8 (publication)
ISSN 2585-6901 (PDF)
ISBN 978-9916-80-189-5 (PDF)
DOI <https://doi.org/10.23658/taltech.47/2024>
Printed by Joon

Gyimah, N. (2024). *Closed-Loop Droplet Size Control in Microfluidics* [TalTech Press].
<https://doi.org/10.23658/taltech.47/2024>

TALLINNA TEHNIKAÜLIKOOL
DOKTORITÖÖ
47/2024

Suletud ahelaga tilkade suuruse juhtimine mikrofluidikas

NAFISAT GYIMAH



Contents

LIST OF PUBLICATIONS	7
OTHER RELATED PUBLICATIONS	8
AUTHOR'S CONTRIBUTION TO THE PUBLICATIONS	9
Abbreviations.....	10
1 INTRODUCTION.....	12
1.1 Background and Motivation	12
1.2 Challenges in Droplet Microfluidics	12
1.3 Problem Statement and Research Questions	14
1.4 Contribution of the Thesis	14
1.5 Organization of the Thesis	17
2 SIMULATION OF CLOSED LOOP DROPLET SIZE CONTROL	18
2.1 Closed-loop simulation for parameter space evaluation	18
2.1.1 State-of-the-Art	18
2.1.2 Methodology	19
2.1.2.1 Simulation Framework and Numerical model	19
2.1.2.2 Control theory and Design.....	23
2.1.3 Results and Discussion	26
2.1.3.1 Droplet Formation & Effect of Fluid Flow Rates.....	26
2.1.3.2 Controller performance evaluation	27
2.2 Genetic Algorithm (GA) for controller tuning	29
2.2.1 State-of-the-Art.....	29
2.2.2 Methodology of GA-tuned-PID controllers.....	31
2.2.3 Results and Discussion	34
2.3 Summary	37
3 BRIDGING CLOSED-LOOP CONTROL SIMULATIONS WITH EXPERIMENT	38
3.1 State-of-the-art and Proposed Framework	38
3.2 Methodology: Experimental setup and Data collection	39
3.3 Results and Discussions	41
3.3.1 System modeling and GA tuning.....	41
3.3.2 Results of PID Implementation for Pressure Control	44
3.4 Simulations aiding development of an empirical model	44
3.5 Conclusion	45
4 DEEP REINFORCEMENT LEARNING PROXIMAL POLICY OPTIMIZATION ALGO-	
RITHM FOR DROPLET SIZE CONTROL	46
4.1 State-of-the-Art: Machine Learning for Microfluidics Control	46
4.2 Methodology	47
4.2.1 Implementation Framework & Flow Modeling	47
4.2.2 Near real-time Droplet Size Estimation.....	50
4.2.3 PPO Algorithm Theory and Implementation	50
4.3 Results and Discussion	55
4.3.1 Mesh Independence Studies and Model Verification.....	55
4.3.2 Environment Characterization and Probe Configuration	57

4.3.3	PPO Performance in the Presence and Absence of Disturbances	58
4.4	Summary	64
5	CONCLUSION AND FUTURE WORK	65
5.1	Future research direction	65
5.2	Conclusion	66
	List of Figures	69
	List of Tables	72
	References	73
	Acknowledgements	83
	Abstract	84
	Kokkuvõte	86
	Appendix 1	89
	Appendix 2	99
	Appendix 3	107
	Appendix 4	139
	Appendix 5	153
	Curriculum Vitae	170
	Elulookirjeldus	171

LIST OF PUBLICATIONS

The present Ph.D. thesis is based on the following publications that are referred to in the text by Roman numbers.

- I **N. Gyimah**, O. Scheler, T. Rang, and T. Pardy, "Digital twin for controlled generation of water-in-oil microdroplets with required size," in *2022 23rd International Conference on Thermal, Mechanical and Multi-Physics Simulation and Experiments in Microelectronics and Microsystems (EuroSimE)*, pp. 1–7, IEEE, 2022
- II **N. Gyimah**, R. Jõemaa, K. Pärnamets, O. Scheler, T. Rang, and T. Pardy, "Pid controller tuning optimization using genetic algorithm for droplet size control in microfluidics," in *2022 18th Biennial Baltic Electronics Conference (BEC)*, pp. 1–6, IEEE, 2022
- III R. Jõemaa, **N. Gyimah**, K. Ashraf, K. Pärnamets, A. Zaft, O. Scheler, T. Rang, and T. Pardy, "Cogniflow-drop: Integrated modular system for automated generation of droplets in microfluidic applications," *IEEE Access*, 2023
- IV K. Pärnamets, A. Udal, A. Koel, T. Pardy, **N. Gyimah**, and T. Rang, "Compact empirical model for droplet generation in a lab-on-chip cytometry system," *IEEE Access*, vol. 10, pp. 127708–127717, 2022
- V **N. Gyimah**, O. Scheler, T. Rang, and T. Pardy, "Deep reinforcement learning-based digital twin for droplet microfluidics control," *Physics of Fluids*, vol. 35, no. 8, 2023

OTHER RELATED PUBLICATIONS

- VI **N. Gyimah**, O. Scheler, T. Rang, and T. Pardy, "Can 3d printing bring droplet microfluidics to every lab?—a systematic review. *micromachines* 2021, 12, 339," 2021
- VII Invention: Integrated modular system for automated generation of droplets in microfluidic applications and method thereto; Owners: Tallinn University of Technology, Tallinn University of Technology, Faculty of Science, Institute of Chemistry and Biotechnology; Authors: Kaiser Pärnamets, Kanwal Ashraf, Nafisat Gyimah, Rauno Jõemaa, Tamás Pardy; Priority number: P202300024; Priority date: 20.09.2023

AUTHOR'S CONTRIBUTION TO THE PUBLICATIONS

- I In I, As the first author, I developed a simulation of a closed-loop feedback system for microdroplet size regulation in microfluidic systems. This involved a literature review, framework conceptualization, and computational model integration with a Proportional Integral (PI) controller. The system closely mimics real-world operating conditions to construct the simulation. Through evaluations, I compared its performance with the open-loop method and across different droplet sizes to assess the complete parameter space. I analyzed data, created figures, and authored the manuscript, with supervisor input during revisions.
- II In II, As the first author, I introduced genetic algorithm (GA) optimization as the tuning method for PID controllers in closed-loop droplet microfluidics control. I initiated the study by conducting a literature review and conceptualizing the framework. Subsequently, I implemented the GA tuning method, designed the controller, and integrated it with the system model (derived from experimental data) in a simulation environment. I evaluated GA performance using various performance error indices and compared its efficacy against traditional approaches. I analyzed data, prepared the figures, and authored the manuscript, with revisions made based on supervisors' inputs
- III In III, As a co-author, I contributed to the experimental implementation of a dynamic dual feedback control system for droplet generation in a microfluidic system. My contributions included co-proposing the framework, designing controllers in the simulation environment, establishing the transfer process from simulation to experimental setup, and co-designing controller codes for experimentation. I also analyzed data, created figures, and authored specific sections(Section III-B-1, III-A-1, III-A-1, IV-A-1, IV-A-2) of the manuscript, with input from supervisors during revisions.
- IV In IV, As a co-author, I contributed to developing an empirical mathematical model for predicting droplet generation characteristics. Specifically, I constructed a simulation model to capture the dynamics of droplet generation in microfluidic systems. The initial model provided a foundation for further refinements by other authors. They developed mathematical adjustments to simulate the transition from 2D to 3D in structures. These modifications aimed to improve alignment with experimental outcomes, among others.
- V In V, As the first author, I developed the Deep Reinforcement Learning (DRL) algorithm, Proximal Policy Optimization (PPO), for controlling droplet size. I conceptualized the framework, setup up simulations in the CFD environment, developed the PPO algorithm in a machine learning framework, and integrated both environments. I conducted numerical model validation and analyses to assess the framework's performance across various targets and its ability to adapt to external disturbances. I analyzed the findings, and authored the manuscript, with revision inputs from supervisors.

Abbreviations

PCR	Polymerase Chain Reaction
HTS	High-Throughput Screening
PLGA	Poly Lactic-co-Glycolic Acid
CV	Coefficient of Variation
SEDS	Self-Emulsifying Delivery Systems
SMEDS	Self-Micro-Emulsifying Delivery Systems
SNEDS	Self-Nano-Emulsifying Delivery Systems
MSCs	Mesenchymal Stem Cells
Ca	Capillary Numbers
PID	Proportional-Integral-Derivative
PI	Proportional-Integral
CFD	Computational Fluid Dynamics
RQ	Research Question
DRL	Deep Reinforcement Learning
ML	Machine Learning
3D	Three-Dimensional
2D	Two-Dimensional
LSM	Level Set Method
FFD	Flow-Focusing Device
FST	Fluid surface tension
VOF	Volume-of-Fluid
LS	Level-Set
PFM	Phase-Field Models
PFPE-PEG-PFPE	Perfluoropolyether-Polyethylene Glycol-Perfluoropolyether
ODEs	Ordinary Differential Equations
DAEs	Differential-Algebraic Equations
SISO	Single-Input Single-Output
GA	Genetic Algorithm
IAE	Integral Absolute Error
ISE	Integral Square Error
ITAE	Absolute Value of the Error
ITSE	Integral Squared Error
MSE	Mean Squared Error
PDMS	Polydimethylsiloxane
FPE	Akaike's Final Prediction Error
Cvp	Voltage-to-Pressure Coefficient
DQN	Deep Q-Network
MFEC	Model-Free Episodic Controller
TRPO	Trust Region Policy Optimization
DDPG	Deep Deterministic Policy Gradient
SAC	Soft Actor-Critic
PPO	The Proximal Policy Optimization
ANN	Artificial Neural Network
HFE	Hydrofluoroether
GAE	Generalized Advantage Estimation

MULES	Multi-Dimensional Limiter
PIMPLE	Combination of PISO and SIMPLE
PISO	Pressure Implicit with Splitting of Operator
SIMPLE	Semi-Implicit Method for Pressure-Linked Equations
MaxCo	Maximum Courant Number

1 INTRODUCTION

1.1 Background and Motivation

Microfluidics represents an advanced scientific discipline, focusing on manipulating minute fluid volumes within microfluidic chips. These chips, capable of handling volumes ranging from nanoliters to femtoliters, hold potential across various scientific disciplines [1]. Unique fluid characteristics, such as a high surface-to-volume ratio and the prevalence of viscous forces over inertial forces, are inherent in this scale. These, in turn, enable precise fluid manipulation, fast mass and heat transfer processes, integration of multiple functions within a single chip, and advances towards portable lab-on-chip platforms [2].

Droplet microfluidics, a specialized subset of microfluidics, focuses on the generation and manipulation of sub-micrometer-sized droplets using immiscible fluids. The two immiscible fluids, namely the dispersed phase and the continuous phase, are introduced into the chip via passive hydrodynamic pressure or active external actuation. These fluids flow through microchannels within the chip and converge at junctions where droplet formation occurs, driven by the interplay of surface tension and viscous drag forces.

Microdroplets are produced for diverse applications in biotechnology and pharmaceuticals [3]. In biological applications, a common configuration involves using oil as the continuous-phase fluid and water as the dispersed phase, resulting in the formation of single emulsion droplets. These droplets, along with more intricate structures like double emulsions, serve various purposes, including single-cell analysis and controlled drug delivery [4].

The use of droplets as self-contained micro-reactors allows for control over reaction conditions and reduces problems, such as biofilm formation. Additionally, their volume ranges enable the isolation of single cells within droplets, providing a unique capability for studying population heterogeneity and observing cellular responses with exceptional precision. Moreover, their high surface area-to-volume ratios ensure fast and even heat transfer, which is advantageous for processes such as polymerase chain reaction (PCR) [5, 6].

Despite alternative approaches like digital microfluidics for control over individual droplets on a two-dimensional surface [7, 8], traditional droplet microfluidics remain at the forefront. Its emphasis on high throughput, uniformity, and reliability, and droplet manipulations underscores its potential, especially in high-throughput screening (HTS) applications.

1.2 Challenges in Droplet Microfluidics

Advancing droplet microfluidics requires overcoming challenges in controlling droplet characteristics, as highlighted in reference [8]. The size of droplets, whether in volume or diameter, is crucial for various processes. Deviations in droplet size can lead to increased error rates during manipulation, potentially compromising overall performance.

In food production, maintaining uniform droplet size is preferred to reduce emulsifier usage and lipid oxidation, impacting food texture and shelf-life [9]. Similarly, in drug development, droplet size influences medication effectiveness, as demonstrated in studies involving encapsulated cancer medication [10]. Furthermore, the uniformity in microspheres produced through droplet microfluidics affects drug release kinetics [11]. In enzymatic reactions, droplet size influences enzymatic activity, with smaller droplets exhibiting decreased activity due to higher adsorption and enzyme inactivation [12]. Additionally, droplet size impacts various fluid dynamics phenomena such as mixing dynamics, flow resistance, breakup, coalescence, and collective behavior [13].

In summary, droplet size plays a critical role in determining the concentration, volume, and composition of substances encapsulated within microscale entities, thereby impacting various applications. Therefore, generating uniform droplets with user-defined or application-specified sizes is imperative. Droplet uniformity is typically assessed using the coefficient of variation (CV), where a CV exceeding 5% indicates polydispersity [14, 15, 16, 17]. Ideally, maintaining a low CV, approaching a theoretical 0%, is desired.

However, consistently generating droplets of the required size remains challenging due to complex dynamics and a lack of predictive understanding [18]. Fabrication defects, disturbances, and pressure oscillations further complicate the process [19, 20], especially when these systems operate at high throughput or for extended periods. Though various parameters, such as channel dimensions, fluid properties, and flow rates or pressures, influence droplet size [13, 21, 22, 23, 24], the exact mechanism governing droplet size remains incompletely understood.

To tackle this challenge, researchers investigate mathematical-empirical models to establish relationships between flow properties and droplet sizes. Studies on T-junction geometries, for instance, reveal linear relationships at low capillary numbers ($Ca \leq 0.1$) but nonlinear variations at higher capillary numbers ($0.1 \leq Ca \leq 1$) [25]. Similarly, in flow-focusing microchannels, nonlinear relationships across low and high capillary numbers have been demonstrated [26]. Despite progress, empirical models have limitations, including challenges in generalizing across different conditions and fluid properties [27]. Recent advancements in machine learning offer promise in addressing these limitations [28, 29, 30, 31, 32, 33].

Additionally, research focuses on developing tunable droplet sizes to expand the achievable range within a single platform. Studies explore various techniques, including co-flow microfluidic devices [34], single-layer valve designs [35], piezoelectric actuators [36], and multi-device microfluidic chips [37]. However, reliance on specialized chips introduces challenges such as complexity and scalability limitations [38]. To address this, efforts are underway to standardize chip designs and utilize basic laboratory tools to make scientific exploration more accessible. This has led to research integrating control methods with microfluidics and for droplet control, as depicted in Figure 1.

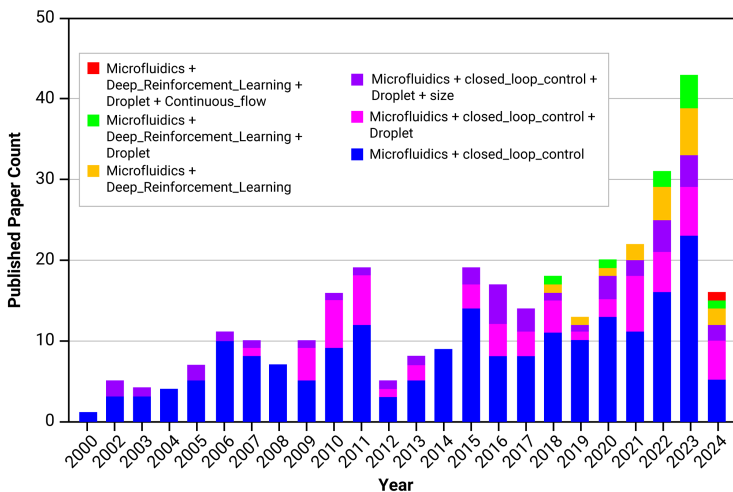


Figure 1: Trend of studies on microfluidics integration of control methods

Closed-loop feedback systems emerge as superior solutions for achieving and maintaining the desired droplet size and uniformity. The prevalent closed-loop method typically integrates a Proportional-Integral-Derivative (PID) controller [39, 40]. While closed-loop systems offer promising solutions, challenges remain, including limited evaluation of droplet size ranges, controller-tuning inefficiencies, and complexity of classical closed-loop control methods. Therefore, this thesis aims to address these challenges by proposing innovative solutions to enhance the adaptability, efficiency, and reliability of closed-loop feedback systems in microfluidic applications.

1.3 Problem Statement and Research Questions

Despite significant progress, there are still research gaps in droplet size control. One such gap is the limited evaluation of droplet size ranges in closed-loop feedback systems, which limits their flexibility. This raises questions about how to effectively assess and optimize the range of droplet sizes that can be produced and controlled. Another gap lies in the inefficiencies of traditional tuning methods for closed-loop controllers, like PID controllers, in microfluidics. This prompts questions about improving tuning methods to enhance performance and robustness. Moreover, the modeling complexity of classical closed-loop control in microfluidics poses a significant challenge. This underscores the need to reduce reliance on explicit complex models via alternatives.

Hypotheses include exploring advanced computational techniques to predict the effects of different control parameters on droplet size distribution and investigating strategies to achieve broader tunability. Alternative tuning algorithms, like genetic algorithms, may optimize controller parameters more effectively, improving system dynamics and performance metrics. Additionally, leveraging advanced control techniques like deep reinforcement learning could autonomously regulate droplet size without explicit models. Insights from system identification approaches could develop more accurate and robust control algorithms, addressing these research gaps.

To tackle these challenges, this research integrates flow modeling with controller design simulations. It also explores experimental implementations of proposed solutions. As such, the following research questions were developed:

- RQ1: How can a simulated system effectively evaluate the complete parameter space and improve precision in droplet generation within microfluidic systems?
- RQ2: Can an optimal control solution developed for a simulated environment of a flow-focusing junction be successfully implemented in an experimental droplet generation setup?
- RQ3: Is model-free control of droplet generation achievable through machine learning techniques?
- RQ4: Which set of machine learning tools can facilitate robust, adaptable, and stable control of droplet generation in microfluidic systems?

Addressing these research questions aims to improve droplet size control.

1.4 Contribution of the Thesis

This thesis contributes to the field in relation to the RQs in the following ways:

Contribution 1 (addressing RQ1): A simulation for controlling microdroplet generation in microfluidic devices is presented. The simulation methodology utilizing

Computational Fluid Dynamics (CFD), and its integration with controller design for closed-loop control is implemented. The controller’s effectiveness in regulating droplet size is demonstrated, along with an evaluation of the parameter space for droplet control.

Contribution 2 (as a support to address RQ1): Additionally, the thesis proposes the use of genetic algorithm optimization for controller tuning in the simulated microfluidic environment. This approach showcases significant improvements in process response metrics compared to traditional tuning methods.

Contribution 3 (addressing RQ2): A dynamic dual feedback control microfluidic system for droplet generation is implemented in an experimental setting. It leveraged on insights from RQ1. Controller parameters are primarily informed by the simulation’s insights transferred to physical system control. This demonstrates successful transferability from the simulation to the experimental setup, albeit with the need for minor adjustments. The outcome is a prototype capable of rapid pressure stabilization and uniform droplet generation.

Contribution 4 (as a support to address RQ2): Building upon the RQ1 simulation, an empirical model for droplet generation is developed. Through simulations, an effective adjustment from 2D to 3D structure is proposed to enhance agreement with experimental outcomes.

Contribution 5 (address RQ3 and RQ4): Deep Reinforcement Learning (DRL) with a computational fluid dynamics (CFD) droplet generator model integration is proposed and implemented. This approach achieves precise droplet size control with minimal variability through model-free (RQ3) and adaptive control (RQ4). Verification of the numerical model against published experimental data demonstrates a good agreement. Additionally, the system’s robustness to external disturbances, such as mechanical vibrations, is evaluated, demonstrating its adaptiveness in effectively handling such challenges within defined limits.

Table 1 provides a summary of the state-of-the-art, incorporating publications that form the basis of this thesis. Table 2 offers a concise overview, mapping the contributions and research questions to associated research papers listed in Appendices A-C***.

Table 1: State-of-the-art for closed-loop microfluidic droplet size control.

Paper	Con- troller	Con- troller tuning method	Open loop CV% or R ² or RMSE	Closed- loop CV% or R ² or error	Response time (s)	Droplet size range	SIM. or Exp.	Year
Classical Control methods								
[41]	PID	trial and error method	10 - 20.1	<7.6	~0.3	0.25 -1.4 nL	Exp.	2023

[42]	PI	-	5	2	<0.2	100-700 μm (6 points)	Exp.	Feb, 2022
[43]	PID	Ziegler-Nichol's method	-	<5%	7-10	150, 200, 250 μm	Exp.	2013
[44]	PI	Ziegler-Nichol's method	-	$R^2=0.98$	<10	14-24 μm	Exp.	2020
[45]	PID	-	(RSME= 3.4)	Error RSME= 0.48	-	100, 140, 160 μm	Exp.	2021
[39]	PID	trial and error method	3.78	0.32	0.05	550 pL	Exp.	2017
Publication I	PI	trial and error method	<15%	<2% ($R^2= 0.993$)	-	30-60 μm (6 points tested)	SIM. (COMSOL and MATLAB)	Apr, 2022
Publication II	PID	Genetic algorithm	-	Error ITAE =0.2367	0.088	50 to 350 μm	SIM (Simulink and MATLAB)	Oct, 2022
Publication III	Dual PIDs	Genetic algorithm + adjustment	-	5-10%,	10	50-200 μm	Exp.	Sept, 2023

Machine Learning methods

Papers	Con-troller	Agent action space	Perfor-mance evalua-tion	CV %	Time to reach peak per-formance	Droplet size range	SIM. or Exp.	year
[46]	DQN, MFEC	Discrete action	Time to reach peak performance, algorithm vs human performance		sur-passed human-level performance DQN = ~27 hrs MFEC = within minutes	54 μm	Exp.	2018
Publication V	PPO	Continu-ous action	Droplet size variation in open-loop vs closed-loop control	open loop = 6-8% Vs closed-loop PPO = 2-5%		50-80 μm	SIM. (Open-FOAM_Py-Torch)	2023

Exp. Experiment Simulation
SIM Environment
RMSE Root Mean Squared Error
ITAE Integral Time Average Error

Table 2: Summary of Contributions in Relation to Research Papers

RQ	Contributions	Publication 1	Publication 2	Publication 3	Publication 4	Publication 5
RQ1	1,2	✓	✓			
RQ2	3,4			✓	✓	
RQ3	5					✓
RQ4	5					✓

The above-mentioned contributions are related to research papers (listed previously and available in full in appendices A-E).

1.5 Organization of the Thesis

This PhD thesis is structured into five chapters;

1. **Introduction:** The introductory chapter provides an overview of the background, motivation, and current research trends in droplet size control within microfluidic devices.
2. **Chapter 2:** delves into closed-loop simulations to enhance droplet generation precision, addressing challenges in control system parameter evaluation and PID controller optimization. It follows a chronological discussion of literature review, methodologies, results, and conclusions.
3. **Chapter 3:** Bridging simulations with practical applications, this chapter explores dual-PID control strategies and genetic algorithm-tuned controllers in experimental setups. Furthermore, it explores how simulations contribute to the formation of empirical models.
4. **Chapter 4:** Introducing the Proximal Policy Optimization (PPO) algorithm, this chapter evaluates its effectiveness for precise droplet size control, including its resilience to external disturbances and numerical model validation against experimental data. It discusses the state-of-art, methodology, results, and conclusions.
5. The final chapter serves as the conclusion, summarizing the findings presented in the thesis and future research direction.

2 SIMULATION OF CLOSED LOOP DROPLET SIZE CONTROL

This study proposes using a simulated closed-loop feedback control in microfluidics. The simulation create virtual replicas of real systems. They provide a risk-free environment for experimenting with new control functionalities and parameter optimization, saving both time and cost. This approach is especially useful when iterative experiments in real-life settings are expensive and time-consuming.

The study introduces simulated environment integrating microfluidic devices with PID and PI controllers to tackle specific challenges. Publication I focuses on evaluating the complete parameter space of controllers, while Publication II focuses on optimizing controller performance through an alternative tuning method.

Publications I: (Section 2.1)

Gyimah, N., Scheler, O., Rang, T., & Pardy, T. (2022). Digital twin for controlled generation of water-in-oil microdroplets with required size. 1-7. 10.1109/EuroSimE54907.2022.9758876.

Publication II: (Section 2.2)

N. Gyimah, R. Jõemaa, K. Pärnamets, O. Scheler, T. Rang, and T. Pardy, "PID Controller Tuning Optimization Using Genetic Algorithm for Droplet Size Control in Microfluidics," 2022.

2.1 Closed-loop simulation for parameter space evaluation

2.1.1 State-of-the-Art

Recent studies have shown progress in closed-loop microfluidic control, especially with classical methods like PID and PI controllers. Miller et al. [35] introduced automated droplet generation in 2010, which included syringe pumps, a droplet sensor, and a control algorithm. However, challenges arose due to unclear image processing, leading to limited droplet uniformity of $\pm 5\%$. attributed to an unclear and slow image processing method. Subsequent advancements have showcased diverse approaches. Fu et al.'s [47] electrical-detection system in 2016 employed a PI controller for precision, albeit focusing on a single droplet size (200 μm).

Wang et al. [48] demonstrated robust performance and high uniformity ($\pm 3\%$) in automated droplet characterization in 2016 but were confined to a singular droplet size (100 μm). Cantwell et al. [49] improved capabilities by integrating image-based closed-loop feedback to control droplet size and composition, resulting in significant enhancements. However, their evaluations were restricted to two droplet size setpoints of 300 pL and 200 pL volumes. Zeng et al.'s [50] study established a closed-loop control system for monodisperse droplet size control, revealing a linear relation between droplet length and flow rate ratio. However, the focus remained on a single droplet length step response in a T-junction microdroplet generator.

Notably, recent years have seen a paradigm shift toward exploring controller evaluations across a broader spectrum of droplet sizes. For instance, Duan et al.[41] achieved precise control over droplet sizes ranging from 0.25 to 1.4 nL using a PID controller. In their study, Zeng et al. [42] achieved a closed-loop CV% of less than 2% using a PI controller. The experiment focused on droplet sizes between 100 μm and 700 μm and tested six different setpoints. The results showcased enhanced versatility. Xie et al. [44] achieved droplet size target R_2 value of 0.98 for a PI controller regulating droplet sizes ranging from

14 to 24 μm . Mottaghi et al. [45] demonstrated advanced closed-loop control precision by utilizing a PID controller with a low error RSME of 0.48% for droplet sizes of 100, 140, and 160 μm .

Challenges remain in fully exploring parameter spaces due to resource-intensive experimental evaluations. To address this, integrating simulations is proposed, providing a virtual platform for systematic assessment of controller parameters. This approach expedites research and streamlines the development of more robust closed-loop control strategies for a diverse range of droplet sizes.

2.1.2 Methodology

2.1.2.1 Simulation Framework and Numerical model

The study employs a simulation based on 2D computational fluid dynamics simulation, integrating an external control algorithm to establish a closed-loop system for droplet size control. It ensures an accurate representation of real-world droplet microfluidic systems, encompassing microfluidic devices, immiscible fluids, pumps, and essential components for droplet imaging and measurements. To that effect, the simulated environment emulates a syringe-pump-driven microfluidics device, delivering fluids into the chip at defined flow rates. Within the setup, the microfluidic system incorporates a chip where adjustable flow rates are applied at channel inlets, alongside a selection of fluids of interest and a droplet measurement scheme, creating a controlled model.

Choosing 2D modeling over 3D is driven by tailored assumptions for microfluidics, like high aspect ratios and minimal vertical effects [51]. This maintains accuracy while enabling efficient computations, validated by prior studies [52, 53].

The microfluidic chip is modeled on the Flow-Focusing Device (FFD) geometry. The choice to model the microfluidic chip on the Flow-Focusing Device (FFD) geometry is based on its similarity to prior experimental setups in our research group and its relevance. This geometry presents challenges in predicting droplet size due to nonlinear relationships with flow-rate parameters observed in past research, underscoring the need for thorough investigation and tailored control strategies [54, 26, 55].

In replicating real-world droplet detection, droplets are identified at a specific section of the Flow-Focusing Device (FFD) outlet channel referred to as the sensor (of the droplet size). At this location, the droplet interface is captured to estimate the droplet size or diameter. Droplet size is equated to the droplet diameter, consistent with many previous numerical modeling works[56, 57, 58, 59]. Post-processing of sensed droplet interface data conducted in near real-time as the droplets are produced at the outlet.

Recognizing the influence of factors such as flow rate, viscosity, surface tension, and geometry on droplet size, our study emphasizes flow rate as a critical and versatile parameter that can be automatically adjusted via the controller. The control strategy focuses on a singular fluid phase flow rate as the control variable, maintaining fixed values for other parameters, aligning with established practices[45, 43].

Finally, the integrated Proportional-Integral (PI) controller for closed-loop control operates independently. Functioning in a distinct programming environment, it seamlessly interfaces with the computational fluid dynamics simulation, ensuring effective coordination between the control system and the simulation.

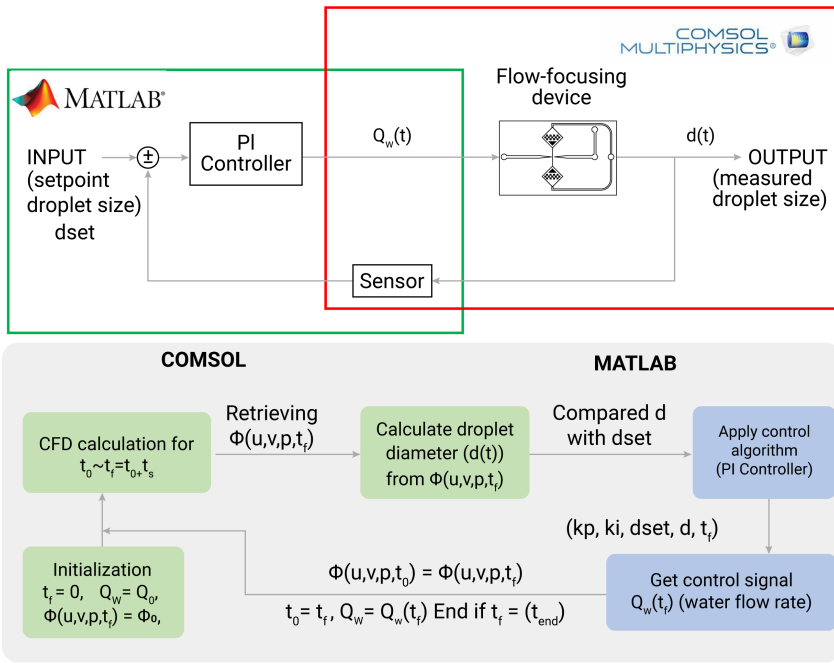


Figure 2: Simulation Framework for Droplet Size Control (a) Flow-focusing device as the plant model with user-defined droplet size ($dset$) and control flow rate ($Q_w(t)$). COMSOL LiveLink interface enables MATLAB's PI controller to adjust ($Q_w(t)$) based on feedback ($d(t)$). (b) Illustration of simulation settings: t_0 as initialization time, t_f as current simulation time, t_s for feedback loop sampling time, t_{end} as simulation end time. (u, v) denote variable velocities and pressure relative to ϕ .

The loop-control environment is constructed using COMSOL Multiphysics software (version 5.4) for Computational Fluid Dynamics (CFD) simulation and MATLAB software for the PI controller implementation. The integration of these two software platforms is facilitated through COMSOL LiveLink for MATLAB, ensuring a seamless combination of their capabilities. Additionally, Autodesk Inventor software is employed for the 2D microfluidic chip model design, which is then imported into COMSOL as the system/plant model. Figure 2 illustrates the framework.

Within this framework, the flow-focusing device serves as the plant model, with the user-defined droplet size represented by the $dset$ signal. The control flow rate signal, denoted as $Q_w(t)$, is applied to an inlet channel of the microfluidic chip, while the measured droplet diameter ($d(t)$) is obtained in the sensor region. The measured droplet data $d(t)$ is actively exchanged via the LiveLink interface, and the PI controller in MATLAB interprets this feedback data. It computes a control signal, adjusting the phase flow rate $Q_w(t)$, which is then transmitted back to COMSOL for automated application as the modified control signal after each simulation iteration. This continuous exchange via LiveLink continues until the user-defined droplet size ($dset$ signal) is reached and maintained with the final control signal output. The model response to change in controlled signal is visualized within the COMSOL interface. This efficient bidirectional communication establishes closed-loop droplet size control with the PI controller.

In exploring numerical method, the focus is on the continuum method within Computational Fluid Dynamics (CFD), addressing challenges related to multiphase fluid flow and continuously deforming interfaces [60]. The use of an interface-capturing method, em-

ploying a continuous "indicator function" to distinguish phases, is highlighted for its ability to manage topological changes smoothly without intricate grid realignment, offering advantages over interface-tracking methods [61, 62]. Among interface-capturing methods, the Level Set Method (LSM) stands out for its accurate interface representation and continuous level set function, addressing discontinuity issues observed in other methods like Volume-of-Fluid (VOF) [63]. LSM's successful extension to droplet generation scenarios underscores its instrumental role in investigating the impact of geometric and fluidic parameters on droplet characteristics [63, 64, 65, 66].

COMSOL Multiphysics, although not employing VOF, offers LSM and phase-field models (PFM), with LSM preferred for its smoother interface representation and support from other researchers in droplet microfluidics studies using COMSOL software [67, 68, 69]. These considerations collectively emphasize the robustness and suitability of LSM as the chosen numerical method [60, 63].

The CFD model utilizes a two phase level-set numerical method (LSM) to simulate water-in-oil droplet dynamics within an FFD microfluidic chip. The governing equations for the two-phase fluids, representing the dispersed phase (water) and the continuous phase (oil), comprise the incompressible Navier-Stokes equation (1), the continuity equation (2), and the level-set equation (3). The delineation of the interface between the dispersed and continuous phases is precisely captured by the 0.5 level-set of the function ϕ , following the modified conservative LSM proposed by Olsson and Kreiss[63]. This function seamlessly transitions over a constant thickness layer from zero (indicating the continuous oil phase) to one (representing the dispersed water phase).

Navier-Stokes equation

$$\rho \left(\frac{\partial u}{\partial t} \right) + \rho(u \cdot \nabla)u = \nabla \cdot \left(-pI + \mu (\nabla u + (\nabla u))^T \right) + F_{st} \quad (1)$$

Continuity equation

$$\nabla \cdot u = 0 \quad (2)$$

Level set equation

$$\rho \left(\frac{\partial \phi}{\partial t} \right) + u \cdot \nabla \phi = \gamma \nabla \cdot (-\phi(I - \phi)(\nabla \phi / |\nabla \phi|) + \varepsilon \nabla \phi) \quad (3)$$

Key variables in these equations include velocity (u , m/s), density (ρ , kg/m³), pressure (p , N/m²), dynamic viscosity (μ , Ns/m²), surface tension force (F_{st} , N/m³), and a re-initialization parameter γ (m/s). The construction of the level-set function (ϕ) in equation 3 is intricately linked to the velocity values obtained by solving equations 1 and 2. The parameter ε (m) controls the interface thickness over which ϕ transitions from 0 to 1, with its value carefully chosen to align with the computational mesh size[70]. Specifically, γ and ε are set at 0.2 m/s and 5e-6 m, respectively.

The density (ρ) and dynamic viscosity (μ) in equation 1 are calculated using equations 4 and 5, incorporating ρ_0 and ρ_w , μ_0 and μ_w as the densities and viscosities of the continuous and dispersed phases, respectively.

$$\rho = \rho_0 + (\rho_w - \rho_0)\phi \quad (4)$$

$$\mu = \mu_0 + (\mu_w - \mu_0)\phi \quad (5)$$

Additionally, the critical parameter of effective droplet diameter (d) is computed in COMSOL using Equation (6). This calculation determines the maximum area in the sensor

region corresponding to the dispersed phase where $\phi > 0.5$.

$$d = 2\sqrt{(1/\pi)} \int_{(-\phi \geq 0.5)} d\Omega \quad (6)$$

Leveraging the inherent horizontal axis of symmetry of the microfluidic device, the simulation refines the original model illustrated in Figure 3a. Specifically concentrating on the upper half of the 2D model, as depicted in Figure 3b, and generating only half-droplets, foresees a substantial computational time reduction by a factor of 2. In the post-processing phase, the simulated upper half is mirrored to replicate the lower half, facilitating the visualization of complete droplets. Further simplification involves excluding the air inlet near the chip's outlet channel, initially designed as a pressure gauge outlet, due to its negligible impact on droplet formation. Notably, the model incorporates rhomboid filters along the oil liquid path, effectively eliminating contaminants, including dust particles, in experimental setups. The streamlined model specifies key dimensions, including a water inlet width (W1) of 600 μm , an outlet width (W5) of 90 μm , oil inlet width (W6), and junction width (W4) of 120 μm each, along with a sensor region length (L5) of 100 μm . For comprehensive details, including these dimensions, see Table I in the Appendix 1.

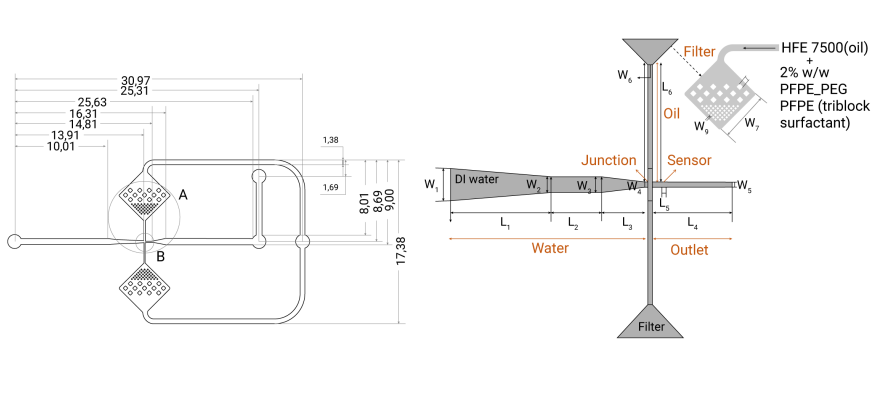


Figure 3: Flow-Focusing Device Geometry. Left: Full geometry. Right: Simplified version. Domains labeled: Oil, Water, Junction, Sensor, Outlet. Rhomboid filters on oil path. Horizontal symmetry, only upper half simulated.

For droplet generation, the continuous phase consists of HFE 7500 (oil)[71] with properties: density (ρ_o) of 1614 kg/m^3 and viscosity (μ_o) of 0.00077 Pa.s. This is blended with a 2% w/w PFPE-PEG-PFPE surfactant solution. The dispersed phase, water, exhibits properties: density (ρ_w) of 1000 kg/m^3 and viscosity (μ_w) of 0.001 Pa.s. The surface tension (FST) between fluid interfaces is precisely set at 1.9e-3 N/m^2 [72, 73].

In terms of boundary conditions, both inlet and outlet channels are subjected to laminar inflow conditions. Fully developed volumetric flow rates (Q_w for dispersed phase, Q_o for continuous phase) are precisely specified at their respective channel inlets, with the outlet channel pressure set at 0 Pa (gauge). The channel walls are characterized by a slip length of 5e-6 m, and a no-slip boundary condition is applied to the solid wall, maintaining a fixed fluid-wall contact angle of 135 degrees. In 2D microfluidics simulations, the assumption of complete wall wetting with the continuous phase fluid is considered valid. This is supported by the fact that the length of the microchannel is typically much

greater than its width, resulting in negligible flow in the corners. The application of this assumption can be found literature [74, 75].

Within the fluidic domains, laminar flow and level-set physics interfaces seamlessly operate, under the two-phase level-set method. Extending beyond the Laminar flow and Level set domains, the incorporation of Domain Ordinary Differential Equations (ODEs) and Differential-Algebraic Equations (DAEs), along with the Global equations domain, facilitates the tracking of state variables such as velocities and pressures, and the level-set function in the sensor region to establish conditions for estimating droplet size at each simulation timestep. For Droplet tracking and defining of conditions for applying control signal, the expressions below are used;

Tracking Droplet Area: $\text{nojac}(\text{if}(\text{d}(\text{diameter},t) > 0 \text{ d}(\text{diameter},t) < 1\text{e-}5, \text{aveop1}(u_2) [\text{m}], \text{diameter}))$

Condition to apply control signal : $u_4 (\text{u4- nojac}(\text{if}(\text{d}(\text{aveop1}(u_3),t) = 0, Q_w, u_4)))$

where Velocity (u), dependent variables u_2, u_3 , state variable u_4 , and pressure (p), computations are carried out by solver.

For the study's time-dependence, a time range spanning from 0 to 0.1 seconds with a step of 0.0005 seconds is employed to ensure simulation convergence. All boundary conditions are consolidated in Table 2 (Appendix 1). Finally, for mesh generation, predominantly, quadrilateral elements are employed, with node sizes customized for each domain as illustrated in Figure 4. Following this, a mesh independence study is conducted to ensure accuracy. The primary goal of this study is to achieve minimal variation, ideally within 2%, in droplet area measurements by optimizing the mesh design. Simulation are executed on a computing setup comprising a Core i5-10210U CPU, 32 GB RAM, and a 1 TB NVMe SSD. Each simulation required approx. 10 to 20 hours to complete.



Figure 4: Tailored quadrilateral mesh with region-specific density. Avg. mesh quality: 97%. Total elements: 270,908. Mesh independence study confirms <1% droplet area variation with $\geq 225,000$ elements (Appendix section of Appendix 1)

2.1.2.2 Control theory and Design

The study adopts a classical control approach, employing well-established principles and mathematical models to design controllers, with a focus on closed-loop systems utilizing feedback for sustained target performance. A Proportional-Integral (PI) controller is chosen for regulating droplet size in Computational Fluid Dynamics (CFD) models. The PI controller is defined by two components, as depicted in equation 7: the proportional (K_p) term and the integral (K_i) term. The proportional term delivers an immediate response to the present error ($e(t)$), representing the disparity between the desired setpoint and the actual system output. On the other hand, the integral term takes into account the historical accumulation of past errors over time [76].

$$u(t) = K_p \dot{e}(t) + K_i \int_0^t e(\tau) d\tau \quad (7)$$

Where:

- $u(t)$ is the control output.
- K_p is the proportional gain.
- K_i is the integral gain.
- $e(t)$ is the error at time t .
- $\int_0^t e(\tau) d\tau$ represents the integral of the error over time.

Unlike PID controllers, PI controllers exclude the derivative term to sidestep sensitivity issues, ensuring effective control loop performance. The controller design involved tuning the PI controller through adjustments of the parameters K_p and K_i to achieve the desired system response. This process requires striking a balance between system stability, response time, and minimizing overshoot. The controller design involves tuning the PI controller parameters (K_p and K_i) to balance system stability, response time, and overshoot. MATLAB's Control System Designer Toolbox [76] facilitates controller design through interactive tuning, aligning with specified design criteria. Initial conditions of experimental setting are considered in the modeling process explained in section C of Appendix 1.

The design criteria included:

- Zero steady-state error
- Rise time ≤ 0.5 s
- Settling time ≤ 4 s
- Maximum overshoot $\leq 10\%$.

To meet specific design criteria, the PI controller's gain parameters were adjusted, balancing between achieving a fast response and minimizing overshoot, depending on the application's unique requirements. The implementation involved automatic adjustment of the PI controller using the PID tuner in the Control System Designer Toolbox. Transfer function models of the closed loop were imported into the toolbox, and the PID Tuner App was utilized to configure PID block settings for controller type, form, time domain, and sample time, in accordance with the design criteria. Detailed tuning processes, including parameters and settings, can be referenced in [15]. The result is a PID compensator transfer function with corresponding step response, as illustrated in Figure 5.

Finally, while continuous-time signals (analog signals) have been used in this simulation, digital control with discrete-time signals is widely adopted in practice. Analog controllers use continuous-time signals, while digital controllers work with discrete-time signals. An analog controller can be built using operational amplifiers, capacitors, and resistors [77], but it cannot be directly used with computers or microprocessors. To make it compatible, it needs to be converted into a discrete-time controller [78], requiring additional components like A/D (Analog to Digital) and D/A (Digital to Analog) converters to convert between continuous and discrete signals. This conversion from continuous-time to discrete-time results in an approximation of the original controller. The key processes involved in this conversion are sampling and quantization. Sampling involves taking measurements of the continuous-time signal at specific intervals, while quantization involves

mapping the amplitude of these samples to discrete levels. By using a high sampling rate and high-resolution quantization, aliasing and quantization noise can be minimized. This ensures the Signal-to-Noise Ratio (SNR) remains high. If the maximum difference between the digitized quantity and its analog value is below the noise level, the effects of digitization become negligible.

Alternatively, a controller can be designed directly in the discrete-time domain. Continuous-time controllers are typically designed in the frequency domain (s -domain), while discrete-time controllers are designed in the difference domain (z -domain). To design a controller in the discrete-time domain, the plant's transfer function must be converted from the s -domain to the z -domain [79]. This can be done using a zero-order hold (ZOH) approximation [80]. Overall, both converting a continuous-time PID controller and designing a discrete-time PID controller directly are viable methods for use.

To demonstrate the shift from analog to digital control practically, the follow-up study (Appendix 3, Section II-B-5) implemented a controller on a Raspberry Pi. This setup minimized signal digitization effects through a three-stage process. The first stage involved using a 2nd order Sallen-Key low pass filter to capture the droplet feedback signal. This filter, with a cutoff frequency of approximately 7.26 kHz, could process up to 5000 droplets per second with minimal distortion. Its primary function was to reduce noise, especially from switch-mode power supplies. Next, an adjustable inverting amplifier stage was employed to scale the filtered signal to match the input limits of the 16-bit ADC (ADS8681 from Texas Instruments). This adjustment optimized the amount of information captured per bit during the analog-to-digital conversion process. Finally, the 16-bit ADC converted the scaled analog signal into digital format, preparing it for further processing. To detect droplets from the feedback signal as they moved over an optical sensor, the average loop duration on the Raspberry Pi, handling ADC polling and its evaluation, was about 6.5 μ s, translating to a maximum ADC sampling rate of approximately 153 kHz. This setup ensured efficient signal handling within the Raspberry Pi's digital environment, demonstrating successful analog-to-digital conversion with minimal impact from digitization.

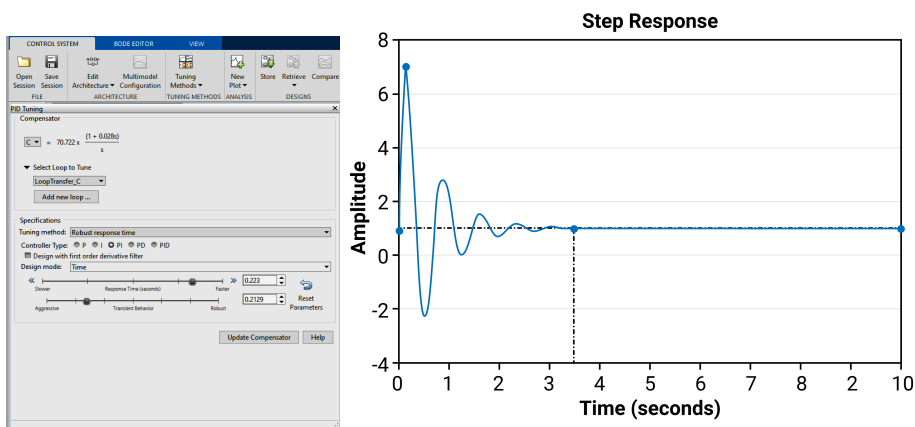


Figure 5: Controller Design Interface in MATLAB Control Systems Designer Toolbox (left) and Step Response Based on Design Criteria (right)

2.1.3 Results and Discussion

2.1.3.1 Droplet Formation & Effect of Fluid Flow Rates

In the study, droplets were observed in the dripping flow regime, where the dispersed phase exerts an inward force, causing droplets to break near the channel junction. This occurs when the Capillary number (Ca) exceeds 10^{-2} , and the dispersed phase flow rate is lower than the continuous phase flow rate. The four stages of droplet formation in this regime were identified and presented in Figure 6: Filling (Figure 6a), Necking (Figure 6b), Growing (Figure 6c), and Detachment (Figure 6d).

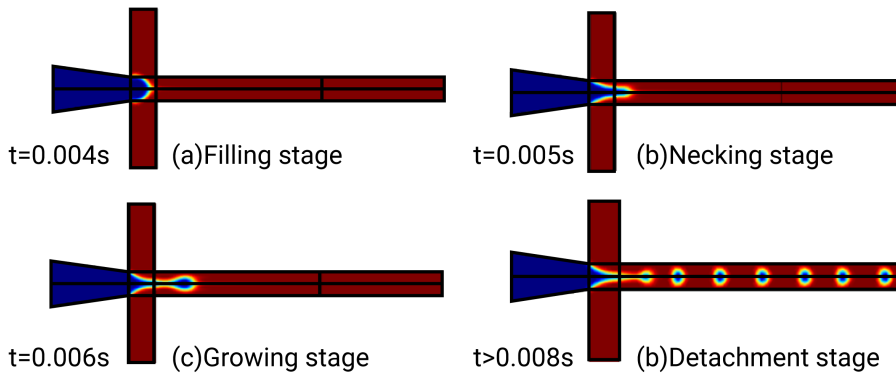


Figure 6: Dripping Regime observed for droplet formation, in stages (a) Filling stage, (b) Necking stage, (c) Growing stage, and (d) Detachment stage.

During the Filling stage (0.020 s – 0.040 s), continuous and dispersed phase fluids converge at the microchannel junction. In the subsequent Necking stage (0.040s – 0.050s), the dispersed phase undergoes constriction in the junction by the continuous phase, influenced by fluid flow rates, surface tension, and viscous forces, resulting in a capillary instability. This instability leads to the oil phase inducing a flow-focusing effect on the water phase in the third stage (0.050s–0.060s), forming a growing water bulb immediately after the junction. The stages culminate in the Detachment stage ($> 0.080s$), where the growing water bulb breaks into droplets close to the junction, defining the characteristic dripping regime [81].

In addition, the research explored how fluid flow rates affected droplet size by keeping one rate constant while varying the other. Initially, the impact of continuous phase flow rate was studied with a constant dispersed phase flow rate of $30 \mu\text{L}/\text{min}$. The continuous phase flow rate ranged from $100 \mu\text{L}/\text{min}$ to $400 \mu\text{L}/\text{min}$. In Figure 7a, it was observed that as the continuous phase flow rate increased, the average droplet diameter decreased. Specifically, when the oil flow rate increased from $100 \mu\text{L}/\text{min}$ to $400 \mu\text{L}/\text{min}$ (a 300% increase), the droplet diameter reduced by 70%, from $110 \mu\text{m}$ to $33 \mu\text{m}$, indicating a non-linear relation.

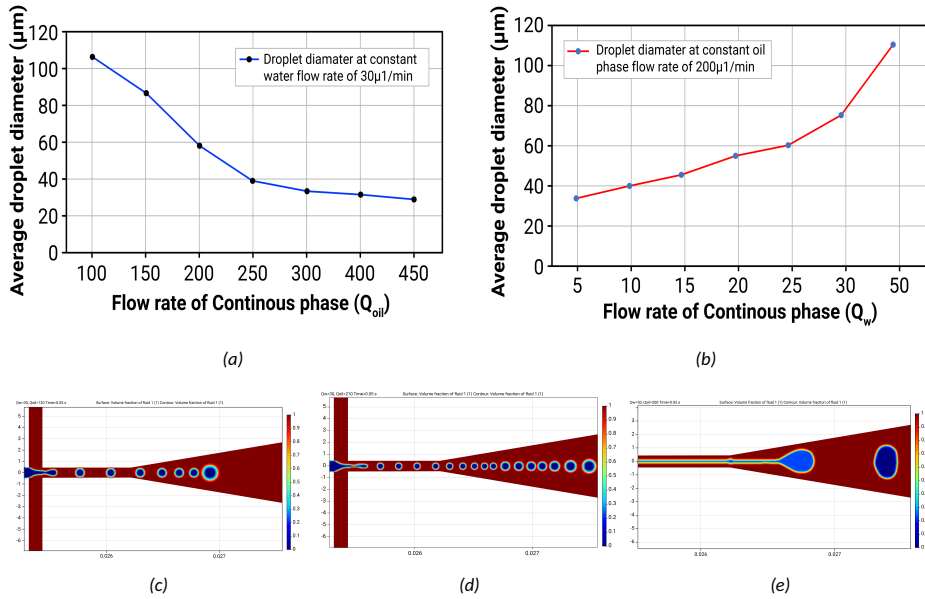


Figure 7: Influence of Flow Rate on Droplet Size(a) Varied oil flow rates (100 $\mu\text{l}/\text{min}$ to 400 $\mu\text{l}/\text{min}$) with constant water flow rate (30 $\mu\text{l}/\text{min}$) (b) Varied water flow rates (5 $\mu\text{l}/\text{min}$ to 50 $\mu\text{l}/\text{min}$) with constant oil flow rate (200 $\mu\text{l}/\text{min}$). Further illustration of droplets for Q_w/Q_{oil} at (c)30/210 (d) 30/120 (e) 50/200. Sensitivity of droplet size to changes higher for water flow rate than oil flow rate.

Subsequently, the influence of the dispersed phase flow rate on droplet size was examined with a constant continuous phase flow rate of 400 $\mu\text{L}/\text{min}$ and adjusting the dispersed phase flow rate from 5 to 50 $\mu\text{L}/\text{min}$. Figure 7b showed a contrasting trend—as the dispersed phase flow rate increased, the average droplet diameter significantly grew. With the water flow rate increasing from 5 $\mu\text{L}/\text{min}$ to 50 $\mu\text{L}/\text{min}$ (a 900% increase), the droplet diameter increased by 223.529%, from 34 $\mu\text{L}/\text{min}$ to 110 μm .

Thus, the droplet size exhibited non-linear sensitivity to the flow rates of both fluids and could be manipulated by adjusting either the continuous phase fluid flow rate or the dispersed phase fluid flow rate. The study highlighted a more pronounced influence on droplet size with variations in the dispersed phase flow rate. Consequently, the dispersed phase flow rate was identified as the key control variable.

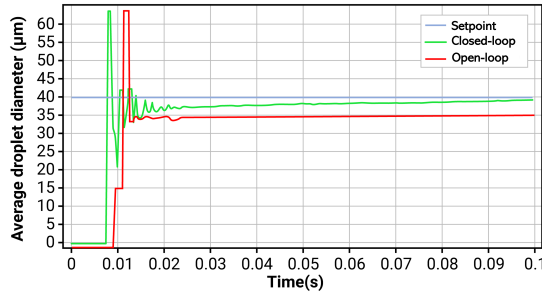
2.1.3.2 Controller performance evaluation

The implemented controller, with gains $K_p = 2$ and $K_i = 70$ regulates droplet size using the dispersed phase flow rate ($Q_d(t)$) with the control law $Q_d(t) = K_p * e(t) + K_i * \int e(t)dt$ based. These gains provide a moderate proportional response ($K_p = 2$), striking a balance between response speed and stability.

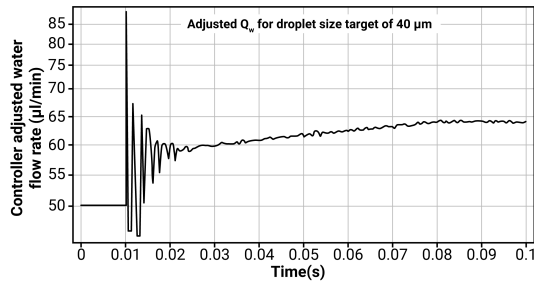
To effectively showcase the controller's performance, a comparison between open-loop and closed-loop scenarios was conducted and showcased in (Figure 8a) In the open-loop scenario, where the system lacked automatic adjustments, a setpoint droplet size of 40 μm was targeted with a continuous phase flow rate of 400 $\mu\text{l}/\text{min}$ and an initial dispersed phase flow rate of 50 $\mu\text{l}/\text{min}$. In the open-loop control, the system exhibited a

noticeable deviation ($CV \sim 15\%$) from the setpoint, reaching around $34 \mu\text{m}$ by the simulation end. Conversely, the closed-loop feedback scenario, equipped with a PI controller for autonomous adjustments, achieved a measured droplet size of $39 \mu\text{m}$ within 1 second. The $CV\%$ reduced from 15% to 2% , closely matching the setpoint. Continuous adjustments maintained the desired droplet size, and the dispersed phase flow rate stabilized at $63.9 \mu\text{l}/\text{min}$ (Figure 8b). Although an initial disparity existed between measured and desired droplet sizes in the closed-loop feedback scenario, this difference diminished over time, approaching zero. The closed-loop system demonstrated superior accuracy and consistency in droplet size control compared to open-loop.

Moreover, in the assessment of the complete parameter space of the PI-controlled system, the generation of droplets across various setpoints ranging from $30 \mu\text{m}$ to $60 \mu\text{m}$ was analysed. This evaluation covered six specific setpoints, as depicted in Figure 9, showcasing the PI controller's efficacy. The results illustrated in Figure 9(a-c) for setpoints of $30 \mu\text{m}$, $35 \mu\text{m}$, and $45 \mu\text{m}$, showed the controller maintained a diameter offset/error of less than 3% within a simulation time of 1s. The agreement between the target and measured droplet diameters, with a coefficient of determination (R^2) value of 0.9937 , serves as a demonstration of the controller's efficiency across the $30\text{-}60 \mu\text{m}$ range, as depicted in Figure 9d. This analysis established the complete parameter space of the controller.



(a)



(b)

Figure 8: Open-loop vs. Closed-loop Droplet Control: (a) Open-loop aimed for a $40 \mu\text{m}$ droplet with $400 \mu\text{l}/\text{min}$ continuous phase and $50 \mu\text{l}/\text{min}$ initial dispersed phase flow rates, resulting in $CV \sim 15\%$ deviation to around $34 \mu\text{m}$. Closed-loop with a PI controller rapidly achieved $39 \mu\text{m}$ within 1 s, reducing CV to 2% (b) Controller maintained desired droplet size with stable dispersed phase flow rate at $63.9 \mu\text{l}/\text{min}$.

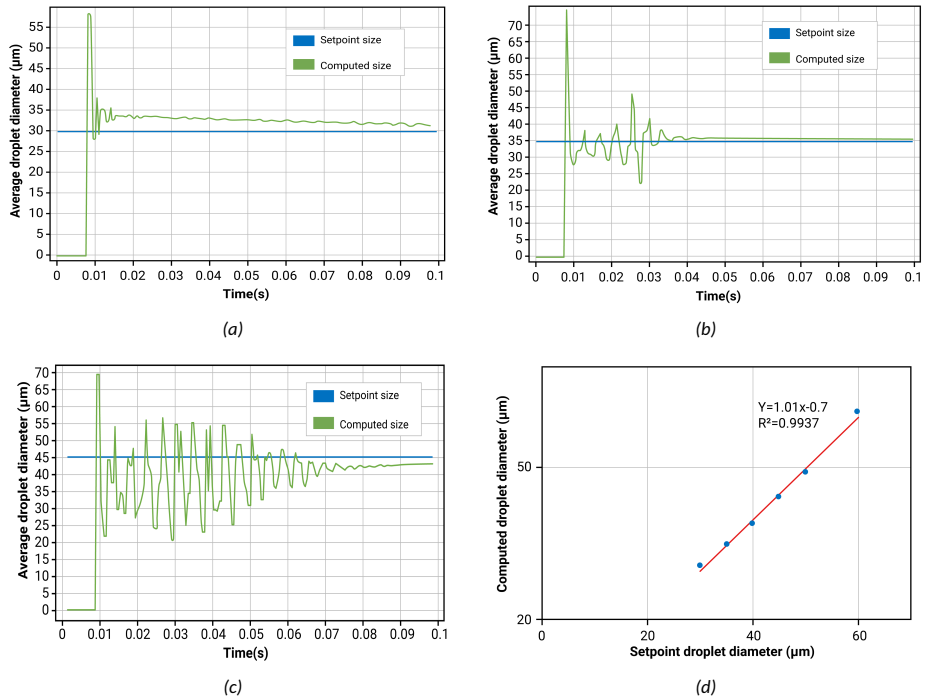


Figure 9: Closed-loop Droplet Size Control at setpoints (a) 30 μm , (b) 35 μm , and (c) 45 μm (d) Comparison of setpoint diameters to observed diameters (30 μm -60 μm range). The PI controller maintains a diameter error under 3%, with a coefficient of determination (R^2) value of 0.9937

2.2 Genetic Algorithm (GA) for controller tuning

2.2.1 State-of-the-Art

The study investigates extended settling times in feedback systems. Miller et al. employed a closed-loop PI control system for microfluidic droplet production, but with a relatively high settling time of around 100 seconds [35]. Xie et al. implemented a closed-loop system for adjusting microbubble diameters, but despite a high agreement between setpoint and measured sizes, settling times remained relatively high, under 10 seconds [44]. Kebriaei et al. showcased settling times ranging from 7 to 10 seconds in their closed-loop system utilizing a pressure-driven flow-focusing junction and a PID controller [43]. Duan et al. presented a closed-loop feedback control model for droplet generation with a relatively low settling time of around 0.3 seconds [41]. Crawford et al. demonstrated closed-loop feedback with significantly lower settling times of 0.05 seconds [39]. Zeng et al. designed a closed-loop control microfluidic system with a response time of less than 0.2 seconds [42].

The study recognizes the importance of minimizing settling times, particularly for high throughputs exceeding 500 Hz in flow-focusing microfluidic devices [44]. Reduced settling times are vital for effective real-time regulation of droplet size, aligning with goals of enhancing microfluidic system efficiency. To address the challenge of extended settling times, the study focuses on tuning methodology, acknowledging the impact of the pumping system on control system response. Anticipating quicker responses in pressure-driven systems compared to syringe pumps [39], the study aims to optimize tuning processes in controller design. Thus, it explored advanced soft computing optimization technique,

specifically the genetic algorithm (GA), in deriving optimal PID controller parameters [82]. The Genetic Algorithm (GA) is an optimization technique inspired by natural selection and genetics. The genetic algorithm offers robust searching capabilities and simplicity, making it suitable for addressing nonlinear systems and optimizing complex problems. The genetic algorithm offers robust searching capabilities and simplicity, making it suitable for addressing nonlinear systems and optimizing complex problems.

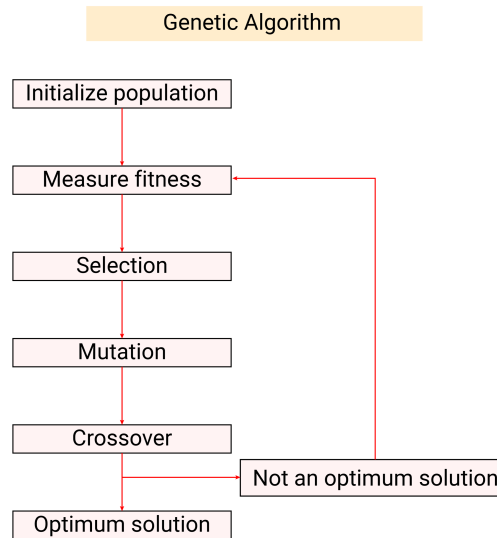


Figure 10: Genetic Algorithm Workflow

Genetic algorithms (GAs) are search methods inspired by biological evolution and Darwin's concept of survival of the fittest. They excel in handling complex problems and avoiding misleading solutions encountered in gradient descent methods [83].

The GA process begins with generating a random population, where each chromosome represents a potential solution. An objective function evaluates individual performance based on goals like minimizing overshoot and achieving rapid settling time. Chromosomes with higher fitness values are selected for the next generation, akin to a "survival of the fittest" strategy. Crossover and mutation operations create offspring with favorable attributes from their parent chromosomes, refining the population iteratively. The algorithm continues until a satisfactory solution is found [84].

Convergence towards optimal solutions requires parameter tuning like population size, crossover and mutation rates, and termination criteria. The choice of chromosome representation and the design of the objective function also influence the GA's effectiveness [82].

A PID controller (Equation 8) is utilized, incorporating proportional (K_p), integral (K_i), and derivative gains (K_d). Unlike in PI controllers, the derivative component, which reacts to changes in the error rate, is included. In designing a GA-tuned PID controller, the objective is to minimize the error $e(t)$ in the controlled system, considering factors like overshoot, rise time, and settling time, represented by the variable f in the optimization problem (Equation 9) [85]. This variable captures the transient step response of the system and serves as the objective function.

$$u(t) = K_p e(t) + K_i \int_0^t e(\tau) d\tau + K_d \frac{de(t)}{dt} \quad (8)$$

$$\min f(k_p, k_i, k_d) \quad (9)$$

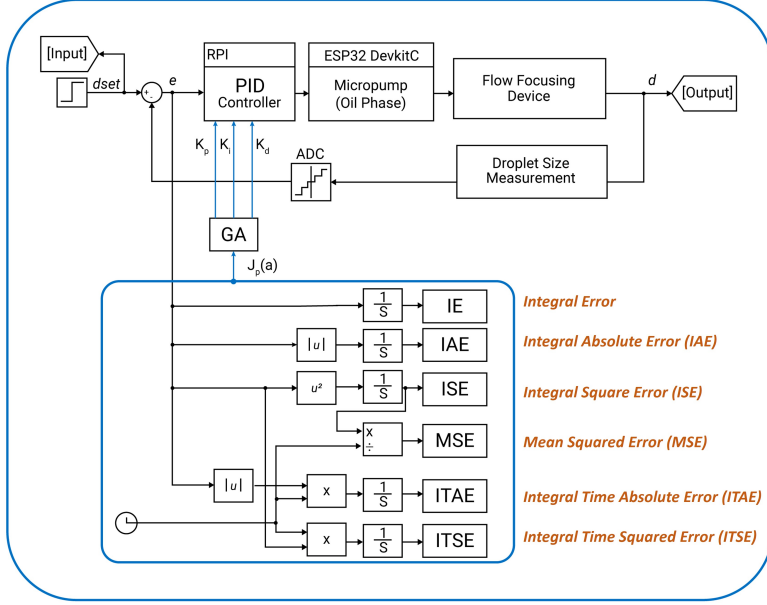


Figure 11: Schematic representation of PID parameters (K_p , K_i , K_d) tuning using Genetic algorithm to minimize error between desired and measured droplet size, considering performance criteria (IAE, ISE, ITAE). Setup conducted using MATLAB and Simulink.

2.2.2 Methodology of GA-tuned-PID controllers

The framework of the Genetic Algorithm (GA)-tuned PID controlled system is depicted in Figure 11. Chromosomes in the population represent PID controller parameters, K_p , K_i , and K_d , selected based on fitness values, particularly the error index [86]. After selection, high-fitness chromosomes undergo arithmetic crossover and mutation operations. A mutation probability of 0.1 is employed, randomly modifying a gene within an individual's chromosome [87]. The population size is 20, with a maximum of 30 generations, and the bounds for controller gain parameters K_p , K_i , K_d are set as $[0 \ 1; 1 \ 70; 0 \ 1e - 4]$, respectively. In the optimization process (Figure 11), the objective function $J_n(\alpha)$ refines PID controller gains α , evaluated against performance criteria n [88, 89]. Six performance indices gauge the GA optimization: Integral Absolute Error (IAE) covers both positive and negative errors, Integral Square Error (ISE) penalizes errors in both polarities, and Integral Time Absolute Error (ITAE) prioritizes reducing prolonged transients. Additional metrics like Integral of Time multiplied by the Squared Error (ITSE) and Mean Squared Error (MSE) offer further insights [88, 89].

MATLAB and Simulink are utilized for system modeling and genetic algorithm setup. MATLAB's optimization toolbox facilitates GA setup, while Simulink dynamically updates PID parameters during each iteration [86, 87]. Simulations continue until termination criteria (i.e. fitness value and maximum iteration number) are met [88, 89].

To model the dynamic characteristics of system components in the Simulink environment for the pressure-driven microfluidics setup, a combination of system identification techniques and analytic modeling was employed. The System Identification Toolbox in MATLAB (R2021b) facilitated this process [90, 91]. Figure 12 illustrates the system identification process used for modeling the pump and the microfluidic chip. Analytic modeling was utilized to create mathematical representations of the droplet measurement circuit (Section B of Appendix 2).

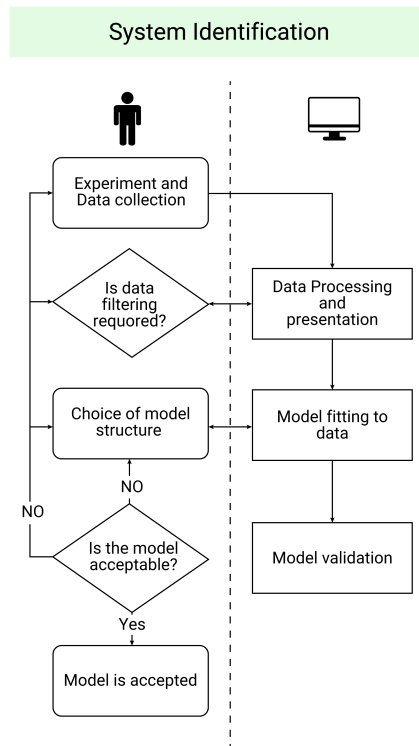


Figure 12: Steps in System Identification Technique

The experimental setup, depicted in Figure 13, included the following components:

- Flow-focusing PDMS microfluidic chip
- Fluidic add-ons: a. fluid connectors b. Teflon (0.8 mm) tubing c. chip handling frame
- Reagents: a. mineral oil + 2% w/w Span 80 surfactant (continuous phase) b. deionized water (dispersed phase)
- Pumping system [92]
- ADC (ADS8681)
- MPRLS0015PG0000SA Pressure Sensors
- Droplet size measurement circuitry (Section B of Appendix 2)
- Raspberry Pi 4B

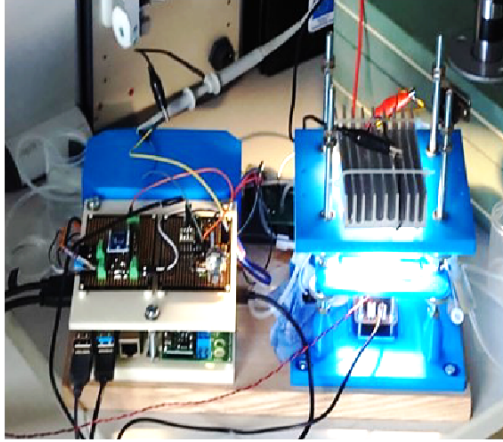


Figure 13: Experimental Setup for Microfluidic System Characterization. Featuring PDMS chip, fluid connectors, pumping system, ADC, pressure sensors, droplet size circuitry, and Raspberry Pi 4B

The input-output response data were collected under experimental conditions, where the dispersed phase piezoelectric driving pump maintained a constant frequency of 200 Hz, while the continuous phase driving pump operated at a constant frequency of 50 Hz. These pumps were connected to the inlets of the Flow Focusing Device (FFD) chip. The adjustment of the continuous phase pressure regulated the droplet size on the FFD chip. Droplet measurements were obtained from high-frame-rate videos captured with a camera positioned below the FFD chip's outlet microchannel. Droplet images from multiple video frames were analyzed using ImageJ software to determine droplet sizes. The droplet measurement circuit was not utilized in these experiments; however, it was analytically modeled, as described in Section B of Appendix 2.

Data collection for pump system modeling involved recording pressure readings from the pressure sensor while varying input voltage settings from 50 V to 250 V for oil pumps. These experiments were conducted at fixed water pressure values of 5 kPa, 10 kPa, and 16 kPa. For modeling the dynamics of the FFD chip droplet generation process, pump pressure for the oil phase ranged from 5 to 34 kPa. The corresponding measurements were plotted and discussed in Section 1.3 (Results and Discussion). A crucial step is the selection of an appropriate model structure; in this case, a transfer function model (Equation 11) has been chosen. Determining the order of the model comes next, involving the incremental adjustment of poles and zeros based on observed system responses to strike a balance between accuracy and simplicity.

$$H(s) = \frac{\sum_{m=0}^M b_m s^m}{s^N + \sum_{n=0}^{N-1} a_n s^n} = \frac{b_0 + b_1 s + b_2 s^2 + \dots + b_M s^M}{a_0 + a_1 s + a_2 s^2 \dots + a_{(N-1)} s^{N-1} + s^N} \quad (10)$$

Equation 18 represents a continuous linear time-invariant system transfer function, where M and N denote the order of the numerator and denominator polynomials, and b_n and a_n represent the coefficients. The order determination process initiates with a single pole and zero, gradually increasing up to the 1st to 3rd order, following this systematic methodology employed in a previous study [93]. The subsequent parameter estimation step yields values $a_1, a_2 \dots a_{(N-1)}, b_1, b_2 \dots b_M$ in (18) for both the pump and the FFD chip.

Advancing to the next stage, the focus is on parameter estimation explained and depicted in Figure 5 in Section D of Appendix 2. Known vectors r and y represent experi-

mental inputs and observed outputs, respectively. The vector θ comprises unidentified parameters (a_2, b_1, b_2 , etc.) critical for constructing an accurate transfer function model (Equation 10). The MATLAB System Identification Toolbox is then employed to automatically select an estimation method based on the dataset's characteristics. The Nonlinear Least Squares (NLS) technique is chosen for datasets exhibiting nonlinear features, minimizing differences between observed and predicted outputs. Additionally, the Instrumental Variable Estimator contributes by generating an initial set of parameters, acting as a favorable starting point for subsequent parameter estimation.

Once parameters are estimated, the identified model undergoes thorough validation by comparing predicted and observed outputs. In the validation phase of the model derived from the system identification procedure, MATLAB utilized various quantifiable metrics, serving as benchmarks to evaluate the model's performance [93].

Fit to Estimation Data Percentage: This metric assesses the proximity of the model to the actual system, providing a quantitative measure of how well the model aligns with the estimation data. **Mean-Square Error (MSE):** calculated by averaging the squared differences between predicted and actual values. A lower MSE signifies better predictive performance, highlighting less variability between predicted and actual outcomes.

Akaike's Final Prediction Error (FPE): This measure evaluates the quality of the model by simulating its performance on a dataset generated by the toolbox. It evaluates the model's error in relation to the original dataset's response. **Cross-Validation:** Employed to estimate the expected level of fit of a model to two datasets independent of the data used for model estimation. This offers an important understanding of the model's generalizability and reliability.

2.2.3 Results and Discussion

The experimental data presented in Figure 14(a) exhibits a consistent and proportional correlation between applied voltage and oil pressure across various water pressure levels (5 kPa, 10 kPa, and 16 kPa). At each water pressure setting, there is a uniform rise in oil pressure ranging from 4 to 11 kPa. However, when examining the relationship between pump pressure for the oil phase and measured droplet sizes on the FFD chip under different water pressures in Figure 14(b), a more complex pattern emerges. Although there is a general trend of decreasing droplet size with increasing oil pressure, no clear linearity is observed within the specified pressure ranges. These results present the microfluidic system dynamics.

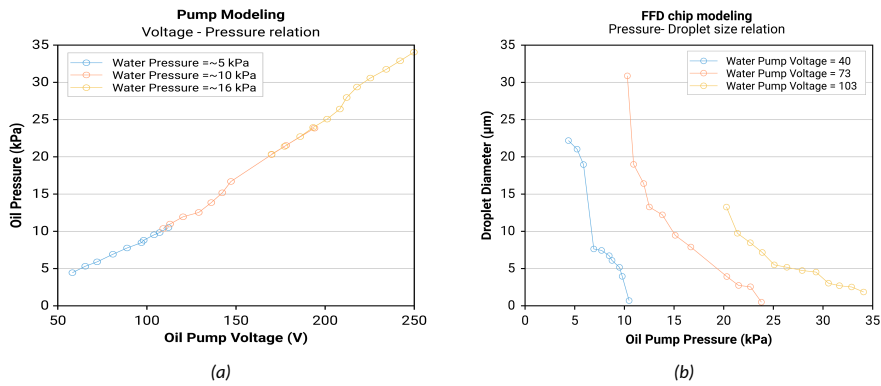


Figure 14: Experimental Results on Pump Parameters and Droplet Generation. (a) Voltage (V) vs Pressure (kPa) for the oil driving pump. (b) Droplet diameter (μm) vs Pressure (kPa) for the oil driving pump.

For the evaluation of system component models at varying model order, detailed results for the FFD chip are provided in TABLE 3, while outcomes for pump modeling are outlined in TABLE 4. From the Tables, the 1st order models for both the FFD chip and pump (M2 in Table 3 and Table 4) emerge as the optimal choice. These models exhibit exceptional fit percentages of 94.54% for the pump and 91.5% for the FFD chip, surpassing higher-order models. The selected model, M2 for both components, demonstrates remarkably low FPE and MSE values, indicating successful model validation through rigorous residual analysis. Additionally, the cross-validation fit percentages are notably high, reaching 78.66% for the pump and, 66.63% for the FFD chip. In contrast to the marginal 4% increase in the fit percentage observed with the higher-order M3 model for the pump, M2 is deemed more suitable. This choice prioritizes a reduction in system complexity over a relatively minor improvement in data fit. The section concludes by visually illustrating the closed-loop system through selected transfer functions, as presented in Figure 15.

Table 3: Microfluidic Chip (Input Water Pressure-Output Droplet Size Relation) model

Model No.	Transfer Function	Poles, Zeros	FPE	MSE	Max. validation Fit %	Est. data Fit %
M1	$\frac{-0.007136}{s+0.27085}$	1,0	3374	2024	58.8	-36.7
M2	$\frac{19.04s - 0.3391}{s+0.2745}$	1,1	15.59	7.79	66.6	91.5
M3	$\frac{.1597}{s^2+0.00017s+0.03}$	2,0	210.4	86.6	53.5	71.7
M4	$\frac{-53.34s+8.045}{s^2+242.5s+37.8}$	2,1	1022	340	89.7	43.9
M5	$\frac{10.7s^2+12.1s-0.14}{s^2+1.64s+0.251}$	2,2	22.26	5.85	64.9	92.6
M6	$\frac{-0.01801}{s^3 0.31s^2+0.34s+0.1}$	3,0	9549	2513	58.1	-52.3
M7	$\frac{102.9s-1.34}{s^3+1.1s^2+10.6s+2}$	3,1	34.7	6.94	65.7	92
M8	$\frac{-266.5s^2-38.95s-0.7091}{s^3+1.67s^2+13.15s+2.114}$	3,2	37.16	5.30	65.0	93
M9	$\frac{8.75s^3+4.8s^2-14.7s+0.27}{s^3+2.80s^2+1.96s+0.261}$	3,3	5918	538	82.7	29.5

Table 4: Pump (Input Voltage-Output Pump Pressure Relation) System Model.

Model No.	Transfer Function	Poles, Zeros	FPE	MSE	Max. validation Fit %	Est. data Fit %
M1	$\frac{0.04412}{s+0.2862}$	1,0	0.20	0.122	76.5	92.1
M2	$\frac{0.02948s+0.01886}{s+0.1057}$	1,1	0.11	0.058	78.6	94.5
M3	$\frac{0.009749}{s^2+0.1281s+0.0671}$	2,0	0.01	0.005	86.7	98.4
M4	$\frac{-15.05s-1.942}{s^2+136.7s+17.17}$	2,1	1668	556.0	-260	-434
M5	$\frac{-0.053s^2-0.05s+0.0265}{s^2+0.63s+0.1103}$	2,2	0.09	0.025	61.2	96.4
M6	$\frac{0.05401}{s^3+1.25s^2+2.38s+0.2}$	3,0	0.04	0.012	74.1	97.5
M7	$\frac{(1.949s+0.7371)}{s^3+21.5s^2+9.06s+5.1}$	3,1	0.39	0.078	79.9	93.7
M8	$\frac{2.187s^2-0.02s+0.3311}{s^3+17.1s^2+0.14s+2.4}$	3,2	0.13	0.018	66.9	96.9
M9	$\frac{0.09s^3-0.04s^2-0.1s+0.17}{s^3+0.57s^2+1.0s+1e^{-9}}$	3,3	92.7	8.430	73.3	34.2

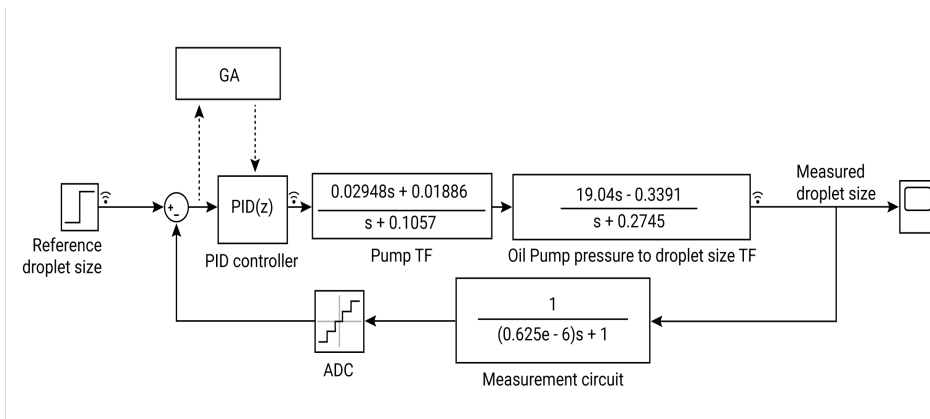


Figure 15: Closed-Loop System Transfer Functions. First-order models derived from system identification for the pump and chip, and from the analytical model (Section B of Appendix 2) for the droplet sensor.

To assess their effectiveness, a comparison was conducted between classical tuning and the genetic algorithm (GA) tuning approaches. The evaluation considered standard controller performance measures, including settling time (5% criterion), percent overshoot, and rise time (0-95% criterion). Classical tuning, achieved through a trial-and-error process, resulted in PID parameters ($K_p = 0.1$, $K_i = 15$, $K_d = 1e-4$) successfully attaining the target droplet size of $100\mu\text{m}$. The corresponding closed-loop response exhibited a rise time of 1.57s, overshoot percentage of 1.5%, and settling time of 0.338s, as illustrated in Appendix 2, Section B-1 (Figure 8).

In contrast, the GA-tuned PID controller results (Appendix 2, Section B-2 (Figure 9)), showcased significant improvements in process response for the same $100\mu\text{m}$ droplet size setpoint. The closed-loop response displayed a reduction in overshoot percentage from 1.5% to 0.5% and settling time from 0.34s to approximately 0.088s, as shown in Table 6. The evaluation extended to analyzing the six performance indices measures in the genetic

algorithm approach. Although these indices showed very close or similar dynamics, the Integral of Time Absolute Error (ITAE) emerged as the optimal criterion. It produced the system response with the lowest fitness value (error) of 0.2367, as outlined in TABLE 6. This comparative analysis underscores the efficacy of the GA tuning method in achieving enhanced controller performance. The results provide insights for optimizing closed-loop systems in this setting.

Table 5: System performance - classical tuning of PID controller

K_p	K_i	K_d	Rise Time	Settling Time	Overshoot
0.1	15	1e-4	0.271s	0.338s	1.5%

Table 6: System performance – genetic algorithm tuning of PID controller

Objective function criteria	K_p	K_i	K_d	Fitness Value	Rise Time (ms)	Settling Time (ms)	Over-shoot (%)
MSE	0.975	69.68	3.12 e-5	84.46	54.7	96.4	0.5
ITSE	0.060	46.09	8.62 e-5	1.606	86.8	110.1	0.5
ITAE	0.234	69.40	2.84 e-5	0.2367	56.4	72.4	0.5
ISE	0.937	69.12	2.00 e-5	82.552	71.2	96.8	0.5
IE	0.035	67.83	7.46 e-5	2.1411	60.0	78.0	0.5
IAE	0.173	69.93	4.9 e-5	2.1282	58.4	75.2	0.5

2.3 Summary

In summary, the simulation of a closed-loop droplet microfluidic system, featuring a PI controller, effectively regulated droplet size in a flow-focusing setup. The PI controller dynamically adjusted the dispersed phase flow rate based on the measured droplet diameter, minimizing deviations and achieving near-zero steady-state error across different setpoints. The integration of CFD tool COMSOL and programming tool MATLAB facilitated the development of control environment, proving to be a cost-effective platform for evaluating the parameter space and optimizing design in microfluidics control, promising enhanced precision in future applications. The agreement between the target and measured droplet diameters, with an error deviation of less than 3% and a coefficient of determination (R^2) value of 0.9937, serves as a demonstration of the controller's efficiency across the 30 μm -60 μm range.

Additionally, a PID controller tuned with a genetic algorithm was implemented for closed-loop droplet size control in a microfluidics system. The primary aim was to identify optimal PID controller parameters to minimize settling time and ensure a stable response. Using MATLAB and Simulink, physical models were represented, seamlessly integrating the PID controller tuned with a genetic algorithm. Comparative analysis between classical tuning and the genetic algorithm approach revealed superior results in terms of settling time and overshoot. The adaptive nature of the genetic algorithm enabled flexible droplet size setpoints, ranging from 50 μm to 350 μm , depending on the variable oil pressure value. While classical tuning remains a starting point, this study highlights the efficiency of intelligent optimization methods in achieving optimal tuning for droplet microfluidic systems. Overall, the study showcased advances by integrating simulated flow environments and control algorithms for closed-loop droplet microfluidic control studies.

3 BRIDGING CLOSED-LOOP CONTROL SIMULATIONS WITH EXPERIMENT

This chapter shifts the research from simulations to real-world experimental setups for droplet generation in microfluidic systems. It aims to assess the feasibility of applying control solutions developed in simulations in real applications and evaluate their performance in experiments. It builds on Publication III, which expands on findings from Publication I. Additionally, it uses insights from Publication IV, where simulations introduced in Publication I aided in the understanding of the flow dynamics to develop an empirical model for droplet generation.

Publication III: (Sections 3.1-3.3)

Jõemaa, Rauno & Gyimah, Nafisat & Ashraf, Kanwal & Pärnamets, Kaiser & Zaft, Alexander & Scheler, Ott & Rang, Toomas & Pardy, Tamas. (2023). CogniFlow-Drop: Integrated Modular System for Automated Generation of Droplets in Microfluidic Applications. IEEE Access. PP. 1-1. 10.1109/ACCESS.2023.3316726.

Publication IV: (Section 3.4)

Parnamets, Kaiser & Udal, A. & Koel, Ants & Pardy, Tamas & Gyimah, Nafisat & Rang, Toomas. (2022). Compact Empirical Model for Droplet Generation in a Lab-on-Chip Cytometry System. IEEE Access. PP. 1-1. 10.1109/ACCESS.2022.3226623.

3.1 State-of-the-art and Proposed Framework

Previously, the focus has been on individual strategies for either pressure regulation [109, 33, 110] droplet size control [55, 92]. However, these approaches tend to overlook the interconnected nature of pressure and droplet size dynamics. To fill this gap, this study introduces the Dual-PID Control Strategy, which integrates both pressure and droplet size control into a unified approach.

The Dual-PID Control Strategy (Figure 16) consists of two main components: an inner loop and an outer loop. The inner loop aims to regulate pressure within the microfluidic chip to minimize fluctuations and ensure stability, utilizing PID controllers for each micropump. Conversely, the outer loop of the Dual-PID Control Strategy focuses on maintaining user-defined droplet sizes. This is done by adjusting micropump pressure based on feedback from pressure sensors and error signals derived from desired droplet size set points.

Initially, controllers are designed in a simulated microfluidics environment using MATLAB and Simulink, following the procedure outlined in Chapter 2, Section 2.2. Once fine-tuned in the simulated environment, these controllers are implemented in the actual experimental setup. This involves transferring optimized controller parameters into Python code embedded on a Raspberry Pi and integrating them with the physical microfluidic system. This streamlined process reduces the resources needed for controller tuning, resulting in optimal controller performance. Detailed description of the framework can be found in Appendix 3, Section II-B-2.

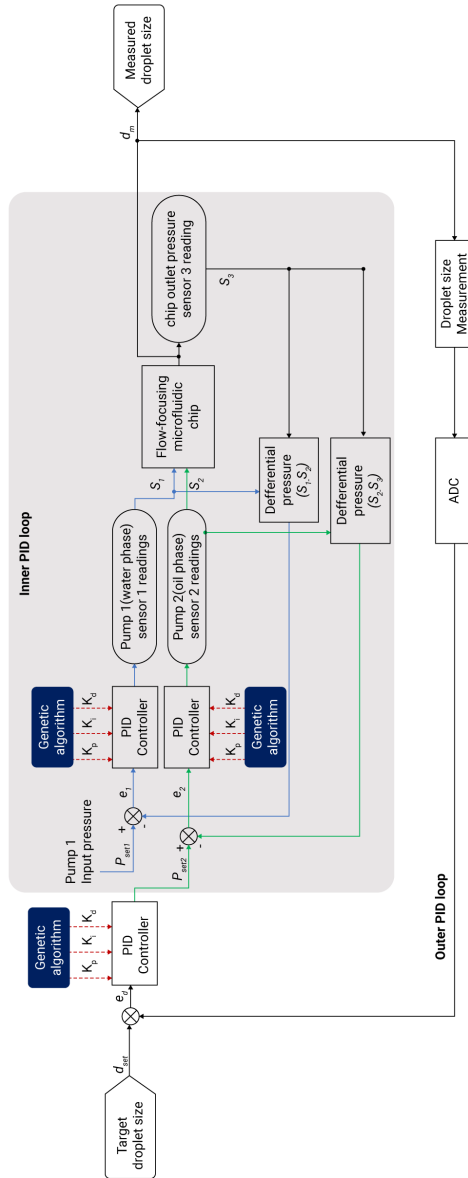


Figure 16: Dual-PID Control Strategy for Microfluidic Droplet Generation. Inner feedback loops (gray background) and an outer feedback loop for regulating pressure and droplet size, respectively.

3.2 Methodology: Experimental setup and Data collection

The experimental setup, known as the CogniFlow-Drop system and shown in Figure 17a, is an automated prototype for generating droplets. It includes several integrated modules and components such as Bartels Mikrotechnik micropumps, a PDMS microfluidic chip, optical imaging with pressure sensors, the main controller (Raspberry Pi), and the fluids involved.

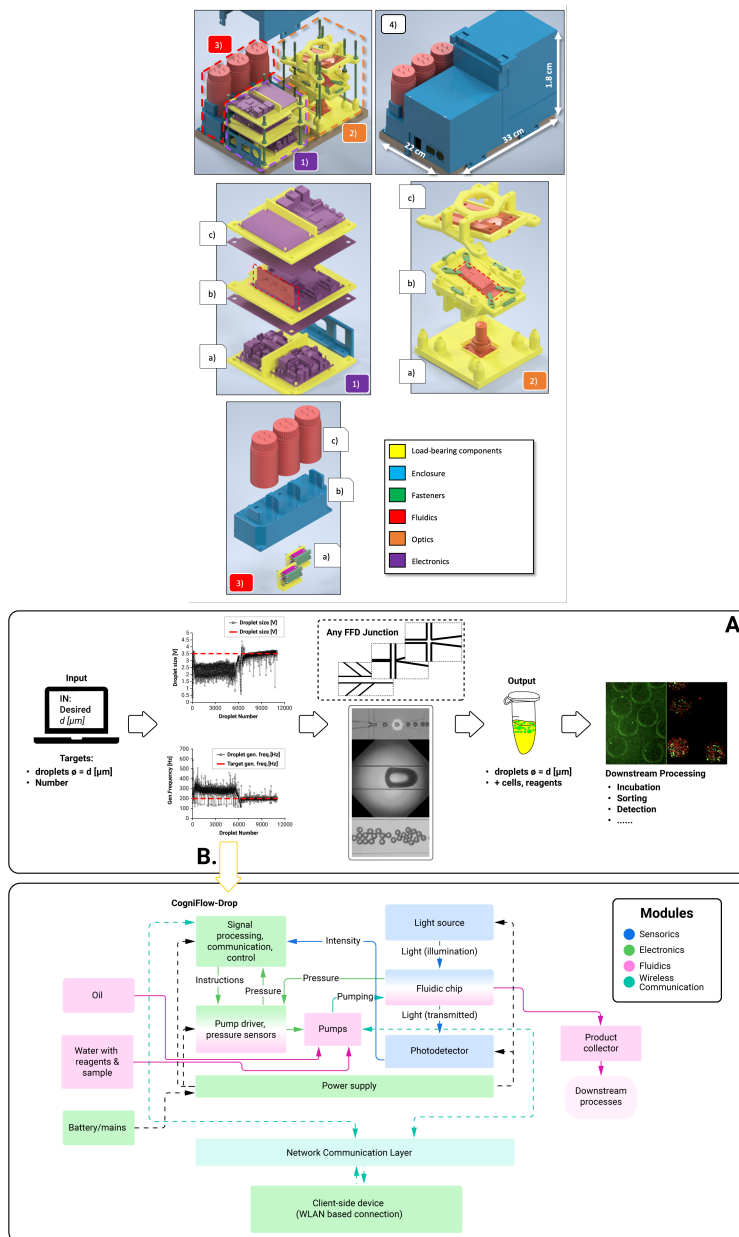


Figure 17: (Top) Prototype assembly: (1) Electronics module with power supply (a) pump driver and pressure sensor (b) RPi4B with ADC and optical sensor circuit (c) copper plates. (2) Sensor module featuring photodiode and lens (a), microfluidic chip mount (b), and light source mount (c). (3) Fluidics module with pump mounts (a) foam-padded enclosure (b) containers for sample, reagent, and product (c). (4) Enclosure with 3D printed walls and wooden base plate for stability (Bottom) (A) Automated generation of user-defined droplets, collected for downstream manipulation. (B) Interconnect blocks and communication flow within the CogniFlow-Drop System [94].

Communication between the main controller (Raspberry Pi) and the pump controller (ESP32 DevKitC) is facilitated via a USB cable, enabling both data exchange and power transfer. Feedback from pressure sensors is crucial for both PID controllers on the ESP32 DevKitC and the Raspberry Pi to ensure synchronized control and accurate regulation of pressure and droplet size during experiments.

The inner feedback loop PID controllers calculate pressure targets for the outer PID controller, enabling coordinated control of the system. Additionally, optical feedback signals undergo signal processing stages before being used for droplet control, including filtering, amplification, and digitization for droplet size measurement. For clarity on the interconnect blocks for the functionalities and communication flow, Figure 17b illustrates the setup. With the CogniFlow-Drop system, the study introduces the dual-feedback control strategy to enhance the reliability and reproducibility of droplet generation. For detailed information about the experimental setup, please refer to Appendix 3.

In this iteration, the focus shifts to controlling pressure within the system, rather than fine-tuning droplet sizes as previously done in Chapter 2, Section 1.2. However, both strategies ultimately aim for practical implementation, albeit in different setups: here, within a physical experimental environment rather than a simulated one. This version of the experimental setup, labeled as V2, boasts enhanced features in pump control, offering more customization compared to its predecessor. Detailed differences between the setups are explained in Appendix 3, Section II-B-2.

For data collection, slight adjustments have been made to the experimental conditions. Key to this iteration are three pressure sensors strategically placed at inlet and outlet points on the chip. These sensors, models MPRLS0015PG0000SA for inlets and MPRLF0250MG0000SA for the outlet, provide real-time feedback on pump output and chip pressure, respectively, at a sampling rate of approximately 166 Hz. The micropumps utilized are Bartels Mikrotechnik's mp6 model. Experiments involved driving voltage tests across three chip variants with different junction widths of 90 μm , 125 μm , and 240 μm . The voltage settings range from 25 V to 250 V, increasing by increments of 25 V. Pressure data is collected over one minute at each voltage step and averaged to establish steady-state values for both water and oil phases. Any unwanted transients or spikes in the experimental data were eliminated using median filtering in MATLAB. Subsequently, the experimental data were used to model the system dynamics for the chip variants.

3.3 Results and Discussions

3.3.1 System modeling and GA tuning

The droplet generation experiments conducted with three chip variants, each featuring unique junction widths, provided insights into their impact on pressure dynamics. Despite variations in chip geometry, a consistent relationship between applied voltage and resulting input pressure across all variants was observed (Figure 16). However, nuances in the correlation between pressure differentials across the chip and pumping voltages were encountered and quantified through the voltage-to-pressure coefficient (C_{vp}). To address these nuances, coefficients (C_{vp}) derived were integrated into the controller design, tailoring the control strategy to account for chip differences.

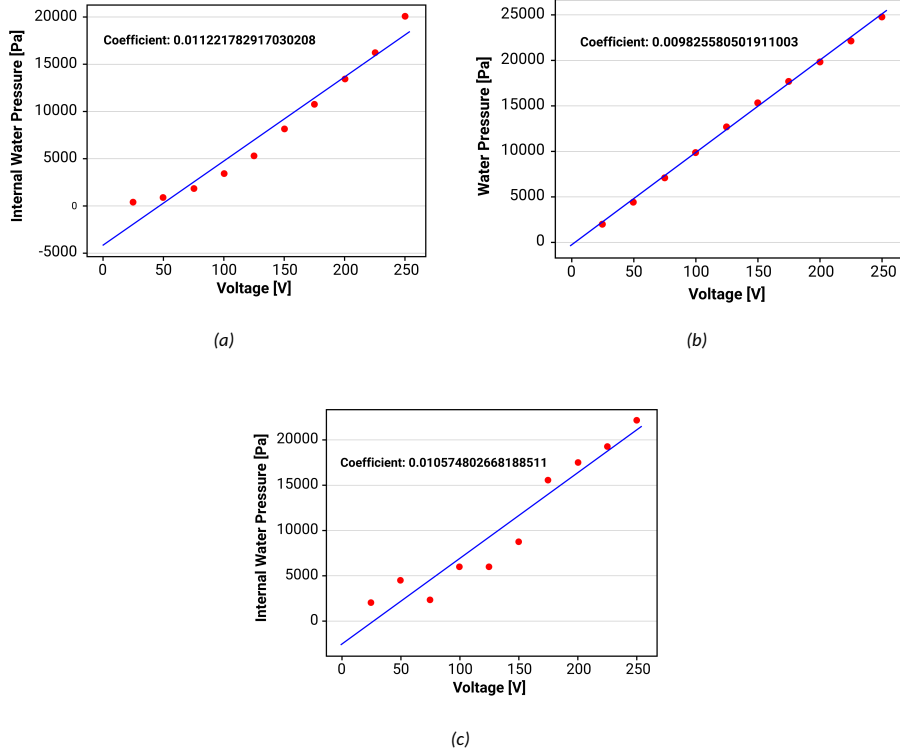


Figure 18: Pressure drops vs. peak-to-peak voltages for chip variants with different cross-junction widths: 90 μm with water pump (a) 125 μm with oil pump (b), and 240 μm with water pump (c). Nuances across the chip variants quantified through the voltage-to-pressure coefficient (C_{vp})

MATLAB were utilized to transform these relations from experiments into Transfer functions. These models, namely $t.f._{pwat}$ for the water pump, $t.f._{poil}$ for the oil pump, and $t.f._{chip90}$ for chip variant A (90 μm junction width), are transfer functions describing system dynamics.

$$t.f._{pwat} = \frac{-17.42s + 83.92}{s + 0.69} \quad (11)$$

$$t.f._{poil} = \frac{-8.40s + 30.6123}{s + 0.216} \quad (12)$$

$$t.f._{chip90} = \frac{19.40s - 0.339}{s + 0.275} \quad (13)$$

where $t.f._{pwat}$ is the transfer function of the water pump, $t.f._{poil}$ is the transfer function of the oil pump, and $t.f._{chip90}$ is the transfer function of the chip variant with 90 μm junction width.

These models were then integrated into Simulink and coupled with the controller to establish a closed-loop feedback system, facilitating controller design and tuning performance in a simulated environment.

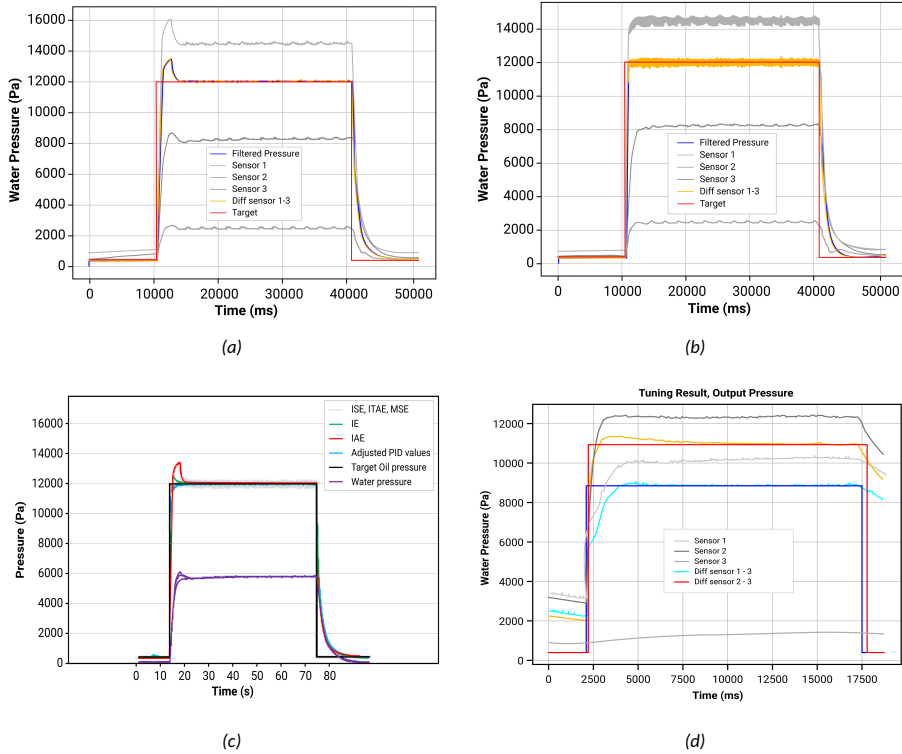


Figure 19: Genetic Algorithm (GA) Tuning Outcome for Pressure Control: (a) IAE, (b) IE, (c) All Metrics, (d) result from controller gains adjustment based on IE and IAE outcomes to minimize overshoot and oscillations

For pressure stabilization or control, two sets of PID parameters for the water pump were derived to achieve optimal performance. The first set ($K_p = 1.89$, $K_i = 4.63$, $K_d = 6.09e - 5$), derived from the Integral of the Absolute Error (IAE) performance index (Figure 17), offered good long-term stability but exhibited approximately 10% overshoot. Conversely, the second set of controller gains ($K_p = 5.35$, $K_i = 6.42$, $K_d = 5.38e - 5$), derived from the Integral of the Error (IE) performance index, resulted in minimal overshoot but slight oscillations around the target value. Hence, manual adjustment of controller gains close to those generated by the GA was made to address these. Similarly, appropriate controller gain values were determined for the oil pump using the same procedure. Furthermore, PID controller parameters achieved for droplet size control in chapter 2, section 2.2 further analyzed.

Importing these parameters into the system necessitated minor refinements of the control parameters, as while target pressure values were achieved, they were accompanied by oscillations by the mean values. This difference between simulated and experimental outcome could be due to variations in real-time environmental conditions and component tolerances that could not be easily accounted for in simulations. Thus, adjusting the control parameters in real-setup was necessary. However, the adjustments were still close to the GA-generated parameters. Table 7 presents a comparison of controller gains between the simulations and the final experimental setup implemented.

Table 7: PID Controller Gain Comparison: Simulation vs. Modified for Experimental Setup

Controller	Parameter	Simulation Value	Experimental Setup Value
Pressure control	water pump driver PID kvals	$K_p: 1.05; K_i: 6.07; K_d: 1.64e-05$	$K_p: 2; K_i: 6.0; K_d: 0.001$
	oil pump driver PID kvals	$(K_p: 5.35; K_i: 6.42; K_d: 5.8e-5)$	$(K_p: 4.0; K_i: 6.0; K_d: 0.01)$
Droplet size Control	water pump driver PID kvals	$K_p: 0.069; K_i: 0.075; K_d: 0.0001$	$K_p: 0.05; K_i: 0.05; K_d: 0.0005$
	oil pump driver PID kvals	$K_p: 0.074; K_i: 0.065; K_d: 0.00043$	$K_p: 0.05; K_i: 0.05; K_d: 0.0005$

3.3.2 Results of PID Implementation for Pressure Control

The performance of the dual PID control strategy was compared to a traditional experimental setup using syringe pumps. Notable differences in response time and stability were observed. Specifically, the dual control strategy demonstrated a faster pressure stabilization time (10 s) compared to the syringe pump-based setup (120 s). These results are illustrated in Figure 20(a-b). This represented a 12-fold reduction in pressure stabilization times compared to syringe pumps. Importantly, the stability time closely resembled results from the simulation setup, as depicted in Figure 19 above. Additionally, it successfully generated monodisperse droplets with coefficients of variation (C_{vs}) between 5% - 10% in the $\sim 50 \mu\text{m}$ - $200 \mu\text{m}$ droplet diameter range, maintaining comparable droplet generation to state-of-the-art.

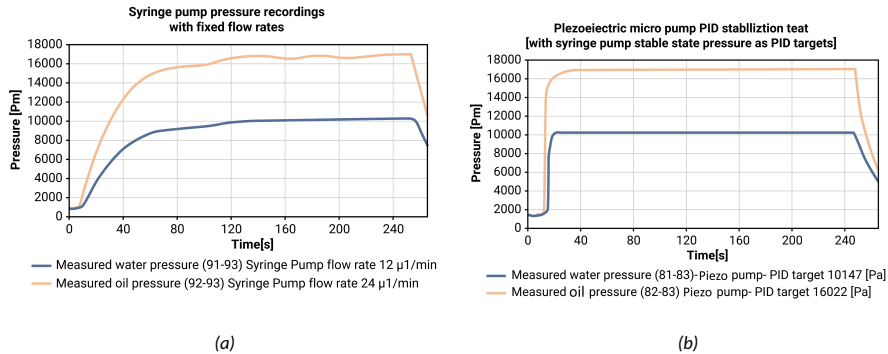


Figure 20: Pressure Stabilization Time Comparison (a) Dual PID control: 10s stabilization time vs. (b) Syringe pumps: 120s.

3.4 Simulations aiding development of an empirical model

Flow simulation has been instrumental in understanding the dynamics of droplet generation. A key challenge was accurately representing the complex three-dimensional experimental setup in simplified two-dimensional simulations.

To address this challenge, discussions in the study's simulations centered on a droplet-volume-based equivalence condition. An auxiliary parameter, termed "effective depth"

(Heff), was introduced to approximate the third dimension in 2D simulations. This aimed to ensure that simulated droplet volumes closely matched experimental observations.

Furthermore, an empirical model for predicting droplet generation rate was developed. It utilized a simple three-parameter set for predicting droplet generation in a specific application case, where droplet sizes ranged from 50 to 70 micrometers and droplet generation rates ranged from 500 to 1500 per second. For more details on this implementation, refer to Appendix 4.

3.5 Conclusion

By transitioning from simulations to real-world experimental setups, this study has demonstrated the feasibility and effectiveness of utilizing simulation-based control strategies. In Publication III, the implementation of a Dual-PID Control Strategy showcases a novel approach to microfluidic control, integrating pressure and droplet size regulation into a unified framework. Through systematic controller design and tuning, informed by simulations, precise control over pressure and droplet size was achieved in experimental setups. The Dual-PID Control Strategy exhibited superior performance compared to traditional syringe pump-based setups, with significantly faster pressure stabilization times and enhanced droplet generation stability. Publication IV delves into the detailed physics-based simulations that underpin the development of an empirical model for droplet generation. By addressing the challenge of accurately representing the complex 3D experimental setup in simplified 2D simulations, the study introduced the concept of effective depth (Heff) to approximate the third dimension. In summary, the synergy between simulation-based and experimental explorations offers a comprehensive understanding of droplet generation dynamics, bridging the gap between theoretical insights and practical applications for droplet control.

4 DEEP REINFORCEMENT LEARNING PROXIMAL POLICY OPTIMIZATION ALGORITHM FOR DROPLET SIZE CONTROL

This chapter shifts from traditional closed-loop systems to machine learning, specifically deep reinforcement learning (DRL). This shift is prompted by the limitations of conventional control methods, which rely heavily on precise, explicit modeling and often struggle with the complex dynamics systems. Introducing DRL serves two main purposes: (a) exploring model-free control and (b) leveraging machine-learning tools for enhanced adaptability and intelligence. Thus, based on Publication V, the study proposes integrating the Proximal Policy Optimization (PPO) algorithm, a type of DRL, with a two-dimensional microfluidic droplet generator fluid model.

Publication V:

Gyimah, Nafisat & Scheler, Ott & Rang, Toomas & Pardy, Tamas. (2023). Deep reinforcement learning-based digital twin for droplet microfluidics control. *Physics of Fluids*. 35. 10.1063/5.0159981.

This proposed approach offers several novelties:

Integration of DRL and CFD in microfluidics: This integration enables the understanding and evaluation of ML building blocks and the sensitivity of ML training models to the microfluidic setting efficiently. The goal is to facilitate practical implementation without extensive hyperparameter tuning or establishing training modalities from scratch.

Introduction of PPO Algorithm: This study pioneers the investigation of the PPO algorithm in microfluidics.

Robustness to External Disturbances Evaluation: The study examines the adaptability of the PPO agent to disturbances to assess its suitability for real-world scenarios.

Numerical model Verification against Experimental Data : The study verifies its droplet generator numerical model by replicating a previously published experimental model and comparing the outcomes.

Overall, the integration of DRL with CFD, combined with the utilization of the PPO algorithm, presents a novel approach to microfluidic control studies.

4.1 State-of-the-Art: Machine Learning for Microfluidics Control

Research on ML control in microfluidics is still in its early stages, with only a few studies conducted so far.

For example, Dressler et al. [46] compared RL algorithms Deep Q Networks (DQN) and model-free episodic controller (MFEC) to human performance. The goal was to control the fluid interface and achieve a target droplet size. They found that both algorithms surpassed human operators, with DQN excelling in long-term and complex experiments, while MFEC was better suited for short and simple tasks. Similarly, Abe et al. [95] utilized an RL algorithm to control micro-valves in peristaltic pumps, enabling various flow conditions such as flow switching and micro-mixing. Furthermore, Lee et al. [96] addressed a flow sculpting problem using an RL algorithm, where their agent learned different solutions for manipulating fluid flow shapes.

However, prevailing research [46, 96, 97] in this domain has mainly relied on discrete control actions, which may not fully exploit the continuous nature of flow dynamics in conventional microfluidics [98, 99]. Discrete control actions involve predefined, distinct actions that the system can take, typically resulting in stepwise changes in control inputs

[100].

While effective for some applications, discrete control actions may pose limitations in scenarios where precise adjustments are required. Furthermore, discretization of the action space can introduce quantization errors and lead to challenges in effectively representing the continuous nature of the underlying physical processes. For microfluidic systems where droplet size regulation demands fine-tuned adjustments, discrete control actions may lead to suboptimal performance. Therefore, the study proposes the use of equally advanced control techniques that can operate in continuous action spaces.

In continuous space control [101], the controller operates directly in a continuous action space, allowing for smooth and precise adjustments of control inputs. Unlike discrete control, continuous control actions enable the system to make infinitesimal adjustments (often within bounds), providing greater flexibility in regulating complex processes such as droplet formation in microfluidic devices. Additionally, continuous control actions can ensure a faithful reproduction of flow dynamics.

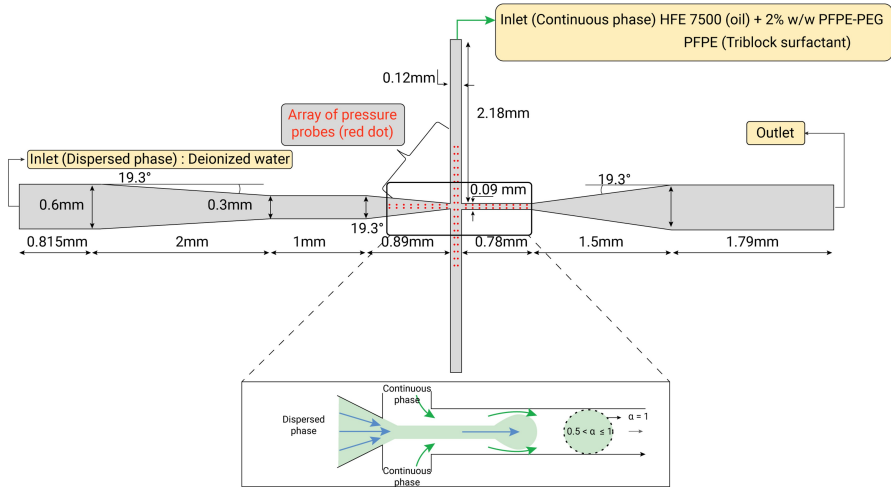
While implementing such continuous control algorithms in physical experiments may initially pose challenges, technological advancements can mitigate these issues, making them feasible even in resource-limited setups. Additionally, control strategies and sensor fusion techniques can help mitigate the sensitivity of continuous control actions to noise and disturbances [102].

Among the advanced continuous space techniques, PPO [103] stands out as a state-of-the-art algorithm for continuous control. PPO optimizes policies by interacting with environments to maximize rewards over time. It works by iteratively updating policy parameters to improve performance while ensuring stability through a constraint mechanism. Also, its effectiveness in balancing exploration and exploitation, making it suitable for various applications. Though originally designed for continuous control, PPO can also adapt to discrete action spaces [103]. Despite being unexplored in microfluidics, PPO has demonstrated remarkable success in related fields, such as active flow control in turbulence [104, 105, 106], suggesting its potential effectiveness in microfluidics. As a result, the PPO algorithm is proposed.

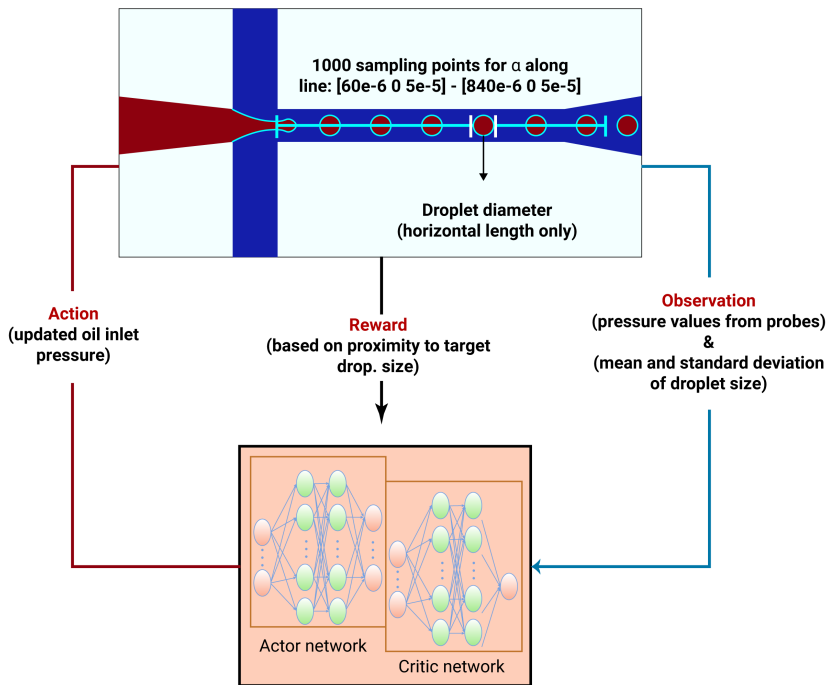
4.2 Methodology

4.2.1 Implementation Framework & Flow Modeling

The implementation framework, as shown in Figure 21b, involves the interaction between a PPO agent and the fluidic environment, with the objective of controlling droplet size. The environment comprises an FFD microfluidic model used in previous chapters, with a junction width of 0.09 mm. Flow characterization is achieved using point probes positioned at various locations within the channel (Figure 21a). In practical setups, these probes can be replaced with pressure sensors connected to microchannels via connecting tubes.



(a)



(b)

Figure 21: (a) Droplet Control Framework. (a) Critical flow area of FFD with pressure-sensing probes indicated by red dots. Droplet interface defined by volume fraction function at 0.5. (b) Implementation framework: PPO agent interacts with the fluidic environment. The agent monitors pressure data and outlet droplet size, adjusts oil inlet pressure, and earns rewards based on proximity to the target droplet size and size variability.

Both microchannel pressure and droplet diameter serve as environment observations for the PPO agent. By incorporating droplet diameter alongside pressure measurements, the model indirectly accounts for the effects of other parameters, such as interfacial tension and viscosities. The agent utilizes these sensed parameters, adjusts the oil inlet pressure as actions, and receives rewards based on the proximity of droplet size to a target value.

The PPO algorithm operates on an episode level within the flow environment, with each episode comprising multiple time steps. At each time step, the agent observes the current state, selects an action, and receiving a reward [107]. The reward mechanism is used to incentivize the agent to reach the target droplet size with minimal variation. Additionally, penalties are enforced when the standard deviation of droplet sizes strays far from a predefined limit. To ensure exploration and effective learning, the agent incorporates randomization by sampling actions from a Beta distribution during episode initiation, promoting exploration of the entire state-action space. Two neural networks are employed by the algorithm: an actor-network responsible for selecting actions based on the current state, and a critic network that evaluates the value of different actions taken by the agent [108]. The flow environment is established using OpenFOAM software, with ParaView utilized for numerical result visualization [109]. The implementation of the PPO algorithm is carried out in the PyTorch platform [110]. CFD (OpenFOAM) + DRL(PyTorch) integrations is established through a Singularity image incorporating PyTorch's precompiled C++ library [107].

The fluid dynamics were simulated using the VOF method, tracking volume fractions of different fluids in discrete cells while solving conservation equations for mass and momentum for each phase [111, 112, 113]. Surface tension effects were considered crucial for precise droplet formation control in microfluidics [114]. The VOF method accurately depicts droplet dynamics with precise fluid boundaries by employing high-resolution interface tracking [113, 115]. The VOF method solves governing equations on the assumption of incompressible two-phase fluids. These equations encompass continuity, momentum balance, and volume fraction equations;

$$\frac{\partial \alpha}{\partial t} + \nabla \cdot (\alpha u) = 0 \quad (14)$$

and α denotes the volume fraction function.

To improve the accuracy of phase boundaries and reduce numerical diffusion, an artificial interface compression velocity, u_r is introduced.

$$\frac{\partial \alpha}{\partial t} + \nabla \cdot (\alpha u) + \nabla \cdot (u_r (\alpha(1 - \alpha))) = 0 \quad (15)$$

u_r influences the interface only where $0 < \alpha < 1$, defined as:

$$u_r = \min(C_a |u|, \max(|u| - C_a |r \cdot \nabla \alpha|, 0)) \quad (16)$$

Here, the compression coefficient C_a regulates the extent of compression at the interface and typically spans from 0 to 4, with $C_a = 1$ commonly utilized in microfluidics studies. Elevated values of can lead to increased nonphysical spurious currents, potentially introducing numerical modeling inaccuracies.[116, 117, 118, 119].

As previously, the continuous phase fluid is composed of HFE 7500 (oil) with a 2% w/w PFPE-PEG-PFPE surfactant, while the dispersed phase is deionized water. Both the continuous and dispersed phases demonstrate Newtonian fluid characteristics, with their corresponding material attributes detailed in Table II of Appendix 5.

In OpenFOAM, the multi-dimensional limiter (MULES) technique was employed to ensure that the volume fraction field remains within the range of 0 to 1 throughout the simulation, as described by reference [120, 121]. The momentum and continuity equations were solved using the PIMPLE algorithm, which is discussed in detail in reference [122]. Temporal terms were discretized using a first-order Euler approach, and divergence terms were managed utilizing the Gauss linear method. Additionally, gradient and Laplacian expressions were discretized by employing the leastSquares and Gauss linear techniques, respectively. To maintain numerical stability, automatic adjustments to the time step were implemented based on the maximum Courant number (MaxCo), restricted to 0.5, and the permissible maximum Courant number for the phase-fraction transport equation (AlphaMaxCo), limited to 0.25, as referenced in [119].

Boundary conditions were applied, including a constant total pressure of 0 at the outlet, a steady pressure of 6000 Pa at the inlet of the dispersed phase, and a customized pressure boundary condition at the continuous phase inlets based on the current network parameters of the DRL algorithm. Additionally, a no-slip constraint was applied at the solid wall, maintaining a constant fluid-wall contact angle of 135°. Mesh generation utilized blockMesh and snappyHexMesh tools in OpenFOAM, and was primarily made of hexahedral cells. A refined region was defined at the fluid intersection to capture flow physics accurately. Its dimensions were determined based on the width of the oil inlet channel, set to 15D5.5D3.4D, centered 5D2.3D1.7D from the microchannel junction. Later, mesh studies in the results section were conducted to identify the optimal mesh properties.

4.2.2 Near real-time Droplet Size Estimation

Real-time or regular interval droplet size estimation is crucial for providing timely and precise feedback to the DRL algorithm, which relies on this data to learn and adapt its control policy based on observed droplet dynamics.

Droplet size estimation utilizes volume fraction function data stored in the fluid environment solver during simulation runs. Post-processing of this data occurs at each time step or regular intervals using OpenFOAM's Python/C API and NumPy. It focuses on analyzing the volume fraction function derived results during simulation runtime at specified time intervals.

Sampling criteria and output file formatting are established using the Sets function object within OpenFOAM [108]. 1000 data points along a sampling line at the outlet channel symmetry line is collected. These data points are then stored in raw ASCII format at 0.5ms intervals for further analysis.

During post-processing, an external Python script executed through the Function Object systemCall creates data arrays representing the water droplet interface, defined as a volume fraction exceeding 0.5. Droplet size estimation is performed by computing the distance between continuous water interface locations, excluding the final droplet's size from calculations based on both experimental observations and simulations, which reveal inconsistent, full formation.

4.2.3 PPO Algorithm Theory and Implementation

DRL combines deep learning with RL, where deep learning processes sensory input via neural networks, enabling RL algorithms to approximate optimal policies or value functions in high-dimensional state spaces.

Meanwhile, model-free DRL approaches like PPO involve direct interaction between the agent and the environment, bypassing explicit environmental modeling. Agents aim

to maximize cumulative rewards by observing partial environmental states. In PPO's actor-critic architecture, the algorithm simultaneously approximates both the state-value and action-advantage functions. The actor(policy) network estimates the action-advantage function, which evaluates the advantage of taking a specific action in a given state compared to other available actions. This function assists the agent in selecting actions that lead to the highest potential rewards in a given state. Meanwhile, the critic(value) network estimates the state-value function, which estimates the expected return that an agent can achieve from a given state. This combined approach allows the agent to effectively learn policies (i.e. the control strategy). Figure 22 provides a visual illustration of the operation of the PPO. Representing the value function with a nonlinear function approximator typically involves addressing a nonlinear regression challenge [107].

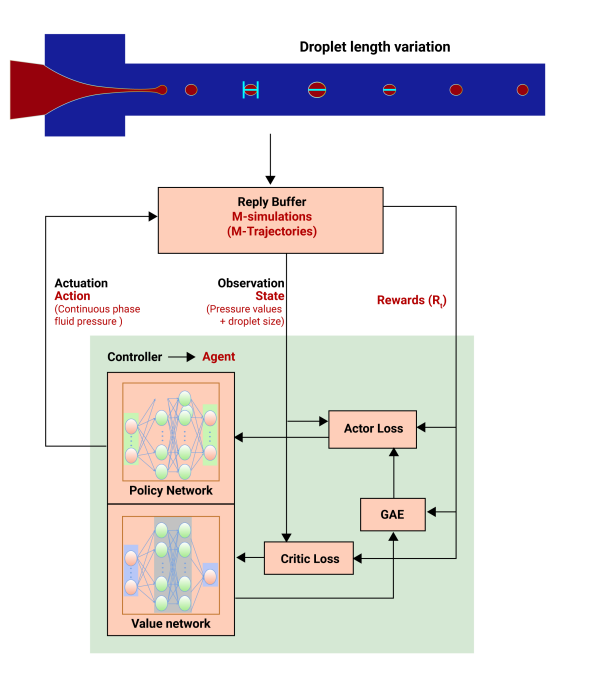


Figure 22: PPO algorithm flow. Visual representation of the PPO (Proximal Policy Optimization) algorithm with policy-value (actor-critic) architecture. The Value Network evaluates action values, guiding policy updates by estimating advantages through the Generalized Advantage Estimation (GAE). The Policy Network determines policy, updated via Actor Loss to maximize expected rewards. The Critic Loss updates the Critic Network based on observed rewards. Rewards, states, and actions are pivotal in driving learning, while trajectories stored in the Reply Buffer facilitate efficient experience replay

$$\underset{\phi}{\text{minimize}} \sum_{n=1}^N \|V_{\phi}(s_n) - \hat{R}_t\|^2 \quad (17)$$

$V_{\phi}(s_n)$ represents the state value derived from the value network with parameters ϕ . The indices n pertain to all time steps in a batch of trajectories. \hat{R}_t denotes the sum of rewards from time step $t = l$ to the conclusion at $t = T$.

$$\hat{R}_t = \sum_{l=0}^T \gamma^l r_{t+l} \quad (18)$$

The value network is adjusted through back-propagation of value loss to estimate the state-value function. This process involves updating the value network's parameters ϕ from ϕ_k to ϕ_{k+1} , aiming to reduce the disparity between collected trajectory data and the network's predictions. Subsequently, the mean-squared error is computed, averaging across all trajectories.

$$\text{value loss} = \frac{1}{|D_k|T} \sum_{\tau \in D_k} \sum_{t=0}^T (V_\phi(s_t) - \hat{R}_t)^2 \quad (19)$$

$$\text{Parameter updating step: } \phi_{k+1} = \arg \min_{\phi} \frac{1}{|D_k|T} \sum_{\tau \in D_k} \sum_{t=0}^T (V_\phi(s_t) - \hat{R}_t)^2 \quad (20)$$

where D_k is the number of trajectories taken from the memory to facilitate updates.

By the actor network, the action-advantage function assesses whether the action is superior or inferior to the policy's default behavior. In this research, Generalized Advantage Estimation (GAE) is applied using the temporal difference method ($TD - \lambda$). The estimation of the action-advantage function is expounded as:

$$\delta_t^V = R_t + \gamma V(s_{t+1}) - V(s_t) \quad (21)$$

δ_t^V signifies the evaluation of the action-advantage function for a given action whereas the advantage function is tailored for k -step

By the actor network, the action-advantage function assesses whether the action is superior or inferior to the policy's default behavior. In this research, GAE is applied using the temporal difference method ($TD - \lambda$). The estimation of the action-advantage function is expounded as:

$$\hat{A}_t^{(k)} := \sum_{l=0}^{k-1} \gamma^l \delta_{t+l}^V = -V(s_t) + r_t + \gamma r_{t+1} + \dots + \gamma^{k-1} r_{t+k-1} + \gamma^k V(s_{t+k}) \quad (22)$$

$\hat{A}_t^{(k)}$ estimates discounted advantages across k -steps. GAE, with parameters γ and λ , is the exponentially weighted average of these k -step estimates.

$$\begin{aligned} \hat{A}_t^{\text{GAE}(\gamma, \lambda)} &:= (1 - \lambda) \left(\hat{A}_t^{(1)} + \lambda \hat{A}_t^{(2)} + \lambda^2 \hat{A}_t^{(3)} + \dots \right) \\ &= \sum_{l=0}^{\infty} (\gamma \lambda)^l \delta_{t+l}^V \end{aligned} \quad (23)$$

$\hat{A}_t^{\text{GAE}(\gamma, \lambda)}$ represents GAE for action a_t . Parameters λ and γ balance bias and variance.

$$\text{Policy loss} = \frac{1}{T} \sum_{t=0}^T \frac{\pi_\theta(a_t | s_t)}{\pi_{\theta_k}(a_t | s_t)} \hat{A}_t \quad (24)$$

Policy optimization utilizes the policy gradient computed via GAE to adjust the parameters of the policy network through minimizing the policy loss via back-propagation.

$\pi_\theta(a_t | s_t)$ signifies the log probability of action at for state s_t under policy π parameterized by θ . π_{θ_k} denotes the previous policy. To ensure that the new policy does not deviate significantly from the previous one, the policy loss is clipped.

$$L(s, a, \theta_k, \theta) = \min \left(\frac{\pi_\theta(a|s)}{\pi_{\theta_k}(a|s)} A^{\pi_{\theta_k}(s, a)}, g(\varepsilon, A^{\pi_{\theta_k}(s, a)}) \right) \quad (25)$$

The clipped policy loss, referred to as $L(s, a, \theta_k, \theta)$, is regulated by the epsilon parameter ε .

Where,

$$g(\varepsilon, A) = \begin{cases} (1 + \varepsilon)A & A \geq 0 \\ (1 - \varepsilon)A & A < 0 \end{cases}$$

PPO ensures policy stability by employing a clipped surrogate objective, penalizing policy updates deviating too much from the old policy. The clipped surrogate objective is defined as:

$$L^{CLIP}(\theta) = \mathbb{E}_t[\min(r_t(\theta) \cdot A_t^{adv}(s_t, a_t), \text{clip}(r_t, 1 - \varepsilon, 1 + \varepsilon) \cdot A_t^{adv}(s_t, a_t))] \quad (26)$$

where

- $r_t(\theta) = \frac{\pi_\theta(a_t|s_t)}{\pi_{\theta^{old}}(a_t|s_t)}$ is the ratio of the probability of taking action a_t under the new policy to that under the old policy.
- ε is a hyperparameter that controls the extent of policy clipping

The pseudo-code of the implementation can be found in Algorithm 1. The networks parameters in Table 8 and hyperparameters for training PPO can be found in Table 9

Algorithm 1 PPO-Clip

- 1: Input: initialize policy parameter θ_0 , initialize value function parameters ϕ_0
- 2: **for** $k = 0, 1, 2, \dots$ **do**
- 3: Get trajectories $D_k = \{\tau_i\}$ by simulating policy $\pi_k = \pi(\theta_k)$ in the flow model.
- 4: Calculate rewards \hat{R}_t .
- 5: Calculate estimated advantage, \hat{A}_t based on the current value function V_{ϕ_k} .
- 6: Policy adjusted to maximize PPO-Clip :

$$\theta_{k+1} = \arg \max_{\theta} \frac{1}{|\mathcal{D}_k| T} \sum_{\tau \in \mathcal{D}_k} \sum_{t=0}^T \min \left(\frac{\pi_\theta(a_t | s_t)}{\pi_{\theta_k}(a_t | s_t)} A^{\pi_{\theta_k}(s_t, a_t)}, g(\varepsilon, A^{\pi_{\theta_k}(s_t, a_t)}) \right),$$

done via Adam optimizer.

- 7: Fix the value function using mean-squared error regression:

$$\phi_{k+1} = \arg \min_{\phi} \frac{1}{|\mathcal{D}_k| T} \sum_{\tau \in \mathcal{D}_k} \sum_{t=0}^T (V_\phi(s_t) - \hat{R}_t)^2,$$

- 8: **end for**
-

Table 8: Neural Network(NN) Architecture

Parameter	Actor (policy network)	Critic (value network)
Activation function	ReLU (Rectified Linear Unit)	ReLU
Neuron number in input layer	81 (pressure points + droplet size)	81 (pressure points + droplet size)
Neuron number in hidden layer	128	128
Number of hidden layer(s)	1	1
Neuron number output layer	2 (α and β for a Beta distribution)	1 ($V_{\phi}(s_n)$)
Learning rate	0.001	0.00075

Table 9: Parameter Values/Details for DRL Training

Parameter	Value/Details
Gamma (Discount Factor)	0.99
Lambda (Coefficient for TD-Lambda Method)	0.97
Number of Sensors (Pressure Probes + Avg. Drop Size)	n_sensor: 2
Target Sizes (r_1)	Target sizes
Measured Droplet Size (r_2)	Mean measured droplet size
Droplet Standard Deviation Limit (dia_{std})	Standard deviation limit
Number of Workers (Parallelization)	n_worker: 81
Policy Optimization Epochs	80
Policy Sample Ratio	1
Policy Clip Range	0.1
Policy Model Maximum Gradient Norm	1
Policy Stopping KL	0.2
Entropy Loss Weight	0.01
Value Optimization Epochs	80
Value Sample Ratio	1
Value Clip Range	Infinite
Value Model Maximum Gradient Norm	1
Value Stopping MSE	25
Main PPO Iteration Range	100-140
Gradient-Based Optimization Method	Adam Optimizer
Training Episodes	140
CPU Processors	4 (Contemporary PC) / 32 (HPC)
Simulation Time Step (t_{sim})	0.5 ms
Control Time Step Factor (k)	20
Tolerance for Standard Deviation	1e-6
Penalty Applied at Diastd	Yes
Action Bounds (Pressure)	(4500, 7000)

PPO implementation involved running two simulations concurrently with two workers, storing results in a replay buffer for each, totaling 140 episodes per worker. Simulation commenced by running fluid flow simulations without active control until a fully developed flow, marked by at least one droplet formation at the outlet, was achieved. This initial setup was saved and reused to commence training. a time delay was introduced between droplet size measurements and control actions to enhance stability. The control time step for the agent set as a multiple ($k = 20$) of the simulation time step (Δt_{sim}).

The reward function R_t assigns a value of -1 if the absolute difference between the target droplet size and the current mean droplet size exceeds a threshold value of $20 \times$

10^{-6} . If not, it offers a positive reward proportional to the proximity to the target size. Furthermore, deviations in droplet size standard deviation from a predefined dia_{std} of 30 micrometers are penalized. Ultimately, the reward perceived by the agent is bounded between -1 and 1.

$$R_t = \begin{cases} -1 & \text{if } val > 20 \times 10^{-6} \\ r_1 - val / r_1 - 0.002 \times \text{Penalty} & \text{otherwise} \end{cases} \quad (27)$$

Here, val represents the absolute difference between the target droplet size r_1 and the mean current droplet size r_2 . More details on the implementation can be found in Appendix 5, Section II.

4.3 Results and Discussion

4.3.1 Mesh Independence Studies and Model Verification

The model mesh, depicted in Figure 23(a), was used for the mesh study. It involved creating eight grids with different settings in snappyHexMesh. By adjusting snappyHexMesh parameters like feature edge and volume region refinement levels, the mesh resolution was controlled at sharp edges and inside the domain. The refinement region, described in Subsection II A, was also present in all eight grids. Mesh assessment focused on droplet interface sharpness, average droplet size, and detachment time (as displayed in Figure 23(b)). Coarser grids (M1-M3) showed a diffuse droplet interface, compromising accuracy in droplet size estimation. Finer grids (M4 -M8) demonstrated improved droplet interface sharpness. Notably, meshes with over 15,000 elements yielded nearly identical droplet diameters and detachment times.

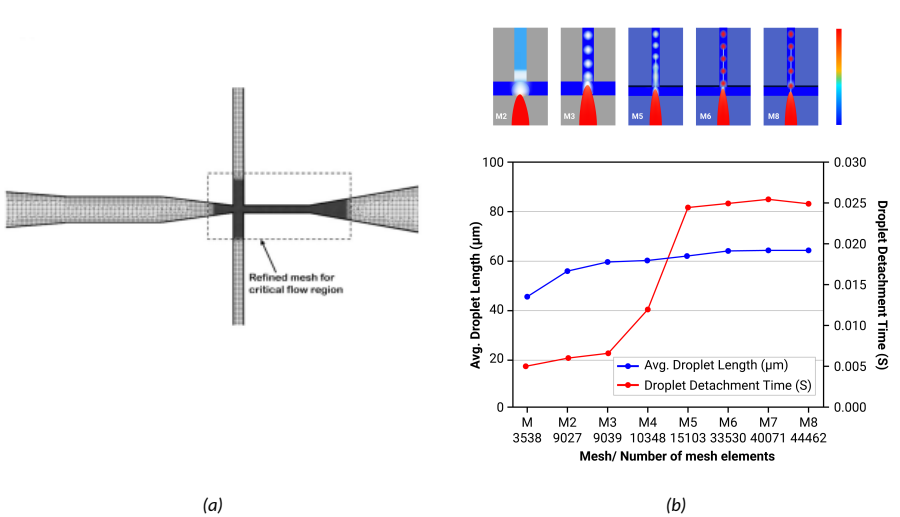


Figure 23: Computational Mesh Optimization. (a) Mesh refinement in gradient-rich areas. (b) (Top) Visualise droplet interface sharpness per mesh (Bottom) Evaluation across meshes M1 to M8 considers interface sharpness, droplet length, and detachment time. Optimal mesh, M6, balances sharpness and grid independence.

Further refinement beyond M6, achieved through a finer background mesh, provided marginal improvements at a notable increase in computational costs, as indicated by the

computational times in Table III of Appendix 5. Thus, Mesh M6, with a feature edge refinement level of 2 and volumetric refinement level of 5, is identified as the optimal option for further simulations.

Further, the study verifies the numerical model's accuracy by comparing it with experimental data from Wu et al. [103] concerning water droplet formation in Freol ALPHA 10G oil. The verification replicates Wu et al.'s droplet generation setup and assesses the model's performance across the same velocities: dispersed phase velocities ranging from 0.00042 m/s to 0.00252 m/s and a fixed continuous phase velocity of 0.00252 m/s. The geometry employed was a flow-focusing device, referenced in their work.

Comparing simulation outcomes with experimental data, as shown in Figure 24, reveals favorable agreements. The numerical model generally exhibits errors of less than 7%, except at 0.00126 m/s, where the error increases to 11%. Previous studies using the VOF method have reported acceptable errors ranging from 10% to 18% [123, 124]. Differences in droplet sizes observed between this study and Wu et al.'s could be attributed to the distinction between 2D simulations and the 3D FFD device. Nonetheless, the model showcases errors of under 11% across all velocity ratios. These verification results affirm the reliability of the numerical model, supporting its suitability for exploration of droplet control.

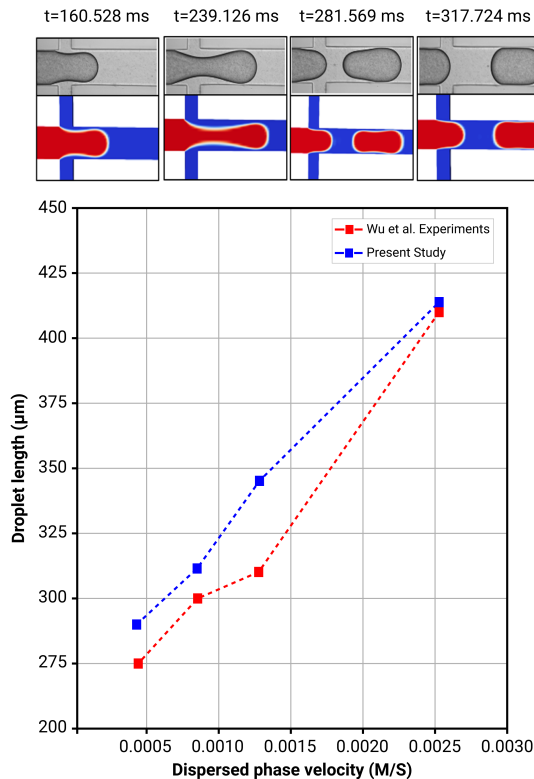
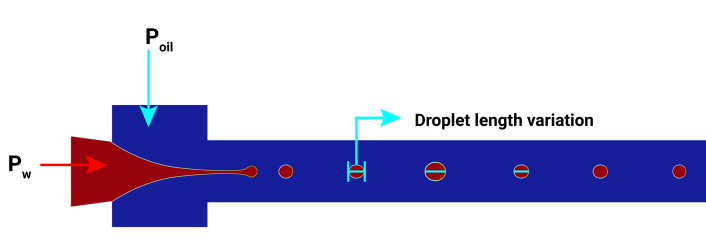


Figure 24: Comparison of Simulation and Experimental Model. (Top) Replicated experimental model with numerical model (colored) vs. Wu et al.'s experimental model (gray). (Bottom) Plot of droplet length vs. dispersed phase velocity at constant oil velocity of 0.00252 m/s. Strong agreement, errors < 7%, except at 0.00126 m/s (11%).

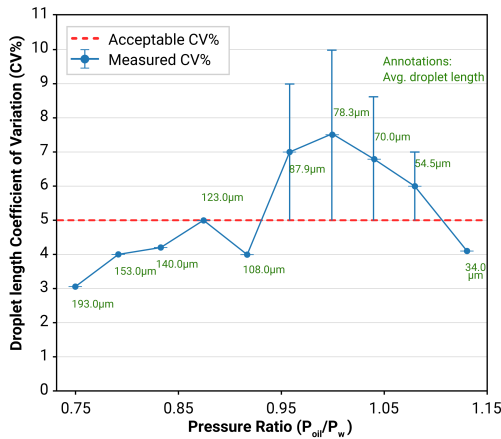
4.3.2 Environment Characterization and Probe Configuration

To define upper and lower bounds for the agent action space, the study characterized the environment without control. By keeping the water pressure constant at 6000 Pa, the impact of pressure ratios (P_w/P_{oil}) ranging from 0.33 to 1.67 on droplet size was evaluated. Figure 25a illustrates the mean droplet size, and the coefficient of variation (CV%).

In Figure 25b, it's observed that the droplet size initially increases with rising pressure ratios until the water pressure matches the oil pressure ($P_w = P_{oil}$). After this point, the CV% consistently decreases. However, droplets with an average size ranging from 55 μm to 88 μm exhibited CV% values exceeding the desired threshold of 5%. This range of sizes with CV above 5% highlights the necessity for control to maintain consistent droplet sizes. Additionally, the study found that droplets were not produced beyond a pressure ratio of 1.13 or below 0.75. Based on these observations, the lower and upper boundaries of the action space were set at continuous phase fluid pressures 4500 Pa and 7000 Pa, respectively.



(a)



(b)

Figure 25: Variations in Droplet Size (a) and Relationship between Pressure Ratio (P_w/P_{oil}) and Droplet Size Variation (CV%). Droplet sizes ranging from 55 μm to 88 μm exceed the 5% CV threshold, with action space boundaries at 4500–7000 Pa.

Moreover, the study investigates various configurations of sensor probes aimed at refining the precision of flow data collection. These probes capture pressure readings at discrete time intervals, providing feedback to the PPO algorithm. Five unique sensor setups, denoted as Probe Sets 1 through 5 (P1–P5), were subjected to evaluation, as depicted in Figure 26(a). P1 comprised 10 probes evenly distributed within the microchannel junc-

tion, while P2 featured 20 probes distributed across both the junction and outlet. P3 and P4 consisted of 40 and 60 probes, respectively, positioned among the oil inlets, junction, and outlet. P5 incorporated 80 probes spanning all phase inlets, the junction, and outlet. These configurations were employed to train the agent to achieve a droplet size target of $60\ \mu\text{m}$. The result portrays the assessment of pressure probe layouts (P1–P5) in PPO algorithm performance. Evaluation centered on the cumulative mean rewards (Figure 26(b)), achieved droplet size, and droplet size coefficient of variation (CV%) (Table IV Appendix 5). Results revealed that P5 achieved the highest mean rewards, reaching 0.91 in the final 10 episodes. It maintained an average droplet size of $60.05\ \mu\text{m}$ with a CV of 2% (Table IV Appendix 5), showcasing precise control over droplet size. Conversely, P1 and P2 exhibited the lowest negative mean rewards and significant deviations from the target droplet size, indicating inferior control performance. While P3 and P4 garnered positive cumulative mean rewards, they did not attain the same level of performance as P5. As a result, the study emphasized that inadequate or imprecise input conditions could hinder system performance in closed-loop control scenarios. While increasing the number of probes enhances control effectiveness by providing sufficient flow field data for optimal learning, expanding the probe count beyond the critical flow region, effectively covered by 80 probes, is unlikely to significantly impact control performance based on flow dynamics.

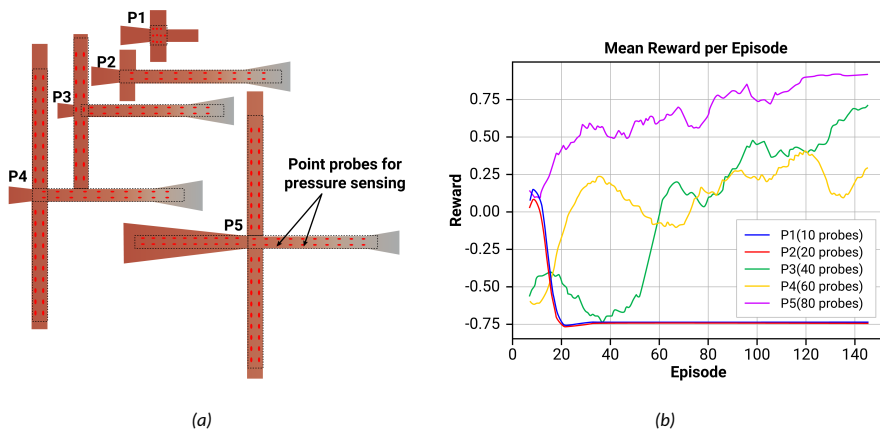


Figure 26: Pressure Probe Layouts (P1–P5) (a). Probe configurations assessed in training for target droplet size of $60\ \mu\text{m}$. Mean rewards serve as performance indicator. P5, with 80 probes, achieved the maximum mean reward of 0.91 upon convergence

4.3.3 PPO Performance in the Presence and Absence of Disturbances

As the primary focus of this study, the evaluation assesses the capability of the PPO algorithm to achieve specific droplet sizes with minimal variation in environments, particularly without external disturbances. Performance is gauged by analyzing the mean rewards accumulated by the DRL agent across different mean droplet size targets ($50\ \mu\text{m}$, $60\ \mu\text{m}$, $70\ \mu\text{m}$, and $80\ \mu\text{m}$), as illustrated in Figure 27. Evaluation metrics include mean total rewards across all episodes and the rewards in the last 15 episodes, providing insights into learning effectiveness and convergence. Results depicted in Figure 28 showcase the effectiveness of the PPO algorithm in achieving a range of droplet sizes, with rewards at convergence ranging from 0.63 to 0.92. convergence is observed after 80 episodes or simulation iterations. For the target droplet size of $50\ \mu\text{m}$, the agent receives negative rewards only

due to variance exceeding $20 \mu\text{m}$. Effecting learning and convergence is seen after 80 episodes or simulation iterations. The algorithm performs well across all tested droplet sizes but with different precision. Exceptional performance is observed for the $60 \mu\text{m}$ droplet size, with the DRL agent achieving high rewards from the start of the episode to convergence. The unsmoothness in rewards can be attributed to stochastic exploration during episodes in the bid to cover the action space to learn the optimal policy. On the other hand, higher rewards throughout episodes of the testing phase are a result of the absence of exploration. The optimal policy is applied for testing purposes, thus consistently yielding rewards exceeding 0.95.

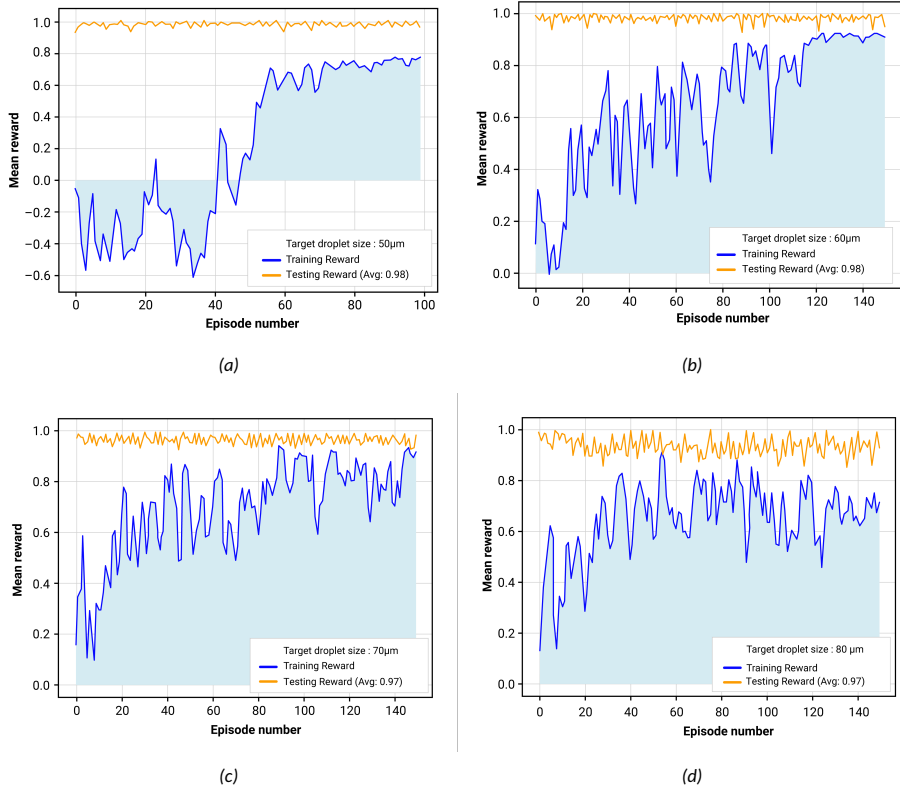
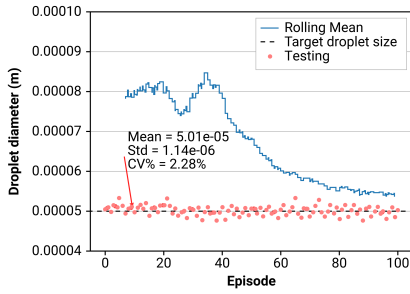
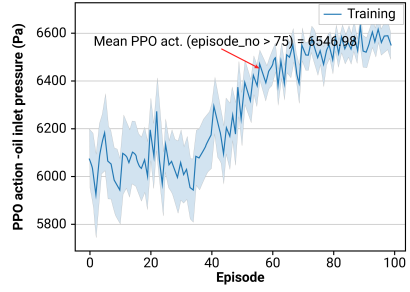


Figure 27: PPO Algorithm Performance for Setpoints (a) $50 \mu\text{m}$, (b) $60 \mu\text{m}$, (c) $70 \mu\text{m}$, and (d) $80 \mu\text{m}$ based on Mean Rewards. Good control achieved with rewards from 0.63 to 0.92 at convergence. Higher rewards during testing due to optimal policy utilization without exploration. Plot smoothing enhances clarity.

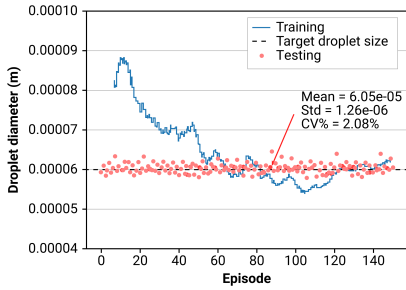
The actions taken by the agent, specifically the manipulation of oil pressure, in pursuit of achieving the various droplet targets are presented. Figure 28 illustrates the achieved droplet size characteristics alongside the actions taken to reach them. Analysis of Figure 28(a-d) reveals that the agent successfully achieves the mean droplet size targets, with a CV of less than 5% in each case. Further, a comparison with the scenario without control (open-loop) indicates that the actions taken by the PPO agent resulted in a reduction in CV by 2.6%, 4.72%, 3.6%, and 0.8% for target sizes of $50 \mu\text{m}$, $60 \mu\text{m}$, $70 \mu\text{m}$, and $80 \mu\text{m}$, respectively.



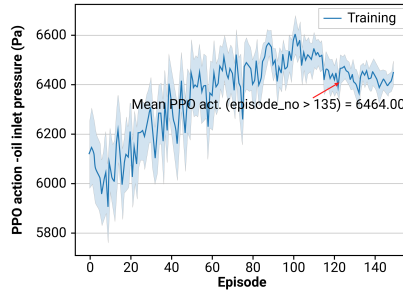
(a)



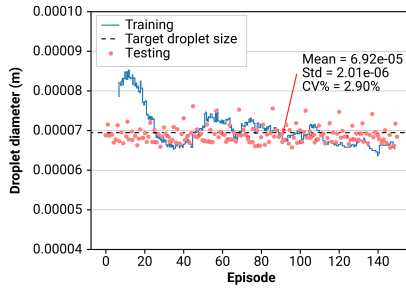
(e)



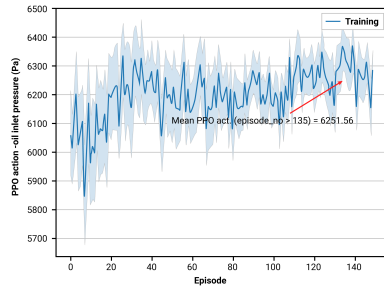
(b)



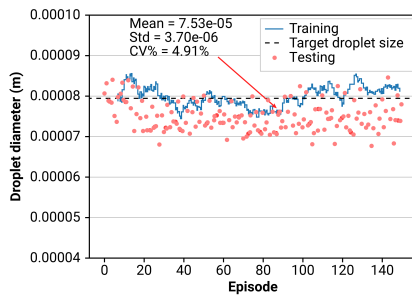
(f)



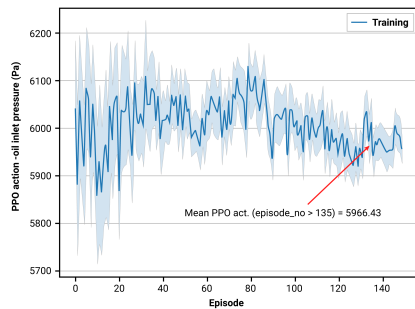
(c)



(g)



(d)



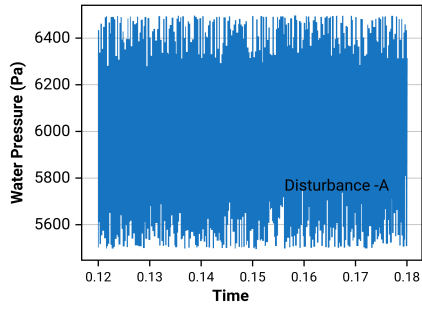
(h)

Figure 28: PPO Agent Droplet Size Control Outcomes. Mean droplet size and CV% achieved for droplet sizes (a) 50 μm , (b) 60 μm , (c) 70 μm , and (d) 80 μm through manipulation of oil pressure by the DRL agent, corresponding to ((d)-(f))

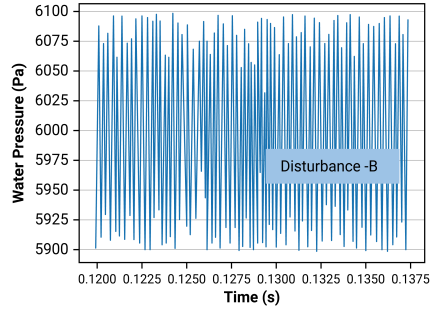
The control actions in Figure 28 (e-h), stabilizing around corresponding pressure values, i.e., 6546.98 Pa, 6465.00 Pa, 6251.56 Pa, and 5966.45 Pa for 50 μm , 60 μm , 70 μm , and 80 μm , respectively. Additionally, it is observed that better pressure stability, as seen in (e), results in smoother convergence in (a). In conclusion, the assessment of the PPO algorithm's performance underscores its effectiveness in achieving precise droplet sizes with minimal variation in environments devoid of external disturbances, demonstrating its capability to successfully achieve and maintain varying droplet size targets with remarkable precision.

Finally, the study assesses the adaptability of the agent to external disturbances. The properties of these disturbances are guided by references [125, 126, 127, 128]. Disturbances in the form of periodic mechanical vibrations are simulated as fluctuations in water pressure via sine wave functions. Three sine wave functions were simulated, varying in frequency (10 Hz, 100 Hz, 10000 Hz) and amplitude (50 Pa, 100 Pa, 500 Pa) around the average water pressure value of 6000 Pa. To evaluate the trained DRL agent's adaptability, the final policies derived from training the agent in an undisturbed environment were tested in the disturbed environment. Figures 27 and 28 illustrate the applied disturbances, the resulting droplet sizes, CV%, and rewards for a droplet size target of 50 μm , aligning with the evaluation criteria utilized in undisturbed conditions.

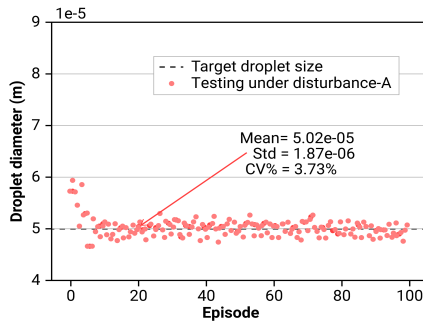
In comparison to the disturbance-free condition, the CV% rose marginally from 2.28% to 3.75% in Disturbance A and from 2.28% to 2.61% in Disturbance B. Nonetheless, the droplet size stayed near the target (CV < 4%), which is lower than the situation without control (CV 6%). The delay before controller adaptation is approximately 10 episodes. The agent adeptly managed disturbances up to an 8% rise in the mean amplitude pressure value it underwent training on, underscoring its adaptability. Disturbance C (10 Pa 50 Hz), featuring lower amplitude and frequency than other disruptions, notably influenced the environment, causing the droplet size distribution to mimic a sine wave pattern with a higher CV of 5.5%. The agent could not effectively recover from this disturbance, highlighting the need for retraining to effectively handle such scenarios. For larger amplitudes or disturbances with low frequencies, retraining was recommended. Figure 31 illustrates the agent's distinct control actions for each disturbance. In summary, the agent exhibits adaptability and responsiveness within known disturbance limits.



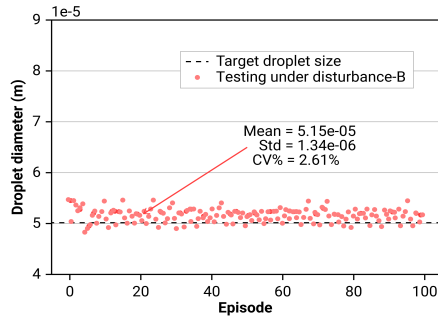
(a)



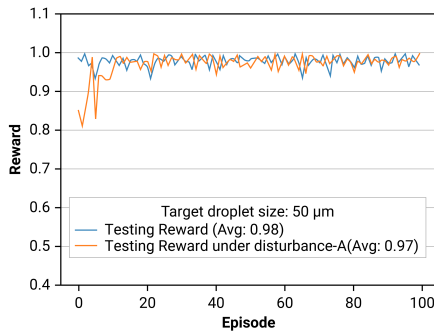
(b)



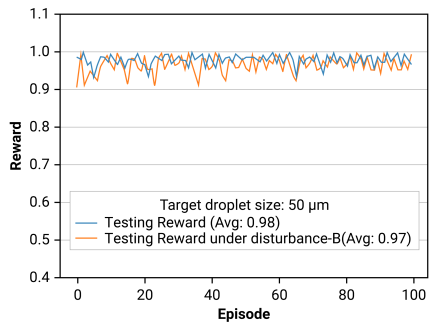
(c)



(d)



(e)



(f)

Figure 29: Agents' Adaptability to Disturbances A (500 Pa, 10 kHz) and B (100 Pa, 10 kHz). Despite slight CV% increases (A: 2.28% to 3.75%, B: 2.28% to 2.61%), droplet size remains near target (CV < 4%), unlike uncontrolled scenarios (CV ~ 6%). The controller adapts after 10 training episodes/iterations, handling up to 8% disturbance amplitude rise (CV < 5%), highlighting adaptability

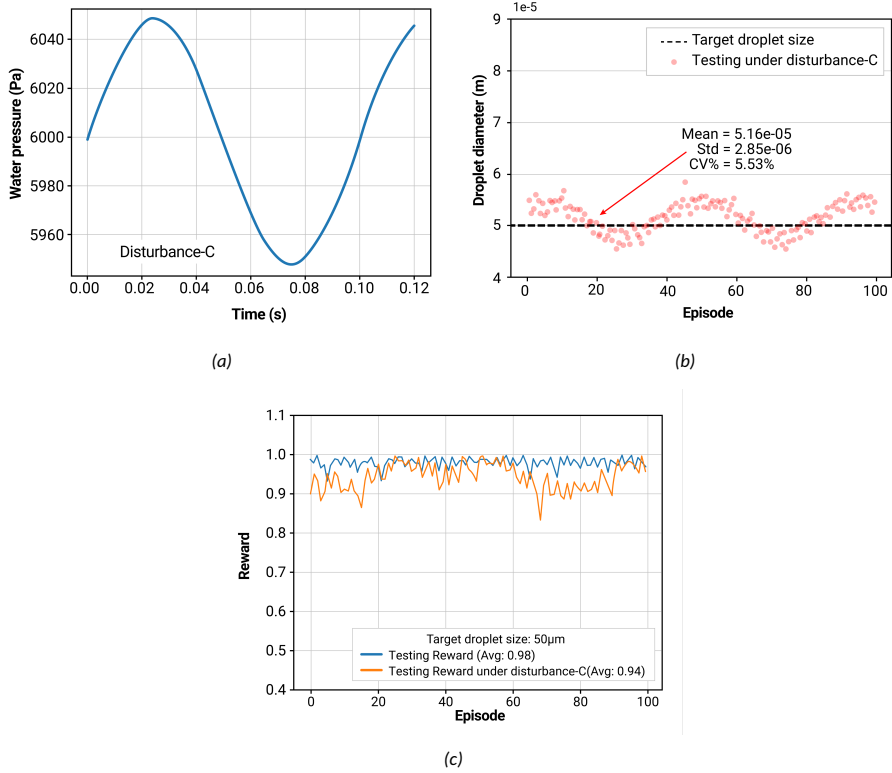


Figure 30: Agent's response to Disturbance C (10 Pa, 50 Hz), revealing (CV < 5%), inability to recover from induced disturbance. Retraining recommended

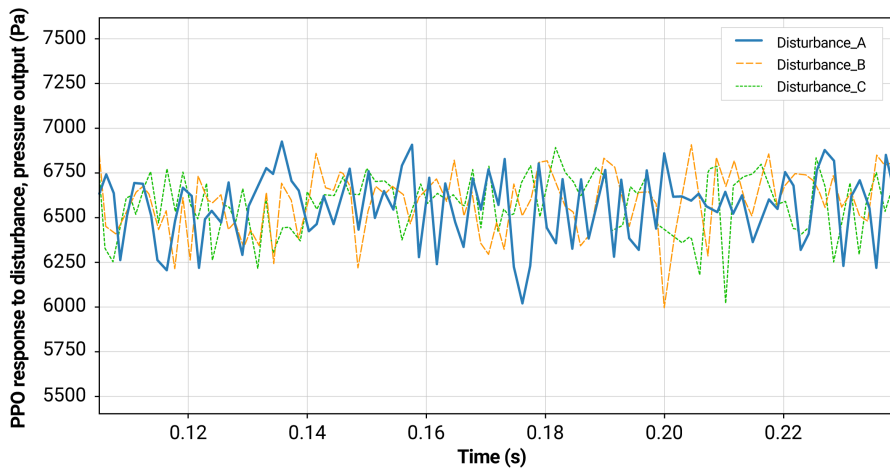


Figure 31: Distinct control actions of the DRL agent in response to disturbances A, B, C.

4.4 Summary

This study utilized Deep Reinforcement Learning (DRL) with the Proximal Policy Optimization (PPO) algorithm alongside a two-dimensional computational fluid dynamics (CFD) model to achieve closed-loop control in microfluidics. The primary objective was to attain the desired droplet size with minimal variability in a microfluidic capillary flow-focusing device. An artificial neural network was employed to map sensing signals, such as flow pressure and droplet size, to control actions, specifically adjusting the continuous phase inlet pressure.

To validate the numerical model's accuracy and reliability, the study conducted verification against experimental data, which yielded favorable agreement, with errors generally remaining below 11%. This affirmed the model's reliability for droplet control exploration. Moreover, mesh independence studies resulted with Mesh M6 as the optimal choice for balancing sharpness and grid independence. In the subsequent phase, the evaluation focused on understanding the impact of pressure ratios on droplet size and optimizing sensor probe configuration.

Furthermore, the study comprehensively assessed the performance of the PPO algorithm in both stable and disturbed environments. The algorithm effectively achieved specific droplet sizes across various targets, demonstrating rewards at convergence ranging from 0.63 to 0.92. Notably, the PPO algorithm showcased improved control across different target sizes (ranging from 50 to 80 μm), maintaining a coefficient of variation (CV%) below 5% for all targets and outperforming scenarios without control. In the presence of disturbances, the PPO algorithm exhibited adaptability within defined limits, allowing for fluctuations of up to 8% in amplitude around the mean input, with minor impacts on droplet size and control effectiveness. However, significant disturbances underscored the need for retraining to ensure optimal performance.

In summary, the integrated DRL-CFD approach demonstrated effectiveness in achieving precise droplet control and adapting to changing environmental conditions, thereby advancing microfluidic technology.

5 CONCLUSION AND FUTURE WORK

5.1 Future research direction

A future study aims to build on previous research using the PPO algorithm. Its goal is to integrate additional DRL algorithms to establish a benchmark for microfluidic-controller design. The primary objective remains achieving precise control over droplet size. This is done by utilizing the established CFD + DRL framework, which combines OPENFOAM with PyTorch. Here, the focus lies in proposing the framework and providing a brief overview. Figure 32 offers a conceptual view of the framework. The newly introduced algorithms include Deep Deterministic Policy Gradient (DDPG), Trust Region Policy Optimization (TRPO), and Double Deep Q-Network (DDQN). DDPG and TRPO excel in continuous action spaces, whereas DDQN operates with discrete action selection. Despite DDQN's discrete nature, assessing its performance against other approaches will provide a clear evaluation. DDPG and PPO both utilize an actor-critic architecture to optimize policies for maximizing cumulative rewards, sharing fundamental similarities. However, their training procedures and optimization objectives exhibit slight differences. PPO places emphasis on policy enhancement through constraint-based optimization, while DDPG prioritizes value function approximation and policy gradient ascent. Additionally, TRPO adopts a trust region approach, constraining policy updates to keep the new policy close to the old one within a defined region.

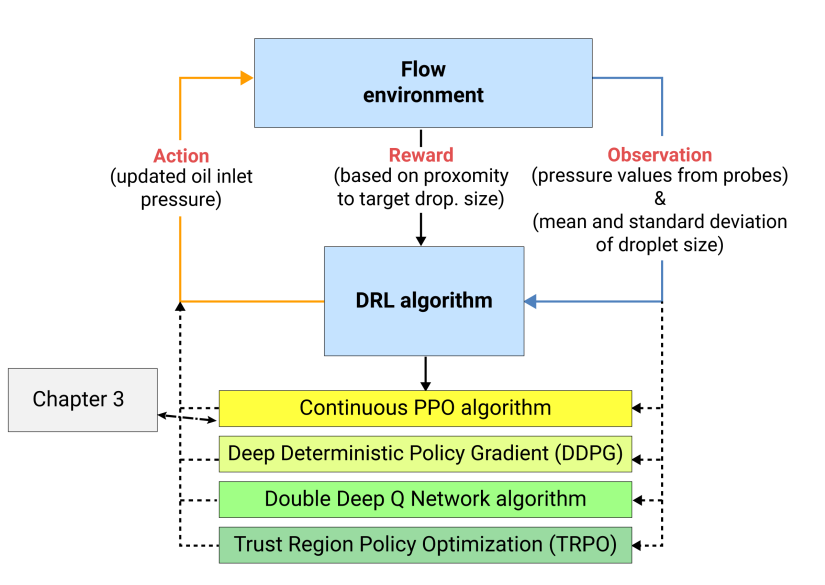


Figure 32: Conceptual view of the integrated DRL framework with PPO, DDPG, TRPO, and DDQN algorithms for microfluidic-controller design benchmarking. Utilizes CFD + DRL framework combining OPENFOAM with PyTorch. Each algorithm's implementation involves customizing neural network architectures. Training conducted on a duplication flow environment interface.

Although TRPO shares similarities with PPO, it directly enforces a constraint on the size of policy updates, aiming for more stable training by limiting policy changes. In contrast, PPO uses a clipped surrogate objective function to restrict the extent of policy updates by clipping the ratio between new and old policy probabilities. However, unlike the PPO algorithm, DDQN operates within discrete action spaces. DDQN is a variant of the Q-learning

algorithm, made to tackle the overestimation bias experienced in traditional Q-learning methods. DDQN enhances the original Deep Q-Network (DQN) by incorporating a separate target network for action selection during training. This addition aids in stabilizing learning processes and mitigating overestimation errors.

The implementation of each DRL algorithm entails customizing neural network architectures to suit their specific requirements. The training process for each DRL model will be conducted on a duplication flow environment interface. Overall, the research will offer valuable insights into achieving precise droplet size control with machine learning, contributing significantly to the advancement of microfluidic technology.

5.2 Conclusion

The primary challenge in droplet microfluidics is achieving and maintaining precise control over droplet size and uniformity. Traditional methods for controlling droplet size often rely on mathematical-empirical models and manual tuning. These methods face issues like extended settling times, overshoots, and limitations in evaluating the full range of droplet sizes feasible for specific applications. Additionally, the reliance on accurate mathematical models for classical closed-loop control introduces complexities that hinder adaptability. To address these challenges, this research proposes innovative strategies that integrate fluid dynamics modeling with real-time feedback control algorithms. By simulating and optimizing controller designs in a simulation environment before experimental implementation, the goal is to develop robust and adaptive control strategies. Therefore, this research addresses the following questions(RQ):

- RQ1: How can a simulated system effectively evaluate the complete parameter space and improve precision in droplet generation within microfluidic systems?
- RQ2: Can an optimal control solution developed for a simulated environment of a flow-focusing junction be successfully implemented in an experimental droplet generation setup?
- RQ3: Is model-free control of droplet generation achievable through machine learning techniques?
- RQ4: Which set of machine learning tools can facilitate robust, adaptable, and stable control of droplet generation in microfluidic systems?

To address these questions, the following studies were conducted:

Closed-Loop Simulation of Microfluidic System Integrated with Proportional-Integral (PI) Control (Publication I, addressing RQ1) : This study leverages COMSOL Multiphysics and MATLAB via LiveLink to develop an automated feedback system for a microfluidic model. The PI controller adjusts the dispersed phase flow rate based on real-time measurements of droplet diameter. In open-loop scenarios, the system exhibits a coefficient of variation (CV) of approximately 15%, indicating significant deviations from setpoints of 40 μm . However, in closed-loop feedback mode, the PI controller consistently maintains a measured droplet size of 39 μm , reducing the CV to approx. 2%. Further evaluations demonstrated a diameter offset/error of less than 3% within the simulation time, achieving a coefficient of determination (R^2) value of 0.9937. This approach effectively addresses the challenge of evaluating the complete parameter space of the controlled parameters across a range of droplet sizes.

Genetic Algorithm (GA) for PID Controller Tuning Optimization (Publication II, addressing RQ1 as support): This study explores the use of a Genetic Algorithm (GA) for tuning PID controllers in microfluidic systems to address the challenge of extended settling times, which is critical for applications requiring high throughput and precise control of droplet sizes. Existing literature on PID controller tuning methods, such as trial-and-error adjustment and Ziegler-Nichols methods, highlights the issue of prolonged settling times in closed-loop systems. These extended settling times can range from milliseconds to several seconds, underscoring the need for more efficient control methodologies. To optimize PID controller parameters, GA is employed due to its robust search capabilities and suitability for nonlinear systems. PID parameters are encoded as chromosomes within a population and evaluated based on fitness criteria. MATLAB and Simulink facilitate dynamic modeling of system components, integrating advanced system identification techniques crucial for accurately representing pressure-driven microfluidic setups. Results demonstrate that GA-tuned PID controllers significantly reduce settling times and overshoot compared to conventional tuning methods. The GA approach achieves an overshoot of 0.5% and a settling time of approximately 0.088 seconds. In contrast, classical tuning methods typically yield longer settling times around 0.338 seconds with a higher overshoot of 1.5%. The optimization process signifies superior performance in controller tuning by minimizing the time required for the system to stabilize.

Dual-PID Control Strategy Implementation in Experimental Setup (Publication III, Addressing RQ2): In implementing the Dual-PID Control Strategy, a significant advancement in microfluidic control methodologies was achieved by integrating pressure regulation and droplet size control within a unified framework. Unlike conventional methods that treat these variables separately, this strategy recognizes their interdependence, ensuring precise control to enhance system performance and reliability. Initially developed and optimized through MATLAB and Simulink simulations, the strategy enabled precise tuning of controller parameters before practical deployment using Python on a Raspberry Pi, effectively bridging the simulation-to-real-world gap. During practical implementation, minor adjustments were necessary to address oscillations around target pressure values. The implementation outcome included a remarkable reduction in pressure stabilization times in the CogniFlow-Drop system from 120 seconds (typical with traditional syringe pump setups) to just 10 seconds—a twelve-fold improvement. Moreover, the strategy facilitated the production of monodisperse droplets with coefficients of variation (CVs) between 5% and 10% across a range of droplet diameters from approximately 50 μm to 200 μm . Comparing simulations with real-world results, pressure stabilization times were approximately 20 seconds in simulations and 10 seconds in practical setups, underscoring the strategy's reliability and effectiveness in practical microfluidic applications.

Simulations aid the development of an empirical model (Publication IV, Addressing RQ2 as support): The study highlights the challenge of accurately representing complex three-dimensional experimental setups in simplified two-dimensional simulations. To overcome this limitation, the introduction of the "effective depth" parameter (H_{eff}) in 2D simulations approximates the third dimension, ensuring simulated droplet volumes can closely align with real-world observations. Additionally, the study develops an empirical model for predicting droplet generation rates. This model incorporates a simple three-parameter set tailored to forecast droplet generation under specific conditions, predicting droplet sizes from 50 to 70 micrometers and generation rates from 500 to 1500 per second.

Reinforcement Learning (DRL) Integration with CFD Models for microfluidic control (Publication V, Addressing RQ3 and RQ4): Integrating Deep Reinforcement Learning (DRL) with Computational Fluid Dynamics (CFD) models marks a significant advancement in microfluidic control systems. Unlike traditional closed-loop systems that rely on explicit mathematical models, this study adopts a model-free approach using the Proximal Policy Optimization (PPO) algorithm within a two-dimensional CFD framework. PPO's capability to handle continuous action spaces allows for seamless adjustments of control inputs. Implemented with OpenFOAM and PyTorch integration, the PPO agent utilizes an actor-critic network to observe pressure and droplet size, adjusting inlet pressure and receiving rewards based on objectives achieved. The numerical model validation against experimental data showed strong agreement between simulated and actual results, with errors consistently below 11%. A notable achievement was achieving precise droplet size control, reducing the Coefficient of Variation (CV) from 4.72% to 0.8% across a range of droplet sizes (50 μm to 80 μm). The study also emphasized the PPO algorithm's resilience to external disturbances, maintaining mean droplet sizes close to targets even with pressure variations up to 8% amplitude, keeping the CV below 5%. However, it noted that larger disturbances or low-frequency fluctuations might necessitate model retraining for improved performance. In conclusion, this study supports Research Questions 3 and 4 by demonstrating the feasibility of model-free droplet generation control using machine learning techniques, showcasing adaptability to disturbances.

Overall, this research underscores the advancement towards more efficient and reliable droplet microfluidics through innovative control strategies and computational techniques. Future directions may include further refinement of machine learning algorithms, integration of multi-scale modeling, and validation across broader ranges of operational conditions to enhance robustness and applicability in diverse microfluidic environments.

List of Figures

1	Trend of studies on microfluidics integration of control methods	13
2	Simulation Framework for Droplet Size Control (a) Flow-focusing device as the plant model with user-defined droplet size (dset) and control flow rate ($Q_w(t)$). COMSOL LiveLink interface enables MATLAB's PI controller to adjust ($Q_w(t)$) based on feedback ($d(t)$). (b) Illustration of simulation settings: t_0 as initialization time, t_f as current simulation time, t_s for feedback loop sampling time, t_{end} as simulation end time. (u, v) denote variable velocities and pressure relative to ϕ	20
3	Flow-Focusing Device Geometry. Left: Full geometry. Right: Simplified version. Domains labeled: Oil, Water, Junction, Sensor, Outlet. Rhomboid filters on oil path. Horizontal symmetry, only upper half simulated.	22
4	Tailored quadrilateral mesh with region-specific density. Avg. mesh quality: 97%. Total elements: 270,908. Mesh independence study confirms <1% droplet area variation with $\geq 225,000$ elements (Appendix section of Appendix 1)	23
5	Controller Design Interface in MATLAB Control Systems Designer Toolbox (left) and Step Response Based on Design Criteria (right).....	25
6	Dripping Regime observed for droplet formation, in stages (a) Filling stage, (b) Necking stage, (c) Growing stage, and (d) Detachment stage.	26
7	Influence of Flow Rate on Droplet Size(a) Varied oil flow rates (100 $\mu\text{l}/\text{min}$ to 400 $\mu\text{l}/\text{min}$) with constant water flow rate (30 $\mu\text{l}/\text{min}$) (b) Varied water flow rates (5 $\mu\text{l}/\text{min}$ to 50 $\mu\text{l}/\text{min}$) with constant oil flow rate (200 $\mu\text{l}/\text{min}$). Further illustration of droplets for Q_w/Q_{oil} at (c)30/210 (d) 30/120 (e) 50/200. Sensitivity of droplet size to changes higher for water flow rate than oil flow rate.....	27
8	Open-loop vs. Closed-loop Droplet Control: (a) Open-loop aimed for a 40 μm droplet with 400 $\mu\text{l}/\text{min}$ continuous phase and 50 $\mu\text{l}/\text{min}$ initial dispersed phase flow rates, resulting in CV $\approx 15\%$ deviation to around 34 μm . Closed-loop with a PI controller rapidly achieved 39 μm within 1 s, reducing CV to 2% (b) Controller maintained desired droplet size with stable dispersed phase flow rate at 63.9 $\mu\text{l}/\text{min}$	28
9	Closed-loop Droplet Size Control at setpoints (a) 30 μm , (b) 35 μm , and (c) 45 μm (d) Comparison of setpoint diameters to observed diameters (30 μm -60 μm range). The PI controller maintains a diameter error under 3%, with a coefficient of determination (R^2) value of 0.9937	29
10	Genetic Algorithm Workflow	30
11	Schematic representation of PID parameters (K_p, K_i, K_d) tuning using Genetic algorithm to minimize error between desired and measured droplet size, considering performance criteria (IAE, ISE, ITAE). Setup conducted using MATLAB and Simulink.....	31
12	Steps in System Identification Technique	32
13	Experimental Setup for Microfluidic System Characterization. Featuring PDMS chip, fluid connectors, pumping system, ADC, pressure sensors, droplet size circuitry, and Raspberry Pi 4B	33
14	Experimental Results on Pump Parameters and Droplet Generation. (a) Voltage (V) vs Pressure (kPa) for the oil driving pump. (b) Droplet diameter (μm) vs Pressure (kPa) for the oil driving pump.	35

15	Closed-Loop System Transfer Functions. First-order models derived from system identification for the pump and chip, and from the analytical model (Section B of Appendix 2) for the droplet sensor.	36
16	Dual-PID Control Strategy for Microfluidic Droplet Generation. Inner feedback loops (gray background) and an outer feedback loop for regulating pressure and droplet size, respectively.	39
17	(Top) Prototype assembly: (1) Electronics module with power supply (a) pump driver and pressure sensor (b) RPi4B with ADC and optical sensor circuit (c) copper plates. (2) Sensorics module featuring photodiode and lens (a), microfluidic chip mount (b), and light source mount (c). (3) Fluidics module with pump mounts (a) foam-padded enclosure (b) containers for sample, reagent, and product (c). (4) Enclosure with 3D printed walls and wooden base plate for stability (Bottom) (A) Automated generation of user-defined droplets, collected for downstream manipulation. (B) Interconnect blocks and communication flow within the CogniFlow-Drop System [94].	40
18	Pressure drops vs. peak-to-peak voltages for chip variants with different cross-junction widths: 90 μm with with water pump (a) 125 μm with oil pump (b), and 240 μm with water pump (c). Nuances across the chip variants quantified through the voltage-to-pressure coefficient (C_{vp}).	42
19	Genetic Algorithm (GA) Tuning Outcome for Pressure Control: (a) IAE, (b) IE, (c) All Metrics, (d) result from controller gains adjustment based on IE and IAE outcomes to minimize overshoot and oscillations	43
20	Pressure Stabilization Time Comparison (a) Dual PID control: 10s stabilization time vs. (b) Syringe pumps: 120s.	44
21	(a) Droplet Control Framework. (a) Critical flow area of FFD with pressure-sensing probes indicated by red dots. Droplet interface defined by volume fraction function at 0.5. (b) Implementation framework: PPO agent interacts with the fluidic environment. The agent monitors pressure data and outlet droplet size, adjusts oil inlet pressure, and earns rewards based on proximity to the target droplet size and size variability.	48
22	PPO algorithm flow. Visual representation of the PPO (Proximal Policy Optimization) algorithm with policy-value (actor-critic) architecture. The Value Network evaluates action values, guiding policy updates by estimating advantages through the Generalized Advantage Estimation (GAE). The Policy Network determines policy, updated via Actor Loss to maximize expected rewards. The Critic Loss updates the Critic Network based on observed rewards. Rewards, states, and actions are pivotal in driving learning, while trajectories stored in the Replay Buffer facilitate efficient experience replay	51
23	Computational Mesh Optimization. (a) Mesh refinement in gradient-rich areas. (b) (Top) Visualise droplet interface sharpness per mesh (Bottom) Evaluation across meshes M1 to M8 considers interface sharpness, droplet length, and detachment time. Optimal mesh, M6, balances sharpness and grid independence.	55

24	Comparison of Simulation and Experimental Model. (Top) Replicated experimental model with numerical model (colored) vs. Wu et al.'s experimental model (gray). (Bottom) Plot of droplet length vs. dispersed phase velocity at constant oil velocity of 0.00252 m/s. Strong agreement, errors < 7%, except at 0.00126 m/s (11%).	56
25	Variations in Droplet Size (a) and Relationship between Pressure Ratio (P_w/P_{oil}) and Droplet Size Variation (CV%). Droplet sizes ranging from 55 μm to 88 μm exceed the 5% CV threshold, with action space boundaries at 4500–7000 Pa.	57
26	Pressure Probe Layouts (P1–P5) (a). Probe configurations assessed in training for target droplet size of 60 μm . Mean rewards serve as performance indicator. P5, with 80 probes, achieved the maximum mean reward of 0.91 upon convergence	58
27	PPO Algorithm Performance for Setpoints (a) 50 μm , (b) 60 μm , (c) 70 μm , and (d) 80 μm based on Mean Rewards. Good control achieved with rewards from 0.63 to 0.92 at convergence. Higher rewards during testing due to optimal policy utilization without exploration. Plot smoothing enhances clarity.	59
28	PPO Agent Droplet Size Control Outcomes. Mean droplet size and CV% achieved for droplet sizes (a) 50 μm , (b) 60 μm , (c) 70 μm , and (d) 80 μm through manipulation of oil pressure by the DRL agent, corresponding to ((d)-(f))	60
29	Agents' Adaptability to Disturbances A (500 Pa, 10 kHz) and B (100 Pa, 10 kHz). Despite slight CV% increases (A: 2.28% to 3.75%, B: 2.28% to 2.61%), droplet size remains near target (CV < 4%), unlike uncontrolled scenarios (CV \sim 6%). The controller adapts after 10 training episodes/iterations, handling up to 8% disturbance amplitude rise (CV < 5%), highlighting adaptability	62
30	Agent's response to Disturbance C (10 Pa, 50 Hz), revealing (CV < 5%), inability to recover from induced disturbance. Retraining recommended	63
31	Distinct control actions of the DRL agent in response to disturbances A, B, C.	63
32	Conceptual view of the integrated DRL framework with PPO, DDPG, TRPO, and DDQN algorithms for microfluidic-controller design benchmarking. Utilizes CFD + DRL framework combining OPENFOAM with PyTorch. Each algorithm's implementation involves customizing neural network architectures. Training conducted on a duplication flow environment interface.	65

List of Tables

1	State-of-the-art for closed-loop microfluidic droplet size control.	15
2	Summary of Contributions in Relation to Research Papers	17
3	Microfluidic Chip (Input Water Pressure-Output Droplet Size Relation) model	35
4	Pump (Input Voltage-Output Pump Pressure Relation) System Model.	36
5	System performance - classical tuning of PID controller	37
6	System performance – genetic algorithm tuning of PID controller	37
7	PID Controller Gain Comparison: Simulation vs. Modified for Experimental Setup.....	44
8	Neural Network(NN) Architecture	54
9	Parameter Values/Details for DRL Training	54

References

- [1] A.-G. Niculescu, C. Chircov, A. C. Bîrcă, and A. M. Grumezescu, "Fabrication and applications of microfluidic devices: A review," *International Journal of Molecular Sciences*, vol. 22, no. 4, p. 2011, 2021.
- [2] S. Regmi, C. Poudel, R. Adhikari, and K. Q. Luo, "Applications of microfluidics and organ-on-a-chip in cancer research," *Biosensors*, vol. 12, no. 7, p. 459, 2022.
- [3] T. N. D. Trinh, H. D. K. Do, N. N. Nam, T. T. Dan, K. T. L. Trinh, and N. Y. Lee, "Droplet-based microfluidics: applications in pharmaceuticals," *Pharmaceuticals*, vol. 16, no. 7, p. 937, 2023.
- [4] A. Lashkaripour, D. P. McIntyre, S. G. Calhoun, K. Krauth, D. M. Densmore, and P. M. Fordyce, "Design automation of microfluidic single and double emulsion droplets with machine learning," *Nature Communications*, vol. 15, no. 1, p. 83, 2024.
- [5] T. Trantidou, M. Friddin, A. Salehi-Reyhani, O. Ces, and Y. Elani, "Droplet microfluidics for the construction of compartmentalised model membranes," *Lab on a Chip*, vol. 18, no. 17, pp. 2488–2509, 2018.
- [6] J. Shi, Y. Zhang, Y. Fan, Y. Liu, and M. Yang, "Recent advances in droplet-based microfluidics in liquid biopsy for cancer diagnosis," *Droplet*, vol. 3, no. 1, p. e92, 2024.
- [7] S. R. Barman, I. Khan, S. Chatterjee, S. Saha, D. Choi, S. Lee, and Z.-H. Lin, "Electrowetting-on-dielectric (EWOD): Current perspectives and applications in ensuring food safety," *Journal of Food and Drug Analysis*, vol. 28, no. 4, p. 595, 2020.
- [8] K. Choi, A. H. Ng, R. Fobel, and A. R. Wheeler, "Digital microfluidics," *Annual Review of Analytical Chemistry*, vol. 5, pp. 413–440, 2012.
- [9] J. R. d. O. Bianchi, L. G. De la Torre, and A. L. R. Costa, "Droplet-based microfluidics as a platform to design food-grade delivery systems based on the entrapped compound type," *Foods*, vol. 12, no. 18, p. 3385, 2023.
- [10] K. Muijlwijk, C. Berton-Carabin, and K. Schroën, "Cross-flow microfluidic emulsification from a food perspective," *Trends in Food Science & Technology*, vol. 49, pp. 51–63, 2016.
- [11] Q. Xu, M. Hashimoto, T. T. Dang, T. Hoare, D. S. Kohane, G. M. Whitesides, R. Langer, and D. G. Anderson, "Preparation of monodisperse biodegradable polymer microparticles using a microfluidic flow-focusing device for controlled drug delivery," *Small*, vol. 5, no. 13, pp. 1575–1581, 2009.
- [12] A. B. Theberge, F. Courtois, Y. Schaerli, M. Fischlechner, C. Abell, F. Hollfelder, and W. T. Huck, "Microdroplets in microfluidics: an evolving platform for discoveries in chemistry and biology," *Angewandte Chemie International Edition*, vol. 49, no. 34, pp. 5846–5868, 2010.
- [13] M. Nekouei and S. A. Vanapalli, "Volume-of-fluid simulations in microfluidic T-junction devices: Influence of viscosity ratio on droplet size," *Physics of Fluids*, vol. 29, no. 3, 2017.
- [14] Z. Peng, S. Iwabuchi, K. Izumi, S. Takiguchi, M. Yamaji, S. Fujita, H. Suzuki, F. Kambara, G. Fukasawa, A. Cooney, *et al.*, "Lipid vesicle-based molecular robots," *Lab on a Chip*, 2024.

- [15] L. Amirifar, M. Besanjideh, R. Nasiri, A. Shamloo, F. Nasrollahi, N. R. de Barros, E. Davoodi, A. Erdem, M. Mahmoodi, V. Hosseini, *et al.*, "Droplet-based microfluidics in biomedical applications," *Biofabrication*, vol. 14, no. 2, p. 022001, 2022.
- [16] J. I. Park, *Microfluidic Development of Bubble-templated Microstructured Materials*. PhD thesis, 2010.
- [17] T. B. Tan, M. Nakajima, and C. P. Tan, "Effect of polysaccharide emulsifiers on the fabrication of monodisperse oil-in-water emulsions using the microchannel emulsification method," *Journal of food engineering*, vol. 238, pp. 188–194, 2018.
- [18] A. Lashkaripour, C. Rodriguez, N. Mehdipour, R. Mardian, D. McIntyre, L. Ortiz, J. Campbell, and D. Densmore, "Machine learning enables design automation of microfluidic flow-focusing droplet generation," *Nature Communications*, vol. 12, no. 1, p. 25, 2021.
- [19] A. Kalantarifard, E. A. Haghighi, and C. Elbuken, "Damping hydrodynamic fluctuations in microfluidic systems," *Chemical Engineering Science*, vol. 178, pp. 238–247, 2018.
- [20] P. M. Korczyk, O. Cybulski, S. Makulska, and P. Garstecki, "Effects of unsteadiness of the rates of flow on the dynamics of formation of droplets in microfluidic systems," *Lab on a Chip*, vol. 11, no. 1, pp. 173–175, 2011.
- [21] S. K. Jena, T. Srivastava, S. S. Bahga, and S. Kondaraju, "Effect of channel width on droplet generation inside T-junction microchannel," *Physics of Fluids*, vol. 35, no. 2, 2023.
- [22] F. H. Arnold, S. R. Quake, R. W. Roberts, and T. Thorsen, "Dynamic Pattern Formation in a Vesicle-Generating Microfluidic Device," *Physics Review Letter*, vol. 86, no. 18, pp. 4163–4166, 2001.
- [23] P. Kumar and M. Pathak, "Dynamic wetting characteristics during droplet formation in a microfluidic T-junction," *International Journal of Multiphase Flow*, vol. 156, p. 104203, 2022.
- [24] W. Zeng, B. Wang, H. Chang, and P. Neuzil, "Quantitative study of droplet generation by pressure-driven microfluidic flows in a flow-focusing microdroplet generator," *Physics of Fluids*, vol. 36, no. 3, 2024.
- [25] W. Zeng, Z. Tong, X. Shan, H. Fu, and T. Yang, "Monodisperse droplet formation for both low and high capillary numbers in a T-junction microdroplet generator," *Chemical Engineering Science*, vol. 243, p. 116799, 2021.
- [26] P. Garstecki, I. Gitlin, W. DiLuzio, G. M. Whitesides, E. Kumacheva, and H. A. Stone, "Formation of monodisperse bubbles in a microfluidic flow-focusing device," *Applied Physics Letters*, vol. 85, no. 13, pp. 2649–2651, 2004.
- [27] D. McIntyre, A. Lashkaripour, P. Fordyce, and D. Densmore, "Machine learning for microfluidic design and control," *Lab on a Chip*, vol. 22, no. 16, pp. 2925–2937, 2022.
- [28] Y. Mahdi and K. Daoud, "Microdroplet size prediction in microfluidic systems via artificial neural network modeling for water-in-oil emulsion formulation," *Journal of Dispersion Science and Technology*, vol. 38, no. 10, pp. 1501–1508, 2017.

- [29] S. A. Damiati, D. Rossi, H. N. Joensson, and S. Damiati, "Artificial intelligence application for rapid fabrication of size-tunable PLGA microparticles in microfluidics," *Scientific Reports*, vol. 10, no. 1, p. 19517, 2020.
- [30] S. Mottaghi, M. Nazari, S. M. Fattahi, M. Nazari, and S. Babamohammadi, "Droplet size prediction in a microfluidic flow focusing device using an adaptive network based fuzzy inference system," *Biomedical Microdevices*, vol. 22, pp. 1–12, 2020.
- [31] A. Lashkaripour, M. Goharimanesh, A. A. Mehrizi, and D. Densmore, "An adaptive neural-fuzzy approach for microfluidic droplet size prediction," *Microelectronics Journal*, vol. 78, pp. 73–80, 2018.
- [32] L. Chagot, C. Quilodrán-Casas, M. Kalli, N. M. Kovalchuk, M. J. Simmons, O. K. Matar, R. Arcucci, and P. Angeli, "Surfactant-laden droplet size prediction in a flow-focusing microchannel: a data-driven approach," *Lab on a Chip*, vol. 22, no. 20, pp. 3848–3859, 2022.
- [33] C. Barnes, A. R. Sonwane, E. C. Sonnenschein, and F. Del Giudice, "Machine learning enhanced droplet microfluidics," *Physics of Fluids*, vol. 35, no. 9, 2023.
- [34] S. Yazdanparast, P. Rezaei, and A. Amirfazli, "Microfluidic Droplet-Generation Device with Flexible Walls," *Micromachines*, vol. 14, no. 9, p. 1770, 2023.
- [35] E. Miller, M. Rotea, and J. P. Rothstein, "Microfluidic device incorporating closed loop feedback control for uniform and tunable production of micro-droplets," *Lab on a Chip*, vol. 10, no. 10, pp. 1293–1301, 2010.
- [36] A. Bransky, N. Korin, M. Khoury, and S. Levenberg, "A microfluidic droplet generator based on a piezoelectric actuator," *Lab on a Chip*, vol. 9, no. 4, pp. 516–520, 2009.
- [37] M. K. Mulligan and J. P. Rothstein, "Scale-up and control of droplet production in coupled microfluidic flow-focusing geometries," *Microfluidics and Nanofluidics*, vol. 13, pp. 65–73, 2012.
- [38] M. Joanicot and A. Ajdari, "Droplet control for microfluidics," *Science*, vol. 309, no. 5736, pp. 887–888, 2005.
- [39] D. Crawford, C. Smith, and G. Whyte, "Image-based closed-loop feedback for highly mono-dispersed microdroplet production," *Scientific reports*, vol. 7, no. 1, p. 10545, 2017.
- [40] W. Zeng, S. Li, and Z. Wang, "Closed-loop feedback control of droplet formation in a T-junction microdroplet generator," *Sensors and Actuators A: Physical*, vol. 233, pp. 542–547, 2015.
- [41] X. Duan, Z. Zheng, Y. Luo, and C. Song, "Closed-loop feedback control for droplet-based microfluidics: a characteristic investigation on passive and on-demand droplet generation," in *International Conference on Optical and Photonic Engineering (icOPEN 2022)*, vol. 12550, pp. 196–201, SPIE, 2023.
- [42] W. Zeng, S. Yang, Y. Liu, T. Yang, Z. Tong, X. Shan, and H. Fu, "Precise monodisperse droplet generation by pressure-driven microfluidic flows," *Chemical engineering science*, vol. 248, p. 117206, 2022.

- [43] R. Kebriaei and A. S. Basu, "Autosizing closed-loop drop generator using morphometric image feedback," in *17th International Conference on Miniaturized Systems for Chemistry and Life Sciences, MicroTAS*, vol. 2013, pp. 1944–1946, 2013.
- [44] Y. Xie, A. J. Dixon, J. Rickel, A. L. Klibanov, and J. A. Hossack, "Closed-loop feedback control of microbubble diameter from a flow-focusing microfluidic device," *Biomeicrofluidics*, vol. 14, no. 3, 2020.
- [45] S. Mottaghi, M. Nazari, M. Nazari, N. Sepehry, and A. Mahdavi, "Control of droplet size in a two-phase microchannel using PID controller: A novel experimental study," *Amirkabir Journal of Mechanical Engineering*, vol. 53, no. 7, pp. 4279–4292, 2021.
- [46] O. J. Dressler, P. D. Howes, J. Choo, and A. J. deMello, "Reinforcement learning for dynamic microfluidic control," *ACS omega*, vol. 3, no. 8, pp. 10084–10091, 2018.
- [47] H. Fu, W. Zeng, S. Li, and S. Yuan, "Electrical-detection droplet microfluidic closed-loop control system for precise droplet production," *Sensors and Actuators A: Physical*, vol. 267, pp. 142–149, 2017.
- [48] Z. Wang, R. Samanipour, M. Gamaleldin, K. Sakthivel, and K. Kim, "An automated system for high-throughput generation and optimization of microdroplets," *Biomeicrofluidics*, vol. 10, no. 5, 2016.
- [49] C. Cantwell, J. S. McGrath, C. A. Smith, and G. Whyte, "Image-Based Feedback of Multi-Component Microdroplets for Ultra-Monodispersed Library Preparation," *Micromachines*, vol. 15, no. 1, p. 27, 2023.
- [50] W. Zeng, S. Li, and Z. Wang, "Closed-loop feedback control of droplet formation in a T-junction microdroplet generator," *Sensors and Actuators A: Physical*, vol. 233, pp. 542–547, 2015.
- [51] A. Sugar, M. Serag, U. Buttner, M. Fahs, S. Habuchi, and H. Hoteit, "Experimental and numerical investigation of polymer pore-clogging in micromodels," *Scientific Reports*, vol. 13, no. 1, p. 8245, 2023.
- [52] Y. Kim, S. Joshi, L. Davidson, P. Leduc, and W. Messner, "Dynamic control of 3d chemical profiles with a single 2d microfluidic platform," *Lab on a chip*, vol. 11, no. 13, pp. 2182–2188, 2011.
- [53] C. Serra, G. Schlatter, N. Sary, F. Schönfeld, and G. Hadziioannou, "Free radical polymerization in multilaminated microreactors: 2d and 3d multiphysics cfd modeling," *Microfluidics and Nanofluidics*, vol. 3, pp. 451–461, 2007.
- [54] Z. Nie, M. Seo, S. Xu, P. C. Lewis, M. Mok, E. Kumacheva, G. M. Whitesides, P. Garstecki, and H. A. Stone, "Emulsification in a microfluidic flow-focusing device: effect of the viscosities of the liquids," *Microfluidics and Nanofluidics*, vol. 5, pp. 585–594, 2008.
- [55] J.-P. Kruth, X. Wang, T. Laoui, and L. Froyen, "Lasers and materials in selective laser sintering," *Assembly Automation*, vol. 23, no. 4, pp. 357–371, 2003.
- [56] A. M. Ibrahim, J. I. Padovani, R. T. Howe, and Y. H. Anis, "Modeling of droplet generation in a microfluidic flow-focusing junction for droplet size control," *Micromachines*, vol. 12, no. 6, p. 590, 2021.

- [57] A. Chandorkar and S. Palit, "Simulation of droplet-based microfluidics devices using a volume of fluid (VOF) approach," in *Technical Proceedings of Conference & Expo 2009*, vol. 3, pp. 396–400, 2009.
- [58] F. Santos, G. Tryggvason, and G. Ferreira, "Droplet-based logic gates simulation of viscoelastic fluids under electric field," *Scientific Reports*, vol. 14, no. 1, p. 1771, 2024.
- [59] A. Mohammadi Nafchi, "Numerical Simulation of Droplet Formation in a Microfluidic Ice Nucleating Particle Measurement Device," 2019.
- [60] L. Wu, J. Qian, X. Liu, S. Wu, C. Yu, and X. Liu, "Numerical modelling for the droplets formation in microfluidics-a review," *Microgravity Science and Technology*, vol. 35, no. 3, p. 26, 2023.
- [61] H. Liu, "QL-75j6hNex.pdf," 2010.
- [62] H. Liu and Y. Zhang, "Droplet formation in a T-shaped microfluidic junction," *Journal of Applied Physics*, vol. 106, no. 3, 2009.
- [63] J. Liu and N. Trung Nguyen, "Numerical simulation of droplet-based microfluidics-a review," *Micro and Nanosystems*, vol. 2, no. 3, pp. 193–201, 2010.
- [64] S. Bashir, J. M. Rees, and W. B. Zimmerman, "Simulations of microfluidic droplet formation using the two-phase level set method," *Chemical Engineering Science*, vol. 66, no. 20, pp. 4733–4741, 2011.
- [65] D. Hernández-Cid, V. Pérez-González, R. Gallo-Villanueva, J. González-Valdez, and M. Mata-Gómez, "Modeling droplet formation in microfluidic flow-focusing devices using the two-phases level set method," *Materials Today: Proceedings*, vol. 48, pp. 30–40, 2022.
- [66] L. Peng, M. Yang, S.-s. Guo, W. Liu, and X.-z. Zhao, "The effect of interfacial tension on droplet formation in flow-focusing microfluidic device," *Biomedical microdevices*, vol. 13, pp. 559–564, 2011.
- [67] A. Amani, N. Balcázar, J. Castro, and A. Oliva, "Numerical study of droplet deformation in shear flow using a conservative level-set method," *Chemical Engineering Science*, vol. 207, pp. 153–171, 2019.
- [68] A. Singh, "Effect of Interfacial Tension on Droplet Generation in T-Junction Microfluidic Device."
- [69] A. Lashkaripour, A. Abouei Mehrizi, M. Rasouli, and M. Goharimanesh, "Numerical study of droplet generation process in a microfluidic flow focusing," *Journal of Computational Applied Mechanics*, vol. 46, no. 2, pp. 167–175, 2015.
- [70] H. Hua, J. Shin, and J. Kim, "Level set, phase-field, and immersed boundary methods for two-phase fluid flows," *Journal of Fluids Engineering*, vol. 136, no. 2, p. 021301, 2014.
- [71] 3M Company, "Product data sheet - Novec 7500 Engineered Fluid." http://multimedia.3m.com/mws/mediawebserver?mwsId=SSSSSufSevTsZxtUO8_ZP8fSevUqevTSevTSevTSeSSSSSS--&fn=prodinfo_nvc7500.pdf, 2008.

- [72] M. Leman, F. Abouakil, A. D. Griffiths, and P. Tabeling, "Droplet-based microfluidics at the femtolitre scale," *Lab on a Chip*, vol. 15, no. 3, pp. 753–765, 2015.
- [73] I. Bureau, "Wo 2014/201196 a2," 2014.
- [74] S. L. Anna, "Droplets and bubbles in microfluidic devices," *Annual Review of Fluid Mechanics*, vol. 48, pp. 285–309, 2016.
- [75] D. Hoang, L. Portela, C. Kleijn, M. Kreutzer, and V. Van Steijn, "Dynamics of droplet breakup in a T-junction," *Journal of Fluid Mechanics*, vol. 717, p. R4, 2013.
- [76] W. Paper, "Zi_Whitepaper_Principles_of_Pid_Controllers," White Paper July, Zurich Instruments AG, 2023.
- [77] P. Podržaj, "Contionuous vs discrete pid controller," in *2018 IEEE 9th International Conference on Mechanical and Intelligent Manufacturing Technologies (ICMIMT)*, pp. 177–181, IEEE, 2018.
- [78] K. Abidi and J.-X. Xu, "Advanced discrete-time control," *Studies in Systems, Decision and Control*, vol. 23, 2015.
- [79] I. A. El-Sharif, F. O. Hareb, and A. R. Zerek, "Design of discrete-time pid controller," in *International Conference on Control, Engineering & Information Technology (CEIT'14)*, pp. 110–115, 2014.
- [80] J. L. Tong and J. P. Bobis, "A model for designing digital pid controllers," in *Proceedings of the 1992 International Conference on Industrial Electronics, Control, Instrumentation, and Automation*, pp. 1157–1162, IEEE, 1992.
- [81] Z. Li, X. Yang, Q. Zhang, W. Yang, H. Zhang, L. Liu, and W. Liang, "Non-invasive acquisition of mechanical properties of cells via passive microfluidic mechanisms: A review," *Biomicrofluidics*, vol. 15, no. 3, 2021.
- [82] T. Alam, S. Qamar, A. Dixit, and M. Benaida, "Genetic algorithm: Reviews, implementations, and applications," *arXiv preprint arXiv:2007.12673*, 2020.
- [83] A. Albero Ortíz, J. Monzó Cabrera, A. B. Díaz Morcillo, M. E. Requena Pérez, *et al.*, "Combined use of genetic algorithms and gradient descent optimization methods for accurate inverse permittivity measurement," *IEEE Microwave Theory and Techniques Society*, 2006.
- [84] J. F., O. Aviles, and A. Chica Leal, "Design and implementation of a controller using genetic algorithms," *International Journal of Applied Engineering Research*, vol. 12, pp. 1469–1477, 01 2017.
- [85] D. A. R. Wati and R. Hidayat, "Genetic algorithm-based pid parameters optimization for air heater temperature control," in *2013 International Conference on Robotics, Biomimetics, Intelligent Computational Systems*, pp. 30–34, IEEE, 2013.
- [86] M. B. Sundareswari, K. Dhanalakshmi, S. S. Nakshatharan, and D. J. S. Ruth, "Optimal design of PID controller for shape memory alloy actuated ball on beam system."
- [87] C. Singh, "Genetic algorithms based PID controller design," *International Journal of Engineering Development and Research*, vol. 3, no. 3, pp. 2–5, 2015.

- [88] K. M. Hussain, R. A. R. Zepherin, and M. Shantha, "Comparison of PID controller tuning methods with genetic algorithm for FOPTD system," *criterion*, vol. 16, p. 17, 2014.
- [89] A. S. El-Wakeel, A. E.-E. K. M. Ellissy, and A. M. Abdel-hamed, "A hybrid bacterial foraging-particle swarm optimization technique for optimal tuning of proportional-integral-derivative controller of a permanent magnet brushless DC motor," *Electric Power Components and Systems*, vol. 43, no. 3, pp. 309–319, 2015.
- [90] L. Ljung, *System identification toolbox 7: Getting started guide*. The MathWorks, 2008.
- [91] T. Mathworks, *System Identification Toolbox™ User's Guide R2016*, 2016.
- [92] R. Joemaa, M. Grosberg, T. Rang, and T. Pardy, "Low-cost, portable dual-channel pressure pump for droplet microfluidics," in *2022 45th Jubilee International Convention on Information, Communication and Electronic Technology (MIPRO)*, pp. 205–211, IEEE, 2022.
- [93] P. Collignon, *Mathematical Modelling Using Calculus*. No. 2001, Woodhead Publishing, 2012.
- [94] R. Jöemaa, **N. Gyimah**, K. Ashraf, K. Pärnamets, A. Zaft, O. Scheler, T. Rang, and T. Pardy, "Cogniflow-drop: Integrated modular system for automated generation of droplets in microfluidic applications," *IEEE Access*, 2023.
- [95] T. Abe, S. Oh-hara, and Y. Ukita, "Integration of deep reinforcement learning to simple microfluidic system toward intelligent control: Demonstration of simultaneous microbeads manipulation," *Sensors and Actuators B: Chemical*, vol. 397, p. 134636, 2023.
- [96] X. Y. Lee, A. Balu, D. Stoecklein, B. Ganapathysubramanian, and S. Sarkar, "A case study of deep reinforcement learning for engineering design: Application to microfluidic devices for flow sculpting," *Journal of Mechanical Design*, vol. 141, no. 11, p. 111401, 2019.
- [97] X. Y. Lee, A. Balu, D. Stoecklein, B. Ganapathysubramanian, and S. Sarkar, "Flow shape design for microfluidic devices using deep reinforcement learning," *arXiv preprint arXiv:1811.12444*, 2018.
- [98] A. Jahn, J. E. Reiner, W. N. Vreeland, D. L. DeVoe, L. E. Locascio, and M. Gaitan, "Preparation of nanoparticles by continuous-flow microfluidics," *Journal of Nanoparticle Research*, vol. 10, pp. 925–934, 2008.
- [99] X. C. i Solvas and A. DeMello, "Droplet microfluidics: recent developments and future applications," *Chemical Communications*, vol. 47, no. 7, pp. 1936–1942, 2011.
- [100] O. Delalleau, M. Peter, E. Alonso, and A. Logut, "Discrete and continuous action representation for practical rl in video games," *arXiv preprint arXiv:1912.11077*, 2019.
- [101] J. Viquerat, P. Meliga, A. Larcher, and E. Hachem, "A review on deep reinforcement learning for fluid mechanics: An update," *Physics of Fluids*, vol. 34, no. 11, 2022.

- [102] B. A. Wallace and J. Si, "Continuous-time reinforcement learning: New design algorithms with theoretical insights and performance guarantees," *arXiv preprint arXiv:2307.08920*, 2023.
- [103] J. Schulman, F. Wolski, P. Dhariwal, A. Radford, and O. Klimov, "Proximal policy optimization algorithms," *arXiv preprint arXiv:1707.06347*, 2017.
- [104] C. Vignon, J. Rabault, and R. Vinuesa, "Recent advances in applying deep reinforcement learning for flow control: Perspectives and future directions," *Physics of fluids*, vol. 35, no. 3, 2023.
- [105] Q. Wang, L. Yan, G. Hu, C. Li, Y. Xiao, H. Xiong, J. Rabault, and B. R. Noack, "Drinflu-ids: An open-source python platform of coupling deep reinforcement learning and openfoam," *Physics of Fluids*, vol. 34, no. 8, 2022.
- [106] F. Ren, J. Rabault, and H. Tang, "Applying deep reinforcement learning to active flow control in weakly turbulent conditions," *Physics of Fluids*, vol. 33, no. 3, 2021.
- [107] D. Thummar, "Active flow control in simulations of fluid flows based on deep reinforcement learning," 2021.
- [108] OpenFOAM, "The Open Source CFD Toolbox," 2018.
- [109] OpenFOAM, "Paraview self-directed tutorial," 2023. accessed: July 01, 2023.
- [110] Pytorch, "[https://pytorch.org/.](https://pytorch.org/)"
- [111] S. Naji, A. Rahimi, V. Bazargan, and M. Marengo, "Numerical and artificial neural network analysis of an axisymmetric co-flow-focusing microfluidic droplet generator using active and passive control," *Physics of Fluids*, vol. 35, no. 6, 2023.
- [112] G. Houston, P. Capobianchi, and M. S. Oliveira, "Flow focusing with miscible fluids in microfluidic devices," *Physics of Fluids*, vol. 35, no. 5, 2023.
- [113] S. Li, L. Wen, and W. Wang, "Asymmetric breakup of a single droplet through a Y-junction microchannel with non-uniform flow rate," *Physics of Fluids*, vol. 35, no. 4, 2023.
- [114] M. Shams, A. Q. Raeini, M. J. Blunt, and B. Bijeljic, "A numerical model of two-phase flow at the micro-scale using the volume-of-fluid method," *Journal of Computational Physics*, vol. 357, pp. 159–182, 2018.
- [115] Q. Li, H. Zhu, S. Lu, M. Lei, W. Xu, and Z. Liu, "Numerical investigation on formation mechanism and flow law of droplet in t-junction by electric field," *Physics of Fluids*, vol. 35, no. 6, 2023.
- [116] M. Fatehifar, A. Revell, and M. Jabbari, "Non-newtonian droplet generation in a cross-junction microfluidic channel," *Polymers*, vol. 13, no. 12, p. 1915, 2021.
- [117] P. Desir, T.-Y. Chen, M. Bracconi, B. Saha, M. Maestri, and D. G. Vlachos, "Experiments and computations of microfluidic liquid–liquid flow patterns," *Reaction Chemistry & Engineering*, vol. 5, no. 1, pp. 39–50, 2020.
- [118] S. Malekzadeh and E. Roohi, "Investigation of different droplet formation regimes in a T-junction microchannel using the VOF technique in OpenFOAM," *Microgravity Science and Technology*, vol. 27, pp. 231–243, 2015.

- [119] Q. Chen, J. Li, Y. Song, D. M. Christopher, and X. Li, "Modeling of Newtonian droplet formation in power-law non-Newtonian fluids in a flow-focusing device," *Heat and Mass Transfer*, vol. 56, pp. 2711–2723, 2020.
- [120] S. S. Deshpande, L. Anumolu, and M. F. Trujillo, "Evaluating the performance of the two-phase flow solver interFoam," *Computational science & discovery*, vol. 5, no. 1, p. 014016, 2012.
- [121] Y. Wang and P. Ming, "Dynamic and energy analysis of coalescence-induced self-propelled jumping of binary unequal-sized droplets," *Physics of Fluids*, vol. 31, no. 12, 2019.
- [122] J. Cheng, Q. Li, C. Yang, Y. Zhang, and Z. Mao, "CFD-PBE simulation of a bubble column in OpenFOAM," *Chinese Journal of Chemical Engineering*, vol. 26, no. 9, pp. 1773–1784, 2018.
- [123] G. Sontti and A. Atta, "CFD analysis of microfluidic droplet formation in non-Newtonian liquid," *Chemical Engineering Journal*, vol. 330, pp. 245–261, 2017.
- [124] X. Li, L. He, Y. He, H. Gu, and M. Liu, "Numerical study of droplet formation in the ordinary and modified T-junctions," *Physical Fluids*, vol. 31, p. 082101, 2019.
- [125] P. Zhu, X. Tang, and L. Wang, "Droplet generation in co-flow microfluidic channels with vibration," *Microfluidics and Nanofluidics*, vol. 20, pp. 1–10, 2016.
- [126] P. Dhananchezhian and S. S. Hiremath, "Optimization of multiple micro pumps to maximize the flow rate and minimize the flow pulsation," *Procedia Technology*, vol. 25, pp. 1226–1233, 2016.
- [127] M. Nabavi and L. Mongeau, "Numerical analysis of high frequency pulsating flows through a diffuser-nozzle element in valveless acoustic micropumps," *Microfluidics and nanofluidics*, vol. 7, pp. 669–681, 2009.
- [128] S. M. Recktenwald, C. Wagner, and T. John, "Optimizing pressure-driven pulsatile flows in microfluidic devices," *Lab on a Chip*, vol. 21, no. 13, pp. 2605–2613, 2021.

Acknowledgements

I want to express my deepest gratitude to my PhD advisor, Dr. Tamás Pardy, for his consistent support, mentorship, and the growth opportunities he has provided me with. I am also grateful to my assistant supervisor, Assistant Professor Ott Scheler, for his guidance and invaluable feedback throughout my journey. Special appreciation goes to Dr. Alar Kuusik, the Head of the Thomas Johann Seebeck Department of Electronics at Tallinn University of Technology, for allowing me to conduct my PhD research within his esteemed department.

Additionally, I express my heartfelt thanks to Professor Toomas Rang for accepting me to be a part of the Lab-on-a-Chip and Microfluidics Research team. I am grateful to my colleagues and the entire Thomas Johann Seebeck Department of Electronics for creating a supportive and nurturing environment where I could thrive both as a researcher and as an individual.

I acknowledge the privilege of having a loving and supportive family, especially my spouse, Abdul-Wahab, who fully shares in my joys, and provides unwavering support during challenging times. I extend my appreciation to the organizations that provided financial support during my PhD studies:

- Estonian Research Council through the Institutional Research Project PRG620 and PUT1435
- TTU Development Program 2016-2022, Project Code 2014-2020.4.01.16-0032
- Study IT in Estonia Programme
- ICT Doctoral School at Tallinn University of Technology
- DoRa Programme
- TALTECH ERASMUS CHARTER FOR HIGHER EDUCATION 2021-2027

Their support has been instrumental in my academic journey.

Abstract

Closed-Loop Droplet Size Control in Microfluidics

Droplet microfluidics is known for efficiently producing microdroplets in large quantities. However, maintaining consistent droplet size and uniformity is technically challenging. These difficulties arise from the complex nature of multiphase flow dynamics and the intricate relationships with input parameters. Long-term experiments are particularly sensitive to disturbances and pressure fluctuations, which can disrupt droplet uniformity and have profound implications for scientific research, industrial processes, and biomedical applications. Inconsistent droplet sizes not only affect result reliability but also pose risks to critical tasks like single-cell analysis, polymerase chain reaction (PCR), and drug discovery screenings. Additionally, pressure fluctuations can cause damage to delicate cell structures in cellular studies.

To tackle the challenge of tuning droplet size, traditional methods like mathematical-empirical models and manual tuning have been proposed. More recently these are replaced by automated closed-loop feedback systems, notably Proportional-Integral-Derivative (PID) controllers, which offer automation and precision. However, optimizing these systems for microfluidic applications remains a challenge. This research presents a new approach to address these challenges by simulating and optimizing controller designs integrated into microfluidic flow models before experimental implementation.

Firstly, it deals with the limited evaluation of droplet size range for tunability by using a simulation of a closed-loop feedback control of a microfluidic setup with a Proportional-Integral (PI controller). This system achieves better accuracy and consistency compared to the open-loop scenario, reducing the variation in droplet size from 15% to 2% and closely matching the desired size. Additionally, an evaluation of the complete parameter space of the PI-controlled system shows effective regulation of droplet size across various set-points.

Secondly, the research confronts extended settling times and overshoot in traditional controller tuning by proposing a PID controller tuned with a genetic algorithm (GA). GA tuning achieves enhanced performance in droplet size control, significantly reducing overshoot and settling time compared to classical tuning methods. Specifically, with GA tuning PI controller achieves a $100\mu\text{m}$ target droplet size with reduced overshoot (0.5%) and settling time (approx. 0.088s) compared to classical tuning (1.5% overshoot, 0.338s settling time).

Thirdly, the challenge of transferring a control solution from a simulation environment to an experimental setup is addressed through the CogniFlow-Drop system. This integrated, modular, and automated droplet generation solution utilizes dynamic dual-feedback control strategy in experimental setting. This thesis contributes to the development of efficient controllers by initially designing them in a simulated microfluidics environment and then transferring the optimized controller parameters to experimental software implementation. This streamlines controller tuning which can be resource-intensive. The results show that the GA-generated controller parameters required minor adjustments for optimal performance in the real system, closely resembling simulated values and minimizing tuning iterations. The proposed control framework was essential for achieving the desired outcome of a rapid pressure stabilization time of 10 seconds. This is in contrast to the 120 seconds needed with the syringe pump-based approach.

Lastly, the study addresses the complexity and reliance on accurate mathematical models in classical closed-loop control for microfluidics by proposing the integration of the Deep reinforcement learning (DRL) Proximal Policy Optimization (PPO) algorithm with a two-dimensional Computational Fluid Dynamics (CFD) numerical model. Validation of

the numerical model against experimental data demonstrated strong agreement, with errors below 11%, verifying the model's reliability in simulating droplet formation. The DRL-CFD framework effectively regulated droplet size through manipulation of input inlet pressure, supported by precise observation measurements. Additionally, optimizing the probe layout for field pressure measurement enhanced control performance. The result of the PPO algorithm is the CV% (Coefficient of Variation) reduction ranged from 0.8% to 4.72% across droplet sizes of 50 μm to 80 μm , respectively. Further, the study evaluated the performance of the PPO algorithm in the presence of external disturbances, particularly periodic mechanical vibrations affecting droplet microfluidics systems. Disturbances, varying in frequency (10 Hz and 10 kHz) and amplitude (50 Pa, 100 Pa, and 500 Pa), influenced the behaviour of the agent. The agent effectively handled disturbances up to an 8% increase in the mean amplitude pressure value it was trained on. It maintained the mean droplet size close to the target with a CV below 5%, showcasing its adaptability. Retraining is recommended for larger amplitudes or low frequency disturbances.

Overall, the agent demonstrated effectiveness within specific disturbance limits, suggesting potential for robust control under varying conditions. Overall, the findings of this research highlight the importance of innovative control strategies and simulation-based optimization techniques in advancing droplet microfluidics technology.

Kokkuvõte

Suletud ahelaga tilkade suuruse juhtimine mikrofluidikas

Tilga mikrofluidikat kasutatakse suurtes kogustes vesi-õlis mikrotilkade tegemiseks. Tilkade ühtlase suuruse säilitamine protsessi käigus võib olla aga tehniliselt keeruline. Need raskused tulenevad mitmefaasilise voolu dünaamika keerulisest olemusest ja keerulistest seostest sisendparameetritega. Pikaajalised katsed on eriti tundlikud häirete ja rõhukõikumiste suhtes, mis võivad häirida tilkade ühtlust ja avaldada sügavat mõju teadusuuringutele, tööstusprotsessidele ja biomeditsiinilistele rakendustele. Ebaühtlased tilkade suurused võivad mõjutada tulemuste usaldusväärsust erinevates biotehnoloogilistes rakendustes, nagu näiteks üheraku analüüs, polümeraasi ahelreaktsioon (PCR) ja ravimite avastamise sõeluuringud. Lisaks võivad rõhu kõikumised rakuuuringutes kahjustada õrnu rakustruktuure.

Tilkade suuruse paremaks kontrollimiseks on pakutud traditsioonilisi meetodeid, nagu matemaatilisi-empüürlisi mudelid ja käsitsi häälestamine. Hiljuti on need asendatud automatiseeritud suletud ahelaga tagasisidesüsteemidega, eriti proportsionaalsete integraal-diferentsiaalsete (PID) kontrollritega, mis pakuvad automatiseerimist ja täpsust. Nende süsteemide optimeerimine mikrofluidiliste rakenduste jaoks on aga endiselt väljakutse. Antud teadustöö pakub uut lähenemisviisi nende väljakutsete lahendamiseks, simuleerides ja optimeerides mikrofluidset vool kontrollereid enne eksperimentaalset rakendamist.

Esiteks käsitleb see tilkade suuruse vahemiku piiratud hindamist häälestatavuse jaoks, kasutades digitaalset kaksikut koos proportsionaalse integraalse (PI) kontrollriga. See süsteem saavutab parema täpsuse ja järjepidevuse võrreldes avatud ahelaga stsenaariumiga, saavutades ligilähedaselt soovitud suuruse ning vähendades tilkade suuruse varieerumist 15% pealt 2% peale. Lisaks võimaldab PI-ga juhitava süsteemi täieliku parameetri-ruumi hindamine tilkade suuruse tõhusat reguleerimist erinevate seadeväärtuste vahel.

Teiseks käsitleb teadustöö PID kontrolleri omase pikendatud reageerimisaja ning üle-häälestamis probleemiga, pakkudes välja geneetilise algoritmiga (GA) häälestatud PID-kontrolleri. GA-ga häälestamine tagab parema tilkade suuruse reguleerimise parema, vähendades märkimisväärselt reageerimisaja ning ülereguleerimist võrreldes klassikaliste häälestusmeetoditega. Täpsemalt, GA häälestusega saavutab PI-kontroller 100 μm tilkade sihtsuuruse vähendatud ülereguleerimise (0,5%) ja reageerimisaja (umbes 0,088 s) võrreldes klassikalise häälestamisega (1,5% ülereguleerimine, 0,338 s reageerimisaja).

Kolmandaks lahendatakse CogniFlow-Drop süsteemi kaudu kontroll-lahenduse üle-kandmine digitaalsest kaksikust eksperimentaalsesse seadistusse. See integreeritud, modulaarne ja automatiseeritud tilkade genereerimise lahendus kasutab eksperimentaalses seadistuses dünaamilist topelt-tagasiside juhtimisstrateegiat. Antud lõputöö aitab kaasa tõhusate kontrollerite väljatöötamisele, projekteerides need algselt simuleeritud mikrofluidika keskkonnas ja seejärel kandes optimeeritud kontrolleri parameetrid üle eksperimentaalsesse tarkvararakendusse. See muudab ressursimahuka kontrolleri häälestamise sujuvamaks. Tulemused näitavad, et GA-ga genereeritud kontrolleri parameetrid nõudsid reaalses süsteemis optimaalse jõudluse saavutamiseks väiksemaid kohandusi, mis sarnanevad üsnagi simuleeritud väärtustega ja minimeerivad häälestamise iteratsioone. Kavandatav juhtimisraamistik oli hädavajalik, et saavutada kiire 10-sekundilise rõhu stabiliseerimine. Kasutades süstalpumpa, on rõhu stabiliseerimiseks vajalik aeg 120 sekundit.

Viimaseks käsitleb teadustöö klassikalise suletud ahela juhtimise keerukust mikrofluidikas ja selle sõltuvust täpsetest matemaatilistest mudelitest. Töö pakub välja kahe-mõõtmelise arvutusvedeliku dünaamikaga (CFD) numbrilise mudeli integratsiooni sügava tugevdamise õppimise (DRL) proksimaalse poliitika optimeerimise (PPO) algoritmiga.

Numbrilise mudeli valideerimine eksperimentaalsete andmetega näitas tugevat kok-

kulangevust, mille vead olid alla 11%, kinnitades mudeli usaldusväärsust tilkade moodustumise simuleerimisel. DRL-CFD raamistik reguleeris tõhusalt tilkade suurust, manipuleerides sisendrõhku, mida toetasid täpsed vaatlusmõõtmised. Lisaks parandas sondi paigutuse optimeerimine juhtimisjõudlust välirõhu mõõtmiseks. PPO-algoritmi tulemuseks on dispersioonikoefitsendi protsendi (CV) vähenemine vahemikus 0,8% kuni 4,72% tilkade puhul, mille läbimõõt on 50 μm kuni 80 μm . Lisaks hinnati uurimistöös PPO algoritmi toimimist väliste häirete, eriti perioodiliste mehaaniliste vibratsioonide korral, mis mõjutavad tilkade mikrofluidika süsteeme. Häired, mis olid erineva sagedusega (10 Hz ja 10 kHz) ja amplituudiga (50 Pa, 100 Pa ja 500 Pa) mõjutasid algoritmi toimimist. Algoritm käsitles treeningul tõhusalt häireid kuni 8% keskmise amplituudi rõhu väärtuse suurenemiseni. See hoidis tilkade keskmise suuruse sihtmärgi lähedal, CV alla 5%, mis näitab selle kohanemisvõimet. Suuremate amplituudide või madala sagedusega häirete korral on soovitatav ümberõpe. Üldiselt näitas algoritm tõhusust konkreetsete häirete piirides, mis viitab tugeva kontrollipotentsiaalile erinevates tingimustes. Üldiselt näitavad selle uuringu tulemused uuenduslike juhtimisstrateegiate ja simulatsioonipõhiste optimeerimismeetodite tähtsust tilkade mikrofluidika tehnoloogia edendamisel.

Appendix 1

I

N. Gyimah, O. Scheler, T. Rang, and T. Pardy, "Digital twin for controlled generation of water-in-oil microdroplets with required size," in *2022 23rd International Conference on Thermal, Mechanical and Multi-Physics Simulation and Experiments in Microelectronics and Microsystems (EuroSimE)*, pp. 1-7, IEEE, 2022

Digital twin for controlled generation of water-in-oil microdroplets with required size

Nafisat Gyimah*, Ott Scheler*, Toomas Rang* and Tamas Pardy*

* Tallinn University of Technology/Thomas Johann Seebeck Department of Electronics

Ehitajate tee 5, 12616 Tallinn, Estonia

nafisat.gyimah@taltech.ee

ott.scheler@taltech.ee

toomas.rang@taltech.ee

tamas.pardy@taltech.ee

Abstract

In this paper, we report a digital twin of a droplet microfluidic system with closed-loop droplet size control. Compared to the state-of-the-art, this digital twin allows evaluating the system for a wider range of droplet sizes. We constructed a digital twin of a microfluidic Flow-Focusing Device (FFD) that used a Proportional Integral (PI) controller to automatically adjust the flow rate of the dispersed phase, to obtain the required droplet size. The efficacy of the digital twin was evaluated using six droplet diameters ranging from 30-60 μm . The simulation results show good agreement between the tested and measured droplet sizes ($R^2=0.993$).

1. Introduction

The ability to generate uniform droplets with user-defined or application-specified characteristics has aided the widespread adoption of droplet microfluidics for a variety of applications. Accordingly, precise control of droplet characteristics such as the droplet size is critical.

Our work builds on recently reported results in closed-loop control of droplet sizes in microfluidic chips using PI/PID (Proportional Integral/Proportional Integral Derivative) controllers [1–3]. Closed-loop automated control eliminates the difficulty in achieving the required droplet size by adjusting the fluid flow rate, which was characteristic of manual tuning of flow parameters previously common in research [4,5]. In contrast to previously reported droplet generators using PI/PID control, we implement our system in a simulated digital twin. Moreover, rather than demonstrating only one or two droplet size setpoints, we explore the evaluation of a droplet microfluidic system over a wider set of input parameters.

A digital twin is a simulated replica of the real system, whose advantages are more pronounced when real-life experiments are expensive and time-consuming. In this work, our digital twin integrates finite element modelling with control systems simulation, a combination that harnesses the predictive and engineering capabilities of each realm. In particular, the digital twin designed is a simulation of a flow-focusing microfluidic 2D model integrated with a PI controller for droplet size control. The digital twin will serve as a proof-of-concept for the implementation of an automated closed-loop PI control system to produce droplets of various user-defined sizes.

2. Construction of the digital twin

A. Framework of the digital twin

A digital twin of a microfluidic Flow-Focusing Device (FFD) with Proportional Integral (PI) control of droplet size was implemented. The implementation relied on COMSOL Multiphysics for the Computational Fluid Dynamics (CFD) simulation (Section 2.B.), MATLAB for the controller (Section 2.C.) and COMSOL LiveLink for MATLAB to connect the controller and the simulated model, as illustrated in Fig. 1. Using the dispersed phase flow rate as the control variable, the controller regulated the measured droplet size to obtain the desired droplet size.

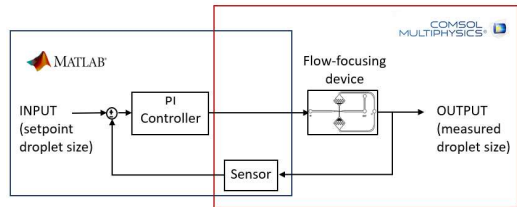


Fig. 1. Framework of the digital twin for closed-loop droplet size control. COMSOL Multiphysics was used for simulating the flow-focusing device and sensor, and MATLAB was used to implement the PI controller. The interface between the simulated model and the controller was established using COMSOL LiveLink with MATLAB

B. COMSOL FFD simulation model

i. Model parameters

The digital twin was built assuming the same actuation method, and a nearly identical microchannel layout to that previously used in our experiments [6,7]. To reduce computational time, a two-dimensional (2D) model was used. Furthermore, because the model was symmetrical along the vertical y-z axis, the simulation was limited to only half of the model by cutting along the line of symmetry and mirroring the solution. To further simplify the model, we excluded the air inlet close to the chip's outlet channel, as this section has negligible impact on droplet formation. The model (Fig. 2.) was designed in Autodesk Inventor. Model dimensions are summarized in Table I. In experiments, the rhomboid filters on the oil liquid path in our channel design were for filtering out contaminants, such as dust particles. For the formation of water-in-oil droplets, HFE 7500 (oil) + 2% w/w PFPE-PEG-PFPE (Perfluoropolyether-polyethylene glycol-

perfluoropolyether) surfactant was used as the continuous phase fluid and Deionized (DI) water was used as the dispersed phase fluid. Materials used in the model are summarized in Table II.

TABLE I. DIMENSIONS USED IN SIMULATION MODEL

Chip feature	Dimension on Fig. 2.	Value [mm]
Water inlet	W_1	0.6
	W_2	0.29
	W_3	0.29
	L_1	2.0
	L_2	1.0
Oil inlet	W_6	0.12
	L_6	2.18
Outlet	W_5	0.09
	L_4	3.5
Junction	W_5	0.09
Sensor	L_5	0.1
Filter	W_7	3.9
	W_8	0.3
	W_9	0.12

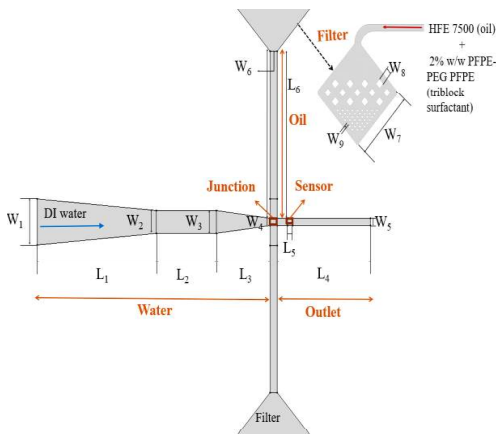


Fig. 2. The geometry and dimensions of the simulated microfluidic flow-focusing device (FFD). For fluid flow directions, blue arrows represent the inlet and flow direction of water, red arrows represent the inlet and flow direction of oil, and black arrows represent the outlet. Oil, Water, Junction, Sensor, and Outlet domains are the primary domains (in brown text). The sensor domain is where droplet size is measured. Rhomboid filters on the oil path used to filter out contaminants in experiment. Only half of the system was simulated due to device symmetry along its y - z axis

TABLE II. MATERIAL PROPERTIES USED IN SIMULATION MODEL

Model domain	Material	Dynamic viscosity [Pa s]	Density [kg/m ³]
Water	De-ionized water	1e-3	1000
Oil	HFE 7500 + 2% w/w PFPE-PEG-PFPE [10]	7.7e-4	1614

ii. CFD simulation methodology

The key governing equations in microfluidics are the incompressible Navier–Stokes equation (1), the continuity equation (2), and the level set equation (3) [11]. The numerical method used is the two-phase level set method (LSM). This method is recommended for simulating two-phase flow because it can easily deal with fast-moving topological changes in time varying curved objects like water droplets in oil [12].

Navier–Stokes equation

$$\rho(\partial u/\partial t) + \rho(u \cdot \nabla) u = \nabla \cdot [-pI + \mu(\nabla u + (\nabla u)^T)] + F_{st} \quad (1)$$

Continuity equation

$$\nabla \cdot u = 0 \quad (2)$$

Level set equation

$$\rho(\partial \phi/\partial t) + u \cdot \nabla \phi = \gamma \nabla \cdot (-\phi(1-\phi)(\nabla \phi/|\nabla \phi|)) + \varepsilon \nabla \phi \quad (3)$$

Equations (1-3) were solved by COMSOL (version 5.6). u denotes velocity (m/s). The value of u is obtained from solving (1) and (2), which is then used in (3) to construct the level set function ϕ [5]. ρ denotes density (kg/m³), t is time (s), μ is dynamic viscosity (Pa s), p is pressure (Pa), and F_{st} is surface tension force (N/m³).

The parameter γ is the re-initialization parameter, and an acceptable value for γ is the highest magnitude of the velocity. The thickness of the interface is denoted by ε . In this simulation, a level set function value of 0 is assigned to the continuous phase fluid interface and a value of 1 to the dispersed phase fluid interface. γ and ε are 0.2 m/s and 5e-6 m, respectively, and F_{st} is 1.9e-3 N/m² [13].

Effective droplet diameter

$$d = 2 \sqrt{(1/\pi) \int (-\phi > 0.5) d\Omega} \quad (4)$$

The effective droplet diameter d , which is a key parameter in this work, was calculated as Equation (4) in COMSOL by using the integrator operator to find the maximum area corresponding to the dispersed phase, where $\phi > 0.5$.

iii. Domains, boundary conditions, mesh

Domains, physics interfaces used, corresponding boundaries, and boundary conditions are summarized in Table III. For microchannel walls, the wetted wall boundary condition was used with 135° contact angle and a 5e-6 m slip length. The contact angle is formed when the fluid interface comes into contact with the microchannel wall, and the slip length is a distance between the boundary

and the virtual point outside the flow domain with zero fluid velocity. All fluidic domains used laminar flow and level set physics interfaces, coupled together in a two-phase flow Multiphysics interface using the level set method.

For mesh creation, a combination of quadrilateral and triangular mesh elements was used. The size nodes were used to customize the density of the logical meshes such that sections of the geometry close to and including the junction region, which were critical to droplet formation, were denser than the other sections. The average mesh quality achieved was 97%, and the total number of elements was 270908. Furthermore, a mesh independence study was used to assess the numerical scheme's accuracy (see Appendix). The generated grid, when meshed with 225000 or more elements, resulted in less than 1% numerical error (result variation) in droplet area measurements.

TABLE III. DOMAINS, PHYSICS INTERFACES, CORRESPONDING BOUNDARIES AND BOUNDARY CONDITIONS USED IN SIMULATION MODEL

Model domain	Physics interface	Corresponding boundary	Boundary condition
Water	Level set method	Inlet	Laminar inflow (constant, fully developed flow) Q_w
		Outlet	Laminar outflow
Oil	Level set method	Inlet	Laminar inflow (linked to MATLAB control function) Q_{oil}
		Outlet	Pressure (0 Pa)
All	Laminar flow	Channel wall	Wetted wall ($\theta = 135^\circ$)
All	Laminar flow	Channel wall	No-slip
Sensor	Domain ODEs and DAEs	sensor domain	Track droplet area (aveop1(u2) [m]-nojac (if (d diameter,t)>0*d (diameter, t)<1e-5, aveop1(u2) [m], diameter))
Sensor	Global ODEs and DAEs	sensor domain	Define equation for state variable, u4 (u4- nojac (if (d(aveop1(u3),t)=0,Q_w u4))

iv. Solution configuration and runtime

The domain elements were solved for velocity u , dependent variables u_2 , u_3 , state variable u_4 , pressure p , and advection at the interface. Due to the time-dependency of the study, we used a time range of 0 to 0.1 seconds with a step of 0.0005 seconds to ensure the simulation converged. The simulation was run on a Core i5-10210U

CPU, 32 GB RAM, and a 1 TB NVMe SSD. Each simulation took approximately 10 to 20 hours to run.

C. MATLAB controller design

The PI controller was built with MATLAB to tune the droplet size. The first step in designing the PI controller was to obtain the transfer function that characterized the model. The next step was to add the controller and find the optimal values of gain coefficients to achieve a fast rise time, minimal overshoot, and zero steady-state error by using the Control System Toolbox in MATLAB. The closed-loop control of droplet generation in the microfluidic setup can be represented by Fig. 3. the closed loop model was represented by the transfer functions of the microfluidic FFD platform $G(s)$, the droplet sensor $H(s)$, and the controller $C(s)$.

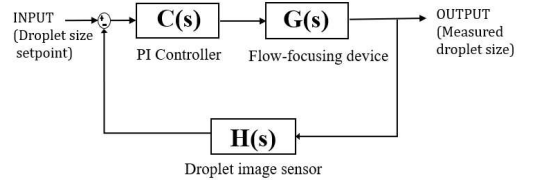


Fig. 3. Closed-loop control of droplet size. Each system component is described as a transfer function in Laplace form in order to generate the mathematical model of the system. $C(s)$, $G(s)$, and $H(s)$ describe the PI control, flow-focusing device, and droplet sensor, respectively. Droplet size setpoint and measured droplet size are the input and output, respectively, of the closed loop system.

The microfluidic FFD, $G(s)$ was represented by a first order model as expressed by (5)[1]

$$G(s) = K_0 / (1 + \tau s) \quad (5)$$

Where, K_0 is a gain coefficient and τ is the system time constant. The gain coefficient can be assumed to be unity for the open-loop control of the pressure-driven device, while the time constant can be calculated using the following formula:

$$\tau = V_0 / (K_1 P_0) \quad (6)$$

Where, V_0 is the fluid container initial volume, P_0 is the fluid container initial pressure, and K_1 is a gain coefficient. Since the flow through the micro-channels is affected by the driven flow rate of the water and oil, proportional gain, by using an approximation of the Bernoulli's equation [10], the gain coefficient can be expressed as

$$K_1 = P_w P_{oil} = (\rho_w Q_w^2) / (\rho_{oil} Q_{oil}^2) \quad (7)$$

Where, P_w and P_{oil} are the pressures of the dispersed phase and continuous phase respectively.

Q_w and Q_{oil} are the flow rates of dispersed phase and continuous phase, and ρ_w and ρ_{oil} are the dispersed phase and continuous phase densities respectively.

Here, with reference to experiments, the initial fluid volume was set as 1130 μl , and the initial flow rates of the continuous phase and dispersed phase were 50 $\mu\text{l}/\text{min}$ and 400 $\mu\text{l}/\text{min}$ respectively.

The droplet image sensor $H(s)$, was also modelled using the following first order transfer function

$$H(s)=1/(1+\tau s) \quad (8)$$

Where, τ is the time constant of the model, which in the case of the droplet image sensor can be represented as a function of the frame rate in absolute value:

$$\tau=fps/1000 \quad (9)$$

The transfer function of a PI controller can be described by

$$F(s)=K_p+(K_i/s) \quad (10)$$

where K_p and K_i are the proportional coefficients and the integral coefficients of the PI controller, respectively. A MATLAB program code was written to take as inputs the initial flow conditions required in (5)-(10) to determine the transfer functions of the system. After computing the transfer functions, the Control System Designer Toolbox in MATLAB is used to design a PI controller based on the following design criteria [14]

$$\text{Rise Time } (T_r) \leq 0.5 \text{ (s)} \quad (11)$$

$$\text{Settling Time } (T_s) \leq 4 \text{ (s)} \quad (12)$$

$$\% \text{ Overshoot } (O_s\%) \leq 10\% \quad (13)$$

After several iterative tuning steps, K_p and K_i values obtained, as shown in Fig. 4, were 2 and 70, respectively. Having obtained the controller coefficients, a MATLAB script was written for the implementation of the PI controller based on the equation

$$Q_d(t) = K_p e(t) + K_i \int e(t) dt \quad (14)$$

Where $Q_d(t)$ is the adjusted value for the dispersed phase flow rate, K_p and K_i are the proportional and integral gains respectively, and $e(t)$ is the difference between the setpoint diameter and the measured diameter. Subsequently, the MATLAB script was added as a MATLAB Function to the COMSOL desktop to achieve closed-loop droplet size control.

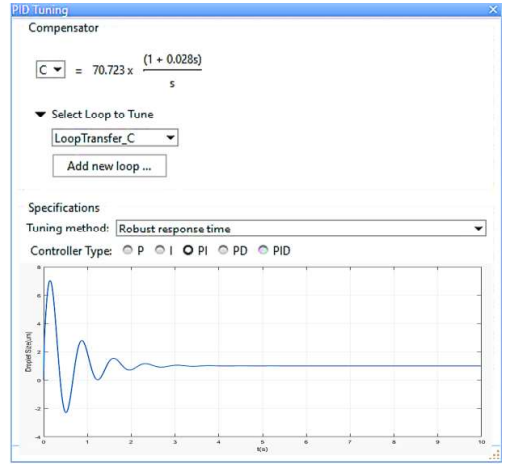


Fig. 4. Design and tuning of the PI controller in MATLAB. The step function response is obtained using the Control Systems Designer toolbox in MATLAB. A PI controller is added to control and tune the input step size, with response time and robustness defined as design criteria. The tuner computes PI parameters that stabilize the system. The values of K_p and K_i are obtained.

3. Evaluation of the digital twin

A. Droplet formation in COMSOL simulation

In our COMSOL FFD simulation, droplet formation was observed to occur in the dripping regime (Fig. 5) The process of droplet formation in the dripping regime can be divided into four stages: Filling stage (Fig. 5/a), necking stage (Fig. 5/b), growing stage (Fig. 5/c), and detachment stage (Fig. 5/d).

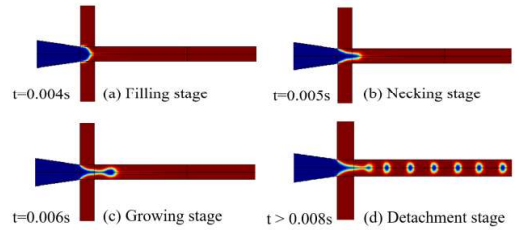


Fig. 5. Dripping regime of droplet formation in the microfluidic device (a) Filling stage (b) Necking stage (c) Growing stage (d) Detachment stage

B. Effect of fluid flow rate on droplet size

The effect of the continuous phase flow rate was first investigated by keeping the flow rate of the dispersed phase constant at 30 $\mu\text{l}/\text{min}$ and varying the flow rate of the continuous phase from 100 $\mu\text{l}/\text{min}$ to 400 $\mu\text{l}/\text{min}$. As depicted in Fig. 6/a, the average diameter of the droplets decreases as the flow rate of the continuous phase increases. When the continuous phase flow rate is

increased from 100 $\mu\text{l}/\text{min}$ to 400 $\mu\text{l}/\text{min}$ (300%), the effective diameter of the droplets decreases by 70% from 110 μm to 33 μm .

The influence of the dispersed phase flow rate on droplet size was also examined, by maintaining the continuous phase flow rate constant at 200 $\mu\text{l}/\text{min}$ and altering the dispersed phase flow rate from 5 $\mu\text{l}/\text{min}$ to 50 $\mu\text{l}/\text{min}$. As shown in Fig 6/b, the average droplet diameter increased significantly when the dispersed phase flow rate was high. Specifically, when the flow rate of the dispersed phase is increased from 5 $\mu\text{l}/\text{min}$ to 50 $\mu\text{l}/\text{min}$ (900%), the effective diameter of the droplets increases by 223.529%, from 34 μm to 110 μm .

Taken together, there are two ways to change the diameter of droplets: either increase the flow rate of the continuous phase or decrease the flow rate of the dispersed phase. However, our simulated microfluidic system showed higher sensitivity to the dispersed phase. Hence, we opted to use the dispersed phase flow rate to regulate the droplet size.

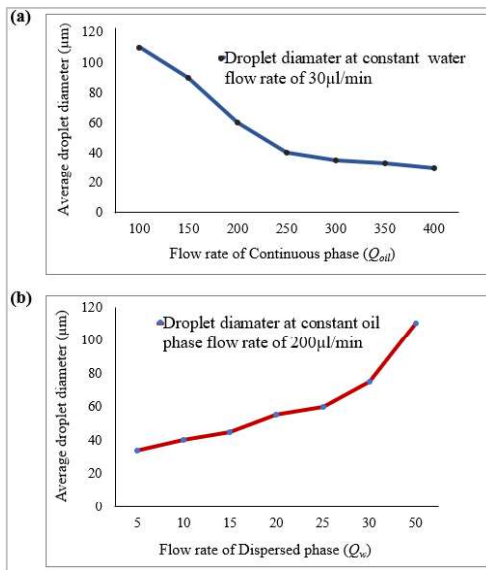


Fig. 6. The effect of flow rate on droplet size for (a) varied oil flow rate ($100\mu\text{l}/\text{min} < Q_{oil} < 400\mu\text{l}/\text{min}$) at water flow rate 30 $\mu\text{l}/\text{min}$ (b) varied water flow rate ($5\mu\text{l}/\text{min} < Q_w < 50\mu\text{l}/\text{min}$) at oil flow rate of 200 $\mu\text{l}/\text{min}$. The size of the droplets was more sensitive to changes in water flow rate than to changes in oil flow rate.

C. Closed-loop PI controller results

To show the controller's performance, a target droplet size of 40 μm was chosen as the controller setpoint. As previously mentioned, the flow rate of the continuous phase is constant and is fixed at 400 $\mu\text{l}/\text{min}$. The flow rate of the dispersed phase was initially fixed at 50 $\mu\text{l}/\text{min}$. The feedback controller automatically adjusted the dispersed

flow rate for droplet size control. The results shown in Fig.7/a, present the case for both open loop (no feedback) and closed loop feedback. As can be seen, there is an obvious deviation of the open-loop measured droplet diameter from the setpoint, as the measured average droplet diameter was approximately 34 μm by the end of the simulation.

In the case of closed-loop feedback, the measured droplet diameter and the target droplet size are eventually consistent. Within 1 second, the measured droplet size was 39.2 μm , which is nearly equal to the setpoint. The corresponding dispersed phase flow rate, as illustrated in Fig. 7/b, was 63.9 $\mu\text{l}/\text{min}$. Specifically, there was a significant difference between the measured and desired droplet sizes at the start of the closed-loop feedback. However, as the simulation time is increased, the deviation shrinks and weakens, eventually approaching zero.

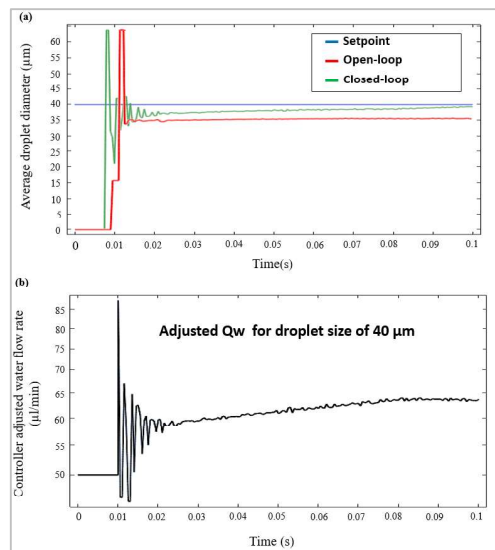


Fig. 7. Droplet size control (a) Average measured droplet diameter in open-loop (red) and closed-loop (green) versus droplet diameter setpoint value of 40 μm (blue). The measured droplet diameter in the open loop deviates significantly from the setpoint. In the closed loop, this deviation decreases and approaches zero. (b) To achieve the setpoint size, the PI controller adjusts the dispersed phase flow rate until minimum steady

Additionally, to assess the PI controller for the generation of droplets at varying setpoints, 6 different setpoints between 30 and 60 μm were tested as indicated in Fig. 8. As shown in Fig 8(a-c), the PI controller accurately controlled the droplet diameters for setpoints 30 μm , 35 μm , and 45 μm with a diameter offset/error of less than 2% at a simulation time of 1s. The linear relationship observed in Fig. 8/d between the setpoint droplet diameter, and the measured droplet diameter ($R^2 = 0.9937$) demonstrated the controller's efficiency for generating droplets at varying setpoints.

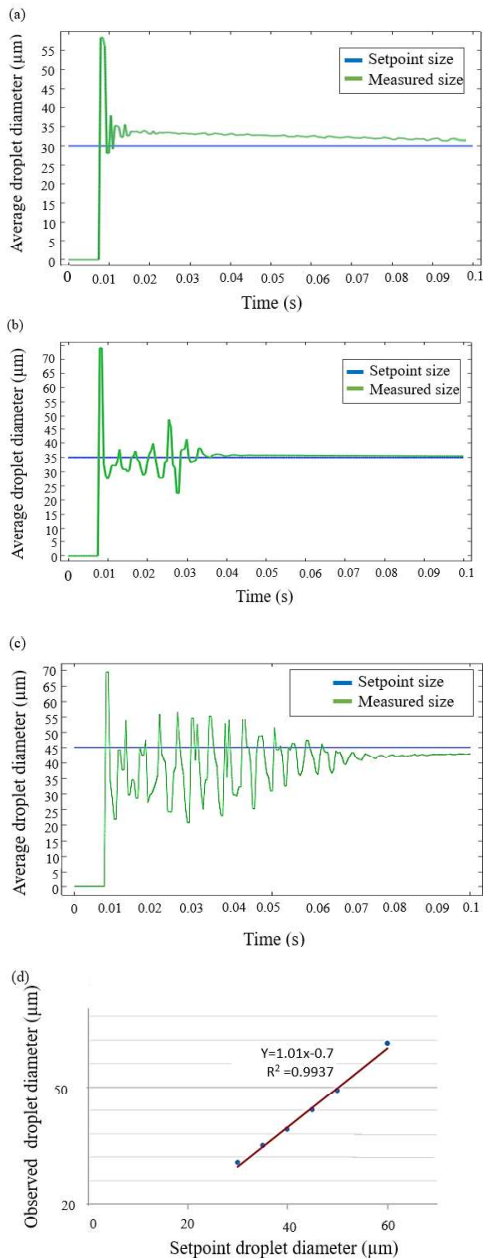


Fig. 8. Droplet size closed-loop control for setpoint diameters of (a) 30 μm , (b) 35 μm , and (c) 45 μm . (d) a comparison of setpoint diameters to Observed diameters in the 30-60 μm range. The setpoint and measured diameters agree well.

4. Conclusions

A digital twin of a droplet microfluidic system with closed loop droplet size control was presented. To control the size of droplets generated in the flow-focusing microfluidic device, the digital twin, a numerical simulation of a flow-focusing microfluidic 2D model and a PI controller using COMSOL Multiphysics – MATLAB integration, was built. Water droplets-in-oil formation occurred in the dripping regime. The influence of fluid flow rates on droplet size was investigated. Fluid flow rates ranging from 30 to 400 $\mu\text{l}/\text{min}$ were considered. While both phase flow rates had a significant effect on droplet size, the dispersed phase flow rate had a greater impact, according to the findings. As a result, the dispersed phase flow rate was chosen as the control variable for tuning droplet size.

The use of a PI controller to control droplet size is critical in this work. The PI controller was implemented in MATLAB. The PI controller receives the measured droplet diameter and adjusts the dispersed phase flow rate to achieve the required droplet size. In the absence of a PI controller, the measured droplet size did not match the setpoint droplet size. However, by incorporating a PI controller, the deviation between the setpoint droplet size and the measured droplet size was significantly reduced, with steady state error eventually approaching zero. Furthermore, the PI controller was evaluated for the formation of droplets at setpoints in the range of 30 μm to 60 μm . At the completion of the 1 second run time simulation, the measured sizes for setpoints 30 μm , 35 μm , 40 μm , 45 μm , 50 μm , 60 μm were 30.8 μm , 34.9 μm , 39 μm , 44 μm , 48.1 μm , 61.5 μm . The controller's efficacy for creating droplets at varied setpoints was proved by the linear relationship observed between the setpoint droplet diameter and the measured droplet diameter ($R^2 = 0.9937$).

If the complexity of the control algorithm is increased (i.e. by adjusting both fluid flow rates), we expect to be able to generate droplets at more setpoints, but the computational cost will inevitably be high. The findings in this paper, we hope, will aid in the design of closed-loop microfluidic droplet control experiments. Researchers can use digital twins like ours to test their designs (geometry, parameters etc.) before building the first physical prototype, saving money and time. Future work will focus on the evaluation of the PI controller in experimental work and how this correlates with the digital twin results. Taking it a step further, advanced controllers for improved precision in microfluidic droplet size control may be incorporated.

Acknowledgment

The authors would like to thank the Estonian Research Council for providing support under projects PUT1435, PRG620, as well as the TTÜ development program 2016-2022, project code 2014-2020.4.01.16-0032.

References

- [1] H. Fu, W. Zeng, S. Li, and S. Yuan, "Electrical-detection droplet microfluidic closed-loop control system for precise droplet production," *Sensors Actuators, A Phys.*, vol. 267, pp. 142–149, 2017, doi: 10.1016/j.sna.2017.09.043.
- [2] W. Zeng, S. Li, and Z. Wang, "Closed-loop feedback control of droplet formation in a T-junction microdroplet generator," *Sensors Actuators, A Phys.*, vol. 233, pp. 542–547, 2015, doi: 10.1016/j.sna.2015.08.002.
- [3] R. Kebriaei and A. S. Basu, "Autosizing, closed-loop drop generator using morphometric image feedback," *17th Int. Conf. Miniaturized Syst. Chem. Life Sci. MicroTAS 2013*, vol. 3, no. October, pp. 1944–1946, 2013.
- [4] R. Samanipour, Z. Wang, A. Ahmadi, and K. Kim, "Experimental and computational study of microfluidic flow-focusing generation of gelatin methacrylate hydrogel droplets," *J. Appl. Polym. Sci.*, vol. 133, no. 29, pp. 24–26, 2016, doi: 10.1002/app.43701.
- [5] X. Wang, G. Camci-unal, K. Wan, R. Liao, and A. Khademhosseini, "Microfluidics-Assisted Fabrication of Gelatin-Silica Core – Shell Microgels for Injectable Tissue Constructs - 2013 - Cha et al.pdf, U.pdf," 2014.
- [6] W. Postek, P. Gargulinski, O. Scheler, T. S. Kaminski, and P. Garstecki, "Microfluidic screening of antibiotic susceptibility at a single-cell level shows the inoculum effect of cefotaxime on *E. coli*," *Lab Chip*, vol. 18, no. 23, pp. 3668–3677, 2018, doi: 10.1039/C8LC00916C.
- [7] S. Bartkova, M. Vendelin, I. Sanka, P. Pata, and O. Scheler, "Droplet image analysis with user-friendly freeware CellProfiler," *Anal. Methods*, vol. 12, no. 17, pp. 2287–2294, 2020, doi: 10.1039/D0AY00031K.
- [8] A. Y. Tenorio-Barajas, M. De La Luz Olvera-Amador, V. Altuzar, R. Ruiz-Ramos, M. A. Palomino-Ovando, and C. Mendoza-Barrera, "Microdroplet formation in microfluidic channels by multiphase flow simulation," *2019 16th Int. Conf. Electr. Eng. Comput. Sci. Autom. Control. CCE 2019*, no. September, 2019, doi: 10.1109/ICEEE.2019.8884520.
- [9] I. L. Chaves, L. C. Duarte, W. K. T. Coltro, and D. A. Santos, "Droplet length and generation rate investigation inside microfluidic devices by means of CFD simulations and experiments," *Chem. Eng. Res. Des.*, vol. 161, pp. 260–270, 2020, doi: 10.1016/j.cherd.2020.07.015.
- [10] R. Qin and C. Duan, "The principle and applications of Bernoulli equation," *J. Phys. Conf. Ser.*, vol. 916, no. 1, 2017, doi: 10.1088/1742-6596/916/1/012038.
- [11] W. Han, X. Chen, Z. Wu, and Y. Zheng, "Three-dimensional numerical simulation of droplet formation in a microfluidic flow-focusing device," *J. Brazilian Soc. Mech. Sci. Eng.*, vol. 41, no. 6, pp. 1–10, 2019, doi: 10.1007/s40430-019-1767-y.
- [12] A. Sharma, "Level set method for computational multi-fluid dynamics: A review on developments, applications and analysis," *Sadhana - Acad. Proc. Eng. Sci.*, vol. 40, no. 3, pp. 627–652, 2015, doi: 10.1007/s12046-014-0329-3.
- [13] I. Bureau, "Wo 2014/201196 a2 (22)," no. 12, 2014.
- [14] Y. Xie, A. J. Dixon, J. M. R. Rickel, A. L. Klibanov, and J. A. Hossack, "Closed-loop feedback control of microbubble diameter from a flow-focusing microfluidic device," *Biomicrofluidics*, vol. 14, no. 3, 2020, doi: 10.1063/5.0005205.

Appendix

TABLE IV. MESH INDEPENDENCE STUDY

Grid No	Number of Mesh Elements	Degree of Freedom	Droplet Diameter (mm)	Relative Error (%)
1	90775	199705	0.76891	31.703
2	108872	228632	0.58382	11.845
3	130440	280446	0.52199	9.447
4	154871	321474	0.47693	5.975
5	188131	432702	0.45004	1.823
6	225750	516967	0.44198	0.242
7	270908	596878	0.44091	

Appendix 2

II

N. Gyimah, R. Jõemaa, K. Pärnamets, O. Scheler, T. Rang, and T. Pardy, "Pid controller tuning optimization using genetic algorithm for droplet size control in microfluidics," in *2022 18th Biennial Baltic Electronics Conference (BEC)*, pp. 1–6, IEEE, 2022

PID Controller Tuning Optimization Using Genetic Algorithm for Droplet Size Control in Microfluidics

Nafisat Gyimah
Thomas Johann Seebeck Department of
Electronics
Tallinn University of Technology
Tallinn, Estonia
nafisat.gyimah@taltech.ee

Ott Scheler
Department of Chemistry and
Biotechnology
Tallinn University of Technology
Tallinn, Estonia
ott.scheler@taltech.ee

Rauno Jõeamaa
Thomas Johann Seebeck Department of
Electronics
Tallinn University of Technology
Tallinn, Estonia
rauno.joemaa@taltech.ee

Toomas Rang
Department of Chemistry and
Biotechnology
Tallinn University of Technology
Tallinn, Estonia
toomas.rang@taltech.ee

Kaiser Pärnamets
Thomas Johann Seebeck Department of
Electronics
Tallinn University of Technology
Tallinn, Estonia
kaiser.parnamets@taltech.ee

Tamas Pardy
Department of Chemistry and
Biotechnology
Tallinn University of Technology
Tallinn, Estonia
tamas.pardy@taltech.ee

Abstract—In this paper, we demonstrate droplet size control in a microfluidics system using a PID controller tuned with a genetic algorithm (GA). In comparison to the state-of-the-art, this controller tuning method provides a robust means of obtaining controller gains that yield good steady-state responses with minimal settling time and transient overshoot. As a result, we developed a simulation of droplet microfluidics systems that is integrated with a genetic algorithm tuned-PID controller to automatically adjust the pressure of the continuous phase fluid to achieve the desired droplet sizes. When compared to the traditional tuning method, the results of the genetic algorithm demonstrated a significant improvement in process response, particularly in overshoot percentage, which decreased from 1.5 percent to 0.5 percent, and settling time, which decreased from 0.34 seconds to approximately 0.088 seconds. Using the controller gains derived from the genetic algorithm tuning, we achieved a droplet size (diameter) setpoint range of 50 to 350 micrometers. Furthermore, among the objective function criteria used in the genetic algorithm, the Integral of Time Absolute Error (ITAE) produced the best system response while having the lowest fitness value.

Keywords—genetic algorithm, PID controller, droplet size, microfluidic chip, settling time

I. INTRODUCTION

Previous studies [1–4] have demonstrated that proportional–integral–derivative (PID) controllers can be used to control droplet size in microfluidic systems. Traditional tuning methods such as the Trial and Error Method [1,3] and the Ziegler–Nichols Method [4,5] were used in these works to obtain controller parameters. While these methods significantly improved controller performance, they were not optimal due to the close-loop feedback system's relatively long settling times [2,4] and high transient overshoot [6]. However, because most flow-focusing (FFD) microfluidic devices produce droplets at high throughputs (typically > 500 Hz) [5], [7], the system response settling time must be reduced. Advanced soft computing optimization methods, such as the genetic algorithm (GA), on the other hand, have recently been used to obtain the PID controller parameters. This is due to GA's strong searching capabilities, heuristic properties, simplicity, global perspective, and inherent parallel

processing as a stochastic global search method. As a result, we extend our previous work on a digital twin for the controlled generation of microdroplets of the required size [8] by incorporating a Genetic Algorithm (GA) tuning method for obtaining the PID controller parameters. The goal is to find the PID controller parameters; proportional gain (K_p), integral gain (K_i), and derivative gain (K_d), that provide the fastest settling time and most stable controller response for tuning droplet size in a flow-focusing microfluidic device. To the best of our knowledge, this is the first instance of a genetic algorithm being used in a droplet microfluidic system.

II. CONTROL MODEL-BUILDING

A. Structure of the proposed GA-tuned PID controller

A PID controller tuned with a genetic algorithm was developed for closed-loop droplet size control in a microfluidics system. The closed-loop control system simulation replicated our actual experimental setup (Section II/B). The control variable was defined as the pressure of the pump driving the continuous phase, while the dispersed phase pressure remained constant (and its driving pump was not included in the simulation). The implementation relied on Simulink and MATLAB to model the system dynamics and to incorporate the genetic algorithm tuned-PID controller. Fig. 1 shows a simplified block diagram of the structure of the control method used in the work.

The PID controller's operation is governed by the formula (1) and the optimization problem under consideration (2) [9].

$$u(t) = k_p e(t) + k_i \int_0^t e(t) dt + k_d \frac{de(t)}{dt} \quad (1)$$

$$\text{Min } f(k_p, k_i, k_d) \quad (2)$$

where f denotes the settling time as well as the overshoot of the controlled system's step response, and K_p , K_i , and K_d are the proportional gain, integral gain, and derivative gain of the controller, respectively. In Fig. 1, the GA method is used to tune the PID controller to obtain PID gains that result in a minimum error e between the setpoint droplet size value d_{set} and the measured droplet size value d in order to solve the optimization problem (2).

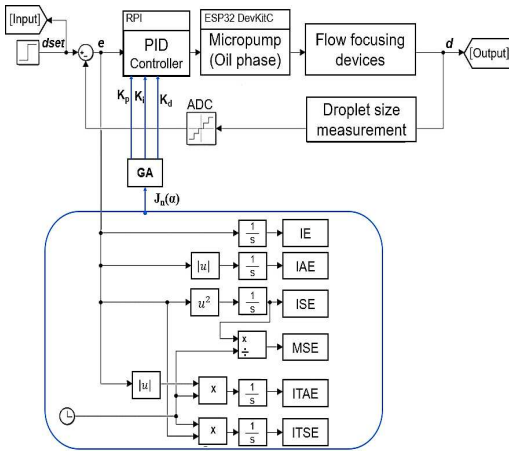


Fig. 1 Structure of PID controller tuning using genetic algorithm for droplet size control

A chromosome is a solution generated by a genetic algorithm, and a population is a group of chromosomes. These chromosomes go through a process known as the objective function to assess the fitness of the GA-generated solution to the problem. Referring to Fig. 1, the objective function is defined as $J_n(\alpha)$, where α represents the PID controller's gains and n is the performance criteria. The following six objective function criteria are discussed in this case; the Integral Squared Error (ISE) criterion, the Integral Time Squared Error (ITSE) criterion, the Integral of Time Absolute Error (ITAE) criteria, the Integral of Absolute Error (IAE) criterion, the Mean Squared Error (MSE) criterion, and the Integral Error (IE) criterion. These objective function criteria (3–8) [10] results were compared in order to determine the optimal GA-generated solution.

$$ISE = \int_0^c e(t)^2 dt \quad (3)$$

$$IAE = \int_0^t (|e(t)|) dt \quad (4)$$

$$ITAE = \int_0^t t(|e(t)|) dt \quad (5)$$

$$MSE = \frac{1}{T} \int_0^T ((e(t))^2) dt \quad (6)$$

$$ITSE = \int_0^t te(t)^2 dt \quad (7)$$

$$IE = \int_0^t (e(t)) dt \quad (8)$$

B. Experimental setup & collection of time-domain signals

To represent the dynamic behavior of the system components in Simulink, system identification techniques as well as analytic modeling were used to derive the transfer functions of the pump, microfluidic chip, and droplet size measurement circuit. The technique of system identification involves developing mathematical models without incorporating the physical laws that govern the system by using input-measured response information from real experiments. This was especially important given the complexity of modeling the droplet microfluidic system using physical laws due to the considerable number of physical parameters and components involved. The system identification procedure was undertaken using the System Identification Toolbox in MATLAB (R2021b).

The following components were used in the experimental setup depicted in Fig. 2:

- Flow-focusing PDMS microfluidic chip
- Fluidic add-ons such as a. fluid connectors b. Teflon (0.8 mm) tubing c. chip handling frame
- Reagents: a. mineral oil + 2% w/w Span 80 surfactant (continuous phase) b. deionized water (dispersed phase)
- Pumping system [10]
- ADC (ADS8681)
- MPRLS0015PG0000SA Pressure Sensors
- Droplet size measurement circuitry (detailed in Fig. 3)
- Raspberry Pi 4B

The drive frequency of the dispersed phase piezoelectric driving pump was kept constant at 200 Hz in all experiments, and that of the continuous phase driving pump was kept

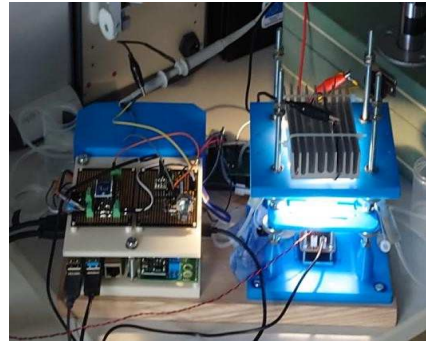


Fig. 2. A snapshot of the droplet microfluidic experimental setup

constant at 50 Hz. These pumps were connected to the Flow Focusing Device (FFD) chip's respective inlets. The size of the droplets on the FFD chip was altered by varying the continuous phase pressure. Droplet measurements were obtained from high-frame-rate videos captured with a camera placed below the FFD chip's outlet microchannel. Video capturing was done with a separate alignment fixture as the camera was not part of the experimental setup in Fig. 2. Droplet images were captured from multiple frames of video and analyzed using ImageJ software to determine droplet sizes. The droplet measurement circuit was not included in these experiments.

The droplet size measurement circuit depicted in Fig. 3 can be mathematically represented by equations (9,10);

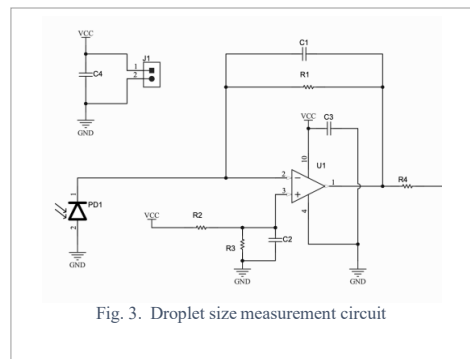


Fig. 3. Droplet size measurement circuit

$$V_{offset} = V_c * \frac{R_3}{R_2+R_3} \quad (9)$$

$$\frac{V_{out}}{I_{IN}} = \frac{-R_1}{1+sC_1R_1} + V_{offset} \quad (10)$$

To collect data for the pump's system modeling, input voltage settings ranging from 50 V to 250 V operating voltages for oil pumps, as well as their corresponding pressure readings from the pressure sensor, for fixed water pressure values of 5 kPa, 10 kPa, and 16 kPa, were collected and shown in Fig. 4/a. For modeling the dynamics of the FFD chip droplet generation process, the pump pressure applied ranged from 5 kPa to 34 kPa for the oil phase, and the corresponding measured droplet sizes were plotted and shown in Fig. 4/b.

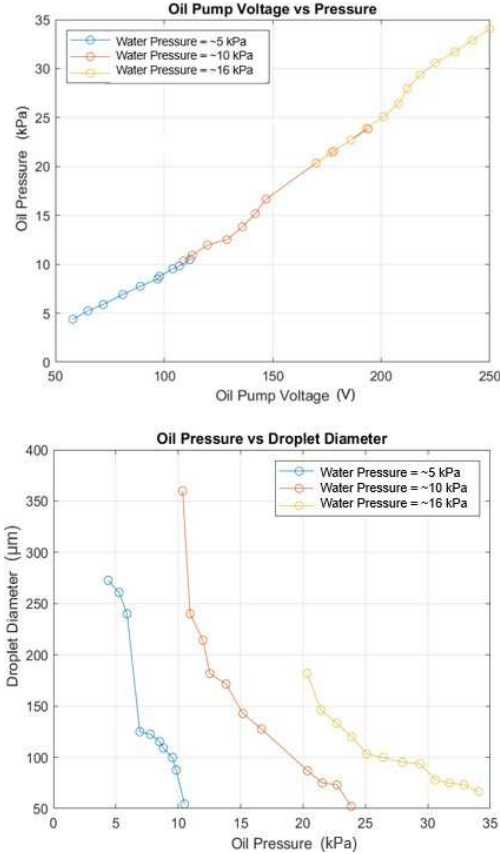


Fig. 4. (a) Voltage (V) vs Pressure (kPa) for oil driving pump (b) Droplet diameter (µm) vs Pressure (kPa) for oil driving pump

C. Selection of Model structure

As previously stated, the transfer function was the model structure chosen. The transfer function model excludes stochastic system behavior and only describes the deterministic component required to derive its mathematical model. It is also necessary to identify the order of the model as part of the model structure. In general, a continuous linear time-invariant system transfer function is represented as (11);

$$H(s) = \frac{\sum_{m=0}^M b_m s^m}{s^N + \sum_{n=0}^{N-1} a_n s^n} = \frac{b_0 + b_1 s + b_2 s^2 + \dots + b_M s^M}{a_0 + a_1 s + a_2 s^2 + \dots + a_{(N-1)} s^{(N-1)} + s^N} \quad (11)$$

Where M and b_m denote the order and m^{th} coefficient, respectively, of the numerator polynomial, and N and a_n denote the order and n^{th} coefficient, respectively, of the denominator polynomial. The zeros and poles of the system are the roots of the numerator polynomial and the denominator polynomial, respectively. The method used to determine the model order was to start with one pole and one zero (based on observed system response resemblance to a first order system) and gradually increase the number of poles and zeros for all possible forms in 1st to 3rd order. At the end of the system identification process, we sort to keep the model's accuracy and simplicity in balance.

The parameter estimation step yields the values $a_1, a_2, \dots, a_{(N-1)}, b_1, b_2, \dots, b_M$ in (11) for both the pump and the FFD chip.

D. Parameter/variable estimation

Fig. 5, adopted from [11], depicts parameter estimation, where r and y are known vectors that represent the experiment's inputs and observed outputs, respectively, and θ is an unknown vector that must be identified in order to construct the transfer function. θ is a matrix of the values a_1, a_2, b_1, b_2 , and so on that comprise the transfer function in equation 11 (12).

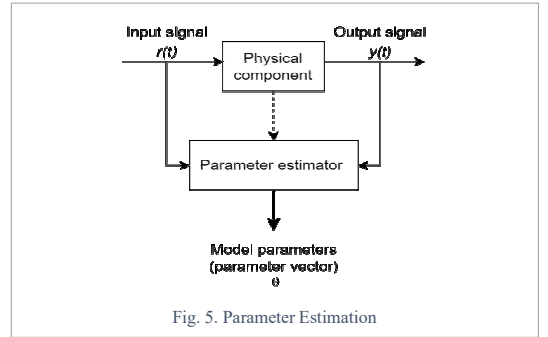


Fig. 5. Parameter Estimation

$$\theta = \begin{bmatrix} a_1 \\ a_2 \\ b_1 \\ b_2 \end{bmatrix} \quad (12)$$

Based on the features of the input-output data, the MATLAB System Identification Toolbox automatically selected the Nonlinear Least Squares (NLS) technique for parameter estimation (if the dataset has nonlinear features). In addition, the Instrumental Variable Estimator was used to generate a favorable set of initial parameters as a start parameter estimation.

III. GENETIC ALGORITHM IMPLEMENTATION

The basic genetic algorithm process used in controller tuning can be broken down into five steps, which are as follows [12]: Step 1: [Begin] Create a random population of chromosomes that represents the number of viable solutions to the problem. Step 2: [Fitness] Assess each chromosome's fitness in the population. Six objective function criteria are considered here. The population is represented by a $p \times 4$ matrix, where p is the population size, with each row representing one

chromosome and containing K_p , K_i , and K_d values, and the last column accommodating fitness values of corresponding chromosomes.

Step 3: [New population] Make a new population by repeating the steps below until the new population is complete:

- a) [Selection] Choose two parent chromosomes from a population based on their fitness. Tournament Selection, Roulette Wheel Selection, and Normalized Geometric Selection are the three selection techniques. Tournament Selection requires more execution time, whereas Roulette Wheel Selection allows the weaker chromosomes to be selected many times, so we choose Normalized Geometric Selection to choose the parent because it is more computationally efficient.
- b) [Crossover] Cross the parents to produce new offspring with a crossover probability of 0.65. If no crossover was performed, the offspring is a replica of the parents.
- c) [Mutation] Produce new offspring at each locus.
- d) [Reproduction] Insert new offspring into the new population.

Step 4: [Replace] Use the newly generated population to run the algorithm again.

Step 5: Proceed to step 2. The generation process is repeated 20 times.

Fig. 6 summarizes the steps in the genetic algorithm, whereas

TABLE 1 summarizes the GA property with relative values and methods.

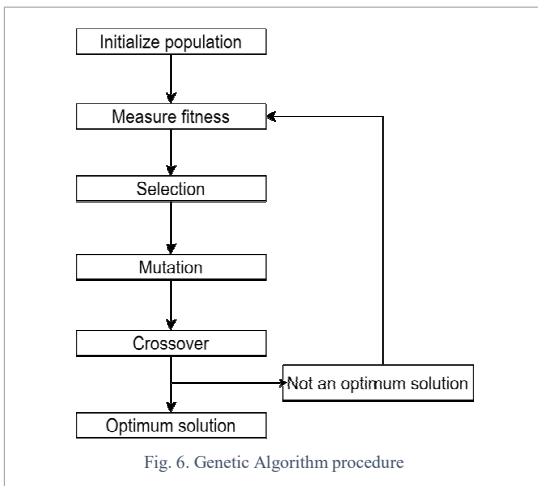


Fig. 6. Genetic Algorithm procedure

TABLE 1. PARAMETERS OF THE GENETIC ALGORITHM IMPLEMENTED

GA property	Value/Method
Population size	20
Max No. of Generations	30
Variable bounds [K_p , K_i , K_d]	[0 1; 1 70; 0 1e-4]
Objective function	ITAE, IAE, MSE, IE, ITSE, ISE
Selection method	Normalized Geometric Selection
Crossover method	Arithmetic crossover
Mutation method	Uniform mutation

IV. EVALUATION METHODOLOGY

A. Model estimation and evaluation

The following MATLAB quantifiable metrics were used to validate the model resulting from the system identification procedure:

- Fit to estimation data percent: measure of the model's closeness to the actual system.
- Mean-Square Error (MSE): average squared difference between the estimated and actual output values.
- Akaike's Final Prediction Error (FPE): A measure of model quality obtained by software simulating the situation in which the model is tested on a toolbox generated dataset to see how much error it produces in comparison to the response generated by the original dataset.
- Cross-validation is used to estimate the expected level of fit of a model to two datasets that were independent of the data used to estimate the model.

Based on these metrics, the model accuracy will be discussed in section V (Results and discussion).

B. Tuning performance evaluation

For the controller, we first compared the performance of the classical tuning method and the genetic algorithm tuning method. In general, unit step input is used to test the system by standard performance measures: settling time (5% criterion), percent overshoot, and rise time (0–95% criterion). In addition, for the genetic algorithm, we compare the performance of the five objective function criteria using these same metrics in addition to the fitness value (section V).

V. RESULTS & DISCUSSION

A. Model estimation and evaluation results

The model estimation and validation results show Akaike's Final Prediction Error (FPE), Fit to Estimation Data Percentage, Mean Squared Error (MSE), and Maximum Fit to Cross-Validation Data Percentage. Using these performance metrics, we compare the performance of transfer function models of various orders for the pump and the FFD chip. The lower the FPE and MSE, and the higher the Fit to Estimation Data percentage and Maximum Fit to Cross-Validation Data percentage, the better the model quality. Thus, the results for the FFD chip are shown in TABLE 2, and those of the pump modeling are shown in

TABLE 3. Among the various model structures, we selected $M2$ (1st order model) as a final choice because it provided the best fit percentages of 94.54% for the pump and 91.5% for the FFD chip, respectively, when compared to the high order models. These model structures were also found to have very low FPE and MSE, passing the model validation test under residual analysis. The cross-validation fit percentages also showed high values of 78.66% for the pump and 66.63% for the FFD chip. In comparison to the $M2$ model, the $M3$ model for the pump, which is of higher order, provides a 4% increase in fit percentage. As a result, $M2$ was chosen as the pump model in favor of reducing system complexity over the low impact gain of 4% increase in data fit. Consequently, the closed loop system is represented by the appropriate transfer functions, as shown in Fig. 7.

TABLE 2. FFD CHIP (PRESSURE TO DROPLET SIZE) MODEL

Model No.	Transfer Function	Poles, Zeros	FPE	MSE	Max. validation Fit %	Est. data Fit %
M1	$\frac{-0.007136}{s + 0.27085}$	1,0	3374	2024	58.8	-36.7
M2	$\frac{19.04s - 0.3391}{s + 0.2745}$	1,1	15.59	7.79	66.6	91.5
M3	$\frac{0.1597}{s^2 + 0.00017s + 0.03}$	2,0	210.4	86.6	53.5	71.7
M4	$\frac{-53.34s + 8.045}{s^2 + 242.5s + 37.8}$	2,1	1022	340	89.7	43.9
M5	$\frac{10.7s^2 + 12.1s - 0.14}{s^2 + 1.64s + 0.251}$	2,2	22.6	5.8	64.9	92.6
M6	$\frac{-0.01801}{s^3 + 0.31s^2 + 0.34s + 0.1}$	3,0	954	251	58.1	-52.3
M7	$\frac{102.9s - 1.34}{s^3 + 1.1s^2 + 10.6s + 2}$	3,1	34.7	6.94	65.7	92
M8	$\frac{-266.5s^2 - 38.95s - 0.70}{s^3 + 1.67s^2 + 13.15s + 2.1}$	3,2	37.16	5.30	65.0	93
M9	$\frac{8.75s^3 + 4.8s^2 - 14.7s + 0.2}{s^3 + 2.80s^2 + 1.96s + 0.2}$	3,3	5918	538	82.7	29.5

TABLE 3. PUMP SYSTEM MODEL

Model No.	Transfer Function	Poles, Zeros	FPE	MSE	Max. validation data Fit %	Est. data Fit %
M1	$\frac{0.04412}{s + 0.2862}$	1,0	0.20	0.122	76.5	92.1
M2	$\frac{0.02948s + 0.01886}{s + 0.1057}$	1,1	0.11	0.058	78.6	94.5
M3	$\frac{0.009749}{s^2 + 0.1281s + 0.0671}$	2,0	0.01	0.005	86.7	98.4
M4	$\frac{-15.05s - 1.942}{s^2 + 136.7s + 17.17}$	2,1	1668	556.0	-260	-434
M5	$\frac{-0.053s^2 - 0.05s + 0.026}{s^2 + 0.63s + 0.1103}$	2,2	0.09	0.025	61.2	96.4
M6	$\frac{0.05401}{s^3 + 1.25s^2 + 2.38s + 0.2}$	3,0	0.04	0.012	74.1	97.5
M7	$\frac{1.949s + 0.7371}{s^3 + 21.5s^2 + 9.06s + 5.1}$	3,1	0.39	0.078	79.9	93.7
M8	$\frac{2.187s^2 - 0.02s + 0.3311}{s^3 + 17.1s^2 + 0.14s + 2.4}$	3,2	0.13	0.018	66.9	96.9
M9	$\frac{0.09s^3 - 0.04s^2 - 0.1s + 0.1}{s^3 + 0.57s^2 + 1.0s + 1e-9}$	3,3	92.7	8.430	73.3	34.2

B. Tuning performance evaluation results

1) Classical tuning

To begin, the PID parameters were calculated using the classical tuning (Trial and error) method, which involved first setting all gains to zero, then increasing K_p until the response overshoots the reference value, then increasing K_i to remove the steady state error, and finally increasing K_d to improve the transient response. We spent some time fine-tuning all three with various variations until we achieved an acceptable response with gain values $K_p = 0.1$, $K_i = 15$, and $K_d = 1e-4$. Fig. 8 depicts the system's closed loop response for unit step input. The performance parameters derived from the response for a droplet size setpoint of $100\mu m$ are rise time = 1.57s, overshoot percentage = 1.5%, and settling time = 0.338s. This result is summarized in TABLE 4. The system response can be improved further to have a relatively fast settling time. Using a genetic algorithm, the PID controller was re-tuned for lower overshoot, settling time, and good steady state response.

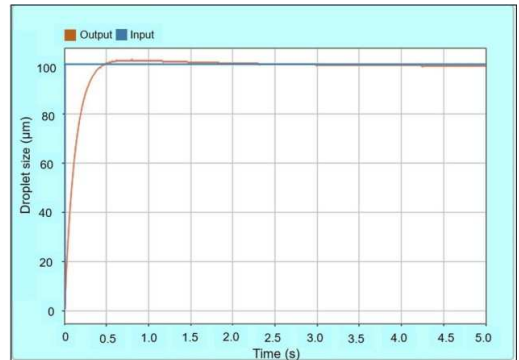


Fig. 8. Closed loop response with classical PID controller tuning

TABLE 4. SYSTEM PERFORMANCE WITH CLASSICAL TUNING FOR PID CONTROLLER

K_p	K_i	K_d	Rise Time	Settling Time	Overshoot
0.1	15	1e-4	0.271s	0.338s	1.5%

2) GA tuning

Fig. 9 depicts the unit step response of the closed loop system with a PID controller tuned using a genetic algorithm for a droplet size setpoint of $100\mu m$. When the results of GA tuning were compared to the results of the classical tuning method, the results showed a significant improvement in process response, especially on overshoot percentage, from 1.5% to 0.5% and settling time from 0.34s to approximately 0.088s. Furthermore, when the performance of the six objective function criteria was compared, the Integral of Time Absolute Error (ITAE) criteria produced the optimal system response with the lowest fitness value (error) of 0.2367. TABLE 5 summarizes the findings.

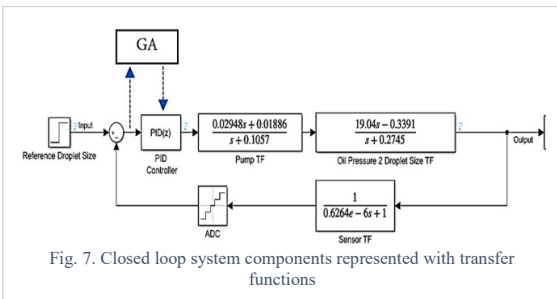


Fig. 7. Closed loop system components represented with transfer functions

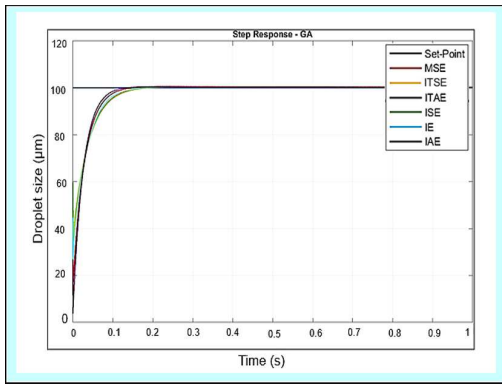


Fig. 9. Closed loop response with genetic algorithm PID controller tuning

TABLE 5. SYSTEM PERFORMANCE WITH GENETIC ALGORITHM TUNING FOR PID CONTROLLER

Objective function criteria	K_p	K_i	K_d	Fitness Value	Rise Time (ms)	Settling Time (ms)	Over-shoot (%)
MSE	0.975	69.68	3.12×10^{-5}	84.46	54.7	96.4	0.5
ITSE	0.060	46.09	8.62×10^{-5}	1.606	86.8	110.1	0.5
ITAE	0.234	69.40	2.84×10^{-5}	0.2367	56.4	72.4	0.5
ISE	0.937	69.12	2.00×10^{-5}	82.552	71.2	96.8	0.5
IE	0.035	67.83	7.46×10^{-5}	2.1411	60.0	78.0	0.5
IAE	0.173	69.93	4.9×10^{-5}	2.1282	58.4	75.2	0.5

VI. CONCLUSION

For the first time, a PID controller tuned with a genetic algorithm is implemented in a microfluidics system for closed-loop droplet size control. The goal was to identify the optimal PID controller parameters for providing the shortest settling time and the most stable controller response. Thus, the work was completed in MATLAB and Simulink by representing the physical models in our experimental setup with transfer function models and integrating this with a PID controller tuned with a genetic algorithm. For comparison, the controller gains and step responses were derived using both the classical tuning and the genetic algorithm methods. It was demonstrated that the genetic algorithm tuning method produced superior results with less settling time and overshoot than the classical tuning method. The optimal controller gains values from the genetic algorithm tuning method were obtained in 20 generations with a population size of 20, corresponding to approximately 400 experiments in real life. Using these, we were able to achieve a droplet size setpoint range of $50\mu\text{m}$ to $350\mu\text{m}$ depending on the fixed water pressure value. Thus, while a classical tuning method can serve as a starting point for calculating controller gains, it can be time consuming. The use of intelligent optimization tuning methods, which result in optimal tuning of droplet microfluidic systems, is a more efficient approach.

ACKNOWLEDGMENT

The authors would like to thank the Estonian Research Council for providing support under projects PUT1435, PRG620, as well as the TTÜ development program 2016-2022, project code 2014-2020.4.01.16-0032.

REFERENCES

- [1] D. F. Crawford, C. A. Smith, and G. Whyte, "Image-based closed-loop feedback for highly mono-dispersed microdroplet production," *Sci. Rep.*, vol. 7, no. 1, pp. 1–9, 2017, doi: 10.1038/s41598-017-11254-5.
- [2] E. Miller, M. Rotea, and J. P. Rothstein, "Microfluidic device incorporating closed loop feedback control for uniform and tunable production of micro-droplets," *Lab Chip*, vol. 10, no. 10, pp. 1293–1301, 2010, doi: 10.1039/b925497h.
- [3] W. Zeng, S. Li, and Z. Wang, "Closed-loop feedback control of droplet formation in a T-junction microdroplet generator," *Sensors Actuators, A Phys.*, vol. 233, pp. 542–547, 2015, doi: 10.1016/j.sna.2015.08.002.
- [4] R. Kebriaei and A. S. Basu, "Autosizing, closed-loop drop generator using morphometric image feedback," *17th Int. Conf. Miniaturized Syst. Chem. Life Sci. MicroTAS 2013*, vol. 3, no. October, pp. 1944–1946, 2013.
- [5] Y. Xie, A. J. Dixon, J. M. R. Rickel, A. L. Klibanov, and J. A. Hossack, "Closed-loop feedback control of microbubble diameter from a flow-focusing microfluidic device," *Biomicrofluidics*, vol. 14, no. 3, 2020, doi: 10.1063/5.0005205.
- [6] S. Motaghi, M. Nazari, M. Nazari, N. Sepehri, and A. Mahdavi, "Control of Droplet Size in a Two-Phase Microchannel using PID Controller: A Novel Experimental Study."
- [7] W. Postek and P. Garstecki, "Droplet Microfluidics for High-Throughput Analysis of Antibiotic Susceptibility in Bacterial Cells and Populations," *Acc. Chem. Res.*, vol. 55, no. 5, pp. 605–615, 2022, doi: 10.1021/acs.accounts.1c00729.
- [8] N. Gyimah, O. Scheler, T. Rang, and T. Parfy, "Digital twin for controlled generation of water-in-oil microdroplets with required size," in *2022 23rd International Conference on Thermal, Mechanical and Multi-Physics Simulation and Experiments in Microelectronics and Microsystems (EuroSimE)*, Apr. 2022, pp. 1–7, doi: 10.1109/EuroSimE54907.2022.9758876.
- [9] D. Ana, R. Wati, and R. Hidayat, "Genetic Algorithm-based PID Parameters Optimization for Air Heater Temperature Control," *2013 Int. Conf. Robot. Biomimetics, Intell. Comput. Syst.*, 2013, doi: 10.1109/ROBIONETICS.2013.6743573.
- [10] A. S. El-Wakeel, A. E. E. K. M. Ellissy, and A. M. Abdel-Hamed, "A hybrid bacterial foraging-particle swarm optimization technique for optimal tuning of proportional-integral-derivative controller of a permanent magnet brushless DC motor," *Electr. Power Components Syst.*, vol. 43, no. 3, pp. 309–319, 2015, doi: 10.1080/15325008.2014.981320.
- [11] S. Gupta, R. Gupta, and S. Padhee, "Parametric system identification and robust controller design for liquid-liquid heat exchanger system," *IET Control Theory Appl.*, vol. 12, no. 10, 2018, doi: 10.1049/iet-cta.2017.1128.
- [12] J. M. Chaparro F., O. F. Aviles S., and A. J. Chica L., "Design and implementation of a controller using genetic algorithms," *Int. J. Appl. Eng. Res.*, vol. 12, no. 8, pp. 1469–1477, 2017.

Appendix 3

III

R. Jõemaa, **N. Gyimah**, K. Ashraf, K. Pärnamets, A. Zaft, O. Scheler, T. Rang, and T. Pardy, "Cogniflow-drop: Integrated modular system for automated generation of droplets in microfluidic applications," *IEEE Access*, 2023

Date of publication xxxx 00, 0000, date of current version xxxx 00, 0000.

Digital Object Identifier 10.1109/ACCESS.2017.Doi Number

CogniFlow-Drop: Integrated modular system for automated generation of droplets in microfluidic applications

Rauno Jõemaa^{1,2}, Nafisat Gyimah¹, Kanwal Ashraf¹, Kaiser Pärnamets¹, Alexander Zafft¹, Ott Scheler², Toomas Rang^{1,2} and Tamás Pardy^{1,2}

¹Thomas Johann Seebeck Department of Electronics, Tallinn University of Technology, Tallinn, 19086, Estonia

²Department of Chemistry and Biotechnology, Tallinn University of Technology, Tallinn, 19086, Estonia

Corresponding author: Rauno Jõemaa (e-mail: rauno.joemaa@taltech.ee).

This research was funded by the Estonian Science Agency ETAg, grant number PRG620, MOBTP109 and by the European Union's Horizon 2020 Research and Innovation Program under Grant 668995, and TTU Development Program 2016–2022 (project no. 2014–2020.4.01.16.0032).

ABSTRACT Droplet microfluidics enables studying large cell populations in chemical isolation, at a single-cell resolution. Applications include studying cellular response to drugs, cell-to-cell interaction studies. Such applications need a reliable and repeatable droplet generation with high monodispersity. Most systems used in research rely on manual tuning of flow parameters on off-the-shelf instruments. Setups are highly customized, limiting reproduction of experimental results. We propose an integrated, modular system for automated aqueous droplet generation with high monodispersity. The system provides dynamic feedback control of droplet size and input pressure. Input pressure is generated by two piezoelectric micropumps. Droplet sizes are determined via light intensity measurement in an LED-photodiode setup. The system is capable of wireless communication and has a low enough power consumption for battery-powered operation. We report on the assembly and the underlying working principle, as well as an in-depth experimental evaluation of the performance of the proof-of-concept prototype in aqueous droplet generation. Evaluation was performed on a modular as well as on a system level. During module-level evaluations, aqueous droplets were generated in a light mineral oil + Span 80 surfactant carrier medium, using 3 different flow-focusing junction geometries. The presented prototype had a significantly faster pressure stabilization time (10 s) compared to a syringe pump-based reference setup (120 s). During system-level evaluation, deionized water droplets were generated in a carrier medium of HFE7500 + PEG-PFPE triblock surfactant. Resultant droplet sizes were benchmarked with microscopy. The system was able to repeatedly generate mono- and polydisperse droplets on demand, with CVs between 5-10% in the ~50-200 μm droplet diameter range.

INDEX TERMS Lab-on-a-Chip, microfluidic, automation, pulsatile flow, droplet size control, droplet generation rate control, optical feedback, pressure feedback, closed-loop control, wireless communication.

I. INTRODUCTION

Droplet microfluidics enables studying the response of cell populations to specific chemicals, in isolation, at a very high throughput [1]. Chemical isolation is given by encapsulating cells into aqueous droplets in an immiscible carrier medium, together with the chemicals for their treatment. For example, antibiotics and resistant bacteria, to screen for antimicrobial susceptibility, or circulating multi-drug resistant tumor cells and chemotherapy drugs to screen for drug response among other analysis targets [2], [3]. Working in droplets enables 1)

higher throughput than conventional batch processing in 2) a compact, highly integrated, automatic system as well as 3) continued work with individual droplets downstream [4]. Furthermore, it enables analysis of single-cells, or cell-to-cell interactions [5]. Droplet microfluidics has additional applications in chemical analysis and synthesis, as well as bioanalyses other than cytometry (e.g., nucleic acids) [6].

However, imaging droplet flow cytometry necessitates reliable and repeatable droplet generation with high droplet monodispersity (1-5% [7], [8]) at moderate droplet

generation rates (~1-3 kHz [9]). To date, open-loop control and/or manual tuning of flow parameters to achieve desired droplet sizes and stable droplet generation are most common [10], [11]. However, the target parameters are difficult to achieve and maintain with manual tuning. Thus, automated droplet generation with closed-loop control (or in other words, an inline quality control system of droplet generation) is necessary. Fu et al [12] demonstrated a reduction of steady-state error to <2% coefficient of variation (CV) across various flow conditions in droplet digital PCR applications [13]. Similarly, Duan et al [14] achieved high monodispersity (<7.6 CV%) by implementing a closed-loop control strategy, which was at least 90% lower than with open-loop control. Additionally, Zen et al [15] addressed the challenge of predicting droplet size by using closed-loop control to account for the nonlinearity of flow-focusing. Moreover, a novel microfluidic system was developed to optimize cell processing conditions using deep learning algorithms for analyzing sensor data and closed-loop control to update a pressure pump and maintain optimal cell flow speed [16]. Several other works have demonstrated closed-loop control of droplet sizes by tuning flow parameters based on an image/video stream of the flowing droplets [17]–[19]. Most demonstrated systems (TABLE I) used droplet imaging for control. However, overall throughput in camera-based tracking is limited by the imaging throughput of the camera (increasing throughput increases cost and heat dissipation). The price/performance ratio of imaging droplets for flow control (in contrast with cell imaging, which is a different application) is also not optimal.

A compact system with a laser-photodiode setup for bubble tracking was demonstrated in [20]. Such an integrated, compact benchtop setup enables portability between labs, which in turn enables transferring experimental workflows with excellent repeatability. It also allows replication of results, thus enabling virtual parallel labs and digital, rather than physical exchange of results and knowledge. However, at present, widely used setups are an ensemble of off-the-shelf instruments, assembled specifically for the experiment on hand, with little to no integration (TABLE I). The lack of integration means the setup (and results created with it) cannot be easily transferred between labs. It is also notable that while in microfluidics in general, syringe pumps are the most popular choice due to their flow stability, affordability, and ease of use, in droplet microfluidics, pressure pumps are also very common, as they do not need refilling. The need to refill the syringe causes interruptions in experimental workflows, and possibly also the need to recalibrate flow parameters. Finally, in our previous reviews, we found a pronounced interest towards low-cost instrumentation and the democratization of instruments for droplet microfluidics [4], [21].

As of today, compact, integrated droplet microfluidics instruments, particularly with wireless communication and low-cost hardware, are uncommon. Setups exist that meet some but not all criteria (TABLE I) for a compact, modular, automated, wirelessly communicating droplet generator.

In this work, we describe a proof-of-concept experimental setup meeting the aforementioned criteria, its underlying methodology, and the evaluation of its performance in droplet generation experiments. The CogniFlow-Drop system concept (Fig. 1) offers the following advantages over the state of the art (TABLE I):

1. It is integrated and modular (some modules can be swapped out for easy upgrades), improving reliability, and enabling portability. These features ensure that results and workflows are transferable between labs (enabling creation of virtual parallel labs).
2. It is low-cost (~650€) compared to commonly used experimental setups built from off-the-shelf components. With future development, modularity will enable customization, affordability will open wider collaboration using the platform.
3. Can offer comparable performance to commonly used droplet generation setups through its dual-PID control of droplet size and generation frequency. With future optimizations, can significantly reduce carrier/sample/reagent waste. Furthermore, through automation, can ensure better repeatability without manual recalibration or in-depth knowledge of the technology.
4. Measures droplet generation in real-time via intensity change in a simple LED-photodiode setup (water droplets, passing between, causing a change compared to the carrier medium).
5. Uses tilting mounts to reliably set up chip, light source, and detector alignment, to optimize channel/droplet visibility in a given microfluidic chip. This also increases reproducibility of results.
6. Uses wireless communication, which enables remote control and monitoring of the system.
7. Has a sufficiently low power consumption (~8.0 W) that it can be powered from batteries for portable operation (based on the estimated consumption, >4.5h battery life on a 10000 mAh Li-ion power bank).

II. COGNIFLOW-DROP SYSTEM PROTOTYPE

In this section, we present a structural overview of the complete prototype assembly (Section II-A), then in following sections (Section II-B to II-D) overview each system module in detail, including both hardware and software, from a structural as well as functional perspective (working principles).

A. Overview

The system prototype (Fig. 2/4) was constructed as a compact, modular assembly with an emphasis on ease of use and low hardware cost. In this section, we overview the assembly and subassemblies, and link to sections with further details on each. The system consisted of three main modules (see also block diagram in Fig. 3) and the enclosure:

- 1) **Electronics module** (Section II-B and Fig. 2/1): functionally responsible for communication, instrument control and signal processing. Physically was constructed as a stack of stages onto which electronic parts were mounted:
 - a) *Power supply unit* (PSU) stage (Fig. 2/1/a): mounted the RJ45 adapter, the power switch, the mains connector, and the PSUs (ECS45US05, XP Power).
 - b) *Pump controller and pressure sensor stage* (Fig. 2/1/b): mounted the pump controller interface (with the low-level pump controller running on an ESP32 DevKitC board) and pressure regulation board. The stage was shielded from noise from above and below by copper plates attached to and grounded through structural conductive threaded rods.
 - c) *Communication, control, and signal processing stage* (Fig. 2/1/c): mounted the Raspberry Pi 4B (RPI), responsible for system control and communication, and the filter-amplifier, analog-to-digital conversion (ADC) board for the optical sensor.
- 2) **Sensorics module** (Section II-C and Fig. 2/2): functionally responsible for optical flow rate measurement. Physically also holds the microfluidic droplet generator chip and consists of the following stack of stages:
 - a) *Photodetector stage* (Fig. 2/2/a): the photodetector PCB and the connecting microscope lens were mounted to the bottom plate.
 - b) *Chip mount stage* (Fig. 2/2/b): included the chip mount with 3 degrees of freedom (DoF; height, roll, pitch) and a removable microfluidic chip holder.
 - c) *Light source mount stage* (Fig. 2/2/c): positioned at the top of the sensorics module was an analogous 3 DoF mount stage for the light source as was for the chip mount stage. The light source was an LED, soldered to a 25 mm x 75 mm sized PCB. A diffuser/lens was attached over the LED. Aluminum or large copper area on the PCB was used for heat dissipation from the LED.
- 3) **Fluidics module** (Section II-D and Fig. 2/3, Fig. 2/1/b, Fig. 2/2/b): functionally responsible for generating

droplets from the carrier medium, reagents, and sample(s). Additionally responsible for dampening secondary vibration and sound produced by piezoelectric micropumps.

- a) *Pump mount* (Fig. 2/3/a): both pumps were mounted on an L-shaped mount. The pumps were fastened to the mount with shock dampening rubber in between.
 - b) *Shock- and audibility-dampening piezopump enclosure* (Fig. 2/3/b): 2-part enclosure with rubber padding fitted around the micropumps for additional sound absorption. The top of the enclosure was designed with slots for three 100 ml lab bottles.
 - c) *Liquid containers* (Fig. 2/3/c): included the reagent and sample containers, as well as the product collector.
 - d) *Pressure sensors* (mounted to electronics module Fig. 2/1/b)
 - e) *Fluidic chip* (mounted to sensorics module Fig. 2/2/b)
- 4) **Enclosure** (Fig. 2/4): held the components together, including the interior walls between compartments, as well as the external enclosure. The base plate was a wooden board of 22 cm x 33 cm x 1.8 cm, selected to provide mechanical support to the assembly. Internal walls were used to route cables and tubing, as well as providing slots for T-junctions that bridged connections between the microfluidic chip, the pumps, and the pressure sensors. All plastic components were 3D printed. Load-bearing components were 3D printed with a Prusa i3 mk3S, the T-junctions [22] with an Anycubic Photon Mono. Electronics and sensorics modules were fastened to the base plate with structural ISO M6 size threaded rods, whose internal components were fastened to load-bearing components with ISO M3 size bolts (metal fasteners are hidden on the explosion views for better clarity). The pump enclosure was fastened to the base plate with ISO M3 size bolts. The chip mount stage was set between spring-loaded knurled nuts (DIN 466 M6) to reduce vibrational sensitivity.

B. Electronics module

1) Flow control strategy

For the pressure-driven droplet generator, a dual-PID controller strategy with two feedback loops (inner and outer feedback loops, Fig. 4/a) was designed and implemented:

- The inner feedback loop was used to rapidly reach target pressure levels in the microfluidic chip and to reduce pressure fluctuations, inherently induced by the droplet pinch-off process, the pulsatile nature of the micropumps and the rapid target pressure level approach. The inner loop consisted of PID controllers for each micropump separately.

- The outer feedback loop was used to reach and maintain user defined droplet size and generation rates through discretized light sensor data.

The proposed design of the dual-PID control strategy (depicted on Fig. 4/a) for the CogniFlow-Drop system can be described as follows:

- 1) The inner PID closed feedback loop used pressure readings from sensors 1 (S_1) and 2 (S_2) of pumps 1 and 2, respectively, as well as pressure readings from sensor 3 (S_3) at the microfluidic chip's output.
- 2) The PID controller associated with each pump regulated the pressure drop across the chip using the differential pressures (i.e., S_1-S_2 , S_1-S_3) as feedback. The accurate and rapid control of pressures produced by the inner feedback loop action improved the stability and precision of the outer feedback loop.
- 3) The outer PID controller achieved user-defined droplet size and droplet generation frequency set points (d_{set} and f_{set}) by adjusting the pressure of pump 1 and 2 respectively (i.e., disperse and continuous phase flows). The size related pressure target was derived from using the error (e_d) between the set point (d_{set}) and the average measured droplet size (d_m). The generation frequency related pressure target was derived from using the error (e_f) between the set point (f_{set}) and the average measured droplet generation frequency (f_m). By fixing the disperse phase pressure, the control variable relationships between "droplet size" to "disperse phase pressure" could be made as "droplet size" to "continuous phase pressure", depending on the sensitivity of the target parameter to the fluid phase type [23].

In reference to our previous work, the PID controller parameters (i.e., proportional gain, integral gain, and derivative gain) were derived using a Genetic Algorithm (GA). The dual-PID control strategy, adapting the framework implemented with MATLAB, Simulink in [24], was modified to include droplet generation frequency control for the presented version of the droplet microfluidics system, using Python.

2) Pump controller and pressure sensor stage

The pumping system embedded into CogniFlow-Drop was an updated version of the non-automated dual-channel piezoelectric pumping device demonstrated in our previous work [25], [26]. Relevant notable modifications to our standalone pump PCBs ([26]) are mentioned in the electronic supporting information (ESI) S1.

While the base design with all its features was carried over, standalone operation (wireless communication and battery power) was not. Wireless communication was not

necessary as the pump controller exchanged commands and sensor data, as well as received power, over a USB cable connecting the pump controller (ESP32) to the main controller (RPI). Additional updates were required to be made to the pump controller firmware from the previous work ([26]) with relevant notable ones mentioned in ESI S1.

3) Communication, control, and signal processing stage

RPI was selected as the main controller for the system due to its quad-core processor and extensive interfacing options. It ran Ubuntu desktop (ver. 21.10) with its tasks written in Python 3.9 and C++. With four cores, the RPI was able to dedicate one for each independent task:

- 1) Communication with the user, over local network, using the methodology described in Section II-B-4.
- 2) Communication with the pump hardware described in Section II-B-2.
- 3) Interpretation of data obtained from the optical sensor, expanded upon in Section II-C.
- 4) Calculation of pumping pressure targets based on both the measured pressure data (obtained from task 2) and the resolved optical data (obtained from task 3), detailed in Section II-B-1.

The interpretation of links between tasks and their interactions with parts of the system, external from the Raspberry Pi, are shown in Fig. 5, and an explanation with more details about the internal mechanism of each task is described in ESI S2.

4) User interface

Data and information flow are critical aspects when considering the design of any bioanalytical device. In our previous work we presented a framework for integrating event-triggered wireless data distribution and information flow into a bioanalytical device [26]. In this work, we focus on structured data serialization (along with metadata) using Google's Protobuf serialization protocol [27]. With this method, the number (and type) of devices in the network could be extended with minor edits to the data structures.

Inter-host communication was performed using an enhanced Communication Abstraction Layer (eCAL, v5.9.5) middleware [29]. The data rate through eCAL was payload dependent, and the employed data-centric communication architecture offered low latency communication with fair reliability.

Data was sent between devices along with a unique device ID and name, chip name, flow rate, transmission/reception status, flag for different process activation, and droplet size (see example in Fig. 6/a) and message ID. On the publisher/sender side, a Protobuf message object (see example in Fig. 6/b), was created based on the data structure defined and serialized using the Protobuf protocol, followed by being broadcast to any listening device. For any device to catch the broadcast data, an eCAL subscriber/receiver function was cyclically polled. Concurrently, the method was

used in reverse to transfer data from the controlled device to the controller. Devices could communicate with each other in an event-triggered wireless or wired manner. The overall data transfer mechanism is shown in Fig. 7.

The CogniFlow-Drop prototype could be controlled via the graphical user interface (GUI, Fig. 8) by defining parameters for droplet generation rate and size and passing them on using the available task specific buttons. If the chosen parameters were not within acceptable limits or of the wrong type, an error was presented, asking for appropriate corrections. The entered parameters were serialized by protocol and sent to the other device in the form of messages. Unless manually halted from the GUI, tasks were halted automatically on the controlled device after completion.

5) Optical feedback signal acquisition

The digitization PCB before signal processing on RPI, was made with three stages.

The first stage, receiving the feedback signal directly from the sensorics module described in Section II-C, was a 2nd order Sallen-Key low pass filter. The filter was designed for detection of up to 5000 droplets per second without distortions, with a cutoff frequency at ~ 7.26 kHz and a quality factor of ~ 0.64 . Filtering was necessary to reduce noise acquired from the system (in most part from the used switch-mode PSUs).

Before discretization with an ADC, to maximize the information gained from the incoming, filtered optical signal, per bit, an adjustable inverting amplifier stage was used. This enabled scaling of captured waveform to the ADC's analog input limits. Additionally, this filter-amplifier circuit was designed to discard any inherent DC component from the optical signal and bias it instead with 2.5 V, to position it in the middle of the 0 to 5 V ADC measurement window.

The converter used was a 16-bit ADC (ADS8681, Texas Instruments). In the presented version of the system, the PCB on which it was installed was a perforated protoboard, which introduced additional noise to the measured signal due to a non-ideal splitting of digital and analog signals.

C. Sensorics module

1) Droplet measurement hardware

In our previous works, we demonstrated cost-effective imaging [30] and non-imaging [31] droplet flow sensor prototypes with up to 750 frames per second throughput. With cost-effectiveness in mind, a more compact setup with a higher throughput for capturing droplets during generation was constructed as follows (Fig. 9):

- A light source constructed of a cold white 1 W wide-beam LED (Fig. 9/a). Soldered to a PCB with large copper areas for heat dissipation. Current-limited to ~ 150 mA using an LED driver.
- The light source was covered with a diffusing lens (Fig. 9/a) to reduce its beam angle and reduce beam

intensity variations from smaller misalignments with the sensor axis.

- A PDMS-glass microfluidic chip, further detailed in Section II-D (Fig. 9/b).
- A thin metal plate, with a noise-reducing micro-drilled pinhole (sized proportionally with the chip's junction width), positioned beneath the microfluidic chip to increase the relative dimming impact of a passing droplet (Fig. 9/b).
- Based on Texas instruments application [32], using a 1 M Ω as feedback resistor instead, to obtain a gain of 1 MV/A and a 1.3 pF capacitor for stability at higher frequencies, a photodiode (PD) sensor (Osram SFH 2240, Fig. 9/c) was connected to a transimpedance amplifier (TIA). A 20x microscope lens was mounted to the PCB, over the sensor, for improved focus of the droplets flowing in the microchannel.

Using the droplet flow sensor setup described above, a theoretical detection throughput was raised above 10000 droplets per second.

2) Detection of droplet shadows

The chip mount (Section II-A-2-b and Fig. 2/2/b) was positioned between the light sensing PD and the light source, all of which were vertically aligned to the pinhole under the outlet junction of the microfluidic chip (Fig. 9). As generated droplets were moving over the pinhole, a shadow was cast through it, onto the PD. The changing current through the PD was converted to voltage using a high-gain TIA, passed on to a connected filter-amplifier circuit in the electronics module (Section II-B-5 and Fig. 2/1). The filtered signal moved through a DC decoupler into an inverting and level-shifting amplifier circuit. The extra amplification also provided compensation when the height of the light source was adjusted. The inversion of the photodiode voltage meant that any increase in the shadow corresponded to an increase in measured voltage. The filtered and amplified photodiode output was discretized with the ADC and sent over to the main control board using SPI. The RPI dedicated 1 of its 4 cores to communicating with the ADC, enabling photodiode voltage sampling rates of up to ~ 440 kHz (without an interpretation algorithm).

D. Fluidics module

1) Droplet generation chips

The microfluidic chip designs used in this work were adapted from the group's previous works, notably the "Droplet counting chip" in the ESI of [33]. The principle design (Fig. 10/a) was a flow-focusing device (FFD) laid out on an SU8 mask in multiple copies with different junction widths and geometries. In TABLE II the chip designs used in experiments in this work are shown. The mask design is openly available on our GitHub [34]. Silanized silicon-SU8 masks were purchased from the BioMEMS group of the

Hungarian Academy of Sciences [35]. PDMS-glass chips were fabricated as follows: 1) PDMS was molded off the mask (PDMS was allowed 3 days at room temperature to cure and degas), 2) the PDMS was punched to create ports using a tissue biopsy tool, 3) PDMS and glass surfaces were cleaned from dust, 4) surfaces were activated with oxygen plasma generated by a handheld corona discharge surface treater, 5) surfaces were bonded, 6) chip walls were coated with Novec™ 1720 Electronic Grade Coating.

2) Mounting of the droplet generation chip

The removable chip holder (Section II-A-2-b) in the sensorics module (Fig. 2/2/b) had a 2 by 2 mm square hole at the center, over which the metal plate (Fig. 9/b) with a pinhole was placed. The pinhole was manually centrally aligned with the square hole in the chip holder. Lastly, a droplet generation chip was positioned on the pinhole plate and fastened to the holder. The chip was aligned to have the pinhole beneath the chip's outlet channel, ~300 μm after the cross-junction. For the used chips, this distance mitigated capturing forming droplets and deforming droplets flowing into the wider section of the outlet where capturing distinct droplets could be jeopardized by the loss of gaps between droplets. The assembly was attached to the top of the 3 DoF chip mount (Section II-A-2-b and Fig. 2/2/b).

III. EVALUATION METHODOLOGY

In this section, we present the prototype system evaluation methodology used for characterization and benchmarking on a system as well as on a submodule level.

The first test series (Section III-A) focused on evaluation of system submodules or groups of submodules. Fine-tuning steps were also taken to prepare for the system integration. The second test series (Section III-B) focused on characterizing and benchmarking the integrated system prototype in droplet generation.

In all test setups, droplets were generated using fluids as described in TABLE III.

In all test setups including a camera, a high-speed camera module (acA640-750uc, Basler) was used. The camera frames were captured in real time on the computer using Basler's pylon Viewer software.

A. Submodule evaluation

The test setup used (Fig. 11/a) in this section was an early proof-of-concept implementation of the full experimental setup presented in Section II-A. The setup was derived from components demonstrated in our previous works ([25], [26]). In the setup, DIW was used as the disperse phase, oil A or B as the continuous phase. Both phases were pumped into the droplet generation chip using our custom pumping system based on Bartels Mikrotechnik micropumps (mp6-liq). Results are presented in Section IV-A.

1) Pressure-based system feedback modelling

Tests done with the following methodology gave results for: characterization of pressure control, definition of voltage to pressure transfer functions and tuned pressure feedback PID gains using the transfer functions.

The pressures at the inlets and outlets of the microchannel were measured using Honeywell pressure sensors MPRLS0015PG0000SA and MPRLF0250MG0000SA, respectively, with a sampling rate of ~166 Hz. To obtain pressure to pump driving voltage relationships, driving voltage tests were conducted. For three chip variants (relevant chip dimensions in TABLE II), the driving voltage of the piezo pumps ranged from 25 V to 250 V, with a step size of 25 V. Corresponding pressures were recorded for a duration of one minute at each step with the steady state averaged as the resulting pressure value. Measurements were done separately for DIW and oil A. Unwanted transients or spikes in the experimental data were removed using median filtering (performed in MATLAB).

To tune the PID gains, experimental data (from our previous works [23], [24]) demonstrating the effect of inlet pressure on droplet size were used in MATLAB to derive pumping system component transfer functions. The transfer functions were implemented in Simulink in a setup-derived closed loop feedback model. PID K-values were found among six objective function criteria obtained from using genetic algorithm method: the Integral Squared Error (ISE) criterion; the Integral Time Squared Error (ITSE) criterion; the Integral of Time Absolute Error (ITAE) criteria; the Integral of Absolute Error (IAE) criterion; the Mean Squared Error (MSE) criterion; the Integral Error (IE) criterion).

2) Syringe pump vs. pressure-driven pump

As laboratories often use syringe pumps for droplet microfluidics, the performance of our pressure-based micropump system against syringe pumps was compared here.

Two syringe pumps (NetPump, SpinSplit LLC, Budapest, Hungary) with plastic syringes were used to pump oil A and DIW into chip variant A. Pressure sensors were set in the established configuration (Fig. 11/a). The syringe pumps were connected to local network via Ethernet and interfaced with SpinStudio (SpinSplit LLC, Budapest, Hungary) on a desktop computer. Droplet formation was observed using a camera, placed beneath the FFD's cross-junction. Syringe pumps were set to run for about four minutes, with fixed flow rates (Fig. 14/a), producing uniform droplets. One minute from the end of the steady state period of the measured oil and water pressure drops over the chip were averaged and used as targets for the pressure pump PIDs corresponding to the matching fluid phase. Followingly, the inlet tubes were disconnected from the syringe pumps and connected to the pressure pumps. For two minutes, pressure pumps were pumping oil and water with closed loop control, with comparable pressure (Fig. 14/b).

3) Sensorics, photodiode voltage interpretation

Before droplet observations with a PD, a camera was used to analyze possible scenarios. Droplets were generated with DIW in separate combinations with oil A and B (TABLE III). Droplets were recorded as image series to a computer and afterwards analyzed visually. Additionally, images of droplets were scanned through a custom pixel color summation program, used to estimate possible collectable waveforms from the PD. The custom program had an additional feature to roughly mimic a variable pinhole (determinable by the angle of the droplet generation chip in the chip mount).

4) System controller benchmarking

The selected controller (RPI) had a quad core processor limiting concurrent tasks to four. Additionally, with RPI running a desktop OS, loop stability of each task, split using multiprocessing Python library, was measured in a one-time operation – finishing with complete termination processes. As this required all connected submodules, the test took place at the final stages of integration. All tasks running in parallel on RPI were timed over a 90 second droplet generation operation using chip variant C with oil B.

Furthermore, three additional 90 second tests were run (2 with chip variant C and 1 with chip variant B). After 45 seconds into the tests, ~3 seconds of ADC data (from task/core 3) was logged in more detail to analyze controller related latency and performance with a custom droplet interpretation algorithm. In the same period, a sample image was taken from the waveform entering the ADC, visualized on a connected oscilloscope (DSO5014A, Keysight).

B. System Evaluation

In system evaluation methodology, unless specified otherwise, oil B (TABLE III) was used as the continuous phase.

1) Droplet size and frequency control

For this evaluation process, two sets of target series tests (size and generation rate) were conducted for each of the two chip variants (B and C) – shown on TABLE IV–VII. All samples in series were given 15 seconds for stabilization which was discarded from further calculations. The remaining 21 seconds for each sample was used for CV% and error calculations. Due to geometric differences between chip variants, target ranges of named series were limited to combinations more likely to produce droplets.

2) Measurement of coefficient of variability of generated droplets

To measure the stability of droplet generation with the proposed system, coefficients of variability (CV%) were calculated from “digitized” droplet data (relative droplet size over the photodiode as voltage and droplet generation rate as

frequency from droplet-to-droplet period) obtained with specified droplet feedback PID targets after the setup was ran through the calibration algorithm described in ESI S3. CVs were calculated from voltage and frequency series obtained from dual-PID tests, allowing 15 seconds for stabilization at the start of each stage. This left 21 seconds of stabilized data on each target for CV calculation. CVs were also calculated from additional datasets made with longer stabilization (30 s) and stable periods (45 s). As generation frequency did not strictly apply to droplet length, CV of generation frequency was not combined with relative size CVs. However, droplet generation frequency target series were further quantitatively analyzed via standard deviations and CVs (further detailed in ESI S4). Multiple CV sets were required for observing the impact from droplet generation frequency, pumping frequency (as piezo pump driving frequency) and average pressure in the chip to droplet size CV.

In addition, to attest to the meaning and comparability of voltages obtained from the photodiode, claimed as corresponding to droplet size, visual data of droplets was needed. For visual data, droplets, generated with fixed pressure targets, were collected into an Eppendorf Tube® to be measured afterwards. Imaging for measurements was done with a trinocular microscope (BX61, Olympus) using a camera (DP70, Olympus) and a 4x/0.16 lens (UPLSAPO, Olympus). CVs and averaged cross-sectional areas and diameters were calculated using ImageJ software (further described in ESI S5). For better viewing, droplets were pushed into Countess™ Cell Counting Chamber Slides (ThermoFisher) with a channel height of 100 μm.

IV. EVALUATION RESULTS AND DISCUSSION

In all tests, droplets were generated with liquids following the naming scheme given in Section III.

A. Submodule evaluation

1) Pressure-based system feedback modelling

With the ramping pump driving voltage (25 V to 250 V) tests, linear correlation between voltage and pressure generated in tests with all chip variants were observed (Fig. 12). The relationship of pressure drops across the chip to pumping voltages varied for the different chip variants. This was quantified with the voltage-to-pressure coefficient (C_{vp}). Furthermore, while the rising trend of the C_{vp} of water tests was rising along with the cross-junction width, the ratio of water and oil C_{vp} was different between chips with different oil entry angles (Fig. 12/a-b vs. Fig. 12/d-e). The coefficients obtained with chip A were used in the controller design to account for differences in junction widths.

Based on our previous works [23], [24], the system components were mathematically represented as transfer functions in eqns. 1-3, using the collected data in MATLAB software.

$$t.f._{pwat} = \frac{-17.42s+83.92}{s+0.69} \quad (1)$$

$$t.f._{poil} = \frac{-8.40s+30.6123}{s+0.216} \quad (2)$$

$$t.f._{chip90} = \frac{19.04s+0.339}{s+0.275} \quad (3)$$

Where $t.f._{pwat}$ is the transfer function of the water pump, $t.f._{poil}$ the transfer function of the oil pump, and $t.f._{chip90}$ the transfer function of the chip variant A. From Simulink results the controller parameters with the lowest fitness values (error) were chosen for real-world experiments. PID's K_p , K_i , K_d values for water pump (10.5, 60.77, 1.64e5), obtained from the IE objective function, resulted in good long-term stability, albeit with an overshoot, whereas K_p , K_i , K_d values (6.69, 46.10, 5.81e-5), obtained from the IAE objective function, resulted in a response with negligible overshoot, but instead with oscillations around the target value. Based on the comparison of GA tuning results (Fig. 13), manual adjustments to K_i were made to prevent overshoot and maintain good stability, with new K_p , K_i , K_d values (10.5, 17.5, 5.81e-5) for water. Following the same process, K_p , K_i , K_d values were found for oil (40.0, 18, 4.78e-4).

2) Syringe pump vs. pressure-driven pump

The pressure stabilization and steady states of the two test scenarios described in Section III-A-2 are shown in Fig. 14. Syringe pumps took approximately 120 seconds to reach a reasonable steady state for new pressure targets, with minor oscillations persisting. Slower response time for syringe pumps was attributed to linear operation of the motors' speeds, however, the likely cause for persistent oscillations was attributed to inconsistent friction of the syringe's rubber gasket. In comparison, pressure-driven micropumps showed better responsiveness and stability between changing input pressure targets, taking about 10 seconds to reach the defined inlet and outlet pressure values.

The faster response rate helped significantly reduce experiment runtimes and reagent waste during the system evaluation tests (Section IV-B, e.g., exploring ranges of producible droplet sizes and generation rates).

3) Sensorics, photodiode voltage interpretation

While generating droplets using oil A, the formed droplets (Fig. 15) indicated that once the droplet's diameter exceeded the larger dimension of the channel (Fig. 15/c), the shadow caused by refractions in the phase transition region would intensify. Furthermore, a central low refraction region would emerge.

The possible impact of the low refraction region on the captured photodiode light intensity waveform was estimated from the custom pixel color summation program (Fig. 16). Given the fixed size moving window on Fig. 16/a-c, it was noted, that even with a longer than "window size" droplet,

whose diameter was less than the larger dimension of the channel (Fig. 16/b), the estimated waveform gained little to no distortions. Mild distortion could be attributed to the bullet-like shape of the droplet. However, a much more noticeable distortion was noted once the low refraction region became significant relative to the window size. The non-phase transition region had the potential to invert the tip of the waveform. The impact of this effect was amplified with a less viscous continuous phase, as that reduced the surface tension of the droplet and the intensity of the droplet's shadow along with it.

Using oil B for the continuous phase, generated droplets showed inherently thinner phase transition regions and gave way for larger low refraction regions (Fig. 17). The images show a case where not only was the phase transition region very thin, but the aligned droplet acted like a lens (Fig. 17/c). To further inspect the impact of such cases, consecutive frames were viewed in the custom pixel color summation program (Fig. 18). Due to the usage of a pinhole, the extra shadows at the edges (background noise) were subtracted from further intensity calculations using the 6th additional frame (Fig. 18/f). Seen from Fig. 18 with a droplet, sized large enough to be squished in the microfluidic channel, flowing in low viscosity oil B, the possible recorded waveform for a single droplet could resemble a much more severe case of Fig. 16/c – instead of a slightly dipping peak, a waveform section representing a single droplet with a possible dip as low as to split into two discernible droplets.

4) System controller benchmarking

Individual task duration details can be seen on TABLE VIII. Maximum loop durations of the waveform interpretation and pumping pressure target calculation tasks (marked with * in TABLE VIII) were caused by spikes in OS latency. Noticeably longer than average maximum loop durations for the remaining tasks were caused by delays from communication termination procedures included in the timing of the last loop. Total durations of tasks other than the pumping pressure target calculation task, where the main operation timer was running, were longer due to beginning their termination process after the defined 90 s time limit. Their difference was caused by sequential termination process (some extending for multiple seconds due to large log file generation). For droplet waveform interpretation task, the average loop duration extended to ~6.5 μ s, resulting in a mean sampling rate of ~153 kHz. The discrepancy between minimum loop duration of pump communication task (~15 ms) and pump sensor update rate of ~166 Hz (6 ms) was attributed to having used asynchronous communication method.

In the OS latency and droplet interpretation algorithm impact analysis, droplet waveform from the first additional test with chip variant C (Fig. 19) indicated that the pinhole-aligned droplets were seen as an increase in light intensity. Meaning that the droplets acted as lenses instead of obstacles.

In this scenario, the “peak” of the alignment was measured at the “trough”. Each “trough” could be imagined as a more severe form of the dip shown in Fig. 16/c. Each “trough” was accompanied by its darker incoming and outgoing edges (Fig. 18/a, 18/e). From the logged ADC data, a sample section (Fig. 20) showed the limits of RPI running code written in Python on a non-real-time OS and specific functions circumstantially interacting poorly with the OS. As the average ADC task loop duration was measured around $\sim 6.5 \mu\text{s}$ (TABLE VIII), Python’s multiprocessing Queue functions `empty()` and `get_nowait()`, called after 100 mV above the average line for every other droplet, delayed the loop duration minimally another $\sim 100 \mu\text{s}$ producing erroneous droplet size measurements. In comparison, the second test with chip variant C (Fig. 21) showed a waveform with similar sharp peaks, but each with longer duration. Long enough to preserve the peaks captured by the ADC (Fig. 22). In the third additional test, with chip variant B, OS latency was spotted causing the loss of 2-3 consecutive droplets (Fig. 23) with an unexpected delay between two ADC sampling cycles. Albeit being relatively rare, the measurement error of such events was mitigated to prevent destabilizing the flow rates. When time delay between two ADC samples exceeded 30% of the average droplet generation period, the following erroneous droplets were excluded from the logs and use in the droplet feedback PIDs. It improved fluidic stability, but in the case of random OS delays, at the cost of up to 10% of generated droplets not getting logged (losses were lower with lower generation rates). Likewise, in the case of `get_nowait()` delay, if it exceeded 30% of the average droplet generation period, the irregular droplet measurement would be excluded from the log and PID feedback.

B. System evaluation

After assembly, programming, and fine-tuning through preliminary testing, connection between a laptop and the CogniFlow-Drop device was established through a Wi-Fi hotspot to validate the communication interface. After a successful connection, the interface effectively transmitted and received message packets every ~ 100 ms, artificially delayed with eCAL message polling delay on the RPI. Other functional tests with the remote control included:

- initiating setup calibration (tied to variables: chip position/angle, chip variant, liquids used),
- initiating droplet generation with desired size and generation rate,
- initiating droplet size (V) target series test,
- initiating droplet generation rate (F) target series test.

Each feature of the GUI (Fig. 8) was proceeded to be used as remote initiator for the following system evaluation steps.

1) Results of droplet size and frequency control test series

During experimentation some target droplet size and generation frequency combinations did not yield droplets regardless of having used selective ranging – highlighted on

TABLE VI-VII. Overall, chip C showed lower ranges for both sizes and generation rates. Additionally, chip C behaved uniquely between voltage and frequency series, as the combination of (400 Hz; 3.4 V) in voltage series did not yield droplets, but in contrast, was unexpectedly stable in frequency series. This hinted to higher sensitivity to size target alterations during droplet production combined with how current droplet feedback PID handles high instability.

Target series over all four sets, named in Section III-B-1, resulted in averaged droplet size errors, seen on Fig. 24, which indicated higher accuracy for droplet size control with chip B, more specifically with droplet size (V) series when the marked outlier of ChipB-Fseries was taken into account. With an average error of -0.06% , ChipB-Vseries obtained averaged sizing errors between $+2.86$ to -1.79% . Contrast of accuracy of reaching average target size, can be seen on droplet capture graphs between ChipB-Vseries (row 4 from TABLE IV) and ChipC-Vseries (row 2 from TABLE VI) on Fig. 24/b and Fig 24/c respectively, with target sizes per sample, segmentally overlayed as orange horizontal lines. Target size errors on Fig. 24/b were $[+0.35; -1.79; -1.56] \%$ respectively. Together with the fixed frequency (200 Hz) accompanied with varying droplet size targets, frequency errors of $[+0.88; -2.00; -5.63] \%$, respectively, showed a decreasing total output volume with the combined error staying further and further below the targets. Target errors on Fig 24/c were $[+5.62; +2.88; -2.03; -7.24] \%$ respectively. For the comparably reduced functional size range that channel geometry of chip C offered, target size control did not yield droplets in all requested sizes. This could largely be contributed to inclinations caused by the channel geometry. This was made clear from its accompanied averaged frequency target errors of $[-1.99; +2.65; -0.73; -0.30] \%$ respectively, which did not follow the pattern of size errors. The secondary contributor was attributed to the erroneous droplet size averaging caused by what was shown on Fig. 20. Due to alterations in perception of captured droplet sizes, calibration for chip C test series had been segmentally impacted where droplet waveforms exhibited shapes more predisposed to peak losses.

Additionally, averaged droplet generation rate errors, seen on Fig. 25/a, again indicated higher accuracy for droplet rate control with chip B, more specifically with generation rate (F) series when marked outliers of ChipC-Fseries were taken into account. With an average error of $+0.94\%$, ChipB-Fseries obtained averaged generation rate errors between $+3.62$ to -1.65% . Contrast of accuracy between the best and the worst captured series of reaching average target generation rate, can be seen on droplet capture graphs between ChipB-Fseries (row 2 from TABLE V) and ChipC-Fseries (row 1 from TABLE VII) on Fig. 25/b and Fig. 25/c respectively, with target sizes per sample, segmentally overlayed as orange horizontal lines. Target averaged frequency errors, with chip B, on Fig. 25/b were $[-1.43; +0.86; +1.83; +1.67] \%$ respectively. Together with the fixed

size target (2.8 V) accompanied with the example varying frequency targets, averaged size errors of [+0.50; -0.61; +0.61; +0.14] % respectively, showed no explicit relationship between size and frequency errors. This alluded to lesser impact from frequency alterations during droplet generation, in other words, lesser impact from changes in oil pressure rather than water pressure. Target averaged frequency errors, with chip C, on Fig. 25/c were [+1.93; +4.11; +6.78; -5.11; -20.61] % with accompanying size target (3.2 V) errors of [+5.91; -0.06; -1.56; -1.09; -1.13] %, respectively, showing little correlation in comparison. This example showed large fluctuations in periodicity, but small droplet size variation (similar to Fig. 24/c from ChipC-Vseries).

2) *Measurement results for coefficient of variability of generated droplets*

a) *Droplet size data (PD voltage discretized with the ADC) from consecutive droplet size and frequency target series*

V and F series performed in Section IV-B-1 resulted in averaged droplet size CVs represented on Fig. 26/a and averaged droplet generation rate CVs represented on Fig. 26/b. Medians of averaged CVs from Fig. 26/a, [6.83; 6.33; 5.78; 6.84] %, respectively, showed that while the measured droplet sizes in tests with chip C were off noticeably more than with chip B, the size stability can be better. However, minimum CVs [3.10; 3.30; 4.40; 3.60] % showed favorability towards chip B. While some maximum CVs reached over 10%, more significant reasons for the larger instabilities stemmed from the chosen pressure combinations working less favorably with chosen chip geometries. From the averaged droplet generation rate results on Fig. 26/b, the difference between chip B and C was hard to mistake. As the CVs between size and rate for chip C, have a noticeable difference in scale, it was evident that the generation frequency of droplets does not inherently link to droplet size in a pulsatile pressure-based pumping system.

Further analysis of target F series provided relationships between the generation rate to generation rate CVs at each obtained average frequency level with standard deviation (SD) bars and between the target generation rate to column averaged SDs (SD averaging for chip C was done conditionally, further explained in ESI S4), for chips B and C respectively on Fig. 27/a and Fig. 27/b (numeric details in ESI S4, TABLE I-IV). Generation rate CVs for chip C revealed behavioral outliers with target size and rate combinations in row 1 of TABLE VII (while producing droplets in a stable manner with size CVs < 10%, the frequency CVs were well above 25%). By omitting the TABLE VII row 1 CVs and SDs from comparison between chip variants, the general rule of increasing SD with increasing

generation rate becomes noticeable. By having excluded row 1 SDs also from averaging of SDs, chip B and C generation rate averaged SDs (\overline{SD}) showed analogous trends. Both show the highest correlation to exponential relationships. Additionally, for both chip types, cropped \overline{SD} s revealed high linear correlation regions up to the second highest tested respective generation rate targets (Fig. 27) which in terms of generation rates would narrow down on the stable frequency region of use for that specific chip geometry and fluidic phase combination. Between the observed initial and cropped data, beyond a certain generation rate, the behavior of frequency stability deteriorates from linear into exponential regime. The possible causes of which could be 1) stability limits, inherited from FFD channel design in combination with pulsatile flow and fluid phase properties, 2) hardware and/or software limits, RPI's droplet interpretation loop delays introducing increasing number of erroneous readings.

b) *Droplet size data (PD voltage discretized with the ADC) from single shot droplet size and frequency targets*

Using chip B with different calibration (chip position slightly tilted in the light tower), one of the better examples with lowest target error in combination with the lowest droplet size CV (400 Hz, 4.4 V) achieved, can be seen on Fig. 28 with graphed droplet sizes and generation rates respectively. From the size dataset on Fig. 28/a, the CV% was calculated to be 1.77% with a percentage error from target droplet size of +0.27%. From frequency dataset on Fig. 28/b, the CV% was calculated to be 6.67% with a percentage error from target droplet generation rate of +0.22%.

c) *Droplet size data (microscope camera → ImageJ) from single shot pressure targets*

Droplets were collected from tests with droplet feedback PIDs disabled to obtain a baseline. Tests were done with fixed water pressure at 9 kPa and several oil pressure targets in the range of 9 kPa – 12 kPa, ran over 90 seconds, where oil pressure at 12 kPa yielded the best results with 7.7% CV, with a spread of cross-sectional areas shown on Fig. 29. Average cross-sectional surface area of recorded droplets was measured 13 558.9 μm^2 , translating into an average planar diameter of 131.4 μm when droplets were flattened in the imaging slide. A sample from a series of images taken of droplets in the droplet imaging slide can be seen on Fig. 30.

V. FUTURE PERSPECTIVE

One of the core principles of the CogniFlow-Drop system is modularity. This modularity opens the way to various future upgrades: use-cases enabled by additional modules

(Section V-A), as well as possible upgrades to the core modules (Section V-B).

A. Application use cases

- Inline imaging cytometry: The addition of a high-speed camera/detection module (and ideally a cell incubation module) could enable inline imaging cytometry.
- Cell sorting: The addition of a droplet sorting module, together with the aforementioned imaging cytometry modules, could enable droplet-based cell sorting for further downstream processing of select cells or cell lines. The single-cell resolution and chemical isolation provided by droplets could greatly increase the throughput, while reducing reagent and sample waste compared to current state-of-the-art flow cytometry setups.

B. Possible upgrades to the prototype system

- To improve the droplet capture rate and reliability, an additional ESP32, or a similar low-cost device with an SPI bus and two cores, could be placed between the RPI and ADC to take over task 3 from the RPI. Additionally, the added computational power could enable more complex waveform analysis (e.g., waveform slope measurement and droplet lensing effect detection).
- To improve the droplet size and generation frequency control accuracy and fault tolerance, machine learning models could be implemented on the RPI.
- To improve automation, the following features could contribute: self-priming, self-cleaning, auto-chip-positioner, auto-pinhole-positioner, self-analyzing (e.g., detection of blockages or leaks in the fluidics module), auto-focusing, and auto-calibration-ranging.
- To improve the user interface, the GUI, after calibration, could offer feasible droplet size and generation frequency ranges, with highlighted combinations yielding the best CV% for that specific chip and position. Furthermore, by user request, the GUI could poll captured waveform samples during operation.
- To correlate relatively inexpensively and rapidly measured droplet sizes from their shadows to real droplet volume, a secondary in-line camera setup could be joined in the communication line over eCAL. To image droplets, as proposed in Section V-A, during cytometry.

VI. CONCLUSIONS

A proof-of-concept prototype of an integrated, modular system for automated aqueous droplet generation with high monodispersity was presented. The system measured droplet

sizes and generation rates using a visible spectrum LED-photodiode setup aligned with the cross-junction of the FFD, converting the droplet's shadow to voltage. Resulting peak-to-peak voltages were correlated with relative size of the droplet whereas the time between the beginnings of droplets were used to obtain the generation rate. We reported on the assembly and the underlying working principle, as well as the experimental evaluation of the performance of the prototype, both on a module level and system level. Module-level evaluation and comparison to reference syringe pumps indicated a 12 times reduction in pressure stabilization times. The system-level evaluation proved that the system was capable of repeatedly generating droplets with stability comparable to other state-of-the-art droplet generation systems. Droplet generation stability was proven over 2 different carrier media and 3 different junction geometries in total. The lowest relative droplet size CV% recorded was 1.77% (~ 0.00031 PDI) using Chip B with fluid phase combination B. With droplets controllably generated in tested relative size targets between 2.0 to 4.4 V, polydisperse (PDI > 0.1) droplets with a stable size distribution can also be generated. Unique characteristics from relationships between droplet size/generation rate and chip geometry were made observable through automated calibration and parameter target test series with different chips. Conditional droplet generation rate analysis also revealed high linear correlation regions for the "SD of the generation rate" with the "target rate" for chips B and C, from 200 Hz up to 600 Hz and 500 Hz respectively. In conclusion, the presented prototype system has comparable droplet generation performance metrics to other state-of-the-art droplet generation setups, but offers several advantages: 1) modularity, integration, wireless communication and the option to run from battery power, enabling portability; 2) affordability; 3) automation and ease of use, increasing repeatability of results and allowing transfer of protocols between labs, as well as reducing manual workloads; 4) user-friendly (re-)calibration of chip alignment.

VII. ACKNOWLEDGEMENTS

The authors would like to thank researcher Simona Bartkova (Department of Chemistry and Biotechnology) from Tallinn University of Technology with their assistance with droplet imaging and droplet generation chip fabrication methods and tools. The perfluoropolyether (PFPE)-poly(ethylene glycol) (PEG)-PFPE triblock surfactant, used with fluorinated oil, was a kind gift from Professor Piotr Garstecki from the Institute of Physical Chemistry, Polish Academy of Sciences. Furthermore, the authors would like to express their gratitude to the Estonian Research Council, European Commission, as well as Tallinn University of Technology for the funding provided.

REFERENCES

- [1] T. S. Kaminski, O. Scheler, and P. Garstecki, "Droplet microfluidics for microbiology: techniques, applications and challenges," *Lab Chip*, vol. 16, no. 12, pp. 2168–2187, 2016, doi: 10.1039/C6LC00367B.
- [2] W. Postek, P. Gargulinski, O. Scheler, T. S. Kaminski, and P. Garstecki, "Microfluidic screening of antibiotic susceptibility at a single-cell level shows the inoculum effect of cefotaxime on *E. coli*," *Lab Chip*, vol. 18, no. 23, pp. 3668–3677, 2018, doi: 10.1039/C8LC00916C.
- [3] O. Scheler *et al.*, "Droplet-based digital antibiotic susceptibility screen reveals single-cell clonal heteroresistance in an isogenic bacterial population," *Sci Rep*, vol. 10, no. 1, p. 3282, Feb. 2020, doi: 10.1038/s41598-020-60381-z.
- [4] K. Pärnamets *et al.*, "Optical detection methods for high-throughput fluorescent droplet microflow cytometry," *Micromachines (Basel)*, vol. 12, no. 3, 2021, doi: 10.3390/mi12030345.
- [5] M. Li, H. Liu, S. Zhuang, and K. Goda, "Droplet flow cytometry for single-cell analysis," *RSC Adv*, vol. 11, no. 34, pp. 20944–20960, Jun. 2021, doi: 10.1039/D1RA02636D.
- [6] Y. Ding, P. D. Howes, and A. J. Demello, "Recent advances in droplet microfluidics," *Anal Chem*, vol. 92, no. 1, pp. 132–149, Jan. 2020, doi: 10.1021/ACS.ANALCHEM.9B05047/ASSET/IMAGES/LARGE/AC9B05047_0009.JPEG.
- [7] S. Stavrakis, G. Holzner, J. Choo, and A. DeMello, "High-throughput microfluidic imaging flow cytometry," *Curr Opin Biotechnol*, vol. 55, pp. 36–43, Feb. 2019, doi: 10.1016/j.copbio.2018.08.002.
- [8] K. Pärnamets *et al.*, "Optical Detection Methods for High-Throughput Fluorescent Droplet Microflow Cytometry," *Micromachines (Basel)*, vol. 12, no. 3, p. 345, Mar. 2021, doi: 10.3390/mi12030345.
- [9] S. Stavrakis, G. Holzner, J. Choo, and A. deMello, "High-throughput microfluidic imaging flow cytometry," *Curr Opin Biotechnol*, vol. 55, pp. 36–43, Feb. 2019, doi: 10.1016/J.COPBIO.2018.08.002.
- [10] C. Cha *et al.*, "Microfluidics-Assisted Fabrication of Gelatin-Silica Core–Shell Microgels for Injectable Tissue Constructs," *Biomacromolecules*, vol. 15, no. 1, p. 283, Jan. 2014, doi: 10.1021/BM401533Y.
- [11] R. Samanipour, Z. Wang, A. Ahmadi, and K. Kim, "Experimental and computational study of microfluidic flow-focusing generation of gelatin methacrylate hydrogel droplets," *J Appl Polym Sci*, vol. 133, no. 29, Aug. 2016, doi: 10.1002/APP.43701.
- [12] W. Zeng, H. Fu, and S. Li, "Characterization of the pressure-driven flows for droplet microfluidics," *IET Conference Publications*, vol. 2018, no. CP743, pp. 309–313, 2018, doi: 10.1049/CP.2018.0090/CITE/REFWORKS.
- [13] W. Zeng *et al.*, "Precise monodisperse droplet generation by pressure-driven microfluidic flows," *Chem Eng Sci*, vol. 248, p. 117206, Feb. 2022, doi: 10.1016/J.CES.2021.117206.
- [14] X. Duan, Z. Zheng, Y. Luo, and C. Song, "Closed-loop feedback control for droplet-based microfluidics: a characteristic investigation on passive and on-demand droplet generation," no. January, p. 31, 2023, doi: 10.1117/12.2666602.
- [15] W. Zeng and H. Fu, "Precise monodisperse droplet production in a flow-focusing microdroplet generator," *Chemical Engineering Research and Design*, vol. 160, pp. 321–325, Aug. 2020, doi: 10.1016/J.CHERD.2020.06.002.
- [16] N. Wang, R. Liu, N. Asmare, C.-H. Chu, O. Civelekoglu, and A. F. Sarioglu, "Lab on a Chip Closed-loop feedback control of microfluidic cell manipulation via deep-learning integrated sensor networks †," vol. 21, 2021, doi: 10.1039/d1lc00076d.
- [17] E. C. Yeh, C. C. Fu, L. Hu, R. Thakur, J. Feng, and L. P. Lee, "Self-powered integrated microfluidic point-of-care low-cost enabling (SIMPLE) chip," *Sci Adv*, vol. 3, no. 3, p. e1501645, Mar. 2017, doi: 10.1126/sciadv.1501645.
- [18] D. F. Crawford, C. A. Smith, and G. Whyte, "Image-based closed-loop feedback for highly monodispersed microdroplet production," *Sci Rep*, vol. 7, no. 1, pp. 1–9, 2017, doi: 10.1038/s41598-017-11254-5.
- [19] B. Miller *et al.*, "Manipulation of microfluidic droplets," EP2411148B1, 2010
- [20] B. van Elburg, G. Collado-Lara, G.-W. Bruggert, T. Segers, M. Versluis, and G. Lajoinie, "Feedback-controlled microbubble generator producing one million monodisperse bubbles per second," *Review of Scientific Instruments*, vol. 92, no. 3, p. 035110, Mar. 2021, doi: 10.1063/5.0032140.
- [21] N. Gyimah, O. Scheler, T. Rang, and T. Pardy, "Can 3d printing bring droplet microfluidics to every lab?—a systematic review," *Micromachines (Basel)*, vol. 12, no. 3, 2021, doi: 10.3390/mi12030339.
- [22] TalTech-LoC, "hw-open-fluidic-infra." <https://github.com/taltechloc/hw-open-fluidic-infra> (accessed May 16, 2023).
- [23] N. Gyimah, O. Scheler, T. Rang, and T. Pardy, "Digital twin for controlled generation of water-in-oil microdroplets with required size," in *2022 23rd International Conference on Thermal, Mechanical and Multi-Physics Simulation and Experiments in Microelectronics and Microsystems (EuroSimE)*, IEEE, Apr. 2022, pp. 1–7. doi: 10.1109/EuroSimE54907.2022.9758876.

- [24] N. Gyimah, R. Joemaa, K. Parnamets, O. Scheler, T. Rang, and T. Pardy, "PID Controller Tuning Optimization Using Genetic Algorithm for Droplet Size Control in Microfluidics," in *2022 18th Biennial Baltic Electronics Conference (BEC)*, IEEE, Oct. 2022, pp. 1–6. doi: 10.1109/BEC56180.2022.9935596.
- [25] R. Joemaa, M. Grosberg, T. Rang, and T. Pardy, "Low-cost, portable dual-channel pressure pump for droplet microfluidics," in *2022 45th Jubilee International Convention on Information, Communication and Electronic Technology (MIPRO)*, IEEE, May 2022, pp. 205–211. doi: 10.23919/MIPRO55190.2022.9803371.
- [26] M. Grosberg, R. Jõemaa, P. Tamas, and T. Rang, "Wireless microfluidic dual-channel pressure pump," P202200009, 2022 [Online]. Available: <https://www.etis.ee/Portal/IndustrialProperties/Display/353426b9-f02b-44b2-b581-e8f21363157a>
- [27] K. Ashraf, Y. Le Moullec, T. Pardy, and T. Rang, "Model-based System Architecture for Event-triggered Wireless Control of Bio-analytical Devices," in *2021 24th Euromicro Conference on Digital System Design (DSD)*, IEEE, Sep. 2021, pp. 465–471. doi: 10.1109/DSD53832.2021.00076.
- [28] Alphabet Inc., "Protocol Buffers | Google Developers," 2022. <https://developers.google.com/protocol-buffers/docs/reference/overview> (accessed Oct. 31, 2022).
- [29] Eclipse, "Welcome to Eclipse eCAL™ — Eclipse eCAL™ documentation," 2022. <https://eclipse-ecal.github.io/ecal/> (accessed Oct. 31, 2022).
- [30] K. Parnamets, A. Koel, T. Pardy, and T. Rang, "Open Source Hardware Cost-Effective Imaging Sensors for High-Throughput Droplet Microfluidic Systems," in *2022 26th International Conference Electronics*, IEEE, Jun. 2022, pp. 1–6. doi: 10.1109/IEEECONF55059.2022.9810383.
- [31] N. A. Prabatama, R. Joemaa, K. Hegedus, and T. Pardy, "Low-cost open-source flow velocity sensor for droplet generators," in *2022 18th Biennial Baltic Electronics Conference (BEC)*, IEEE, Oct. 2022, pp. 1–4. doi: 10.1109/BEC56180.2022.9935606.
- [32] J. Caldwell, "An IMPORTANT NOTICE at the end of this TI reference design addresses authorized use, intellectual property matters and other important disclaimers and information," 2014, Accessed: May 12, 2023. [Online]. Available: www.ti.com
- [33] O. Scheler, T. S. Kaminski, A. Ruzszczak, and P. Garstecki, "Dodecylresorufin (C12R) Outperforms Resorufin in Microdroplet Bacterial Assays," *ACS Appl Mater Interfaces*, vol. 8, no. 18, pp. 11318–11325, May 2016, doi: 10.1021/acsami.6b02360.
- [34] TalTech-LoC, "hw-mvp-chip," 2020. <https://github.com/taltechloc/hw-mvp-chip> (accessed Sep. 21, 2022).
- [35] B. Group, "BioMEMS Group," 2022. <https://biomeems.hu/> (accessed Oct. 31, 2022).
- [36] W. Zeng, S. Li, and Z. Wang, "Closed-loop feedback control of droplet formation in a T-junction microdroplet generator," *Sens Actuators A Phys*, vol. 233, pp. 542–547, 2015, doi: 10.1016/j.sna.2015.08.002.
- [37] Y. Xie, A. J. Dixon, J. M. R. Rickel, A. L. Klibanov, and J. A. Hossack, "Closed-loop feedback control of microbubble diameter from a flow-focusing microfluidic device," *Biomicrofluidics*, vol. 14, no. 3, p. 034101, May 2020, doi: 10.1063/5.0005205.
- [38] S. Motaghi, M. Nazari, N. Sepehri, and A. Mahdavi, "Control of droplet size in a two-phase microchannel using PID controller: A novel experimental study," *Amirkabir Journal of Mechanical Engineering Amirkabir J. Mech. Eng.*, vol. 53, no. 7, pp. 1013–1016, 2021, doi: 10.22060/mej.2020.18250.6783.
- [39] H. Fu, W. Zeng, S. Li, and S. Yuan, "Electrical-detection droplet microfluidic closed-loop control system for precise droplet production," *Sens Actuators A Phys*, vol. 267, pp. 142–149, 2017, doi: 10.1016/j.sna.2017.09.043.



RAUNO JÕEMAA was born in Estonia, in 1991 and is currently a PhD student at the Thomas Johann Seebeck Department of Electronics and a junior researcher at the Department of Chemistry and Biotechnologies in Tallinn University of Technology. He received his bachelor's degree in Electronics and Bionics and master's degree in Communicative Electronics, from Tallinn University of Technology. His research interests include electronics and microfluidics.



NAFISAT GYIMAH received a B.S. in electrical and electronic engineering from Kwame Nkrumah University of Technology in Kumasi, Ghana, in 2013, and an M.S. in communicative electronics from Tallinn University of Technology in Tallinn, Estonia, in 2020. She is currently pursuing a Ph.D. at the Tallinn University of Technology in high-speed droplet microfluidics sorting and encapsulation. Her research interests

include lab-on-a-chip, droplet microfluidic system control, and flow control simulations using computational fluid dynamics (CFD). From November 2021 to January 2022, she worked at SelfDiagnostics Deutschland GmbH on the thermal and electrical characterization of SARS-CoV2 microfluidic Multitest kits. She was a cognitronics engineer at the Tallinn University of Technology from June to December 2020.)



KANWAL ASHRAF is a PhD student at Tallinn University of Technology, Estonia. Kanwal received her Joint-International master's degree in Smart System Integration from Heriot-Watt University, UK, USN, Norway and BME, Hungary in 2020. She holds a bachelor's degree in electrical engineering from the University of the Punjab, Pakistan. Her research interests include the application of Wireless communication in CPSs and Co-Design of Wireless Networked Control Systems for bioanalytical applications.



KAISER PÄRNAMETS (Graduate Student Member, IEEE) was born in Tallinn, Estonia, in January 1989. He received Bachelor of Science in Engineering in 2013 and Master of Science in Engineering in 2016 from the Tallinn University of Technology. In 2016 he started his PhD studies at Tallinn University of Technology. In the years of 2014 to 2017 he was hardware engineer in the electronics industry and since 2018 he has been an electronics lecturer for Bachelor and Master students. His research interests include Lab-on-a-chip and microfluidics.



ALEXANDER ZAFT, born in 1997, completed his Bachelors and master's degree in computer science at the University of Würzburg, Germany in 2019 and 2022 respectively. During the summer of 2022, he joined Tallinn University of Technology, Lab-on-a-Chip group, as an intern. Since November 2022, he is a software engineer at the Heinz-Maier-Leibnitz Zentrum in Garching, Germany.



OTT SCHELER received his PhD in Biotechnology from University of Tartu, Estonia in 2012. Did his postdoc in microfluidics at Institute of physical chemistry, Polish Academy of Sciences 2014-2018. After that he joined Tallinn University of Technology where he is currently associate professor in microfluidics at the Department of chemistry and biotechnology. His research interests are microfluidics, microbiology, biotechnology.



TOOMAS RANG (Senior Member, IEEE) received the PhD degree in semiconductor electronics from the Hungarian Academy of Sciences, 1981. He is currently the Professor Emeritus at the Thomas Johann Seebeck Department of Electronics and senior research fellow at the Department of Chemistry and Biotechnologies at Tallinn University of Technology, Estonia. The research activities relate to R&D activities in the field of applied microfluidics approaches for Lab-on-Chip applications. He has supervised 15 PhD students and has fulfilled the PI position in several European and domestic research and industrial projects. He is the initiator and today the honor chairman of Baltic Electronics Conferences (BEC) series in 1987, supported by IEEE since 1996.



TAMÁS PARDY (Member, IEEE) received the M.Sc. degree in info-bionics engineering from Peter Pazmany Catholic University, Budapest, Hungary, in 2014, and the Ph.D. degree in electronics and telecommunication from Tallinn University of Technology, Tallinn, Estonia, in 2018. He is currently a senior researcher at Tallinn University of Technology. He has supervised 1 PhD thesis and 5 M.Sc. theses and has authored or co-authored over 20 scientific publications. His research interests include flow- and temperature-control of Lab-on-a-Chip devices.

Images, figures, and tables:

TABLE I OVERVIEW OF THE STATE-OF-THE-ART FEEDBACK-CONTROLLED DROPLET GENERATORS COMPARED TO OUR NOVELTY

Reference	Flow actuation	Flow control algorithm	Continuous phase fluid	Discrete phase fluid	Monodispersity (CV%)	Flow sensor	Integrated & standalone?	Communication
[14]	Programmable pressure pump	PID controller	Silicone oil	Calcium chloride solution	<7.6%	N/A	No	USB
[13]	Pressure pump	PI controller	Silicone oil	Water	2%	Pressure sensor		
[18]	Pressure pump	PID controller	Fluorinated oil	Water	0.32%	N/A		
[15]	Pressure pump	PID controller	Silicone oil	Water	N/A	N/A		
[36]	Microvalves	PI controller	Silicone oil	Water	No steady state errors	N/A		
[37]	Syringe pump, and gas regulator	PI controller	BSA in NaCl	Nitrogen	N/A	N/A		
[38]	Syringe pump	PID controller	Paraffin + 10% Span80,	Water	RMSE reduces from 3.4 to 0.48	N/A		
[39]	Pressure pump	Pi controller	Silicone oil	Water	N/A	Pressure sensor		
[20]	Gas-driven	Dual-PID (pressure, bubble size) control	Water + Tween80	C ₄ F ₁₀ /CO ₂ gas	N/A	Laser-photodiode		
Our work	Dual piezo pumps	Dual -PID (pressure, droplet size/gen. rate) control	HFE7500/ mineral oil + tri-block surfactant	Water	5-10%	LED-photodiode	Yes	WLAN

TABLE II MASTER MOULD DESIGN PARAMETERS FOR MICROFLUIDIC DROPLET GENERATOR CHIPS

Chip variant	A	B	C
Junction width [mm]	90	125	280
Junction angle of entry [°]	90	38.33	
Oil inlet width [mm]	360		
Water inlet width [mm]	6		
Outlet width [mm]	0.6		
Number of filters	2		

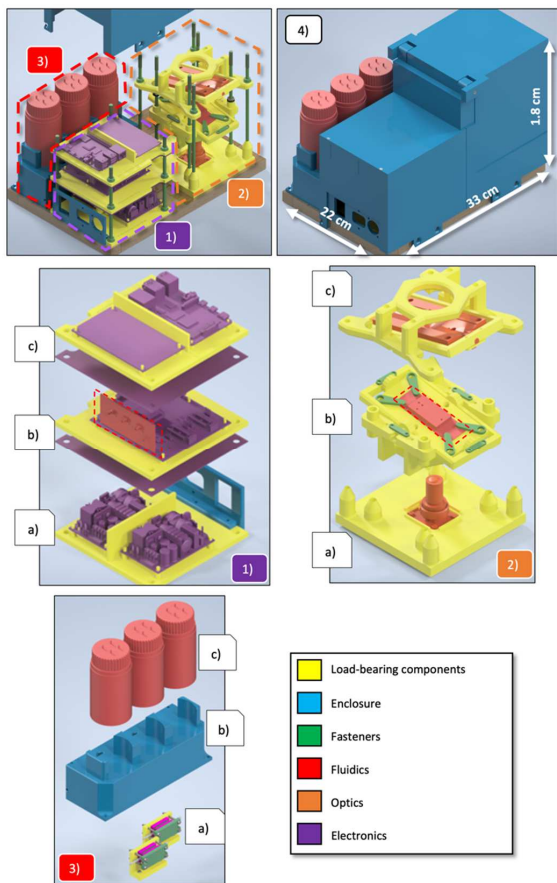


FIGURE 2. Prototype assembly, consisting of modules: (1) electronics module consisting of the power supply stage (a), the pump driver and pressure sensor stage (b) and the stage that contained the RPi4B as well as the ADC and filtering circuit for the optical sensor (c), plus the corresponding copper shielding plates. (2) The sensorics module, consisting of the base stage with the photodiode and lens (a), the microfluidic chip mount stage (b) and the light source mount stage (c). (3) fluidics module, which included L-mounts for the pumps (a) and a foam-padded enclosure (b), as well as (c) sample, reagent, and product collection containers. (4) The enclosure with 3D printed internal and external walls, as well as a wooden base plate to which all modules were mounted for stability. The M5 bolts mounting the stages of the modules are hidden in the close-up explosion views (1-3).

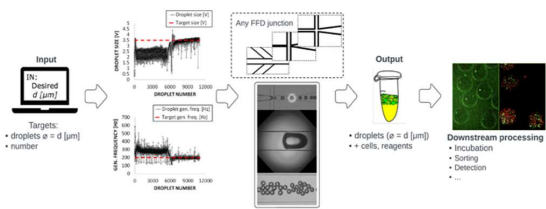


FIGURE 1. CogniFlow-Drop concept: droplets with user-defined process and dimensional parameters are generated automatically from reagents and samples needed by the user, with minimal user interaction, in a compact, standalone device. These can then be collected for further downstream processing, e.g., incubation and detection.

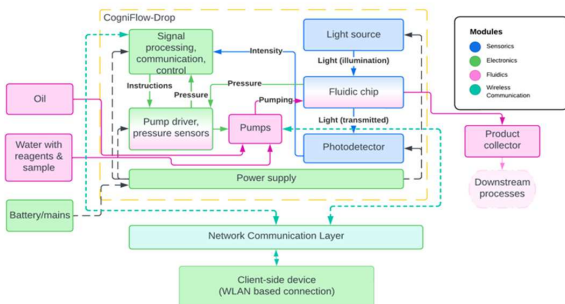


FIGURE 3. CogniFlow-Drop device: in the device, oil-water droplets of a user-defined size are generated, encapsulating cells and reagents of given kinds. The regulation of droplet sizes takes place by means of simultaneous pressure and flow rate control, resulting in a high control precision (in terms of CV% [coefficient of variation] of droplet diameter). The system implements distributed wireless control in an event-triggered manner [27].

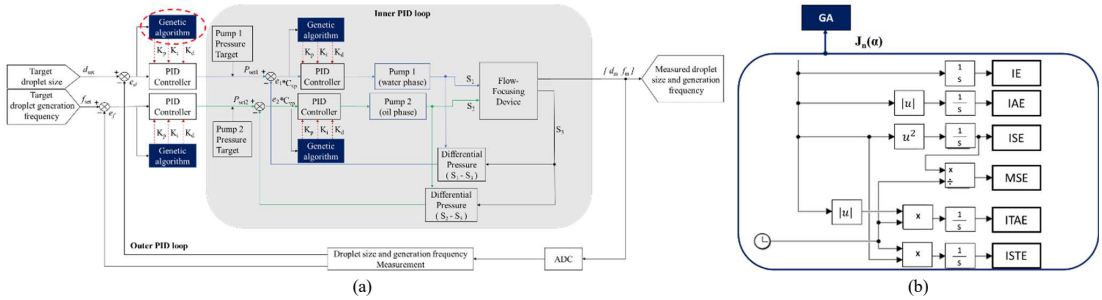


FIGURE 4. a) Structure of dual-loop PID control strategy. The inner feedback loop reduced pressure fluctuations, improved accuracy, and speed of reaching target pressure level. Outer feedback loop adjusted droplet sizes and generation rates based on optical flow rate measurement from module 2 in Fig. 2; b) Structure of PID tuning method with six objective function criteria obtained from using genetic algorithm.

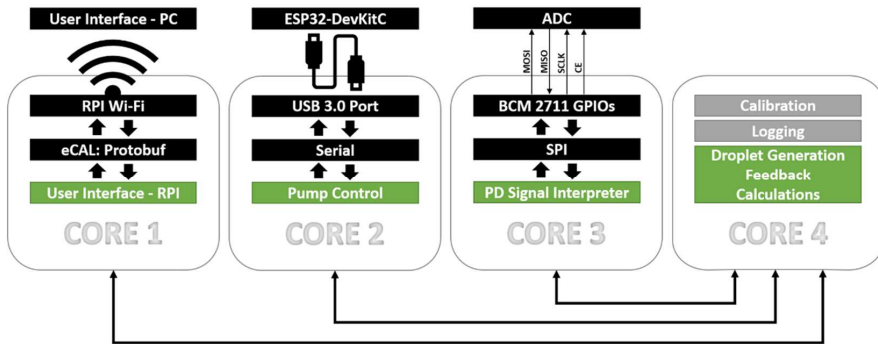


FIGURE 5. Four main tasks (in green) of the system controller were made to run concurrently on separate cores. Core 1 handled user commands received over local network using eCAL API with Protobuf format. Core 2 communicated with the pumping system's control board ESP32-DevKitC via serial protocol. Core 3 received discretized photodiode signal from an ADC in SPI protocol format through Raspberry Pi's BCM 2711 GPIOs and using it to measure running droplet generation parameters. Core 4 managed commands and information from the other three cores to start, stabilize and end droplet generation.

```

1  syntax = "proto3";
2
3  package proto_message;
4
5  message spec
6  {
7    float dsize      = 1;
8    uint32 id        = 2;
9    float drate      = 3;
10   string status     = 4;
11   uint32 command   = 5;
12   string deviceName = 6;
13   string chipName  = 7;
14 }
15
16
174 # set message content
175 specific.dsize = droptime
176 specific.id = message_id
177 specific.drate = input_rate
178 specific.status = status
179 specific.command = command_nr
180 specific.deviceName = device_name
181 specific.chipName = chip_name
182 print("Status is {}".format(specific.status))
183 if command_nr != 1:
184     print("Droplet size {} and rate {}".format(specific.dsize, specific.drate))
185     if chip_name != "None":
186         print("Chip under test: {}".format(specific.chipName))
187     else:
188         print("Chip Name is not defined")
189
190 # send message
191 while ecal_core.ok() and specific.id < repeat_msg:
192     if command_nr != 1:
193         if inputs_in_range is True:
194             pub.send(specific)
195             print("Successful transmission iteration {}".format(specific.id))
    
```

FIGURE 6. Communication interface implementation. (a) Data Structure for CogniFlow-Drop: droplet size (dsize), message id, droplet generation rate (drate), sender status/role, operational command, sender device name, and saved calibration parameters named with corresponding microfluidic chip. (b) instances of eCAL-based message transmissions.

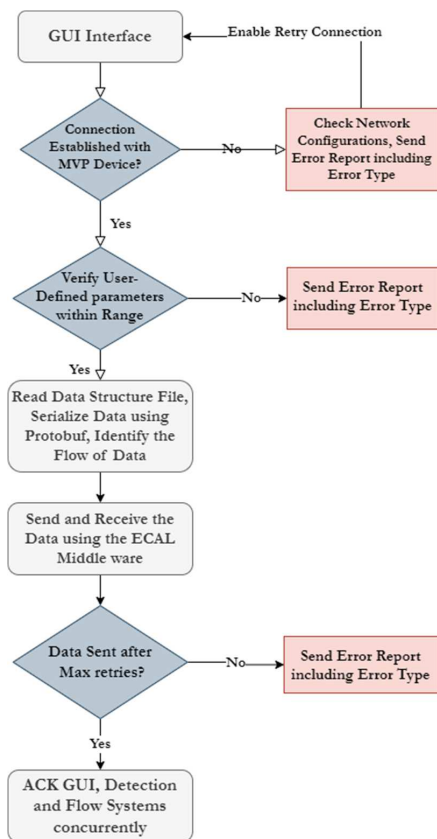


FIGURE 7. Implementation of the communication interface, data transmission, reception, verification, and a Graphical User Interface for accessibility.

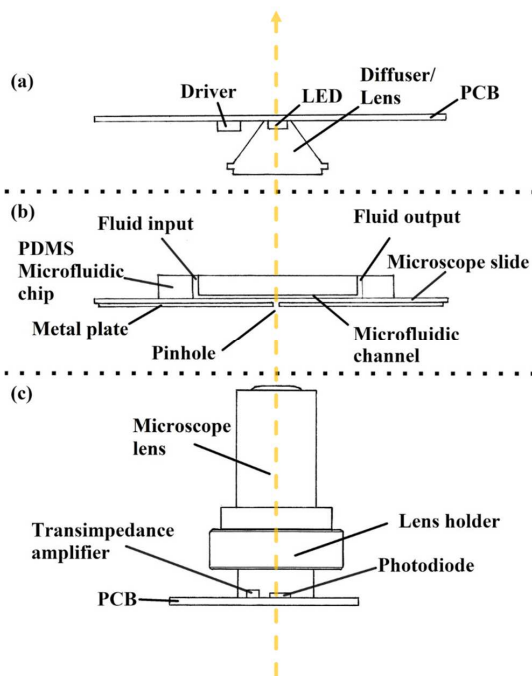


FIGURE 9. Cross-section of the microfluidic droplet measurement system with parts aligned to the axis marked with a dashed yellow line. (a) An LED with an LED driver is soldered to a printed circuit board (PCB) that is used to illuminate the microfluidic chip. In addition, a matted lens is used to diffuse and focus the light. (b) A PDMS-glass microfluidic chip is mounted to the chip holder with a metal plate with a micro-drilled pinhole positioned underneath. (c) A non-imaging photodiode collects light, while a high gain transimpedance amplifier is added nearby. On a custom PCB, components are mounted along with a lens holder and microscope lens.

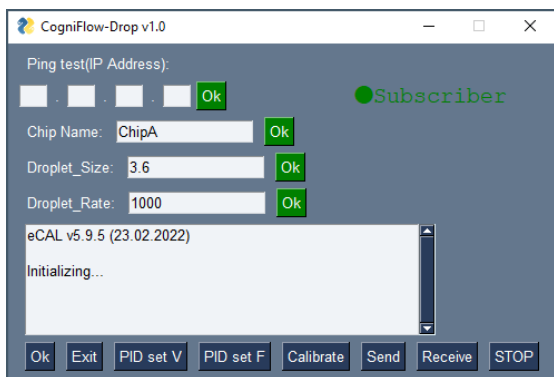


FIGURE 8. ECAL based Graphical User Interface (CogniFlow-Drop v1.0).

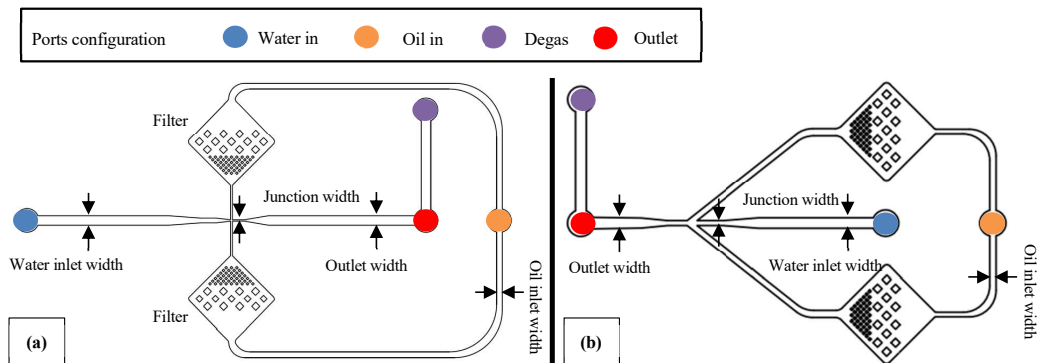


FIGURE 10. Parameterized flow-focusing device for controlled droplet generation. Oil inlet is split equally and filtered through micropillar arrays to prevent impurities on the oil line from clogging the junction. The outlet has a 1 ml gas spring attached to smoothen out flow rate fluctuations coming from the pump. Chip variant A/B (a) had a 90-degree entry in the flow-focusing junction, whereas variant C (b) had a 38.33-degree entry angle and a shorter outlet length. There was no other difference between the 3 chip variants apart from the junction width. Water inlet, outlet and oil line widths were the same.

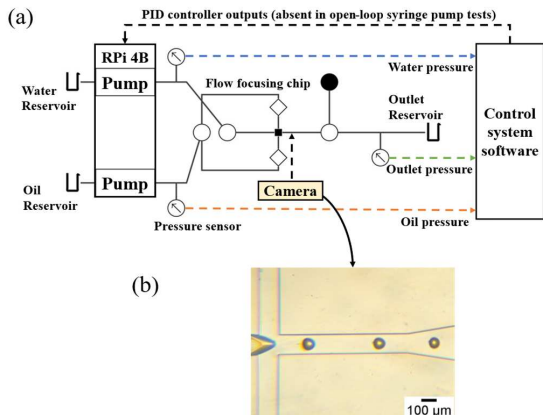


FIGURE 11. Schematic diagram for the experimental setup of droplet microfluidics system: (a) block diagram of the control system, (b) camera image of the droplet generator junction.

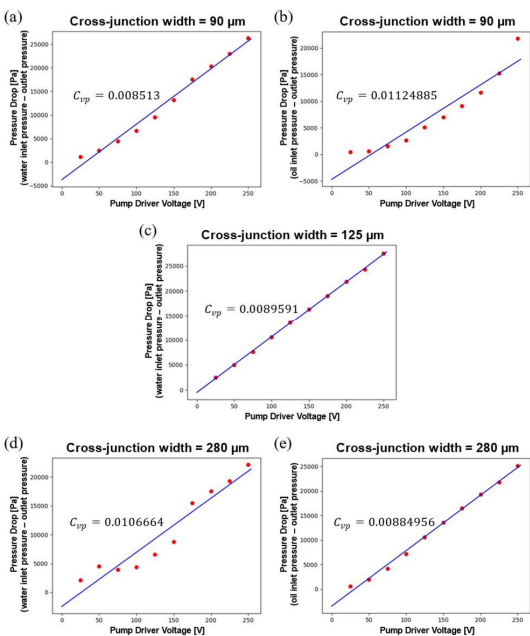


FIGURE 12. Pressure drops vs. peak-to-peak voltages of the piezoelectric micropump for the chip variants with cross-junction widths: 90 μm with DIW (a) and with oil A (b); 125 μm with DIW (c); and 280 μm with DIW (d) and with oil A (e). Driving frequency for water pump was 200 Hz sinewave. The driving voltage waveform was 200 Hz sinewave for the water pump and 50 Hz sinewave for the oil pump.

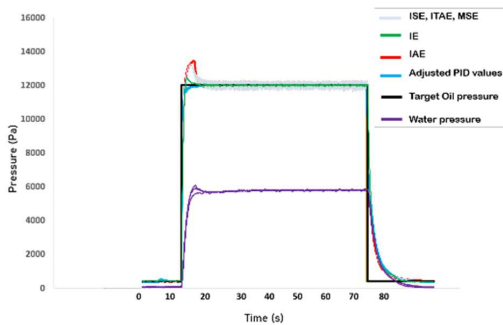


FIGURE 13. Simulation results for pressure feedback PID controller tuning with a genetic algorithm for oil pressure control.

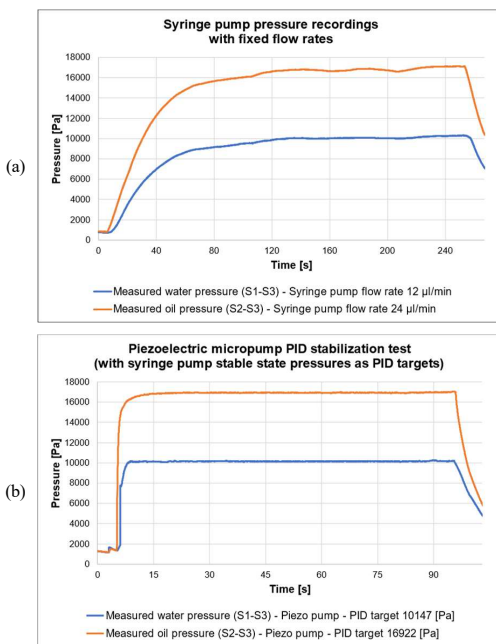


FIGURE 14. Pressure stabilization experiments performed on the setup shown in Fig. 11/a. Syringe pumps were set to pump with 12 $\mu\text{l}/\text{min}$ for DIW and 24 $\mu\text{l}/\text{min}$ for oil A. One minute period from the end of stable state pressures on (a) were averaged and used as pressure targets for the piezoelectric micropump PIDs. a) Responsiveness of flow-rate driven system (with third-party syringe pumps); b) Responsiveness of our pressure-driven system.

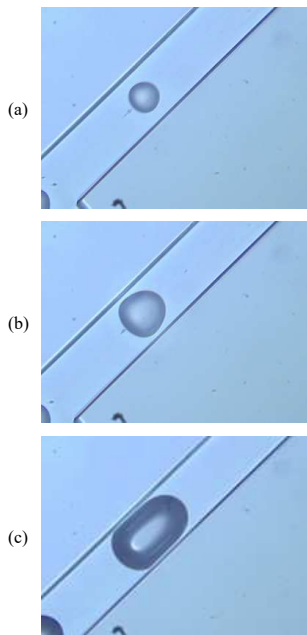


FIGURE 15. Recorded camera images of droplets generated with DIW and oil A in a 125 μm wide microfluidic channel taken at 555 frames per second under brightfield LED. a) $\sim 58.4 \mu\text{m}$ length droplet, generated with 5.2 kPa and 11.0 kPa for water and oil pressures respectively; b) $\sim 112.7 \mu\text{m}$ length droplet, generated with 5.2 kPa and 9.5 kPa for DI water and oil A pressures respectively; c) $\sim 182.0 \mu\text{m}$ length droplet, generated with 5.2 kPa and 7.5 kPa for water and oil pressures respectively.

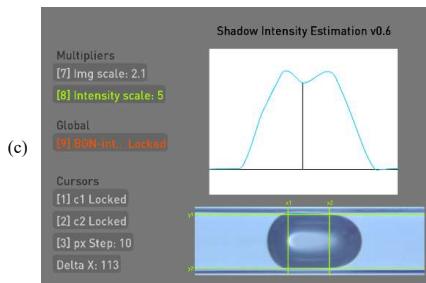


FIGURE 16. Rotated and cropped camera images shown in Fig. 15, respectively, were scanned with a fixed size moving window, indicated by green vertical lines to obtain corresponding intensity graphs (blue waveform above droplet image). a) low-distortion triangular waveform produced by the $\sim 58.4 \mu\text{m}$ length droplet with a relative intensity multiplier of 20.0; b) low-distortion triangular waveform produced by the $\sim 112.7 \mu\text{m}$ length droplet with a relative intensity multiplier of 10.0; c) high-distortion trapezoidal (double-peak) waveform produced by the $\sim 182.0 \mu\text{m}$ length droplet with a relative intensity multiplier of 5.0.

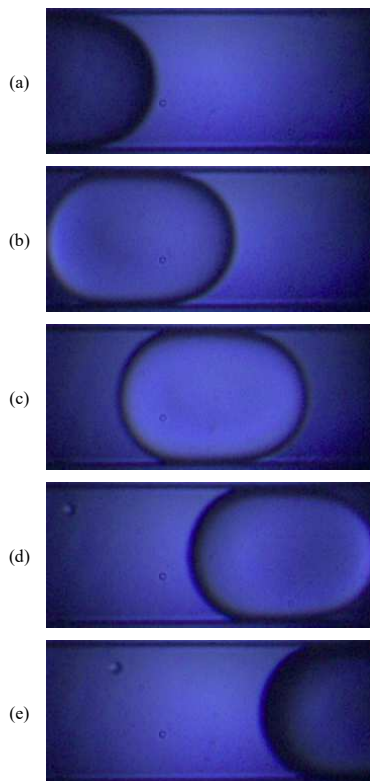
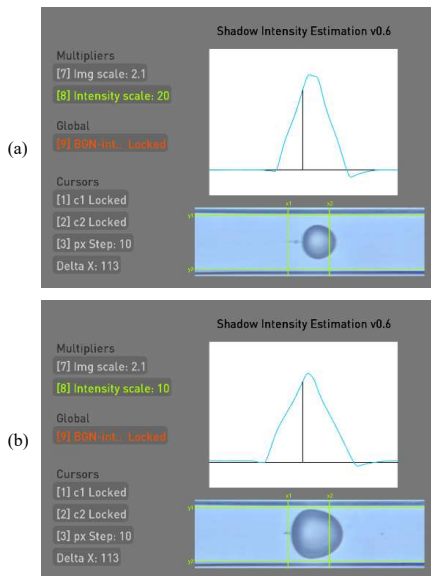


FIGURE 17. Cropped recorded frames of a passing droplet during generation with oil B. Droplet was generated at 5.0 kPa and 5.5 kPa water and oil pressures respectively. Displayed droplet measures $\sim 171.9 \mu\text{m}$ in length and was recorded at 1810 frames per second. A circular $\sim 190 \mu\text{m}$ diameter pinhole was used under the microfluidic chip below the recorded

region to improve the visibility of the droplet. a) reference frame 1 in series, droplet entering the pinhole aperture; b) reference frame 2 in series, droplet approaching the center of the pinhole aperture; c) reference frame 3 in series, droplet in the middle of the pinhole aperture; d) reference frame 4 in series, droplet leaving from the center of the

pinhole aperture; e) reference frame 5 in series, droplet exiting the pinhole aperture.

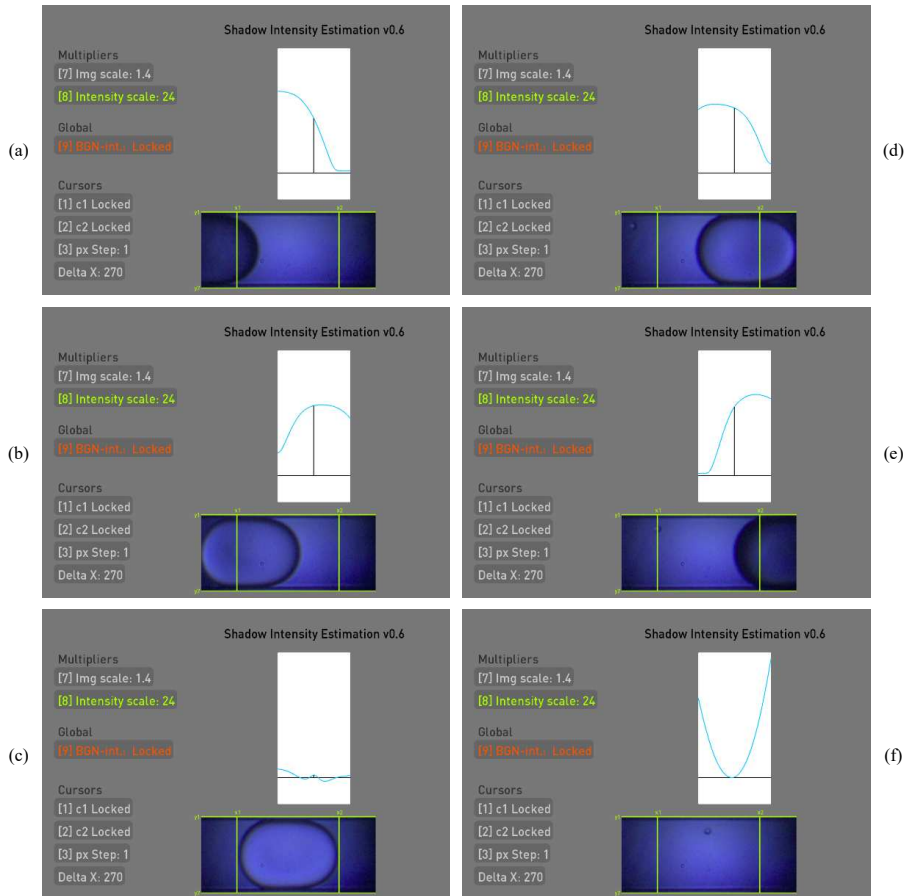


FIGURE 18. Camera images shown in Fig. 17, respectively, and an extra 6th frame were scanned with a fixed size moving window, indicated by green vertical lines to obtain corresponding intensity graphs (blue waveform above droplet image). All intensity graph scaling multipliers were kept at 245.0 for better visualization and comparability. The intensity of the 6th frame, representing the background noise, was recorded first, and locked into memory. Background intensity was subtracted from the following calculations. a) Indicating a rising shadow intensity as the darkest region of the droplet entered the pinhole aperture and the moving window; b) indicating a past-peak shadow intensity as the droplet moved closer to the center of the pinhole aperture and the moving window; c) indicating the lowest shadow intensity while the droplet was positioned at the center of the pinhole aperture; d) indicating an approaching-peak shadow intensity as the droplet was leaving the central region of the pinhole aperture and the moving window; e) indicating a falling shadow intensity as the darkest region of the droplet was exiting the pinhole aperture and the moving window; f) indicating the intensities of the shadows at the edges of the frame, caused by the pinhole.



FIGURE 19. Oscilloscope screen capture of recorded amplified, inverted photodiode voltage during droplet generation with chip variant C, at a rate of ~500 Hz. Droplet alignment with the pinhole noted with blue arrows (at the “troughs”). Instability in the droplet production rate is recognizable by the varying time gaps between the „troughs“.

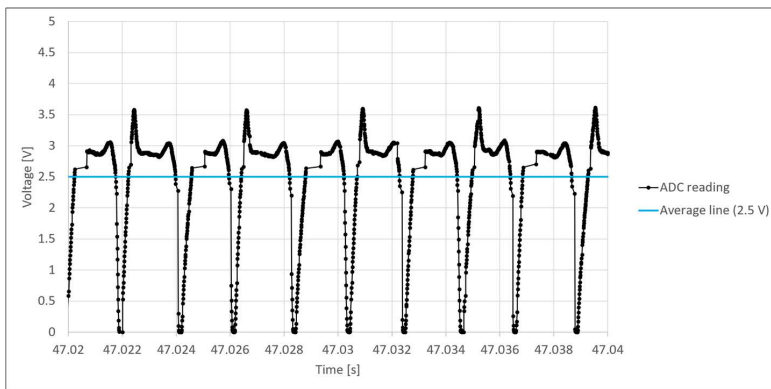


FIGURE 20. Sample frame from ADC measurement log on RPI showing ADC readings and the average line over which droplet detection was handled. Shown graph links with Fig. 19, however, with every other peak cut off due to specific cross-core communication function delays.

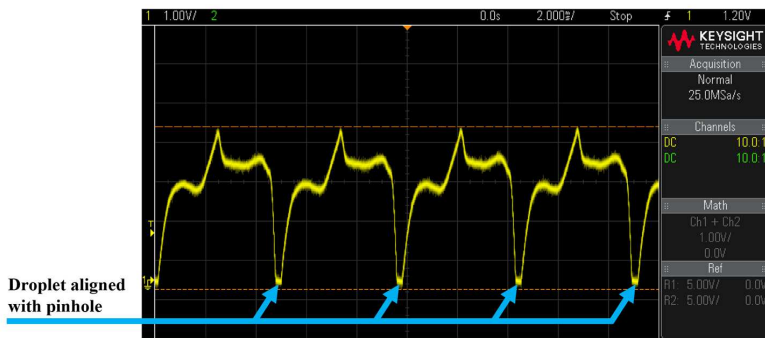


FIGURE 21. Oscilloscope screen capture of recorded amplified, inverted photodiode voltage during droplet generation at a rate of ~200 Hz. Droplet alignment with the pinhole noted with blue arrows (at the “troughs”).

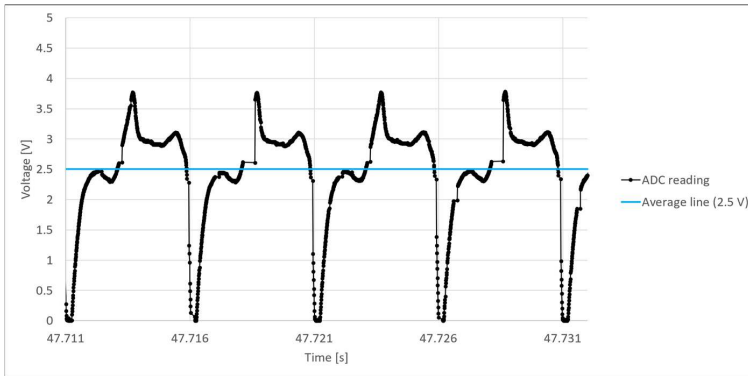


FIGURE 22. Sample frame from ADC measurement log on RPI showing ADC readings and the average line over which droplet detection was handled. Shown graph links with Fig. 21, however, in contrast to Fig. 20, cross-core function delays caused after every other detected droplet, were not long enough to cut off the relevant peaks of the droplet waveform.

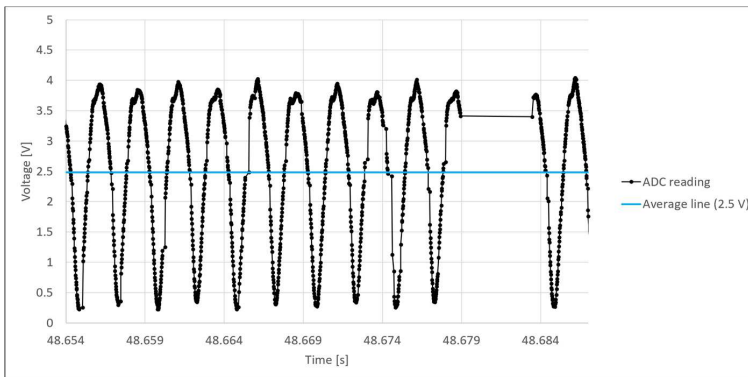


FIGURE 23. Sample frame from ADC measurement log on RPI showing ADC readings and the average line over which droplet detection is handled. In shown example, spontaneous latency delays caused by the operating system running on RPI prevented three consecutive droplets being captured and measured.

TABLE III FLUID PHASES USED IN DROPLET GENERATION EXPERIMENTS

	A	B
Disperse phase	deionized water (DIW)	deionized water (DIW)
Continuous phase	Sigma-Aldrich 33079 mineral oil + 2% w/w surfactant (Span® 80, Sigma-Aldrich)	HFE 7500 fluorocarbon oil + 2% w/w surfactant (perfluoropolyether (PFPE)-poly(ethylene glycol) (PEG)-PFPE triblock)

TABLE IV Chip B – Voltage target series over fixed generation frequency targets.

	Fixed Generation Rate Target	Voltage / Size Target 1	Voltage / Size Target 2	Voltage / Size Target 3
1	200 Hz	2.0 V	2.8 V	3.6 V
2	400 Hz	2.0 V	2.8 V	3.6 V
3	600 Hz	2.0 V	2.8 V	3.6 V
4	800 Hz	2.0 V	2.8 V	3.6 V

TABLE V Chip B – Frequency target series over fixed voltage (size) targets.

	Fixed Voltage / Size Target	Generation Rate Target 1	Generation Rate Target 2	Generation Rate Target 3	Generation Rate Target 4
1	2.0 V	200 Hz	400 Hz	600 Hz	800 Hz
2	2.8 V	200 Hz	400 Hz	600 Hz	800 Hz
3	3.6 V	200 Hz	400 Hz	600 Hz	800 Hz

TABLE VI Chip C – Voltage target series over fixed generation frequency targets.

	Fixed Generation Rate Target	Voltage / Size Target 1	Voltage / Size Target 2	Voltage / Size Target 3	Voltage / Size Target 4
1	200 Hz	3.2 V	3.4 V	3.6 V	3.8 V
2	300 Hz	3.2 V	3.4 V	3.6 V	3.8 V
3	400 Hz	3.2 V	3.4 V	3.6 V	3.8 V
4	500 Hz	3.2 V	3.4 V	3.6 V	3.8 V

TABLE VII Chip C – Frequency target series over fixed voltage (size) targets.

	Fixed Voltage / Size Target	Generation Rate Target 1	Generation Rate Target 2	Generation Rate Target 3	Generation Rate Target 4	Generation Rate Target 5
1	3.2 V	200 Hz	300 Hz	400 Hz	500 Hz	600 Hz
2	3.4 V	200 Hz	300 Hz	400 Hz	500 Hz	600 Hz
3	3.6 V	200 Hz	300 Hz	400 Hz	500 Hz	600 Hz
4	3.8 V	200 Hz	300 Hz	400 Hz	500 Hz	600 Hz

TABLE VIII CONTROLLER SOFTWARE'S TASK LOOP DURATION.

	Core 1 – User interface coms. (Section II-B-3-1)	Core 2 – Pumping system coms. (Section II-B-3-2)	Core 3 – Droplet interpretation (Section II-B-3-3)	Core 4 – Droplet PID calculations (Section II-B-3-4)
Maximum [ms]	203.4370	215.0430	20.25914*	21.05400*
Average [ms]	102.0334	18.98948	0.006515	0.169749
Minimum [ms]	100.6310	14.74400	0.002861	0.104000
Loops counted	1005	4 758	14 640 000	530 200
Total [s]	102.54	90.35	95.38	90.00

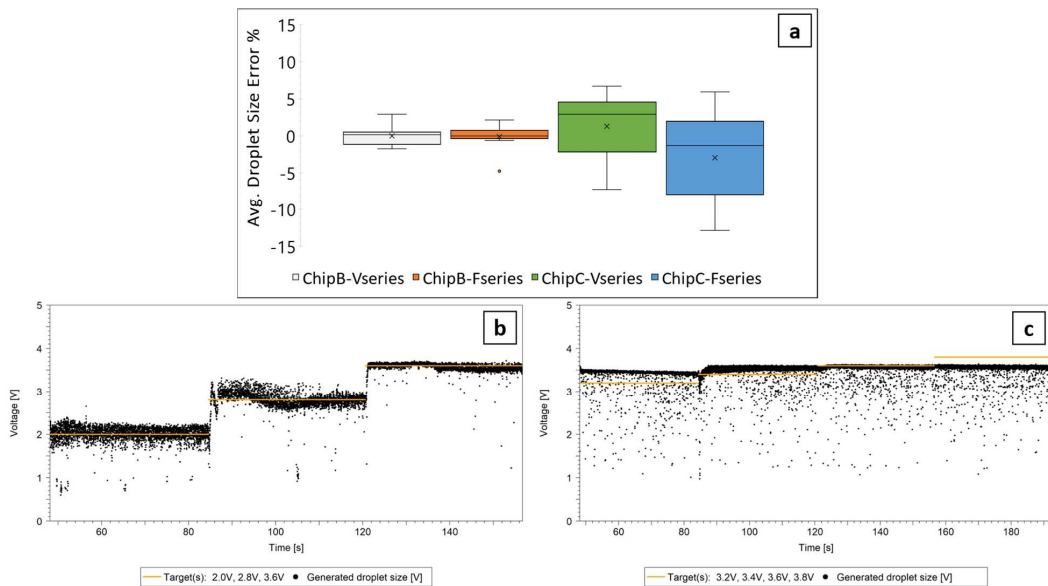


FIGURE 24. Results from Section IV-B-1. a) Averaged droplet size target errors for chips B and C, further split by size and frequency series test sets. Sample sizes for series respectively [12, 12, 9, 16]; b) Droplet size control dataset of row 1 from TABLE IV, from ChipB-Vseries test set. Graph indicating higher accuracy of stabilization around target voltage levels; c) Droplet size control dataset of row 2 from TABLE VI, from ChipC-Vseries test set. Graph indicating lower accuracy of stabilization around target voltage levels, preference to droplet size (influenced by chip geometry).

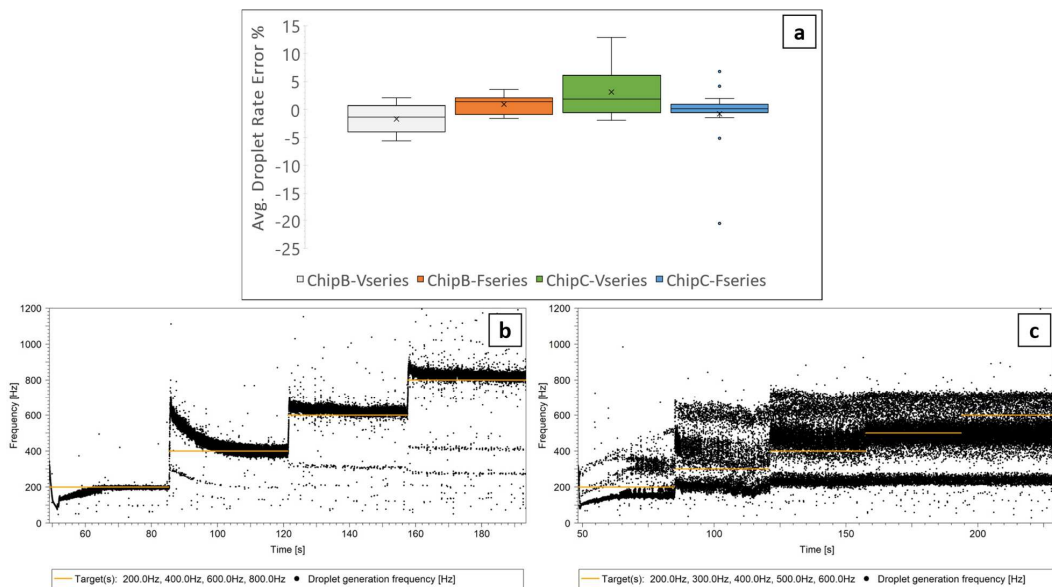


FIGURE 25. Results from Section IV-B-1. a) Averaged droplet rate target errors for chips B and C, further split by size and frequency series test sets. Sample sizes for series respectively [12, 12, 9, 16]; b) Droplet generation rate control dataset of row 2 from TABLE V, from ChipB-Fseries test set. Graph indicating higher accuracy of stabilization around target frequency levels; c) Droplet generation rate control dataset of row 1 from TABLE VII, from ChipC-Fseries test set. Graph indicating lower accuracy of stabilization around target frequency levels and significant fluctuation in periodicity of droplet production.

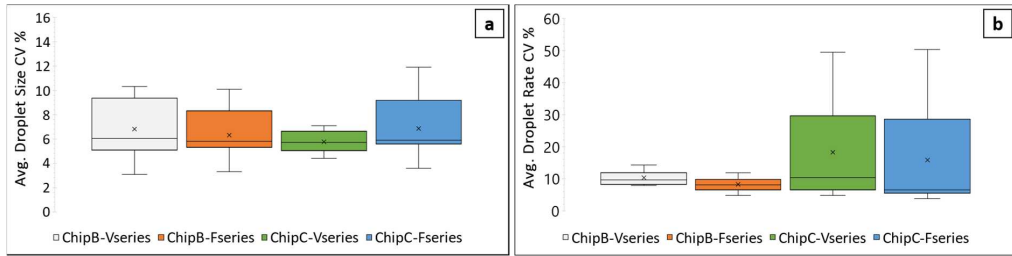


FIGURE 26. Results from Section IV-B-2. a) Averaged droplet size CVs for chips B and C, further split by size (V series) and frequency (F series) series test sets; b) Averaged droplet generation rate CVs for chips B and C, further split by size (V series) and frequency (F series) series test sets. Sample sizes for series respectively [12, 12, 9, 16].

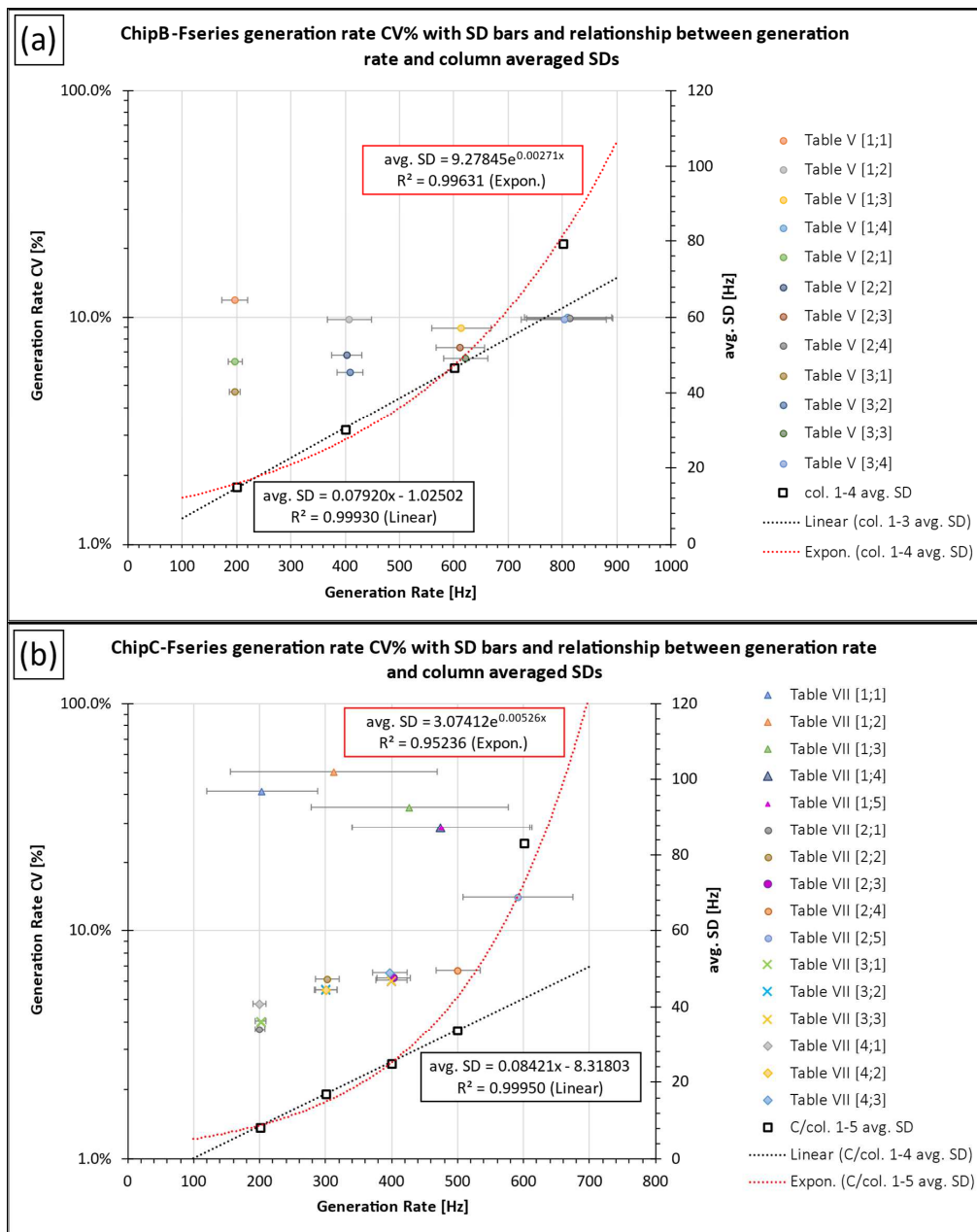


FIGURE 27. Results from Section IV-B-2. Quantitative analysis of F series data. a) Droplet generation rate CV%, from droplet size and rate combinations in TABLE V, plotted against averaged generation rate, calculated over the stabilized generation period. TABLE V column (col.) averaged SDs (from target rate columns 1 to 4 and target size rows 1 to 3) plotted against column target generation rates together with a corresponding exponential regression line. Col. avg. SDs were cropped to columns 1 to 3 to highlight the highly linear correlation region; b) Droplet generation rate CV%, from droplet size and rate combinations in TABLE VII, plotted against averaged generation rate, calculated over the stabilized generation period. TABLE VII column conditionally (C/col.) averaged SDs (from target rate columns 1 to 5 and target size rows 2 to 4 – row 1 conditionally excluded due to indicating a different mode of operation, see ESI S4 for details) plotted against column target generation rates together with a corresponding exponential regression line. C/col. avg. SDs were cropped to columns 1 to 4 to highlight the highly linear correlation region.

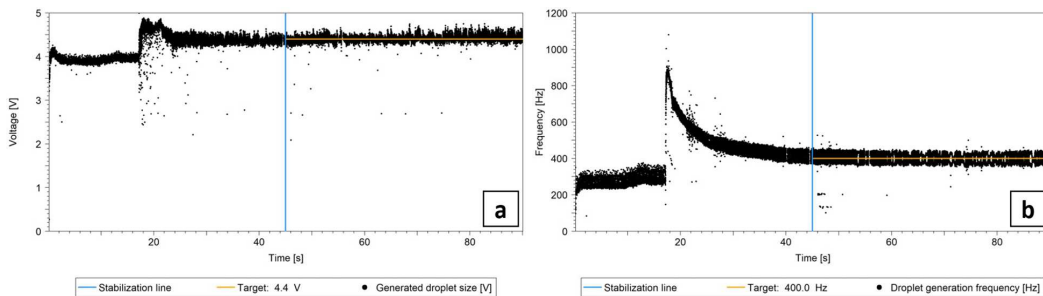


FIGURE 28. Results from Section IV-B-2. a) Droplet size target data set from a combination of [4.4 V; 400 Hz] with chip B. Stabilization period 45 seconds which includes an initial 15 seconds of default initiation period. Stabilization and stable segments are separated by blue vertical line. Target size in voltage is shown with an overlaid horizontal line; b) Droplet generation rate target data set from a combination of [4.4 V; 400 Hz] with chip B. Stabilization period 45 seconds which includes an initial 15 seconds of default initiation period. Stabilization and stable segments are separated by blue vertical line. Target size in voltage is shown with an overlaid horizontal line.

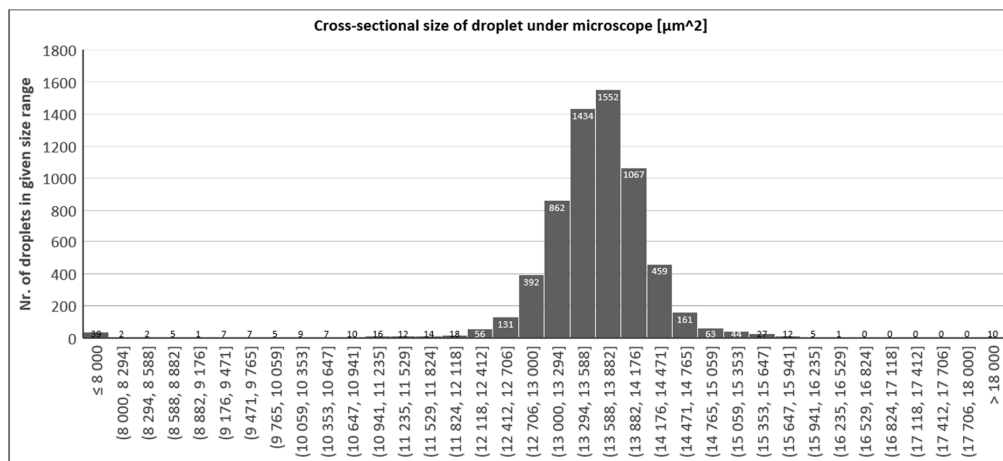


FIGURE 29. Droplet cross-sectional size spread from a droplet generation sample, generated with fixed water and oil pressure of 9 kPa and 12 kPa respectively. 6429 droplets measured over 11 images with ImageJ software.

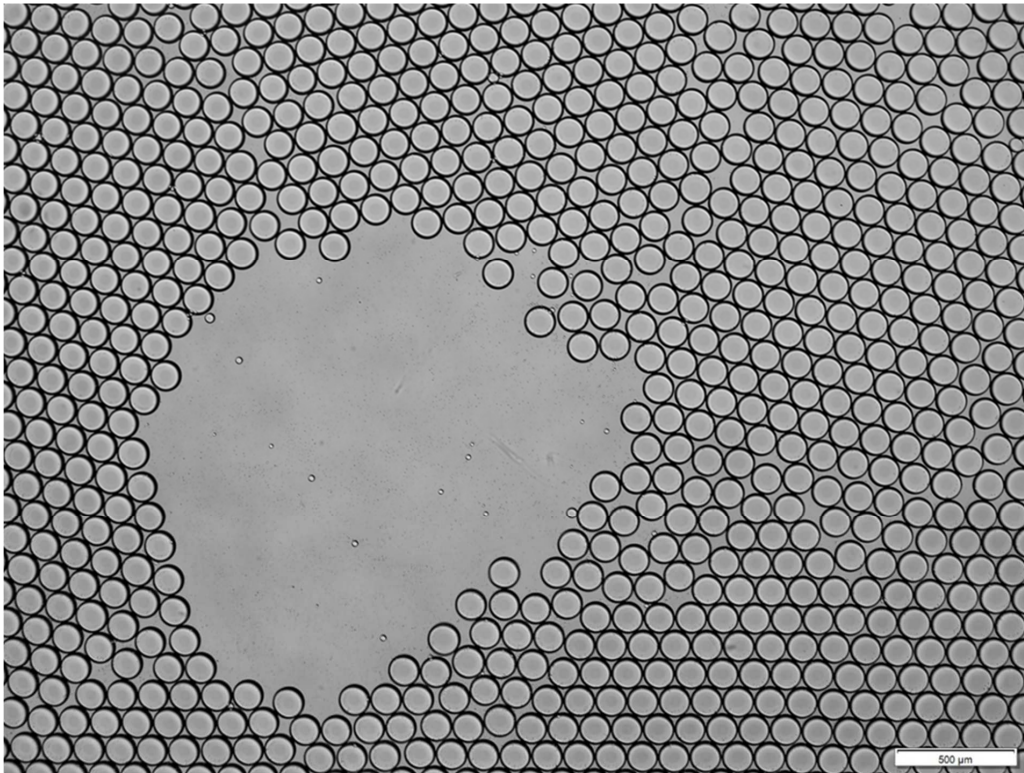


FIGURE 30. Droplets generated with chip design B with fixed water and oil pressures of 9 kPa and 12 kPa respectively, pumped using pressure-based piezoelectric micropumps, viewed under microscope (4x/0.16 lens).

Appendix 4

IV

K. Pärnamets, A. Udal, A. Koel, T. Pardy, **N. Gyimah**, and T. Rang, "Compact empirical model for droplet generation in a lab-on-chip cytometry system," *IEEE Access*, vol. 10, pp. 127708–127717, 2022

Date of publication xxxx 00, 0000, date of current version xxxx 00, 0000.

Digital Object Identifier 10.1109/ACCESS.2017.Doi Number

Compact empirical model for droplet generation in a Lab-on-Chip cytometry system

Kaiser Pärnamets¹, Member, IEEE, Andres Udal², Member, IEEE, Ants Koel¹, Member, IEEE, Tamás Pardy³, Nafisat Gyimah¹ and Toomas Rang^{1,3}, Senior member, IEEE

¹Thomas Johann Seebeck Department of Electronics, Tallinn University of Technology, Ehitajate tee 5, 19086, Tallinn

²Department of Software Science, Tallinn University of Technology, Ehitajate tee 5, 19086, Tallinn

³Department of Chemistry and Biotechnology, Tallinn University of Technology, Ehitajate tee 5, 19086, Tallinn

Corresponding author: Kaiser Pärnamets (e-mail: kaiser.parnamets@taltech.ee).

This research was funded by the Estonian Science Agency ETAg, grant number PRG620, MOBTP109 and by the European Union's Horizon 2020 Research and Innovation Program under Grant 668995.

ABSTRACT This study describes the construction of a compact empirical mathematical model for a flow-focusing microfluidic droplet generator. The application case is a portable, low-cost flow cytometry system for microbiological applications, with water droplet sizes of 50-70 micrometer range and droplet generation rates of 500-1500 per second. In this study, we demonstrate that for the design of reliable microfluidic systems, the availability of an empirical model of droplet generation is a mandatory precondition that cannot be achieved by time-consuming simulations based on detailed physical models. When introducing the concept of a compact empirical model, we refer to a mathematical model that considers general theoretical estimates and describes experimental behavioral trends with a minimal set of easily measurable parameters. By interpreting the experimental results for different water- and oil-phase flow rates, we constructed a minimal 3-parameter droplet generation rate model for every fixed water flow rate by relying on submodels of the water droplet diameter and effective ellipticity. As a result, we obtained a compact model with an estimated 5-10% accuracy for the planned typical application modes. The main novelties of this study are the demonstration of the applicability of the linear approximation model for droplet diameter suppression by the oil flow rate, introduction of an effective ellipticity parameter to describe the droplet form transformation from a bullet-like shape to a spherical shape, and introduction of a machine learning correction function that could be used to fine-tune the model during the real-time operation of the system.

INDEX TERMS Compact empirical model, droplet cytometry, droplet generation, flow-focusing junction, microfluidic chip

I. INTRODUCTION

Bacterial threats have been a noticeable challenge of this century, and a delayed response due to the lack of field-testing options poses risks to human lives and can cause epidemics. Classical microbiological methods are relatively slow, while cytometric methods allow measuring the number and morphology of cells easily, reliably, and quickly. Droplet microfluidics, a new technology developed over the last dozen years, offers breakthrough solutions for creating low-cost, fully portable cytometers for field analysis of bacteria based on very small sample volumes and the possibility of seeking single-cell resolutions.

The present study discusses model-based design of portable cytometer devices based on the concepts of lab-on-a-chip [1]–[3], microfluidics [4], [5], and droplet cytometry [6]–[10].

Specifically, we describe the construction of an empirical mathematical model for the calculation of droplet generation rates and dimensions in the water-in-oil flow-focusing-type [11] droplet generation node of a lab-on-a-chip cytometer. This study was partly based on the digital twin model developed by our group [12].

Figure 1 illustrates the topicality trends of the considered research areas based on the publication statistics of the Clarivate Web of Science database [13]. As demonstrated in Figure 1, the concept of lab-on-a-chip has become popular since the beginning of the 21st century, and is presently showing a saturation trend. The overall area of droplet microfluidics became popular slightly later in years 2003-2004 and has demonstrated linear growth until the present time. The most vital concept is droplet cytometry, for which

exponential growth with a doubling time of 4-5 years started approximately 12 years ago. An overall comparison of regions over the last decade demonstrated the approximate equality of Western Europe, North America, and the People's Republic of China (PRC) [13].

Model-based design has become a mandatory methodology for system design in various applications, including microfluidics [14]–[17]. In the present use case, a model of the droplet generation node is required for the prediction of droplet generation parameters, such as generation rates and diameters, both during the cytometer construction and exploitation phases, to improve the control quality via model predictive control.

An important issue in the construction of a mathematical model for any object is the selection of a detailed physical or formal empirical approach [18]–[21]. The physical approach can be time consuming for both the computer and developer but can yield reliable results for a wide range of operation conditions, provided that the physical mechanisms and relevant key parameter values are known and modelled correctly. In the case of droplet microfluidics, physical models rely on well-known equations and methods of computational fluid mechanics (CFD), which must be supplemented with less reliable multicomponent fluid flow methods [22], [23]. Thus, in addition to the high computational workload, the major problem of the physical approach is often the presence of non-measurable physical parameters and the hidden influence of numerical factors such as reduced spatial dimensionality and mesh step sizes. Although many authors have illustrated their studies with simulated droplet images, for example, [23]–[26], several respected research groups, for example, [24], [27]–[29], emphasize the unreliability of numerical physical modelling, particularly if the droplet size, generation rate, and monodispersity characteristics must all be reliably calculated simultaneously. Moreover, considering the three main droplet generation geometry types – co-axial, T-junction and flow-focused [27], [30], the third option, which is also analyzed in the present study, has been estimated most difficult for the point of view of accurate modelling [20], [30], [31]. Our simulation results with the COMSOL Multiphysics® 5.6 Two-Phase Flow Level Set module [32], described below in the simulation section, confirm the unreliability claims regarding the detailed physical modelling approach. To illustrate the relevant difficulties, it is reasonable to point out that to overcome the aforementioned uncertainties and obtain a reliable practical tool for flow-focusing droplet generator design, a large-scale experimental study was recently conducted by the group of Boston University [24], [28]. In this study, a generalized flow-focusing structure with an orifice was described using six geometrical parameters: 25 orthogonal structure variants were manufactured using the Taguchi formal scheme, over 30 operation modes for each structure were tested, and a statistical empirical model was obtained to cover a reasonably wide range of droplet diameters and generation rates. In comparison with [24], [28], the present

study discusses only one flow-focusing structure without nozzle (orifice) section but, on the other hand, the droplet geometry description includes also the ellipticity factor, droplet generation rates are of 2-3 times higher range and the formula-based analytic formulation having a better transparency and real-time adjustability is used.

In contrast to detailed physical models, the alternative empirical approach is characterized by a formal generalization of experimental data [20], [27], [30]. The empirical approach is usually less labor-intensive and often more accurate, but only for the parameter space covered by the experiments. In practice, the most useful real models are semi-empirical, which means that they combine theoretical principles with available experimental data. In droplet microfluidics, it is reasonable to build all droplet generation models based on the mass conservation principle for the dispersed phase (i.e., droplet fluid-like water), which allows a state connection between three main variables: droplet fluid flow rate, droplet diameter, and droplet generation rate [20], [21], [28], [31]. Some authors, who have investigated the formation of relatively large non-spherical droplets that fill all cross-sections of the generation channel, have added a fourth parameter, the droplet length, for example, [20], [21], [30]. In this study, we introduce an original approach using an effective ellipticity parameter that maintains droplet volume conservation and accounts for experimentally observed droplet shape changes from bullet-like shapes at low continuous-phase flow rates to spherical shapes at high continuous-phase flow rates.

When discussing the droplet diameter empirical models, many authors have used the ratio of dispersed and continuous phase flow rates Q_d/Q_c , for example, [21], [25], [26]. Our droplet image recording results, presented below in the experimental section, do not support the use of this ratio parameter, and demonstrate that for higher water flow values, a proportional oil flow increase is required to achieve a comparable diameter suppression effect.

An important characteristic for the practical applicability of mathematical models is their compactness. We recommend defining compactness based on the following features: 1) the minimal number of adjustment parameters, 2) measurability of the adjustment parameters, 3) low computational workload, and 4) transparency of the set of equations [33]. The concept of a compact model is widely used in the field of electronic and semiconductor microchip design [34] for two main reasons: lowering the computational workload and operation with measurable parameters. In droplet microfluidics, the need for compact models has not yet been explicitly recognized and only a few studies have used this term [35]–[38]. At the same time, nearly 1000 publications (see Figure 1) contain some approximate formulas for the calculation of droplet sizes or generation rates that may be interpreted as compact models for solving some subproblems of droplet microfluidic system design tasks.

An important question in droplet generation model construction is the description of the droplet diameter suppression effect owing to continuous phase (oil) flow. The majority of published results and models, for example, [25], [26], [39], predict a less-than-proportional diameter suppressing effect owing to the increasing continuous phase flow rate Q_c . Few studies support either a proportional decrease in diameter, for example, [31], or a stronger than proportional increase [26]. The present experimental study confirmed the applicability of the linear approximation of the dependence of the water droplet diameter on the oil flow rate. Thus, a linear droplet diameter model may be offered that uses only one proportionality factor for a fixed water flow rate and given droplet generation channel width. If completed with two parameters for the description of effective ellipticity changes, a compact 3-parameter model for the calculation of droplet diameters, ellipticities, and generation rate dependencies on the oil flow rate may be constructed.

In recent years, there has been an urgent need to accelerate and simplify the development of microfluidic droplet generators with desired output parameters via automatization and the application of machine learning methods [24], [40], [41]. To realize these goals via empirical statistical modelling by applying artificial neural networks, large-scale experimental testing [24], [28] or sophisticated computer vision methods for additional droplet data collection [40] have been proposed. In this study, a much narrower task scope was considered and only the desired droplet parameters were obtained by adjusting the water and oil flow rates for a fixed microfluidic chip. However, formula-based transparent presentation of mathematical models offers much better possibilities for solving system optimization and real-time model adjustment (i.e., machine learning) tasks. Although the modification of neural-network-based statistical models [24], [40] requires significant effort and time for the collection of additional data and retraining (transfer learning), the empirical model considered here, in the form of mathematical formulas with adjustable coefficients, offers possibilities for the realization of real-time model adjustment and a cytometer system with an extremely simple feedback loop containing an elementary optical sensor.

The remainder of this paper is organized as follows. In Section 2, the microfluidic chip and the measurement setup are described. In Section 3, a short summary of the detailed numerical simulation results and a discussion of the problems that occurred are presented. Section 4 summarizes the experimental results for the different water and oil flow rates. In section 5, the construction principles, formulas, and fitting results of the compact mathematical model are presented. Section 6 discusses the scope of the application of the proposed model. Section 7 presents the main results of the study.

II. DESCRIPTION OF DROPLET GENERATION CHIP AND MEASUREMENT SETUP

Microfluidic droplets were generated inside a polydimethylsiloxane (PDMS) chip, as shown in Figure 2. The full thickness of the PDMS chip was 5 mm, and it had a microfluidic channel structure with a depth of 100 μm on one surface (Figure 2a), which was covered by a 1 mm thick glass plate (microscope slide plate). From the three main droplet generation geometries, the T-junction, co-flow, and flow-focusing junction [11], the last geometry variant, where water flows with biological agents, is cut into droplets by a continuous oil flow entering the junction area from the two opposite sides (Figure 2a and 2c). Thus, water droplets were formed in the junction area and in the generation channel with cross-sectional dimensions of 84 μm width and 100 μm height. An overview of the droplet generation unit with the inlet and outlet tubes is shown in Figure 2b. Deionized water was used as the dispersed phase (droplets). For the continuous phase, Sigma-Aldrich 330779 mineral oil [42] with a 2% surfactant [43] was used. The water and oil flow rates were maintained using syringe pumps and software manufactured by SpinSplit [44]. The lighting of the droplet generation junction area was realized from the PDMS side of the chip using a white LED group consisting of two LEDs with cold-color temperatures and two LEDs with warm-color temperatures. Photorecording was accomplished using a Basler Ace acA640-750um camera in a reduced resolution mode that allowed a frame rate of up to 3300 per second at an exposure time of 100 μs . Thus, as the experiment shows, a droplet per second (*dps*) generation rate of up to 1600 s^{-1} can be directly determined from the sequence of the recorded images. Additionally, *dps* values up to 2300 s^{-1} can be extrapolated based on the droplet separation distances (see Figure 7).

III. INTRODUCTORY SIMULATIONS OF UNDERLYING PHYSICS

In general, the prerequisite for the construction of a compact model may be the availability of experimental data or, as an alternative, the availability of a sufficiently reliable detailed physical model with necessary input data. In the case of flow-focused droplet generation junctions, the choice of the detailed physical approach can be complicated by the complex nature of the task, that is, the need for accurate modelling of the balance of competing processes of separation and encapsulation of droplets. Another serious problem is the high computational time required for realistic three-dimensional calculations. Therefore, all affordable two-dimensional calculations, even if the parameters of the physical processes are correctly estimated, can only serve as predictions that need to be confirmed by real experiments. Figure 3 shows the critical competing processes that must be accurately modelled in a flow-focused junction. Figure 3 emphasizes the importance of accurately modelling the surface tension forces, viscosities of both liquids, wall friction effects, channel dimensions, and other factors to obtain a realistic picture of both the liquid flow and droplet formation processes.

To test the possibility of using detailed physical modelling to formulate the basis of the droplet generation model, we performed several numerical simulation series using the COMSOL Multiphysics® 5.6 Two-Phase Flow Level Set module [32] in the traditional two-dimensional (2D) axisymmetric approximation of geometry [11]. It is important to emphasize that the crucial point for the accuracy of all modelling approaches is the correct handling of water volumes in the task specification. Oil can be considered an auxiliary substance that splits the incoming water stream and suppresses the diameters of the formed water droplets. Because in the 2D-simulation the droplets are cylindrical rather than spherical, the first question in the specification of the 2D-simulation task is to correctly select the effective size of the simulated structure towards the third dimension. Considering the realistic situation of the 3D-experiment (at high oil flow rates), it can be assumed that the droplets are spheres with a volume

$$V_{exp} = \frac{\pi}{6} D_{exp}^3 \quad (1)$$

where D_{exp} is the droplet diameter used in this experiment. In the 2D simulations, the volume of the droplet was defined using the cylinder formula

$$V_{sim} = \pi \cdot \left(\frac{D_{sim}}{2}\right)^2 \cdot H_{eff} \quad (2)$$

where H_{eff} is the introduced effective size of the structure towards the third dimension (see Figure 4).

The diameter and volume of the droplets must be equal to match the water volume counts in the experiments and simulations. Figure 4 shows the methodology for achieving the aforementioned water volume balance conditions when the auxiliary parameter H_{eff} of the 2D-simulation is specified as follows:

$$H_{eff} = \frac{2}{3} D_{exp} \quad (3)$$

Specifically, if the actual expected droplet diameter is 60 μm (in the 84 μm channel), then a reasonable measure for the structure depth in 2D-simulations should be 40 μm .

Figure 5 summarizes the main results of the COMSOL 2D-simulations with the Two-Phase Flow Level Set module [32] for the droplet generation area described in Figure 2c. For the first adjustment parameter, the effective depth of the structure in the third dimension was specified as 40 μm based on the considerations explained above. For the second essential adjustment parameter, the surface tension coefficient values of $\sigma = 40 \div 50 \text{ mN/m}$ were used to avoid the jetting effect and ensure the acceptable stability of the formed droplets. High surface tension values in a similar range have been recommended for water-to-mineral oil interfaces, for example, in [45], [46]. Next, in presented simulations the “no-slip” sub model of high friction walls was used. Other models, such as the Navier slip model with several additional adjustment parameters, did not cause essential changes.

For the main computational parameters, that is, the spatial mesh size, the two standard cases of “Fine” with 9536 finite elements and “Finer” with 36626 elements were compared. The computational times for the relatively short 20 ms process calculation ranged from 2 h to 14 h on a powerful desktop 16-core Intel i9-computer.

The main results of the COMSOL simulations are shown in Figure 5. The results demonstrate the difficulty of achieving stable droplet diameters and droplet generation rates. When the spatial mesh size was increased to a very high number of final elements, instead of the expected stabilization of the main output parameters, the chaotic behavior of the results demonstrated a remarkable increase, and the definition of certain values of droplet diameters and droplet generation rates became impossible. This emerging instability and uncertainty may be caused by the difficulty of the task, as shown in Figure 3. In summary, detailed physics-based numerical simulations provide supporting explanations for the underlying physical processes. However, the expected results for building a compact model for droplet generation have not been obtained.

IV. SUMMARY OF EXPERIMENTAL RESULTS

For the actual microfluidic chip, the expected droplet generation rates were in the range of 500-1500 per second, with droplet diameters of 50-70 micrometer range. Based on these design goals, three test series with constant water flow rates $Q_w = 4, 8, \text{ and } 12 \mu\text{L/min}$ and varying oil flow rates from value $Q_{oil} = 2Q_w$ to value $Q_{oil} = 60 \div 88 \mu\text{L/min}$ in steps of 4 $\mu\text{L/min}$ were performed. The selection of droplet images recorded in the beginning section of the 84 μm generation channel is presented in Figure 6. The results in Figure 6 show that at low oil flow rates, the droplets resemble bullets (modelled by the effective ellipsoids below in this study). With an increase in the oil flow rate, the droplets begin to resemble spheres. Simultaneously, the diameter can be suppressed by increasing the oil flow rate. The increasing blurring of droplet fronts and backs at higher droplet formation rates is due to camera exposure settings (100 μs).

An overall summary of the experimental results, including the directly recorded and extrapolated dps values from the droplet separation distances, is shown in Figure 7. The experimental diameters of droplet D were obtained by carefully comparing the droplet lateral sizes with a channel width of 84 μm and smoothing the dependencies with the neighboring points. Thus, the estimated accuracy of the diameters was of the order of $\pm 2 \mu\text{m}$. The effective ellipticity numbers, E (approximate ratio of the vertical and horizontal sizes of the droplets in the images), were estimated from the principle of equivalent volumes of the imaginary ellipsoidal and real bullet-like droplets. Additionally, minor smoothing of the experimental diameter and effective ellipticity values was performed to ensure correlation with the real water flow rates.

Owing to the camera frame rate limit, the high droplet rate values over $dps > 1600 \text{ s}^{-1}$ were difficult to define from video recordings but were extrapolated on the basis of the observed

decrease in droplet distances (see inlet in the upper part of Figure 7). Regarding this extrapolation, it should be mentioned that because of the increasing influence of the friction of the channel walls at higher Q_{oil} rates, the size of the effective high-flow-speed center area of the channel may be smaller at high Q_{oil} values; thus, the extrapolated dps numbers may be underestimated.

V. CONSTRUCTION OF THE COMPACT EMPIRICAL MODEL

In the present microfluidic system design, the main purpose of developing a compact droplet generation model is to obtain a tool for estimating the droplet generation rate dps . The latter depends directly on the droplet volume estimation by the sub-models for the droplet size parameters, such as the diameter D and effective ellipticity E , if the water flow rate Q_w is given. The oil flow rate Q_{oil} can be interpreted as an auxiliary factor that suppresses D compact model and can be constructed based on the following approximations:

1) For droplet generation rate dps , recalculation from a single ellipsoidal droplet volume formula $V = E(\pi/6)D^3$ can be applied if the diameter and ellipticity are estimated with reasonable accuracy.

2) Initially, it is reasonable to consider all three water flow rate values $Q_{w,i}$ separately. The final result for any Q_w value can be interpolated based on three separate results for dps_i , D_i , and E_i .

3) Relying on Figure 7 and seeking the principle of minimal complexity, for diameter dependence on oil flow rate $D(Q_{oil})$ the simplest single-parameter linear dependences may be applied; for the zero-oil origin point, the actual channel width value of $84 \mu m$ can be used as a common constant. The changes in dps in the 10% range were acceptable for an approximate adjustable model.

4) For E , the decreasing exponent law can be applied with a final level at high oil rate values close to one, which corresponds to the spherical limit form.

5) For machine learning readiness one real-time adjustable correction function $C_{ML}(Q_w, Q_{oil})$ may be added.

Considering the principles described above, the following set of mathematical equations can be proposed for the compact model (for every water flow rate value $Q_{w,i}$, $i = 1, 2, 3$):

$$dps_i = (557 s^{-1}) \left(\frac{Q_{w,i}}{6 \mu L/min} \right) \left(\frac{1}{E_i} \right) \left(\frac{70 \mu m}{D_i} \right)^3 \quad (4)$$

$$D_i = (84 \mu m) \left(1 - \frac{Q_{oil}}{Q_{D,i}} \right) \quad (5)$$

$$E_i = 1 + (E_{8,i} - 1) \exp \left(- \frac{(Q_{oil} - 8 \mu L/min)}{Q_{E,i}} \right) \quad (6)$$

where, following the goal of minimizing the number of adjustable parameters, only three fitting parameters, $E_{8,i}$, $Q_{E,i}$, $Q_{D,i}$ were introduced for each of the tested water flow rate values: $Q_{w,1} = 4 \mu L/min$, $Q_{w,2} = 8 \mu L/min$, and $Q_{w,3} = 12 \mu L/min$ (see Figure 6).

In systems (4)–(6), equation (4) is constructed to transform the value of the water flow rate to the number of droplets per second, considering the lateral diameter of droplets D_i and the effective ellipticity E_i as key parameters for the calculation of a single droplet volume. Equation (5) postulates the simplest linear decrease law for droplet diameters by introducing only one adjustable parameter $Q_{D,i}$ for every water rate, and using an actual channel width of $84 \mu m$ as a fixed constant for the low oil flow limit. Equation (6) approximates the exponential decrease in effective ellipticity from the initial high value at $Q_{oil} = 8 \mu L/min$ to the final unit value using two adjustment parameters: $E_{8,i}$ and $Q_{E,i}$.

For the general case of any water flow rate between 4 and $12 \mu L/min$, the simplest reliable piecewise linear approximation may be offered, considering that higher-order approximations such as parabolic approximations may distort the monotony of the dependences. In addition, an advanced feature of machine learning readiness may be included in the real-time empirical adjustment function $C_{ML}(Q_w, Q_{oil})$ for dps . In the minimal model formulation, the droplet size parameters may be excluded from the real-time adjustment because they droplet size parameters are difficult to measure during real-time operation.

Thus, the piecewise linear interpolation-based generalization of the droplet generation rate calculation for any water rate value can be performed using equations (7) and (8) given below.

The mathematical formulation of the linear approximation with machine learning adjustment for the first interval $Q_{w,1} \leq Q_w \leq Q_{w,2}$ can be written as

$$dps = C_{ML}(Q_w, Q_{oil}) \left(A_{21} dps(Q_{w,1}) + B_{21} dps(Q_{w,2}) \right),$$

$$A_{21} = \frac{Q_{w,2} - Q_w}{Q_{w,2} - Q_{w,1}}, \quad B_{21} = 1 - A_{21} \quad (7)$$

and for the second interval $Q_{w,2} \leq Q_w \leq Q_{w,3}$ as

$$dps = C_{ML}(Q_w, Q_{oil}) \left(A_{32} dps(Q_{w,2}) + B_{32} dps(Q_{w,3}) \right),$$

$$A_{32} = \frac{Q_{w,3} - Q_w}{Q_{w,3} - Q_{w,2}}, \quad B_{32} = 1 - A_{32} \quad (8)$$

The fitting of the three parameters of models (4)–(6) to determine the best agreement between the model and experimental points in Figure 7 was performed by separately minimizing the root-mean-square (RMS) difference between the experiment and simulation for the three water rate values. The weight scalars for the three main output parameters, dps , D , E were $20 s^{-1}$, $2 \mu m$, and 0.1 , respectively. In addition, the weights of the low oil rate endpoints for the high water rate curves $Q_{w,2}$, $Q_{w,3}$ were increased to obtain a reasonable balance with the low water $Q_{w,1}$ curve. The overall results of the fitting are shown in Figure 8. The values obtained for the model coefficients are listed in Table 1.

VI. DISCUSSION AND APPLICATION AREA

The definition of the application area is an important issue in

empirical models. The general principle is that the reliability of the results can only be assumed in the range of parameter values covered by the experimental results. The application area of the proposed compact empirical model is illustrated in Figure 9.

As shown in Figure 8, the droplet rate calculation accuracy of the proposed compact model remained in the range of 20% when considering the all-parameter area. However, it is important to emphasize that the trends of changes due to water and oil flow rate changes were modelled correctly. Additionally, for the central region of the planned operation around $dps = 500\text{-}1500\text{ s}^{-1}$ the accuracy is much better and is already in the 5-10% range. Moreover, this number can be improved by machine-learning adjustments during real operations if the droplet generation rates are measured using optical measurements.

The reason for the moderate accuracy of the proposed simple 3-parameter model is the simplicity of modelling the droplet diameter using the simplest 1-parameter linear dependence. Since the droplet formation rate depends on the droplet diameter according to the cubic law, small differences in diameters of about 3% were increased to 10% when the formation rates were taken into account. It is possible to introduce a sub-model of a more precise diameter; however, the accompanying increase in the number of model parameters may require additional complex measurements.

From a technical viewpoint, it seems more reasonable to use a simpler model with the possibility of real-time adjustment.

VII. CONCLUSIONS

Compact models are a well-established approach in electronics and microelectronics but are not yet sufficiently appreciated in the relatively young field of droplet microfluidics. Although for design of any technical system, like droplet cytometry portable apparatus in the present use case, the availability of compact models for all subsystems is a highly desirable precondition for the successful design of the system as well for later exploitation of the system. In addition, as demonstrated in the present study, the alternative approach of detailed physical modelling may not yield usable results in the case of the droplet generation task of microfluidics, where the competing balances of different physical mechanisms must be accurately modelled.

The original new results presented in the present study may be summarized as follows:

- 1) The applicability of the linear approximation of the dependence of the droplet diameter on the oil flow rate for the actual flow-focusing microfluidic water droplet generator task (droplet sizes in the 50-70 micrometer range and generation rates in the 500-1500 per second range) was demonstrated.
- 2) The concept of effective ellipticity was introduced to describe a unified model for the change of droplet geometry from a spherical to a spherical shape.
- 3) The methodology for the construction of a minimized

compact 3-parameter droplet generation rate model with 5-10% accuracy for the calculation of the oil flow rate dependence at fixed water flow rates for the desired operation region was described.

- 4) A machine learning extension to the basic model for further adjustment using real-time measurement results was proposed.
- 5) The droplet-volume-based equivalence condition to make 2D-simulations comparable to the real 3D experimental geometry is discussed.

REFERENCES

- [1] P. S. Dittrich and A. Manz, "Lab-on-a-chip: microfluidics in drug discovery," *Nat. Rev. Drug Discov.* 2006 53, vol. 5, no. 3, pp. 210–218, Mar. 2006, doi: 10.1038/nrd1985.
- [2] J. Y. Yoon and B. Kim, "Lab-on-a-Chip pathogen sensors for food safety," *Sensors* 2012, Vol. 12, vol. 12, no. 8, pp. 10713–10741, Aug. 2012, doi: 10.3390/S120810713.
- [3] H. Craighead, "Future lab-on-a-chip technologies for interrogating individual molecules," *Nanosci. Technol. A Collect. Rev. from Nat. Journals*, pp. 330–336, Jan. 2009, doi: 10.1142/9789814287005_0034.
- [4] S. Haeberle and R. Zengerle, "Microfluidic platforms for lab-on-a-chip applications," *Lab Chip*, vol. 7, no. 9, pp. 1094–1110, Aug. 2007, doi: 10.1039/B706364B.
- [5] R. Pol, F. Céspedes, D. Gabriel, and M. Baeza, "Microfluidic lab-on-a-chip platforms for environmental monitoring," *TRAC Trends Anal. Chem.*, vol. 95, pp. 62–68, Oct. 2017, doi: 10.1016/J.TRAC.2017.08.001.
- [6] M. Grafton *et al.*, "Design of a multi-stage microfluidics system for high-speed flow cytometry and closed system cell sorting for cytomics," *Proc. SPIE 6859, Imaging, Manip. Anal. Biomol. Cells, Tissues VI, 68590V*, vol. 6859, pp. 187–198, Feb. 2008, doi: 10.1117/12.764037.
- [7] J. Fattaccioli *et al.*, "Size and fluorescence measurements of individual droplets by flow cytometry," *Soft Matter*, vol. 5, no. 11, pp. 2232–2238, May 2009, doi: 10.1039/B814954B.
- [8] M. Li, H. Liu, S. Zhuang, and K. Goda, "Droplet flow cytometry for single-cell analysis," *RSC Adv.*, vol. 11, no. 34, pp. 20944–20960, Jun. 2021, doi: 10.1039/D1RA02636D.
- [9] M. Vitelli, H. Budman, M. Pritzker, and M. Tamer, "Applications of flow cytometry sorting in the pharmaceutical industry: A review," *Biotechnol. Prog.*, vol. 37, no. 4, p. 17, Jul. 2021, doi: 10.1002/BTPR.3146.
- [10] H. Yang *et al.*, "A droplet-based microfluidic flow cytometry enabling absolute quantification of single-cell proteins leveraging constriction channel," *Microfluid. Nanofluidics*, vol. 25, no. 4, pp. 1–11, Apr. 2021, doi: 10.1007/S10404-021-02427-W/FIGURES/5.
- [11] W. Han and X. Chen, "A review on microdroplet generation in microfluidics," *J. Brazilian Soc. Mech. Sci. Eng.*, vol. 43, no. 5, pp. 1–12, May 2021, doi: 10.1007/S40430-021-02971-0/FIGURES/7.
- [12] N. Gyimah, O. Scheler, T. Rang, and T. Parfy, *Digital twin for controlled generation of water-in-oil microdroplets with required size*. IEEE, 2022, pp. 1–7. doi: 10.1109/EuroSimE54907.2022.9758876.
- [13] "Web of Science. 2022. The Clarivate Web of Science™ publisher-independent global citation database." <https://clarivate.com/webofsciencegroup/solutions/web-of-science/> (accessed Apr. 24, 2022).
- [14] H. Hjalmarsson, M. Gevers, and F. De Bruyne, "For model-based control design, closed-loop identification gives better performance," *Automatica*, vol. 32, no. 12, pp. 1659–1673, Dec. 1996, doi: 10.1016/S0005-1098(96)80003-3.
- [15] J. C. Jensen, D. H. Chang, and E. A. Lee, "A model-based design methodology for cyber-physical systems," *IWCMC 2011 - 7th Int. Wirel. Commun. Mob. Comput. Conf.*, pp. 1666–1671,

- 2011, doi: 10.1109/IWCMC.2011.5982785.
- [16] C. K. Harnett, J. Templeton, K. A. Dunphy-Guzman, Y. M. Senousy, and M. P. Kanouff, "Model based design of a microfluidic mixer driven by induced charge electroosmosis," *Lab Chip*, vol. 8, no. 4, pp. 565–572, Mar. 2008, doi: 10.1039/B717416K.
- [17] A. Savran and G. Kahraman, "A fuzzy model based adaptive PID controller design for nonlinear and uncertain processes," *ISA Trans.*, vol. 53, no. 2, pp. 280–288, Mar. 2014, doi: 10.1016/J.ISATRA.2013.09.020.
- [18] James R. Thompson, *Empirical Model Building: Data, Models, and Reality*, 2nd ed. Hoboken, New Jersey: John Wiley & Sons, Inc, 2011.
- [19] P. A. Fritzon, *Introduction to modeling and simulation of technical and physical systems with Modelica*. John Wiley & Sons, Inc, 2011.
- [20] X. Chen, T. Glawdel, N. Cui, and C. L. Ren, "Model of droplet generation in flow focusing generators operating in the squeezing regime," *Microfluid. Nanofluidics*, vol. 18, no. 5–6, pp. 1341–1353, May 2015, doi: 10.1007/s10404-014-1533-5.
- [21] A. Biral, D. Zordan, and A. Zanella, "Modeling, Simulation and Experimentation of Droplet-Based Microfluidic Networks," *IEEE Trans. Mol. Biol. Multi-Scale Commun.*, vol. 1, no. 2, pp. 122–134, Jun. 2015, doi: 10.1109/TMBMC.2015.2500569.
- [22] M. Wörner, "Numerical modeling of multiphase flows in microfluidics and micro process engineering: a review of methods and applications," *Microfluid. Nanofluidics 2012 126*, vol. 12, no. 6, pp. 841–886, Mar. 2012, doi: 10.1007/S10404-012-0940-8.
- [23] J. Kim, "Phase-Field Models for Multi-Component Fluid Flows," *Commun. Comput. Phys.*, vol. 12, no. 3, pp. 613–661, Sep. 2012, doi: 10.4208/CICP.301110.040811A.
- [24] A. Lashkaripour, C. Rodriguez, L. Ortiz, and D. Densmore, "Performance tuning of microfluidic flow-focusing droplet generators," *Lab Chip*, vol. 19, no. 6, pp. 1041–1053, Mar. 2019, doi: 10.1039/C8LC01253A.
- [25] M. Rahimi, S. Yazdanparast, and P. Rezaei, "Parametric study of droplet size in an axisymmetric flow-focusing capillary device," *Chinese J. Chem. Eng.*, vol. 28, no. 4, pp. 1016–1022, Apr. 2020, doi: 10.1016/J.CJCHE.2019.12.026.
- [26] A. Khater, M. Mohammadi, A. Mohamad, and A. S. Nezhad, "Dynamics of temperature-actuated droplets within microfluidics," *Sci. Reports 2019 91*, vol. 9, no. 1, pp. 1–11, Mar. 2019, doi: 10.1038/s41598-019-40069-9.
- [27] S. L. Anna, "Droplets and Bubbles in Microfluidic Devices," <https://doi.org/10.1146/annurev-fluid-122414-034425>, vol. 48, pp. 285–309, Jan. 2016, doi: 10.1146/ANNUREV-FLUID-122414-034425.
- [28] A. Lashkaripour *et al.*, "Machine learning enables design automation of microfluidic flow-focusing droplet generation," *Nat. Commun. 2021 121*, vol. 12, no. 1, pp. 1–14, Jan. 2021, doi: 10.1038/s41467-020-20284-z.
- [29] A. Grimmer, M. Hamidović, W. Haselmayr, and R. Wille, "Advanced Simulation of Droplet Microfluidics," *ACM J. Emerg. Technol. Comput. Syst.*, vol. 15, no. 3, Apr. 2019, doi: 10.1145/3313867.
- [30] C. N. Baroud, F. Gallaire, and R. Dangla, "Dynamics of microfluidic droplets," *Lab Chip*, vol. 10, no. 16, pp. 2032–2045, Jul. 2010, doi: 10.1039/C001191F.
- [31] W. Lee, L. M. Walker, and S. L. Anna, "Role of geometry and fluid properties in droplet and thread formation processes in planar flow focusing," *Phys. Fluids*, vol. 21, no. 3, p. 032103, Mar. 2009, doi: 10.1063/1.3081407.
- [32] "COMSOL Multiphysics® 5.6, Laminar Flow and Two-Phase Flow, Level Set modules. Two-Phase Flow modeling guidelines." <https://www.comsol.com/support/knowledgebase/1239> (accessed May 03, 2022).
- [33] A. Udal, M. Jurise, J. Kaugerand, and R. Sell, "COMSPECT – a compact model of green vegetation reflectance spectra in the 400–900 nm wavelength range," *Proc. Est. Acad. Sci. Vol. 69, No. 4*, pp. 277–286, 2022.
- [34] G. Gildenblat, *Compact modeling: Principles, techniques and applications*. Springer Netherlands, 2010, doi: 10.1007/978-90-481-8614-3/COVER.
- [35] A. S. Bedekar, Y. Wang, S. Krishnamoorthy, S. S. Siddhaye, and S. Sundaram, "System-level simulation of flow-induced dispersion in lab-on-a-chip systems," *IEEE Trans. Comput. Des. Integr. Circuits Syst.*, vol. 25, no. 2, pp. 294–303, Feb. 2006, doi: 10.1109/TCAD.2005.858354.
- [36] F. Lapiere, N. Wu, and Y. Zhu, *Influence of flow rate on the droplet generation process in a microfluidic chip*, vol. 8204. SPIE, 2011, p. 8, doi: 10.1117/12.903271.
- [37] F. Ender, M. Németh, P. Pálóvics, A. Drozdy, and A. Poppe, "Thermal compact modeling approach of droplet microreactor based Lab-on-a-Chip devices," *Microelectronics J.*, vol. 45, no. 12, pp. 1786–1794, Dec. 2014, doi: 10.1016/J.MEJO.2014.07.005.
- [38] A. Bonament, M. Madec, and C. Lallement, "Compact modeling of reaction-diffusion-advection mechanisms for the virtual prototyping of lab-on-chip," in *Proceedings - IEEE International Symposium on Circuits and Systems*, 2021, vol. 2021-May, doi: 10.1109/ISCASS1556.2021.9401396.
- [39] K. I. Belousov, N. A. Filatov, I. V. Kukhtevich, V. Kantsler, A. A. Evstrapov, and A. S. Bukatin, "An asymmetric flow-focusing droplet generator promotes rapid mixing of reagents," *Sci. Reports 2021 111*, vol. 11, no. 1, pp. 1–10, Apr. 2021, doi: 10.1038/s41598-021-88174-y.
- [40] A. E. Siemenn, E. Shaulsky, M. Beveridge, T. Buonassisi, S. M. Hashmi, and I. Drori, "A Machine Learning and Computer Vision Approach to Rapidly Optimize Multiscale Droplet Generation," *ACS Appl. Mater. Interfaces*, vol. 14, no. 3, pp. 4668–4679, Jan. 2022, doi: 10.1021/ACSAMI.1C19276/ASSET/IMAGES/LARGE/AM1C19276_M067.JPEG.
- [41] S. Srikanth, S. K. Dubej, A. Javed, and S. Goel, "Droplet based microfluidics integrated with machine learning," *Sensors Actuators A Phys.*, vol. 332, p. 113096, Dec. 2021, doi: 10.1016/J.SNA.2021.113096.
- [42] "Sigma-Aldrich Mineral Oil. Sigma-Adrich Mineral Oil 330779-1L data page." <https://www.sigmaaldrich.com/EE/en/product/sial/330779> (accessed May 03, 2022).
- [43] "Sigma-Aldrich surfactant. Sigma-Adrich Span® 80 (code 840123100) data page." <https://www.sigmaaldrich.com/EE/en/product/mm/840123> (accessed May 03, 2022).
- [44] "SpinSplit. Lab equipment for academic research." <https://spinsplit.com/spincube/> (accessed May 03, 2022).
- [45] W. L. Ong *et al.*, "Experimental and computational analysis of droplet formation in a high-performance flow-focusing geometry," *Sensors Actuators A Phys.*, vol. 138, no. 1, pp. 203–212, Jul. 2007, doi: 10.1016/J.SNA.2007.04.053.
- [46] "Surface tension values of some common test liquids for surface energy analysis." <http://www.surface-tension.de/> (accessed May 03, 2022).



KAISER PÄRNAMETS (Student Member, IEEE) was born in Tallinn, Estonia, in January 1989. He received Bachelor of Science in Engineering in 2013 and Master of Science in Engineering in 2016 from the Tallinn University of Technology. In 2016 he started his PhD studies in Tallinn University of Technology. In the years of 2014 to 2017 he was hardware engineer in the electronics industry and since 2018 he has been an electronics lecturer for Bachelor and Master students. His research interests include Lab-on-a-chip and microfluidics.



ANDRES UDAL (Member, IEEE) received the PhD degree in electrical engineering from the Tallinn University of Technology, Tallinn, Estonia, in 1999. He is currently a Senior Research Fellow at the Department of Software Science, Laboratory for Proactive Technologies at Tallinn University of Technology. From 1990 to 1995 he was acting as a visiting researcher and TCAD software designer in Silvaco Int, California, USA, in Darmstadt University of Technology, Germany

and in Uppsala University, Sweden.



ANTS KOEL. (Member, IEEE) was born in Tallinn, Estonia, in August 1962. He received the engineer diploma in industrial electronics from the Tallinn Polytechnic Institute, Estonia, 1980-85, the master's degree in 1998, and the Ph.D. degree from the Tallinn University of Technology, Tallinn, Estonia, in 2014. He has been the Chairman of the Steering Committee of the IEEE-Sponsored Baltic Electronics Conference in 2020 and 2022, participated in ERA Chair projects COEL and 5GSOLAR, led electronics in-kind contribution projects of Estonia in European

Spallation Source. His research interests include semiconductor electronics and devices, TCAD simulations and circuit design.



TAMÁS PARDY received the M.Sc. degree in info-bionics engineering from Peter Pazmany Catholic University, Budapest, Hungary, in 2014, and the Ph.D. degree in electronics and telecommunication from Tallinn University of Technology, Tallinn, Estonia, in 2018. He is currently a senior researcher at Tallinn University of Technology. He has supervised 1 PhD thesis and 3 M.Sc. theses and has authored or co-authored 20 scientific publications. His research interests

include flow- and temperature-control of Lab-on-a-Chip devices.



NAFISAT GYIMAH. received a B.S. in electrical and electronic engineering from Kwame Nkrumah University of Technology in Kumasi, Ghana, in 2013, and an M.S. in communicative electronics from Tallinn University of Technology in Tallinn, Estonia, in 2020. She is currently pursuing a Ph.D. at the Tallinn University of Technology in high-speed droplet microfluidics sorting and encapsulation. Her research interests include lab-on-a-chip, droplet microfluidic system control, and flow control simulations using computational fluid dynamics (CFD). From November 2021 to January

2022, she worked at SelfDiagnostics Deutschland GmbH on the thermal and electrical characterization of SARS-CoV2 microfluidic multitest kits. She was a cognitronics engineer at the Tallinn University of Technology from June to December 2020.).



TOOMAS RANG. (Senior Member, IEEE) received a Ph.D. degree in semiconductor electronics from the Hungarian Academy of Sciences in 1981. He is currently Professor Emeritus at the Thomas Johann Seebeck Department of Electronics, and a senior research fellow at the Department of Chemistry and Biotechnologies, Tallinn University of Technology, Estonia. Research activities related to R&D in the field of applied microfluidic approaches for lab-on-a-chip applications. He supervised 15 PhD students and fulfilled the PI position on several European and domestic research and industrial projects. He was the initiator and honor chairman of the Baltic Electronics Conferences (BEC) series in 1987, and has been supported by IEEE since 1996.

Images and figures:

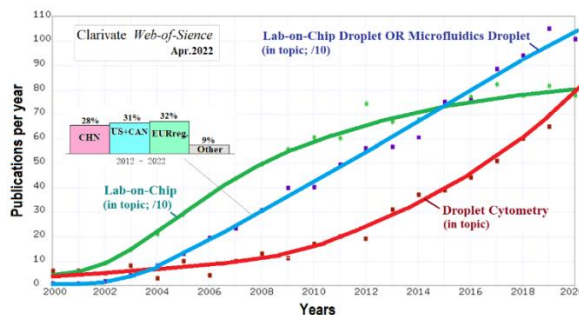


Figure 1. Research intensity trends on basis of Clarivate Web of Science publication statistics [13]. Dynamics of the most relevant subfields as Lab-on-Chip, droplet microfluidics and droplet cytometry is compared. Inlet compares contributions from People's Republic of China, North America and European region (incl. Turkey and Israel).

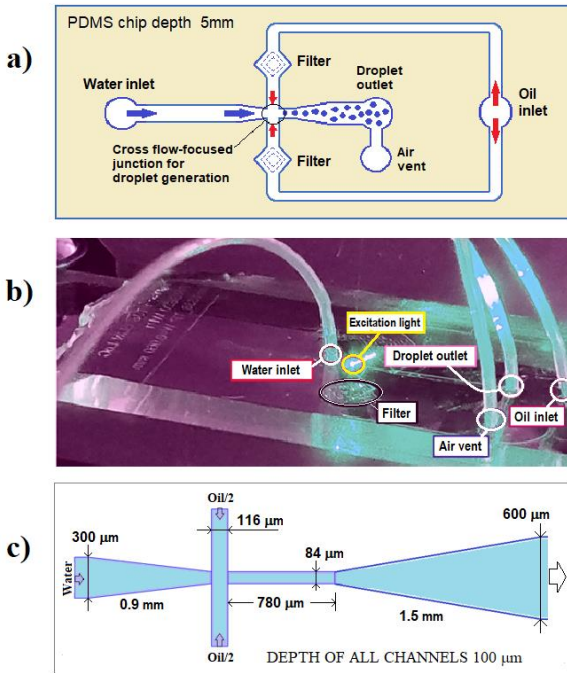


Figure 2. Description of the droplet generation PDMS chip: a) Water droplets generation scheme in the flow focusing cross-junction; b) Photo of the setup with inlet and outlet tubes and photorecording area; c) Exact dimensions of channels near the flow focusing junction.

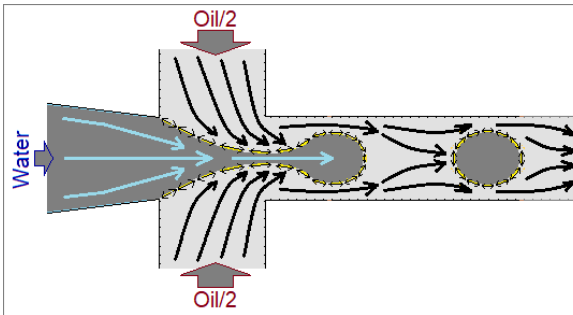


Figure 3. Illustration of competing processes of water droplets generation in a flow-focusing cross-junction. The incoming water stream tries to maintain the minimum surface area due to the surface tension forces but is divided into droplets by the “oil pliers” acting from both sides. After that the surface tension helps to maintain the size of droplets already formed, provided that the adjacent droplets are at a sufficient distance. At that all flow speeds are decelerated near the walls because of the wall friction effect.

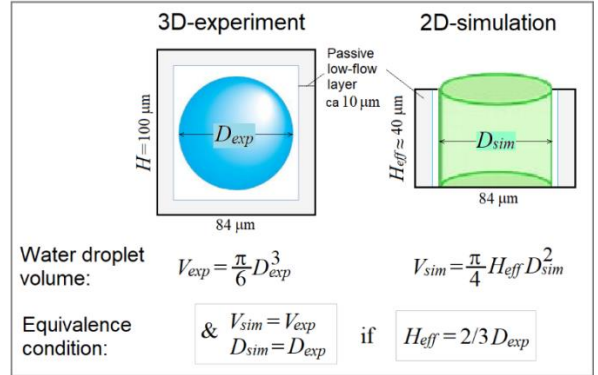


Figure 4. Graphical representation of droplet volumes in real life 3D-experiment and in simplified 2D-simulation.

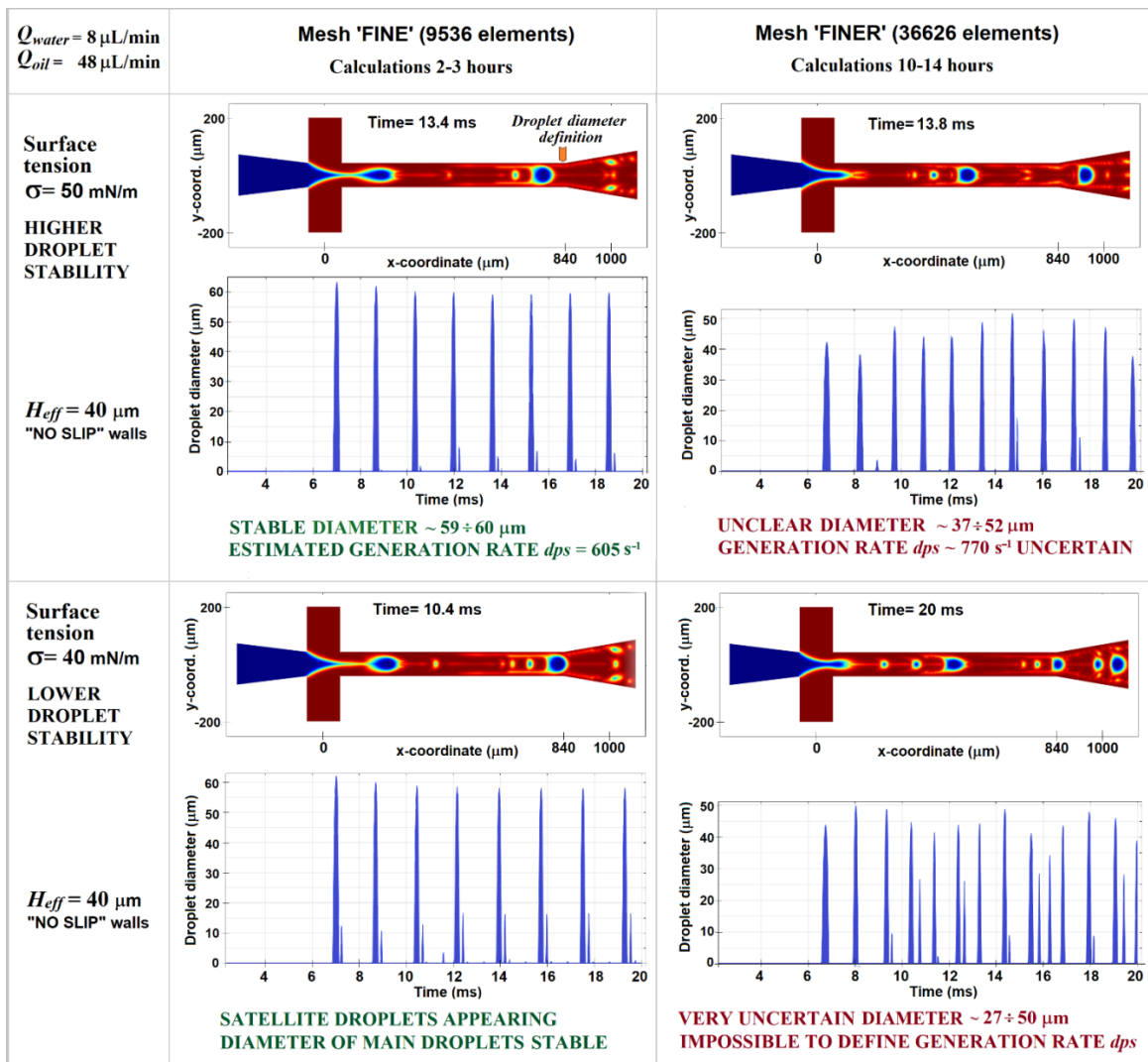


Figure 5. Illustration of appearance of droplet generation instabilities in detailed physical 2D-simulations with COMSOL 5.6 [32].

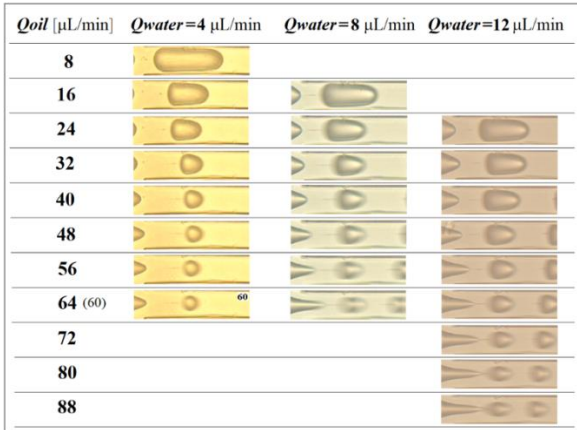


Figure 6. Summary of droplet photos for different water and oil flow rate values in beginning section of 84 μm generation channel. Different coloring is caused by slightly changed LED lighting between experimental series. The transform from bullet-like shapes at low oil flow rates to spherical shapes at high oil flow rates may be observed. Increasing blur of photos at high oil flow rates is caused by camera shutter time 100 μs .

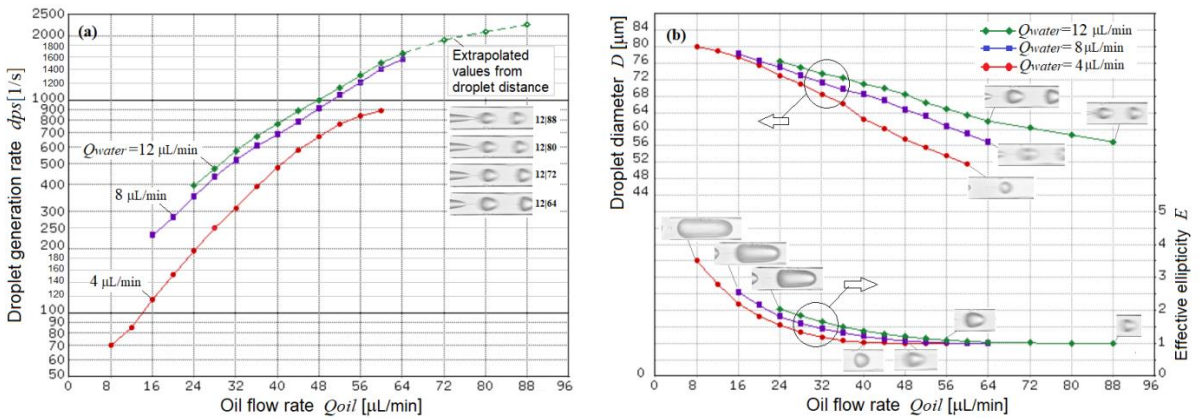


Figure 7. Overall summary of experimental results for droplet generation rates (a) and droplet diameters and ellipticities (b).

TABLE 1. THE BEST FIT COMPACT MODEL PARAMETER VALUES FOR CONSIDERED 3 WATER FLOW RATES.

Water rate series index i	Water flow rate $Q_{w,i}$, $\mu\text{L}/\text{min}$	Ellipticity $E_{B,i}$ at low oil rate $Q_{oil} = 8 \mu\text{L}/\text{min}$	Exponential decay parameter of ellipticity $Q_{E,i}$, $\mu\text{L}/\text{min}$	Linear decay parameter of droplet diameter $Q_{D,i}$, $\mu\text{L}/\text{min}$
1	4	2.6	9.9	157
2	8	3.6	10.4	196
3	12	4.15	12.4	248

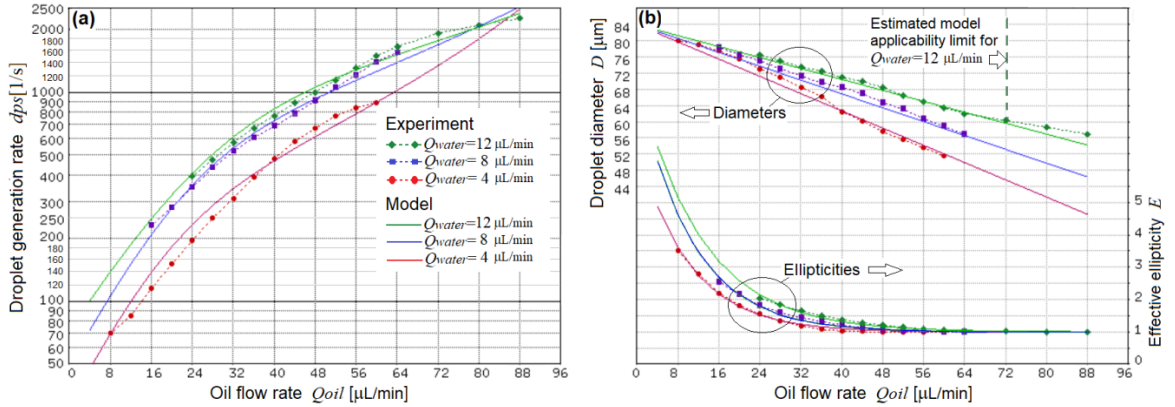


Figure 8. The summary of fitting results of compact empirical model (4)-(6) against experimental points for 3 water flow rate values: droplet generation rates (a); droplet diameters and ellipticities (b). Model results are presented by solid lines, experimental points by dotted lines.

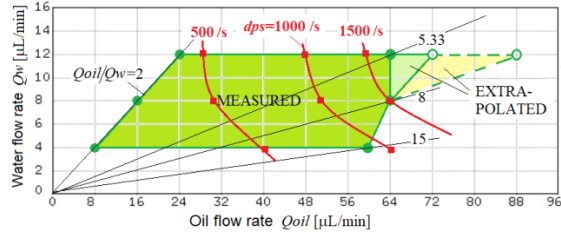


Figure 9. The illustration of application area of compact empirical model on the plane of water and oil flow rates.

Appendix 5

V

N. Gyimah, O. Scheler, T. Rang, and T. Pardy, "Deep reinforcement learning-based digital twin for droplet microfluidics control," *Physics of Fluids*, vol. 35, no. 8, 2023

Deep reinforcement learning-based digital twin for droplet microfluidics control

Cite as: Phys. Fluids **35**, 082020 (2023); doi: 10.1063/5.0159981

Submitted: 29 May 2023 · Accepted: 10 August 2023 ·

Published Online: 24 August 2023



View Online



Export Citation



CrossMark

Nafisat Gyimah,^{1,a)}  Ott Scheler,^{2,b)}  Toomas Rang,^{2,c)}  and Tamás Pardy^{2,d)} 

AFFILIATIONS

¹Thomas Johann Seebeck Department of Electronics, Tallinn University of Technology, Tallinn, Estonia

²Department of Chemistry and Biotechnology, Tallinn University of Technology, Tallinn, Estonia

^{a)} Author to whom correspondence should be addressed: nafisat.gyimah@taltech.ee

^{b)} Electronic mail: Ott.Scheler@taltech.ee

^{c)} Electronic mail: Toomas.Rang@taltech.ee

^{d)} Electronic mail: Tamas.Pardy@taltech.ee

ABSTRACT

This study applied deep reinforcement learning (DRL) with the Proximal Policy Optimization (PPO) algorithm within a two-dimensional computational fluid dynamics (CFD) model to achieve closed-loop control in microfluidics. The objective was to achieve the desired droplet size with minimal variability in a microfluidic capillary flow-focusing device. An artificial neural network was utilized to map sensing signals (flow pressure and droplet size) to control actions (continuous phase inlet pressure). To validate the numerical model, simulation results were compared with experimental data, which demonstrated a good agreement with errors below 11%. The PPO algorithm effectively controlled droplet size across various targets (50, 60, 70, and 80 μm) with different levels of precision. The optimized DRL + CFD framework successfully achieved droplet size control within a coefficient of variation (CV%) below 5% for all targets, outperforming the case without control. Furthermore, the adaptability of the PPO agent to external disturbances was extensively evaluated. By subjecting the system to sinusoidal mechanical vibrations with frequencies ranging from 10 Hz to 10 KHz and amplitudes between 50 and 500 Pa, the PPO algorithm demonstrated efficacy in handling disturbances within limits, highlighting its robustness. Overall, this study showcased the implementation of the DRL+CFD framework for designing and investigating novel control algorithms, advancing the field of droplet microfluidics control research.

Published under an exclusive license by AIP Publishing. <https://doi.org/10.1063/5.0159981>

I. INTRODUCTION

Droplet microfluidics is increasingly used for biomedical and biochemical applications due to its microengineering capabilities¹ and high-precision analysis.² However, the performance of microfluidic devices is inconsistent due to their sensitivity to various factors, including fluid pressure fluctuations and fluid properties.^{3,4} As a result, it is essential to monitor and regulate these factors to achieve and maintain the desired performance. Flow control, which involves adjusting the flow behavior using actuators or fluid pumping systems, is a commonly used approach to achieve a desired performance. Tuning droplet size,⁵ reducing size variations,⁶ and positioning flow interfaces⁷ are common practices. Closed-loop flow control is considered superior to open-loop techniques due to its ability to adapt to real-time changes in flow conditions, leading to enhanced accuracy and precision.⁶ However, classical closed-loop control typically relies on explicit mathematical models, which can be challenging to derive for complex

systems⁸ like microfluidic systems that can exhibit nonlinear behavior. Moreover, once the models are derived, tuning the control parameters becomes another intricate task that necessitates expert knowledge and experience.

Recent studies suggest that machine learning (ML) techniques, particularly deep reinforcement learning (DRL), can overcome these challenges by employing trial-and-error learning and neural networks to represent complex and nonlinear functions without explicit models,⁹ making DRL a promising technique for efficient regulation of microfluidics.

Microfluidics has successfully adopted reinforcement learning for several control tasks, such as flow sculpting,^{10,11} laminar flow interface positioning,¹² and droplet sorting.¹³ However, the control of droplet size has received limited attention, with only one study using deep reinforcement learning. Dressler *et al.*¹² utilized two reinforcement learning algorithms, DQN (Deep Q-Network) and MFEC (model-free

episodic controller), to control laminar flow and droplet size, with five discrete actions to adjust fluid flow rates at a fixed step size of $0.5 \mu\text{l}/\text{min}$. The DRL algorithms achieved the target droplet size of $54 \mu\text{m}$ while outperforming human operators.

The traditional method for regulating droplet size in microfluidics is through the use of a PID (Proportional-Integral-Derivative) controller.^{5,14} While incorporating a PID controller in a droplet microfluidic system for closed-loop droplet size control has shown improvements in device performance in several studies, including our previous works,^{15,16} it requires a precise mathematical model of the controlled system, which can be challenging. Additionally, feedback control performance may result in relatively long settling times,^{5,14} high coefficient of variation (CV%) in droplet size,¹⁷ or high transient overshoot.¹⁸ A summary of the current state-of-the-art for closed-loop droplet size control is shown in Table I.

Previous studies^{11,12,21} on applying deep reinforcement learning (DRL) algorithms in microfluidics have relied on algorithms that control the system using discrete or discretized actions. However, for droplet size control in passive microfluidics, which inherently involves continuous flow dynamics,^{22,23} a more intuitive approach is to implement a smooth and continuous adjustment of control inputs to achieve the desired output. Discrete or discretized control machine learning algorithms can only provide a limited number of predefined control actions, which may not be sufficient to achieve accurate and stable control of droplet size. Thus, equally advanced algorithms that utilize continuous control actions algorithms, such as Trust Region Policy Optimization (TRPO), Proximal Policy Optimization (PPO), Deep Deterministic Policy Gradient (DDPG), and Soft Actor-Critic (SAC), are more suitable. Among these algorithms, the Proximal Policy Optimization (PPO) approach²⁴ has emerged as the state-of-the-art algorithm for continuous control. It has been effectively applied in computational fluid dynamics (CFD) + DRL research, addressing flow control challenges in turbulent settings, such as lift augmentation, drag reduction,²⁵ and flow-induced vibration suppression.⁸ Despite PPO's demonstrated success in various applications, its potential for microfluidic flow control has not yet been explored.

The Proximal Policy Optimization (PPO) algorithm is a deep reinforcement learning technique that is model-free and well-suited for controlling highly sensitive environments where small changes in the actions taken can have a big impact on the outcomes. This study focuses on utilizing Proximal Policy Optimization (PPO) as a control method for precise droplet size regulation in microfluidics. Droplet

size control is critical across various applications, including drug delivery, biochemical assays, material synthesis, and cell analysis.²⁶ Previous investigations have underscored the substantial effect of droplet size on critical factors such as the division and viability of cells from mammalian organisms during their cultivation within droplets.²⁷

Section II describes the methodology and model setup for applying PPO in droplet size control. Section III presents the analysis and discussion of the results. In Sec. IV, we provide a summary of findings and insights, along with future research directions.

II. METHODOLOGY

A. Flow model and governing equations

In our study, we utilized a microfluidic device model that closely resembled the one used in our prior work.¹⁵ The model consisted of a two-dimensional capillary flow-focusing device (FFD) with two inlets for continuous phase fluid: one inlet for the dispersed phase fluid and an outlet. To introduce the immiscible fluids (dispersed phase and continuous phase) into the microchannels, pressure was applied to their respective inlets. The configuration shown in Fig. 1(a) involved the dispersed phase entering through a 0.6 mm wide central inlet channel, while the continuous phase was fed through two side channels, each 0.12 mm wide. The dispersed phase inlet and outlet channels had diverging and converging bifurcations with widths of 0.6 , 0.3 , and 0.09 mm at the inlet, and 0.09 and 0.6 mm at the outlet. Droplets formed when the two fluid phases interacted at a 0.09 mm wide junction [Fig. 1(b)].

To obtain precise pressure profiles of the flow field in the microchannel, we utilized point probes as sensors at different locations within the channel, which are denoted as red dots in Fig. 1(a). In practical physical models, these probes are substituted with pressure sensors well positioned at the inlets, outlets, or both, connected to the microchannel through connecting tubes.

To achieve accurate control over droplet size, we integrated pressure and droplet diameter measurements as sensing parameters in our Deep Reinforcement Learning (DRL) model. By incorporating the droplet diameter, which serves as the controlled variable, as an additional sensing parameter alongside pressure measurements in our artificial neural network (ANN) model, we can implicitly account for the effects of various factors, such as flow rates, interfacial tension, and viscosities. These factors can be characterized by non-dimensional numbers, including the flow rate ratio, viscosity ratio, capillary number (Ca), and Reynolds number.²⁸ Through this integration, we

TABLE I. State-of-the-art approaches for closed-loop microfluidic droplet size control.

Work	CV% or R^2	Response time	Controller	Droplet size (μm)	Experiment or simulation
Present work	<5%	...	PPO	50–80	Sim. (OpenFOAM + PyTorch)
15	$R^2 = 0.993$...	PID	30–60	Sim. (COMSOL + MATLAB)
17	<7.6%	...	PID	0.2–2 nl	Exp.
19	2%	<0.2 s	PI	...	Exp.
14	$R^2 = 0.999$	7–10 s	PID	150, 200, 250	Exp.
20	...	10 s	PI	14–24	Exp.
5	...	>100 s	PID	200–400	Exp.
12	...	27 h	DQN	54	Exp.
12	...	Few minutes	MFEC	54	Exp.

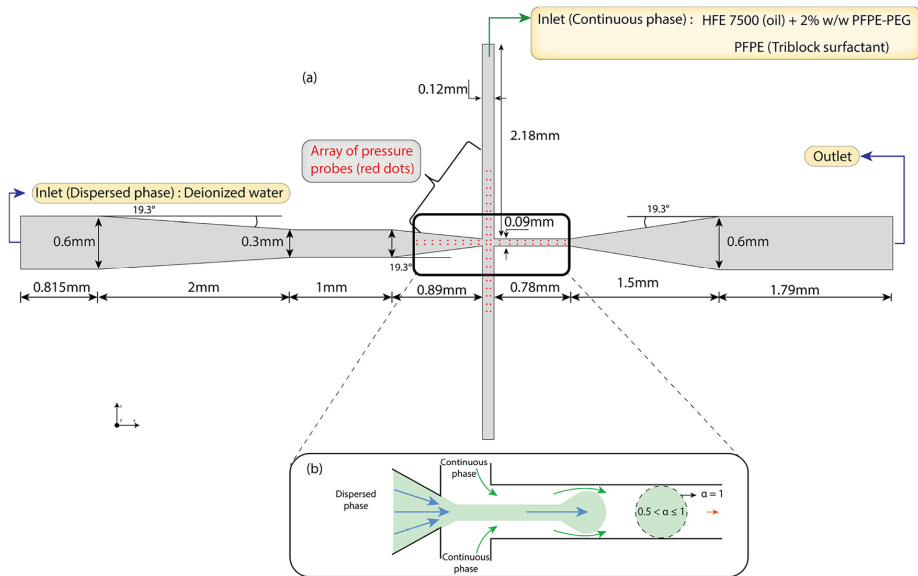


FIG. 1. The two-dimensional flow-focusing device used in this study. (a) The FFD dimensions, critical flow region, and the configuration of pressure-sensing probes (red dots). (b) The interaction of fluid phases for droplet formation, with the droplet interface designated based on the volume fraction function $\alpha \geq 0.5$.

eliminate the need for extensive modifications or additional sensor probes.

Furthermore, past research underscores a wide range of fluids suitable for single and compound drop generation, encompassing both Newtonian and non-Newtonian behaviors. Key dimensionless groups, including Weber and Laplace numbers derived from Reynolds and Capillary numbers, offer insights into the intricate fluid dynamics. The significance of the Deborah number in viscoelastic fluid scenarios is also highlighted.²⁹ Investigations delve into the role of fluid elasticity in droplet behavior,³⁰ surfactant effects on droplet motion,^{31,32} and pertinent electrophysical attributes within microfluidics.³³

The impact of these factors on droplet size has been consistently illustrated in preceding studies. Increasing the capillary number (Ca) generally leads to smaller droplets, while higher viscosity ratios result in larger droplets.³⁴ The flow rate ratio typically influences droplet size, except in the dripping regime at higher Ca values, where it becomes independent of the flow rate ratio.^{2,35} Additionally, higher interfacial tension is associated with larger droplets but reduced formation frequency.³ Importantly, the relative influence of these factors depends on the specific flow conditions, as demonstrated in the literature. By incorporating both pressure and measured droplet size as sensing parameters, our deep learning-aided droplet generation control effectively regulates the input oil pressure (i.e., the manipulated variable) and adapts to environmental changes, thereby optimizing droplet size control under varying conditions.

To model and analyze the behavior of the two-phase flow in our system, we employed the Volume of Fluid (VOF) method, which has been used in previous works.^{2,36,37} This method uses the volume

fraction function α , ranging from 0 to 1, to represent fluid phases and interfaces. In our simulation, we set $\alpha = 0$ for the fluid 1-continuous phase (oil) and $\alpha = 1$ for the fluid 2-dispersed phase (water). The droplet interface was defined as $\alpha \geq 0.5$, as reported in the literature³⁸ and shown in Fig. 1(b). The Volume of Fluid (VOF) method solves the governing equations of the two-phase flow system, which include continuity (1), momentum balance (2), and volume fraction Eq. (3). These equations are based on the assumption that the two-phase fluids are incompressible,^{37,39}

$$\nabla \cdot u = 0, \tag{1}$$

$$\rho \left(\frac{\partial u}{\partial t} + u \cdot \nabla u \right) = -\nabla p + \rho g + \nabla \cdot [\mu(\nabla u + \nabla^T u) + F\sigma], \tag{2}$$

$$\frac{\partial \alpha}{\partial t} + \nabla \cdot (\alpha u) = 0, \tag{3}$$

where u represents the velocity vector, ρ is the density, t represents time, p denotes pressure, g denotes gravitational force, μ is the dynamic viscosity, and $F\sigma$ denotes the continuum surface tension. The volumetric density ρ and viscosity μ in Eq. (2) are computed as weighted averages of the fluid densities and dynamic viscosities, respectively, over the volume fraction function,

$$\rho = \rho_1 \alpha + \rho_2 (1 - \alpha), \tag{4}$$

$$\mu = \mu_1 \alpha + \mu_2 (1 - \alpha). \tag{5}$$

Here, subscripts 1 and 2 represent the continuous phase fluid and dispersed phase fluid, respectively. To improve the resolution of phase interfaces and minimize numerical diffusion, an artificial interface

compression velocity, μ_r , was introduced in Eq. (6) to enhance the volume fraction Eq. (3),

$$\frac{\partial \alpha}{\partial t} + \nabla \cdot (\alpha u) + \nabla \cdot (u_r (\alpha(1 - \alpha))) = 0. \quad (6)$$

However, μ_r only affects the interface region where $0 < \alpha < 1$ and is defined as

$$u_r = u_d - u_c = \min(C_x |u|, \max|u|) \frac{\nabla \cdot \alpha}{|\nabla \cdot \alpha|}. \quad (7)$$

The compression factor C_x determines the degree of compression at the interface and can range from 0 to 4, although $C_x = 1$ is commonly used in microfluidics research.^{40–42} Higher values of C_x tend to increase nonphysical spurious currents, which can cause numerical modeling errors.⁴³

The last term in Eq. (2), $F\sigma$, is modeled using the continuum surface force (CSF) approach developed by Brackbill *et al.*,⁴⁴

$$F\sigma = \sigma k(\nabla \alpha), \quad (8)$$

where k is the interfacial curvature. The governing equations, represented by Eqs. (1)–(3) and expanded into Eqs. (4)–(8), provide the foundation for modeling and analyzing the behavior of the two-phase flow systems.

The continuous phase fluid is composed of HFE 7500 (oil) with a 2% w/w PFPE-PEG-PFPE surfactant, while the dispersed phase is de-ionized water, and the interfacial tension between the fluids is set at 0.005 N/m.⁴⁵ The microscale size of the microfluidic device and low Reynolds number condition⁴⁶ result in laminar flow for these highly viscous fluids. Both the continuous and dispersed phases exhibit Newtonian fluid behavior, with their respective material properties listed in Table II.

B. Numerical setup

The VOF method was used to simulate two-phase flows using the interFoam solver in the OpenFOAM software. To maintain numerical stability and mass conservation, the MULES (Multidimensional Universal Limiter Equation Solver) technique was employed to limit the volume fraction field within the range of 0 and 1 during simulation.^{48,49} The momentum and continuity equations were solved using the pressure-velocity coupling algorithm, PIMPLE (Pressure Implicit with Operator Splitting Multi-Phase Implicit), which combines the PISO (Pressure Implicit with Splitting of Operator) and SIMPLE (Semi Implicit Method for Pressure-Linked Equations) to allow for explicit relaxation of variables and implicit equations.⁵⁰ The temporary terms were discretized using first order Euler scheme, and the divergence terms were discretized using the Gauss linear scheme. The remaining terms, gradient terms and Laplacian terms were discretized using leastSquares and Gauss linear,

respectively. Additional details on the discretization schemes can be found in the OpenFOAM documentation.⁵¹

To maintain numerical stability, the time steps were adjusted automatically according to the maximum Courant number, MaxCo, which was set to 0.5, and the maximum Courant number allowed for the phase-fraction transport equation, AlphaMaxCo, which was set to 0.25. Previous studies have shown that setting MaxCo to be less than 0.6 is effective in ensuring numerical stability in laminar flow microfluidic simulations.⁴³

The boundary conditions for the simulation were set up as follows: a constant total pressure of 0 was applied as the outlet boundary condition, ensuring a zero-gradient velocity. At the inlet of the dispersed phase, a constant pressure of 6000 Pa was imposed. A Custom pressure boundary condition was applied to generate an action vector for the continuous phase inlets based on the current network parameters of the DRL algorithm. During the training phase, this action vector was considered the mean of a multivariate Beta distribution, allowing for exploration and learning of the optimal control policy. However, during the testing phase, the behavior of the action vector became predictable, acting as the oil inlet boundary condition without requiring any further policy updates.

The solid wall was set to a no-slip boundary condition with a fixed fluid-wall contact angle of 135°. In 2D microfluidics simulations, the assumption of complete wall wetting with continuous phase fluid is valid since the length of the microchannel is usually much greater than its width, resulting in negligible flow in the corners. The application of this assumption can be seen in the literature^{40,52} and has been validated.^{53,54}

The mesh was generated using OpenFOAM’s blockMesh and snappyHexMesh tools and consists of mainly hexahedral cells with a relatively low number of prisms and polyhedral cells. The base mesh, created by the blockMesh tool, has 2500 cells in the x-direction, 600 cells in the y-direction, and 300 cells in the z-direction per 1 mm. A refinement region was created at the intersection to capture accurate physics of the flow where high gradients are expected. The dimensions of the refinement region were set to be 15D × 5.5D × 3.4D, where D is the width of the oil inlet channel in micrometers, and were centered 5D × 2.3D × 1.7D from the microchannel junction.

C. Droplet size estimation

To estimate droplet sizes *in situ*, we used OpenFOAM’s Python/C API and NumPy for postprocessing purposes. The field data of interest was the volume fraction function. To set the sampling criteria and output file format, the Sets function object in OpenFOAM package⁵¹ was added to the ControlDict dictionary. The output data consisted of 1000 data points along a sampling line at the channel outlet depicted in Fig. 2. The data were saved in raw ASCII format at 0.5 ms intervals. To postprocess the results, during runtime, we used an external Python script executed through the Function Object systemCall.

TABLE II. Material properties of fluids.

Material	Dynamic viscosity (Pa s)	Density (kg/m ³)	Interfacial tension (N/m)
De-ionized water	1e − 3	1000	
HFE-7500 + 2% w/w PFPE-PEG-PFPE	7.7e − 4 (Ref. 47)	1614	0.005 (Ref. 45)

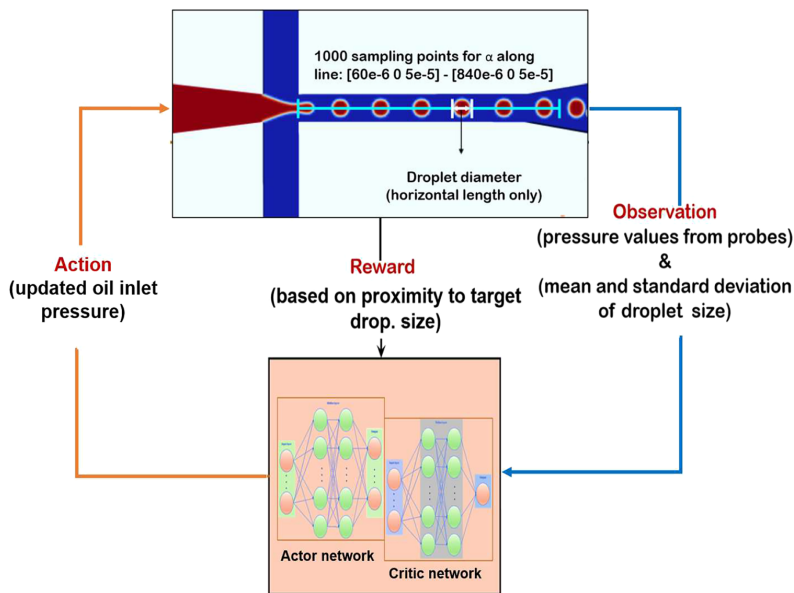


FIG. 2. A representation of the agent-environment interaction for optimizing droplet size in a microfluidic system. The agent observes pressure sensor measurements and mean droplet size, adjusts the oil inlet pressure, and receives rewards based on proximity to a target droplet size and droplet size variation. The neural network is trained using the agent’s data to determine the optimal action plan.

During postprocessing, we created data arrays for $\alpha \geq 0.5$ (assumed as the water droplet interface). The length of a droplet was calculated as the distance between two continuous water interface locations. We excluded the last droplet from the size calculation due to indications that it might not always have been fully formed.^{15,55}

D. DRL algorithm implementation

To seamlessly integrate Deep Reinforcement Learning (DRL) and Computational Fluid Dynamics (CFD), we developed a Singularity image based on Ubuntu 22.04, OpenFOAM-v2112, and PyTorch 1.10.2 (CPU only), following the approach described in the reference.⁵⁶ Our Singularity image includes PyTorch’s precompiled C++ library, libtorch. Additionally, we installed the ParaView⁵⁷ visualization tool to aid in the analysis and interpretation of the results.

The DRL+CFD framework is comprised of two primary components: the environment and the agent. The objective of the agent is to attain a target mean droplet size with minimum droplet size coefficient of variation (CV%) by interacting with the fluid environment through three channels, as illustrated in Fig. 2. The first channel involves observing an array of point probes/sensor pressure measurements at selected locations [as shown in Fig. 1(a)] and the average droplet size calculated using the procedure described in Subsection II C. The second channel is the action taken by the agent, which involves controlling the oil inlet pressure, while we keep the water inlet pressure fixed at 6000 Pa. The third channel is the reward, which is determined based on the

proximity of the droplet size to the target droplet size value. The neural network is trained using the agent’s interaction data with the environment to determine the optimal action plan that maximizes rewards at each time step.

We detail our implementation of the PPO algorithm, including any modifications made to meet the specific requirements of our application. Although the theoretical foundations of PPO have been thoroughly discussed in existing literature,⁵⁸ we provide a brief overview for context.

The Proximal Policy Optimization (PPO) algorithm is a policy-based method used to find the optimal policy for a given task. One advantage of PPO is its ability to sample data from multiple simulations concurrently, which we utilized by employing M episodes and storing them in a replay buffer. To efficiently fill the buffer, we implemented $K = 2$ workers that simultaneously conducted K simulations and saved the results in the buffer memory. We sampled a total of $M = 140$ episodes using a batch size of 2. In addition, the PPO algorithm operated on an episode level, with each episode comprising multiple time steps. At each time step, the agent observed the current state (s_0) from the environment, selected an action (a_0) based on its observation, and received a reward $R_0(s_0, a_0)$. Thus, PPO agent collected state-action-reward combinations in each episode τ , following a control policy,

$$\tau = (\{s_0, a_0, R_0, s_1\}, \{s_1, a_1, R_1, s_2\}, \dots). \tag{9}$$

We obtained the initial states for training episodes by simulating the fluid flow without active control until a fully developed

28 August 2023 06:19:25

flow was observed. A fully developed flow was defined as the point at which at least one droplet formation was observed at the outlet. The corresponding solution was saved and used as a starting point for subsequent learning episodes. The simulation without control lasted for a duration of $\Delta t_c^0 \in [0, 0.12]$, which implies that the training started at 0.12 s and ended at the total control time set to $T = 0.2$ s. The control time step for the DRL agent is defined as

$$\Delta t_c = k \times \Delta t_{sim}. \tag{10}$$

The variable t_{sim} represents the simulation time step and k is an integer factor that determines the frequency of control actions taken by the agent during an episode. In this study, we set the parameter k to 20, which introduces a sufficient time delay between droplet size measurements and the application of control actions. The reward function (R_t) described in Eq. (13) motivates the agent to achieve the desired droplet size while minimizing the standard deviation. The reward function can be written as

$$val = \text{abs}(r_1 - dia), \tag{11}$$

$$Penalty = \text{abs}\left(\frac{r_2 - dia_{std}}{r_2}\right), \tag{12}$$

$$R_t = \begin{cases} -1 & \text{if } val > 20e-6 \\ \frac{r_1 - val}{r_1} - 0.002 \times Penalty & \text{Otherwise.} \end{cases} \tag{13}$$

Here, val represents the absolute difference between the target droplet size (r_1) and the mean current droplet size (dia). If the absolute difference (val) exceeds a threshold of $20 \mu\text{m}$, a reward of -1 is assigned. However, if the droplet size is within the threshold, a positive reward is given proportionally to the proximity of the current mean droplet size to the target size. It is important to note that the reward is penalized if the droplet size standard deviation (dia_{std}) deviates significantly from the constraint (r_2) of $80 \mu\text{m}$. The resulting reward value is bounded between -1 and 1 .

The total rewards at the end of each episode are calculated as the discounted sum of rewards (\hat{R}_t) obtained from each control time step. The discounted sum of rewards represents the total rewards from the current time step $t=1$ to the end of the $t=T$, where γ is a discount factor and $\gamma \in [0; 1]$. The discount factor γ is specifically set to 0 in this case, indicating a focus solely on immediate rewards,

$$\hat{R}_t = \sum_{i=0}^T \gamma^i R_{t+i}. \tag{14}$$

Exploration is crucial in the PPO algorithm to effectively explore the state-action space. To achieve this, the agent incorporates randomization by sampling actions from a Beta distribution $\text{Beta}(\alpha, \beta)$, where α and β are parameters predicted by the policy network. Sampling from this distribution ensures continuous exploration during episode initiation, promoting effective learning.

The PPO algorithm adopts the actor-critic framework and uses two sets of artificial neural networks: an actor-network and a critic network. Both networks have the same input, which is the system state, and the same hidden layer architecture consists of two fully connected

layers with 128 neurons each. However, the networks have different outputs, with the actor-network outputting an action and the critic network generating a prediction of the discounted reward. Appropriate loss functions are used to train both networks. During the critic network's training, a variable called "advantage" \hat{A}_t is utilized to estimate the difference between the predicted discounted rewards [$V_\phi(s_t)$] and actual discounted rewards,⁵⁹

$$\hat{A}_t = \hat{R}_t - V_\phi(s_t). \tag{15}$$

By measuring the discrepancy between the predicted and actual discounted reward, the critic network aims to minimize a loss function,

$$\text{critic loss} = \frac{1}{|D_k|T} \sum_{\tau \in D_k} \sum_{t=0}^T (-\hat{A}_t)^2. \tag{16}$$

The critic loss function is the mean-squared error averaged over the number of episodes, where D_k is the number of episodes from the replay buffer used to update the critic network.

Meanwhile, the actor-network generates actions so that the agent can interact with the environment and learn from reward information to increase its cumulative reward over time. The actor or policy loss is formulated as

$$\text{Actor loss} = \frac{1}{T} \sum_{t=0}^T q_t(\Theta) \hat{A}_t, \tag{17}$$

where

$$q_t(\Theta) = \frac{\pi_\theta(a_t|s_t)}{\pi_{\theta_k}(a_t|s_t)} \tag{18}$$

and $\pi_\theta(a_t|s_t)$ is the log probability of taking action a_t in the state s_t when following policy π with parameter θ . In simple words, π_{θ_k} is the old policy (the old set of network parameters).

Policy/actor loss is clipped to improve PPO performance and speed convergence by ensuring that the new policy does not depart too far from the old policy.⁸ The clipped policy loss can be expressed as

$$\text{clipped actor loss} = \min(q_t(\Theta) \hat{A}_t, \text{clip}(q_t(\Theta), 1 - \epsilon, 1 + \epsilon) \hat{A}_t). \tag{19}$$

This clipped term constraints $q_t(\Theta)$ within the interval $(1 - \epsilon, 1 + \epsilon)$, where ϵ is a hyperparameter set at 0.2, as reported by Schulman *et al.*⁵⁸

To optimize the training process, the PPO algorithm employs the Adam optimizer instead of traditional stochastic gradient descent algorithms. The policy network was trained with a learning rate of 0.0015, while the value network used a learning rate of 0.00075. The source code for implementing this study can be accessed through the provided GitHub link in the data availability section.

The training process was completed in around 24 h, encompassing 140 episodes on a contemporary PC equipped with four processors on a single CPU. However, by leveraging the university's HPC cluster and allocating 32 processors, the training time was significantly reduced by a factor of 10 or more. Furthermore,

parallelizing data sampling from the episodes significantly accelerated the training process. The training process is summarized in Algorithm 1.

ALGORITHM 1. Complete training and control process of PPO algorithm.

```

Result: Optimal policy
Initialize  $s_0$ ;
while  $Episode \neq last\ episode$  do
  PPO Algorithm;
  for  $K = 0, 1, 2, \dots, M$  do
    Control policy:  $\pi_k = \pi(\theta_k)$ ;
    Probability:  $p(a_t|s_t)$ ;
    for  $i = 0, 1, 2, 3, \dots, n$  do
      State-action pairs:  $(D_k = \{\tau_j\})$ ;
      Rewards:  $\hat{R}_t$ ;
      Estimate advantages:  $\hat{A}_t$ ;
      Sequences update using gradient ascent method:  $s_t, a_t, r_t$ ;
      if  $Episode = last\ episode$  then
        Stop
      else
         $i = i + 1$ 
      end
    end
     $K = K + 1$ ;
  end
end
Test optimal policy in the environment

```

III. RESULTS

A. Mesh independence

To ensure a grid independent solution, mesh independence investigations were conducted. The objective was to develop an optimal mesh that balances computational cost and accuracy in capturing physical properties and fluid interfaces. The mesh generation process was summarized in Subsection II A and illustrated in Fig. 3(a). Eight grids have been generated and simulated using various snappyHexMesh parameters. A refinement region was created for all of the grids at the center of the intersection. Table III presents the properties of the designed meshes.

The resulting droplet interface sharpness, average droplet size, and detachment time were evaluated, as shown in Fig. 3(b). Relatively coarse grids, namely, M1, M2, and M3, resulted in a higher diffuse droplet interface, which is unsuitable for accurate droplet size estimations. However, finer grids from M4 to M8 led to improved droplet interface sharpness, with a mesh element number above 15 000 resulting in nearly the same droplet diameter and detachment time. Further refinement beyond M6, arising from a finer background mesh, led to negligible improvements at increased computational costs, as evidenced by computational times presented in Table III. Therefore, Mesh M6, with explicit feature edge refinement level 2 and volumetric refinement level 5, was selected as the optimal mesh for subsequent simulations.

B. Model verification

To validate the accuracy of our numerical model, we compared our simulation results with the experimental data of Wu *et al.*⁶⁰ on water droplet formation in Freol ALPHA 10G oil. We recreated their droplet generation geometry and evaluated our model by comparing droplet sizes with their experimental results at velocity ratios of 1/6, 1/3, 1/2, and 1/1. These velocity ratios corresponded to dispersed phase velocities U_d of 0.000 42, 0.000 84, 0.001 26, and 0.002 52 m/s, respectively, while keeping the continuous phase velocity fixed at $U_c = 0.002 52$ m/s.

The results presented in Fig. 4 demonstrate that our numerical model and the data from Wu *et al.*⁶⁰ exhibit good agreement for both low and high velocity ratios, with errors of less than 7% for dispersed phase velocities, except for 0.001 26 m/s, where the error was 11%. This finding aligns with other research studies that used the Volume of Fluid (VOF) method, which have also reported larger errors ranging from 10% to 18% and overestimated droplet size, particularly at high flow rates of the continuous phase.^{61,62} Although the difference in droplet sizes between our study and the study of Wu *et al.* may be attributed to the use of 2D simulations instead of their 3D FFD device, our numerical model still produces acceptable errors of less than 11% for all velocity ratios, which makes it suitable for further investigation.

C. Characterization of the environment without control

To better understand the environment and identify the feasible limits or bounds of the action space for the DRL, we conducted a study aimed at characterizing the environment. Specifically, we focused on identifying the upper and lower bounds of the oil inlet pressure (i.e., the manipulated variable) that induce droplet production. To achieve this goal, we evaluated the impact of different pressure ratios, represented as P_{oil}/P_w , on droplet size. Our investigation involved maintaining a constant water pressure of 6000 Pa and varying the oil pressures (P_{oil}) within the range of 2000 to 10 000 Pa, resulting in pressure ratios of $0.33 \leq P_{oil}/P_w \leq 1.67$. The results of this analysis are presented in Fig. 5.

In Fig. 5(a), we depict the variation in droplet length generated. Meanwhile, in Fig. 5(b), the results show that increasing the inlet oil pressure leads to smaller droplet sizes. The droplet generation frequency was ~ 120 Hz, and a CV% based droplet count ranges from 100 to 150. Initially, the CV% increases with the pressure ratio until $P_w = P_{oil}$, after which, it continuously decreases. For droplet generation where the average droplet size ranges from 88 and 55 μm , the CV% falls within 8%–6%. However, this exceeds the desired threshold of 5% and necessitates control of the droplet generation process. Droplets were not produced beyond a pressure ratio of 1.13 or below 0.75. Thus, we established the lower and upper bounds of the action space at 4500 and 7000 Pa, respectively. During training, the agent's action pressure values are normalized to a range of -1 to 1 before being input to the neural network.

D. Probe configurations for efficient and accurate flow observation

We optimized flow data collection accuracy by testing five probe layouts, labeled P1–P5, as depicted in Fig. 6(a), which acted as pressure sensors, providing real-time observations to the PPO algorithm.

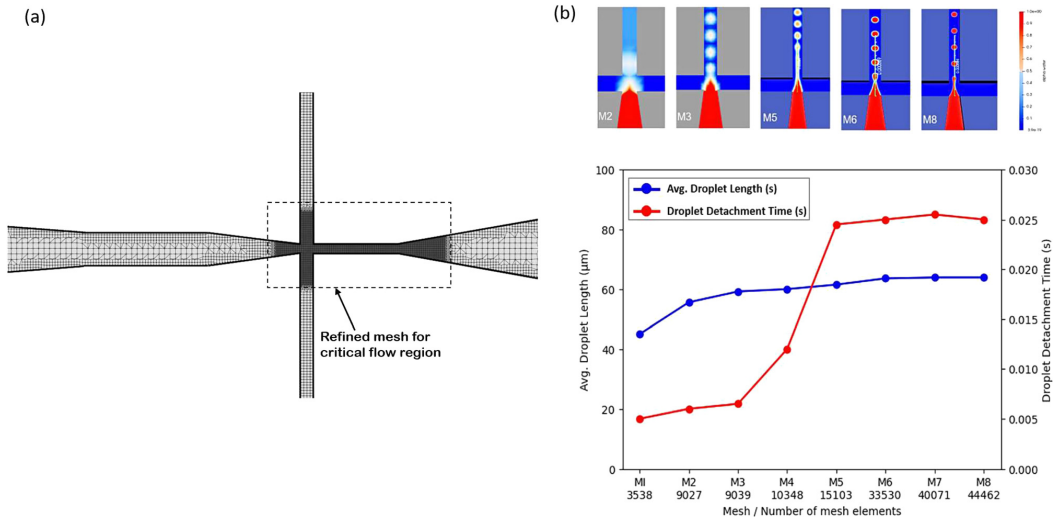


FIG. 3. (a) Computational mesh mainly of hexahedral cells and a resolution of 2500 cells (x), 600 cells (y), and 300 cells (z) per 1 mm. A refinement region captures accurate flow physics in gradient-rich areas. (b) Evaluation of meshes M1–M8 based on interface sharpness (top image), average droplet length, and detachment time (bottom image). Mesh M6 was identified as optimal for subsequent simulations, striking a balance between interface sharpness and result independence. Further mesh refinement does not yield significant improvements.

P1 had 10 equally spaced probes placed only in the microchannel junction; P2 had 20 probes in the junction and outlet; P3 and P4 had 40 and 60 probes, respectively, in the oil inlets, junction, and outlet; and P5 had 80 probes in all phase inlets, the junction, and outlet. We used the probe configurations to train the agent to achieve a droplet size setpoint of $60 \mu\text{m}$, as described in Subsection II D. The probe configurations were evaluated based on mean rewards accumulated [Fig. 6(b)] and achieved droplet size by the end of the training and droplet size CV% (Table IV).

The results demonstrate that P5 had the highest mean rewards of 0.91 for the last 10 episodes, achieved an average droplet size of

$60.05 \mu\text{m}$, and had the lowest CV% of $\sim 2\%$, indicating the most precise droplet size control. In contrast, P1 and P2 achieved the lowest negative mean rewards and the largest deviation from the target droplet size, which highlights their least precise control performance. Although both P3 and P4 had positive cumulative mean rewards, they did not perform as well as P5. The results also indicate that closed-loop control could deteriorate system performance when inadequate or inaccurate input states are provided. Overall, the results indicate that increasing the number of probes enhances control performance by providing sufficient flow field information for effective learning. However, since the arrangement of 80 probes effectively covered the

TABLE III. Properties of designed meshes and computational times for mesh independence study.

Base-Mesh (mm)	Mesh	Feature edge refinement level	Volume region refinement level	Number of mesh elements * (cells)	Avg mesh cell size (m)	Comp. time (s)
250*60*30	M1	1	1	3538	7.97×10^{-5}	21.3
	M2	2	1	9027	7.91×10^{-5}	50.4
	M3	2	2	9039	7.91×10^{-5}	52.8
	M4	2	3	10348	7.87×10^{-5}	55.6
	M5	2	4	15103	7.87×10^{-5}	134.8
	M6	2	5	33530	7.27×10^{-5}	843.9
260*70*30	M7	2	5	40071	7.46×10^{-5}	924.7
260*80*30	M8	2	5	44462	7.12×10^{-5}	1251.2

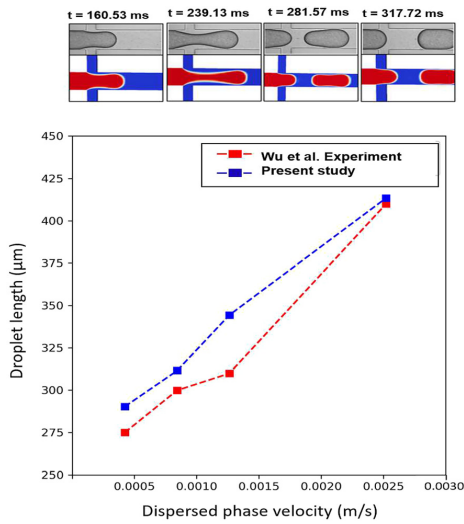


FIG. 4. Validation of our droplet water formation model (colored image) against the experimental data of Wu *et al.*⁶⁰ (gray image). Results show good agreement with the study of Wu *et al.* (errors < 7%), except at 0.00126 m/s (11% error), consistent with other Volume-of-Fluid (VOF) studies,^{61,62} validating our droplet formation model.

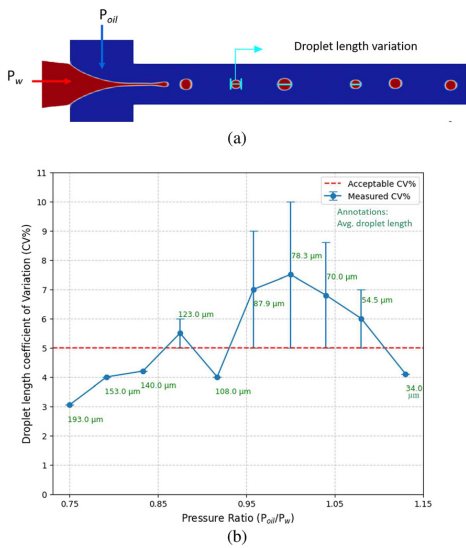


FIG. 5. (a) Depiction of variations in generated droplet sizes (lengths). (b) Effect of pressure ratio on droplet size variation (CV%). The CV% initially increases with the pressure ratio until $P_w = P_{oil}$ and then gradually decreases. Control is necessary for droplet size generation where the CV% exceeds the 5% desired threshold. Droplet production ceases beyond a pressure ratio of 1.13 and below 0.75, with action space bounds set at 4500–7000 Pa for $P_w = 6000$ Pa.

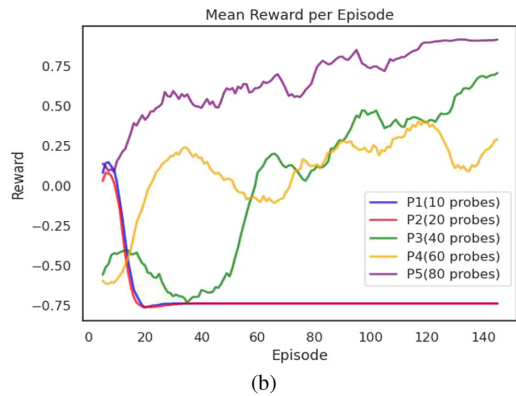
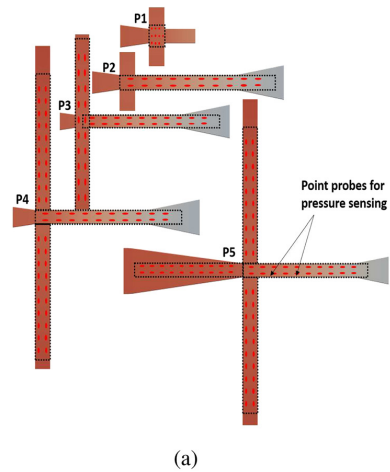


FIG. 6. Evaluation of pressure probe layouts (P1–P5) in PPO algorithm performance. (a) Different probe layouts assessed. (b) Mean rewards are used as the performance metric. Among the layouts, P5 with 80 probes in all phase inlets and junctions achieved the highest mean rewards of 0.91 at convergence, indicating the optimal probe number and positioning for precise droplet size control.

TABLE IV. Control results for achieving the droplet setpoint target of 60 μm with different probe configurations.

Probe configuration	Cumulative mean-rewards* (last 10 episodes)	Average-droplet-size (μm)	CV%
P1	−0.74	176	28.7
P2	−0.74	185	44.7
P3	0.29	65.5	15.9
P4	0.71	63.9	11.2
P5	0.91	60.05	2.13

critical flow region, the influence of adding more probes within or outside this critical region, based on flow dynamics, is unlikely to have a significant impact on control performance.

E. PPO algorithm performance in the absence of external disturbance

In this section, we analyze the PPO algorithm’s performance in achieving a specific droplet size with minimal CV% in the absence of external disturbances.

To evaluate the agent’s performance, Fig. 7 displays the DRL agent’s mean rewards accumulated for different mean droplet size setpoints (50, 60, 70, and 80 μm). We use the mean cumulated reward across all episodes and the last 15 episodes as specific performance metrics. This approach provides a better understanding of the learning effectiveness and agent’s performance as it approaches convergence.

The results presented in Fig. 7 indicate the effectiveness of the PPO algorithm in achieving a range of droplet sizes, as evidenced by rewards at convergence ranging from 0.63 to 0.92. While the algorithm proved effective across all tested droplet sizes, its accuracy varied.

Notably, the DRL agent exhibited outstanding performance for the 60 μm droplet size, achieving the highest reward at convergence and consistently maintaining high rewards throughout the training process. Moreover, the optimal policy was successfully tested for all target droplet sizes, consistently yielding rewards above 0.95.

It is important to acknowledge that the variability and unsmoothness observed in the rewards are attributed to the random exploration employed during the episodes. During training, the agent explores various actions to learn and improve its control strategy. However, in the testing phase, where the agent’s learned policy is evaluated, we observe higher rewards due to the absence of exploration and the application of the optimal policy. Overall, the study effectively demonstrates the effectiveness of the PPO algorithm in successfully controlling droplet size within the given environment.

Furthermore, we present the results of training the controller on the controlled variable (i.e., droplet size) and manipulated variable (oil pressure) as well as the performance of the final policy when tested on the environment in Fig. 8. The controller successfully achieved the mean size target-setpoint for all three experiments, with a CV% of less than 5% in each case. Specifically, the CV% for setpoints 50–70 μm

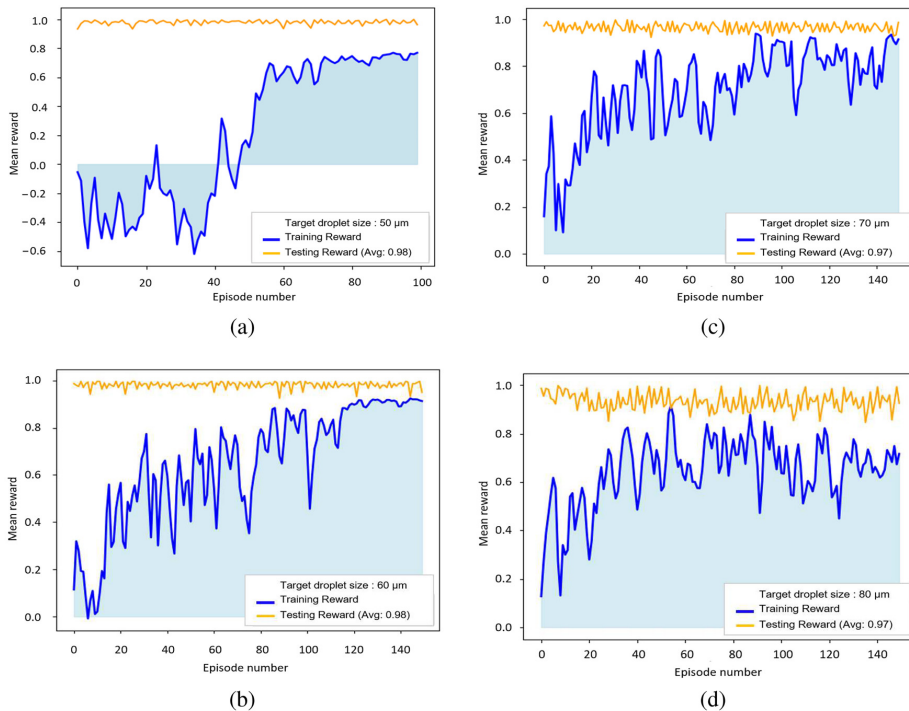


FIG. 7. Evaluation of PPO algorithm performance for different droplet size setpoints: (a) 50 μm, (b) 60 μm, (c) 70 μm, and (d) 80 μm, based on average rewards. Effective droplet size control was achieved with rewards at convergence ranging from 0.63 to 0.92. Excellent performance for 60 μm size, highest reward at convergence, and consistently high rewards during training. In the testing phase, rewards were higher without exploration, as the optimal policy was applied. Smoothing window was used on data for clarity.

28 August 2023 06:19:25

was less than 3%, while for the setpoint of 80 μm , it was $\sim 4.9\%$. The implementation of the controller led to a reduction in CV% by 2.6%, 4.72%, 3.6%, and 0.8% for the target sizes of 80, 70, 60, and 50 μm , respectively, compared to the case without control or open-loop. The corresponding control actions through the manipulated variable, i.e., oil inlet pressure, are shown for each setpoint, with pressure values

converging to 6546.98, 6422.85, 6268.45, and 5966.43 Pa for setpoints 50, 60, 70, and 80 μm , respectively. The corresponding control actions through the manipulated variable, i.e., oil inlet pressure, show that the pressure values converged to the desired setpoint for each droplet size at low CV%, demonstrating the effectiveness of the controller in achieving the desired setpoints.

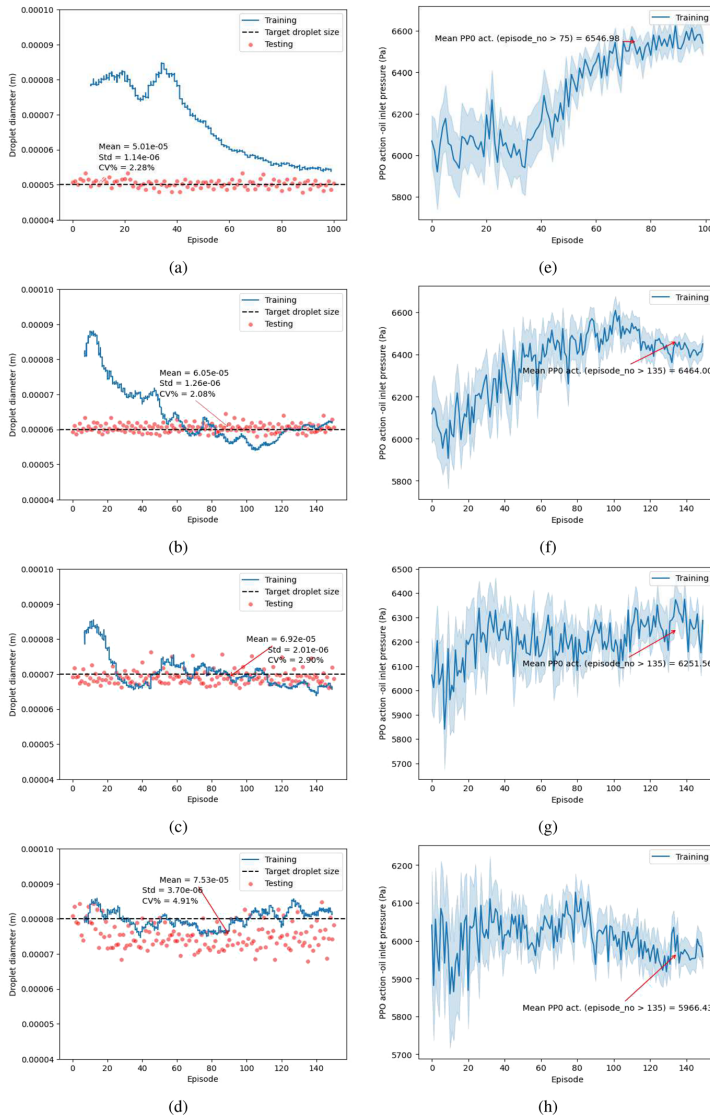


FIG. 8. DRL agent control of droplet size using oil pressure manipulation. The agent achieved CV% values below 3% for droplet size setpoints of 50 μm (a), 60 μm (b), and 70 μm (c). For the 80 μm setpoint (d), the CV% was $\sim 4.9\%$. The agent's control actions are represented by the converging pressure values: 6546.98 Pa (e), 6422.85 Pa (f), 6268.45 Pa (g), and 5966.43 Pa (h) for the respective setpoints.

28 August 2023 06:19:25

F. PPO algorithm performance in the presence of external disturbance

Disturbances in a droplet microfluidics system, such as mechanical vibrations caused by pumps, can introduce fluctuations that impact droplet formation and lead to changes in droplet size and size distribution. In this study, we simulated periodic mechanical vibrations using

a sine wave function to assess the performance of the control system in the presence of these disturbances. Pressure fluctuations in microfluidic systems are influenced by factors, such as the actuation method, frequency, voltage, syringe diameter, and pump design. They occur across a broad frequency range and exhibit varying amplitudes.^{63–66}

The disturbances were introduced by fluctuating the inlet water pressure, which otherwise remained at a constant value. Three forms of

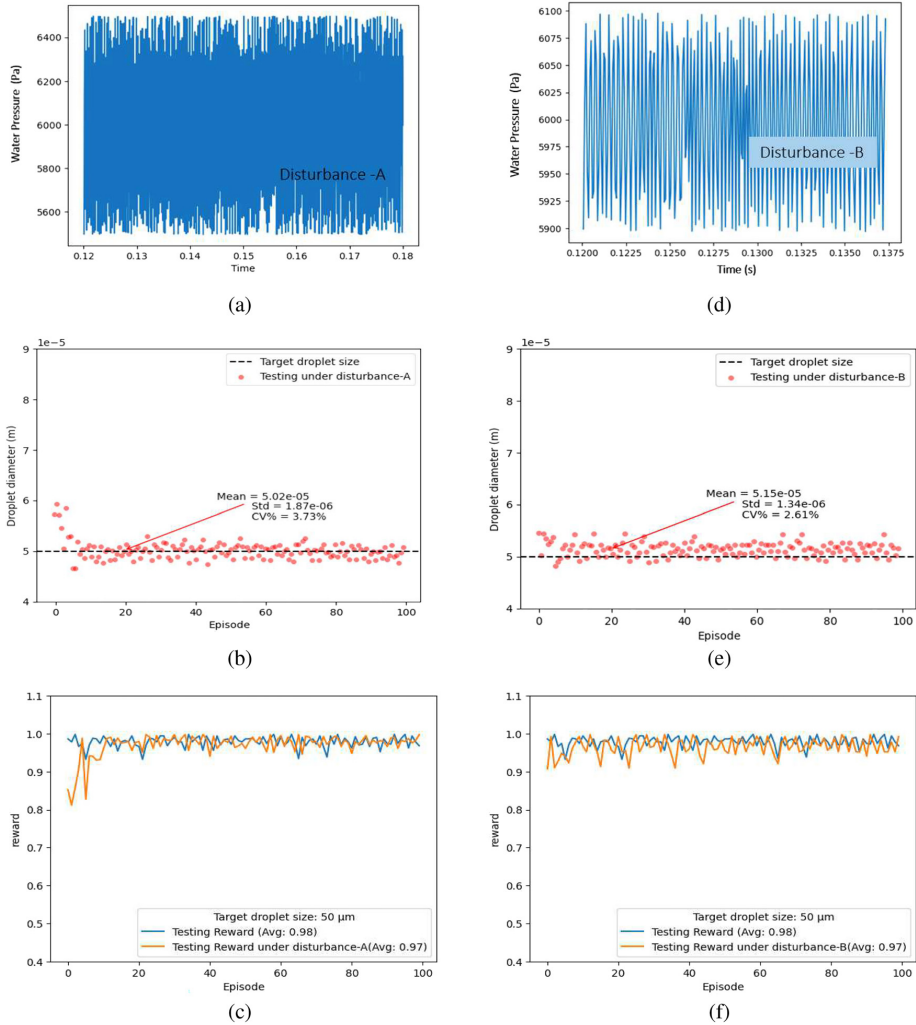


FIG. 9. Environment behavior under Disturbance A (sinusoidal oscillation frequency 10 KHz, amplitude 500 Pa) (a) and Disturbance B (sinusoidal oscillation frequency 10 KHz, amplitude 100 Pa) (d) for a droplet size setpoint of 50 μm . In (b), Disturbance A resulted in a higher droplet CV% of 3.75% compared to Disturbance B in (e) with CV% of 2.61%. Despite the presence of disturbances, the agent adapts; mean rewards for Disturbance A are shown in (c), and those for Disturbance B are shown in (f), which are comparable to the absence of disturbances. The droplet size remained close to the target (CV% below 5%).

28 August 2023 06:19:25

disturbances were considered: varying frequencies (10 and 10000 Hz) and amplitudes (50, 100, and 500) around the mean water pressure value of 6000 Pa. This resulted in water inlet pressure fluctuations within a range of less than 10% from the expected constant pressure.

To assess the effectiveness of the trained DRL agent in the presence of disturbances (Disturbance A, Disturbance B, and Disturbance C) and its ability to achieve the desired droplet size setpoint with minimal coefficient of variation (CV%), the final policies obtained from training agent in a disturbance-free environment were tested without further training. Figures 9 and 10 illustrate the depiction of the disturbances, the achieved droplet size, CV%, and rewards for a droplet size setpoint of 50 μm . The evaluation metric used is consistent with the assessment in the absence of disturbances.

In Figs. 9 and 10, we observed that the agent’s performance was influenced by the frequency and amplitude of the introduced disturbance. Comparing Disturbance A and Disturbance B, both with a frequency of 10,000 Hz but different amplitudes (500 Pa for Disturbance A and 100 Pa for Disturbance B), larger amplitudes caused more deviation from the desired behavior. This led to a slightly higher droplet coefficient of variation (CV%) for Disturbance A (3.75%) compared to Disturbance B (2.61%). These findings indicated that agent was more challenged in adapting and implementing corrective actions with larger disturbance amplitudes. However, when compared to the case without any disturbance, the CV% increased by 1.47% for Disturbance A and 0.33% for Disturbance B. Nonetheless, the mean droplet size remained close to the target, and the CV% in both cases remained below 5%. This indicates an overall improvement achieved through the implementation of closed-loop control. Based on these findings, we conclude that the agent can effectively respond to disturbances with amplitudes up to 0.8 times the mean pressure value it was trained on in this environment. For larger consistent disturbance amplitudes, retraining may be necessary to enhance the agent’s adaptability and performance.

Disturbance C, characterized by a lower amplitude (10 Pa) and a significantly lower frequency of 50 Hz compared to Disturbances A and B, impacts the environment significantly. This could be attributed to low-frequency disturbances potentially inducing system oscillations or resonance, magnifying their effects and posing challenges for the agent to compensate or handle sustained disturbances. Consequently, under Disturbance C, the droplet size distribution exhibits a wave-like pattern with a coefficient of variation (CV%) increase to $\sim 5.5\%$. Although slightly higher than the desired level, this is still an improvement compared to the case without control, where the CV% was $\sim 6\%$. Retraining the agent becomes crucial for handling such scenarios. Furthermore, the agent’s action response to Disturbances A, B, and C is depicted in Fig. 11. Notably, the agent exhibits the ability to compensate for fluctuations in water inlet pressure by employing distinct control actions for each disturbance. In summary, the agent demonstrates adaptability and responsiveness to disturbances within certain limits of amplitude and frequency, but higher or different types of disturbances may necessitate retraining the DRL algorithm.

IV. CONCLUSION

This study successfully employed Proximal Policy Optimization (PPO) and the Volume of Fluid (VOF) method to regulate droplet size in microfluidics. The DRL+CFD framework implementation effectively controlled droplet size by manipulating the continuous phase

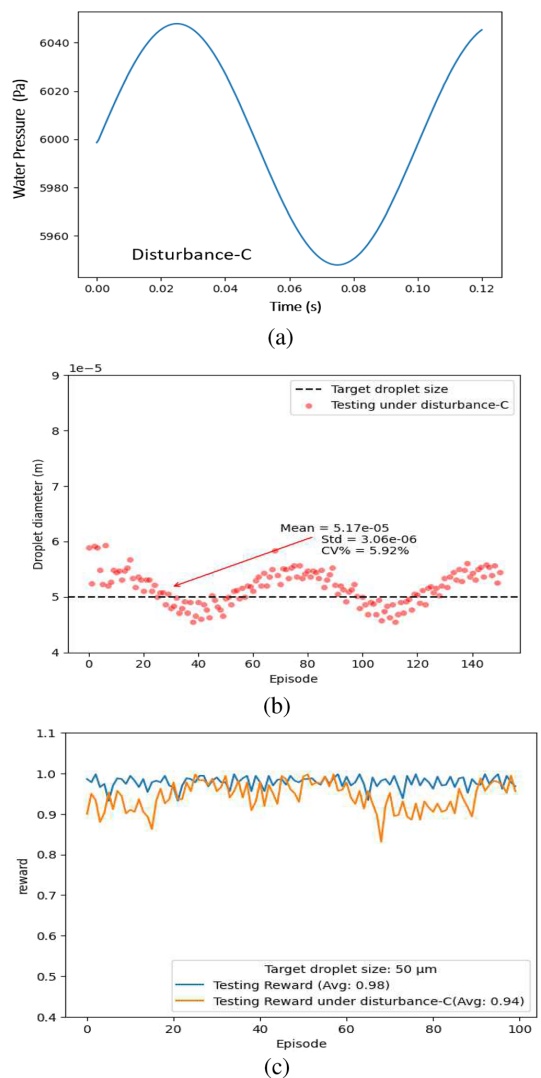


FIG. 10. Impact of Disturbance C (sinusoidal oscillation frequency 50 Hz, amplitude 10 Pa) on the environment. Disturbance C depicted in (a) leads to a wave-like droplet size distribution with an increase in CV% to $\sim 5.5\%$. (b) Low-frequency disturbances (Disturbance C) challenged the agent, resulting in degraded mean rewards. (c) Retraining is required for optimal performance.

inlet pressure, supported by pressure and droplet diameter measurements. Mesh independence investigations identified the optimal mesh density, balancing computational efficiency and accuracy, with simulation results showing good agreement with experimental data (errors

28 August 2023 06:19:25

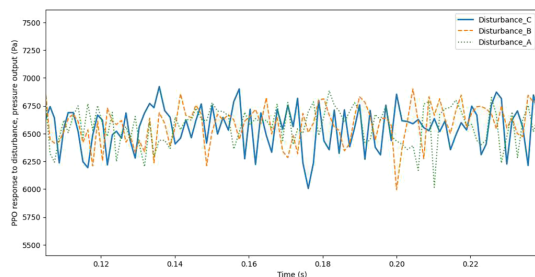


FIG. 11. PPO agent's response to Disturbances A (10 KHz, 500 Pa), B (10 KHz, 100 Pa), and C (10 Pa, 50 Hz). Agent was sensitive to frequency and amplitude, with higher sensitivity to frequency. Disturbance C presents challenges in compensating for sustained disturbances. Agent adapts and responds to disturbances within limits.

below 11%). The optimized probe layout for field pressure measurement improved control performance, reducing droplet size variation. The PPO algorithm achieved droplet sizes with a CV% below 5% for all setpoints (50, 60, 70, and 80 μm), surpassing the case without control. The PPO agent demonstrated adaptability to external disturbances within certain amplitude and frequency ranges, demonstrating its robustness.

This study demonstrates the potential of DRL algorithms in precise droplet size control for microfluidics, advancing the field. By using continuous control DRL algorithms in simulations, we can optimize the design and testing of control algorithms specific to microfluidic devices. Our goal is to transfer these algorithms to experimental setups with minimal modification, reducing resource costs.

Future research directions will involve comparing alternative continuous control ML strategies for evaluating algorithm performance in real-time applications and managing different disturbance scenarios. By addressing these aspects, further improvements and advancements can be made in the study of DRL techniques for regulating droplet size in microfluidics systems, ultimately pushing the field forward.

ACKNOWLEDGMENTS

The authors would like to thank the Estonian Research Council for providing support under Project Nos. PUT1435 and PRG620 as well as the TTU development program 2016-2022, project code 2014-2020.4.01.16-0032.

AUTHOR DECLARATIONS

Conflict of Interest

The authors have no conflicts to disclose.

Author Contributions

Nafisat Gyimah: Conceptualization (equal); Data curation (equal); Formal analysis (equal); Writing – original draft (equal); Writing – review & editing (equal). **Ott Scheler:** Supervision (equal). **Toomas Rang:** Funding acquisition (lead). **Tamas Pardy:** Conceptualization (equal); Supervision (lead); Writing – review & editing (equal).

DATA AVAILABILITY

The data that support the findings of this study are available from the corresponding author upon reasonable request.

REFERENCES

- A. R. Perestrelo, A. C. Águas, A. Rainer, and G. Forte, "Microfluidic organ/body-on-a-chip devices at the convergence of biology and microengineering," *Sensors* **15**, 31142–31170 (2015).
- S. Naji, A. Rahimi, V. Bazargan, and M. Marengo, "Numerical and artificial neural network analysis of an axisymmetric co-flow-focusing microfluidic droplet generator using active and passive control," *Phys. Fluids* **35**, 062008 (2023).
- S. Battat, D. A. Weitz, and G. M. Whitesides, "Nonlinear phenomena in microfluidics," *Chem. Rev.* **122**, 6921–6937 (2022).
- H. Xia, J. Wu, J. Zheng, J. Zhang, and Z. Wang, "Nonlinear microfluidics: Device physics, functions, and applications," *Lab Chip* **21**, 1241–1268 (2021).
- E. Miller, M. Rotea, and J. P. Rothstein, "Microfluidic device incorporating closed loop feedback control for uniform and tunable production of microdroplets," *Lab Chip* **10**, 1293–1301 (2010).
- D. Crawford, C. Smith, and G. Whyte, "Image-based closed-loop feedback for highly mono-dispersed microdroplet production," *Sci. Rep.* **7**, 10545 (2017).
- N. K. Mani, S. Rudiuk, and D. Baigl, "Spatially controlled DNA unzipping by microfluidic interface positioning on a molecule perpendicular to a multicomponent flow," *Chem. Commun.* **49**, 6858–6860 (2013).
- F. Ren, J. Rabault, and H. Tang, "Applying deep reinforcement learning to active flow control in weakly turbulent conditions," *Phys. Fluids* **33**, 037121 (2021).
- R. Vinuesa, O. Lehmkuhl, A. Lozano-Durán, and J. Rabault, "Flow control in wings and discovery of novel approaches via deep reinforcement learning," *Fluids* **7**, 62 (2022).
- J. Viquerat, P. Meliga, A. Larcher, and E. Hachem, "A review on deep reinforcement learning for fluid mechanics: An update," *Phys. Fluids* **34**, 111301 (2022).
- X. Y. Lee, A. Balu, D. Stoecklein, B. Ganapathysubramanian, and S. Sarkar, "A case study of deep reinforcement learning for engineering design: Application to microfluidic devices for flow sculpting," *J. Mech. Des.* **141**, 111401 (2019).
- O. J. Dressler, P. D. Howes, J. Choo, and A. J. de Mello, "Reinforcement learning for dynamic microfluidic control," *ACS Omega* **3**, 10084–10091 (2018).
- M. Shahab and R. Rengaswamy, "Reinforcement-learning designs droplet microfluidic networks," *Comput. Chem. Eng.* **161**, 107787 (2022).
- R. Kebriaei and A. S. Basu, "Autosizing closed-loop drop generator using morphometric image feedback," in *17th International Conference on Miniaturized Systems for Chemistry and Life Sciences, MicroTAS* (2013), Vol. 2013, pp. 1944–1946.
- N. Gyimah, O. Scheler, T. Rang, and T. Pardy, "Digital twin for controlled generation of water-in-oil microdroplets with required size," in *2022 23rd International Conference on Thermal, Mechanical and Multi-Physics Simulation and Experiments in Microelectronics and Microsystems (EuroSimE) (IEEE, 2022)*, pp. 1–7.
- N. Gyimah, R. Joëmaa, K. Párnamentals, O. Scheler, T. Rang, and T. Pardy, "Pid controller tuning optimization using genetic algorithm for droplet size control in microfluidics," in *2022 18th Biennial Baltic Electronics Conference (BEC) (IEEE, 2022)*, pp. 1–6.
- X. Duan, Z. Zheng, Y. Luo, and C. Song, "Closed-loop feedback control for droplet-based microfluidics: A characteristic investigation on passive and on-demand droplet generation," *Proc. SPIE* **12550**, 183–188 (2023).
- S. Motaghi, M. Nazari, M. Nazari, N. Sepehri, and A. Mahdavi, "Control of droplet size in a two-phase microchannel using PID controller: A novel experimental study," *Amirkabir J. Mech. Eng.* **53**, 4279–4292 (2021).
- W. Zeng, S. Yang, Y. Liu, T. Yang, Z. Tong, X. Shan, and H. Fu, "Precise mono-disperse droplet generation by pressure-driven microfluidic flows," *Chem. Eng. Sci.* **248**, 117206 (2022).
- Y. Xie, A. J. Dixon, J. R. Rickel, A. L. Klibanov, and J. A. Hossack, "Closed-loop feedback control of microbubble diameter from a flow-focusing microfluidic device," *Biomicrofluidics* **14**, 034101 (2020).
- X. Y. Lee, A. Balu, D. Stoecklein, B. Ganapathysubramanian, and S. Sarkar, "Flow shape design for microfluidic devices using deep reinforcement learning," *arXiv:1811.12444* (2018).

- ²²A. Jahn, J. E. Reiner, W. N. Vreeland, D. L. DeVoe, L. E. Locascio, and M. Gaitan, "Preparation of nanoparticles by continuous-flow microfluidics," *J. Nanopart. Res.* **10**, 925–934 (2008).
- ²³X. C. i Solvas and A. DeMello, "Droplet microfluidics: Recent developments and future applications," *Chem. Commun.* **47**, 1936–1942 (2011).
- ²⁴C. Vignon, J. Rabault, and R. Vinuesa, "Recent advances in applying deep reinforcement learning for flow control: Perspectives and future directions," *Phys. Fluids* **35**, 031301 (2023).
- ²⁵Q. Wang, L. Yan, G. Hu, C. Li, Y. Xiao, H. Xiong, J. Rabault, and B. R. Noack, "DRLinFluids: An open-source python platform of coupling deep reinforcement learning and OpenFOAM," *Phys. Fluids* **34**, 081801 (2022).
- ²⁶S. G. Sontti and A. Atta, "Regulation of droplet size and flow regime by geometrical confinement in a microfluidic flow-focusing device," *Phys. Fluids* **35**, 081801 (2023).
- ²⁷P. K. Periyannan Rajeswari, H. N. Joensson, and H. Andersson-Svahn, "Droplet size influences division of mammalian cell factories in droplet microfluidic cultivation," *Electrophoresis* **38**, 305–310 (2017).
- ²⁸S. P. Pandey, S. Sarkar, and D. Pal, "Splitting of microbubble mediated by power-law carrier fluid inside a symmetric bifurcating channel," *Phys. Fluids* **35**, 053104 (2023).
- ²⁹A. T. Cerdeira, J. B. Campos, J. M. Miranda, and J. D. Araújo, "Review on microbubbles and microdroplets flowing through microfluidic geometrical elements," *Micromachines* **11**, 201 (2020).
- ³⁰L. Derzsi, M. Kasprzyk, J. P. Plog, and P. Garstecki, "Flow focusing with visco-elastic liquids," *Phys. Fluids* **25**, 092001 (2013).
- ³¹S. Santra, S. Das, S. S. Das, and S. Chakraborty, "Surfactant-induced retardation in lateral migration of droplets in a microfluidic confinement," *Microfluid. Nanofluid.* **22**, 1–19 (2018).
- ³²S.-Y. Teh, R. Lin, L.-H. Hung, and A. P. Lee, "Droplet microfluidics," *Lab Chip* **8**, 198–220 (2008).
- ³³T. Kahali, S. Santra, and S. Chakraborty, "Electrically modulated cross-stream migration of a compound drop in micro-confined oscillatory flow," *Phys. Fluids* **34**, 122015 (2022).
- ³⁴M. D. Nguyen, K. V. Tran, C. T. Dang, G. M. Kim, T. D. Dang, H. D. Ta, and I. L. Ngo, "Generalized correlation for predicting the droplet size in a microfluidic flow-focusing device under the effect of surfactant," *Phys. Fluids* **34**, 032014 (2022).
- ³⁵H. Liu and Y. Zhang, "Lattice Boltzmann simulation of droplet generation in a microfluidic cross-junction," *Commun. Comput. Phys.* **9**, 1235–1256 (2011).
- ³⁶G. Houston, P. Capobianchi, and M. S. Oliveira, "Flow focusing with miscible fluids in microfluidic devices," *Phys. Fluids* **35**, 052015 (2022).
- ³⁷S. Li, L. Wen, and W. Wang, "Asymmetric breakup of a single droplet through a γ -junction microchannel with non-uniform flow rate," *Phys. Fluids* **35**, 042015 (2023).
- ³⁸M. Nekouei and S. A. Vanapalli, "Volume-of-fluid simulations in microfluidic t-junction devices: Influence of viscosity ratio on droplet size," *Phys. Fluids* **29**, 032007 (2017).
- ³⁹Q. Li, H. Zhu, S. Lu, M. Lei, W. Xu, and Z. Liu, "Numerical investigation on formation mechanism and flow law of droplet in t-junction by electric field," *Phys. Fluids* **35**, 062007 (2023).
- ⁴⁰M. Fatehifar, A. Revell, and M. Jabbari, "Non-Newtonian droplet generation in a cross-junction microfluidic channel," *Polymers* **13**, 1915 (2021).
- ⁴¹P. Desir, T.-Y. Chen, M. Bracconi, B. Saha, M. Maestri, and D. G. Vlachos, "Experiments and computations of microfluidic liquid-liquid flow patterns," *React. Chem. Eng.* **5**, 39–50 (2020).
- ⁴²S. Malekzadeh and E. Roohi, "Investigation of different droplet formation regimes in a t-junction microchannel using the VOF technique in OpenFOAM," *Microgravity Sci. Technol.* **27**, 231–243 (2015).
- ⁴³Q. Chen, J. Li, Y. Song, D. M. Christopher, and X. Li, "Modeling of Newtonian droplet formation in power-law non-Newtonian fluids in a flow-focusing device," *Heat Mass Transfer* **56**, 2711–2723 (2020).
- ⁴⁴J. U. Brackbill, D. B. Kothe, and C. Zemach, "A continuum method for modeling surface tension," *J. Comput. Phys.* **100**, 335–354 (1992).
- ⁴⁵M. Leman, F. Abouakil, A. D. Griffiths, and P. Tabeling, "Droplet-based microfluidics at the femtolitre scale," *Lab Chip* **15**, 753–765 (2015).
- ⁴⁶H.-H. Jeong and A. D. Aladese, "Numerical and experimental investigations of uniform fluid distribution for droplet formation in parallelized microfluidics," *Front. Sens.* **34**, 1014864 (2022).
- ⁴⁷3M™ novoc™ 7500 engineered fluid.
- ⁴⁸S. S. Deshpande, L. Anumolu, and M. F. Trujillo, "Evaluating the performance of the two-phase flow solver interFoam," *Comput. Sci. Discovery* **5**, 014016 (2012).
- ⁴⁹Y. Wang and P. Ming, "Dynamic and energy analysis of coalescence-induced self-propelled jumping of binary unequal-sized droplets," *Phys. Fluids* **31**, 122108 (2019).
- ⁵⁰J. Cheng, Q. Li, C. Yang, Y. Zhang, and Z. Mao, "CFD-PBE simulation of a bubble column in OpenFOAM," *Chin. J. Chem. Eng.* **26**, 1773–1784 (2018).
- ⁵¹OpenFOAM, *The Open Source CFD Toolbox, User Guide, Version v2112* (OpenFOAM, 2018).
- ⁵²L. Shui, *Two-Phase Flow in Micro and Nanofluidic Devices* (Wohrman Print Service, Zutphen, the Netherlands, 2007), Vol. 133.
- ⁵³D. Hoang, L. Portela, C. Kleijn, M. Kreutzer, and V. Van Steijn, "Dynamics of droplet breakup in a t-junction," *J. Fluid Mech.* **717**, R4 (2013).
- ⁵⁴S. L. Anna, "Droplets and bubbles in microfluidic devices," *Annu. Rev. Fluid Mech.* **48**, 285–309 (2016).
- ⁵⁵K. Pärnamets, A. Udal, A. Koel, T. Pardy, N. Gyimah, and T. Rang, "Compact empirical model for droplet generation in a lab-on-chip cytometry system," *IEEE Access* **10**, 127708–127717 (2022).
- ⁵⁶D. Thummar, "Active flow control in simulations of fluid flows based on deep reinforcement learning," Zenodo (2021).
- ⁵⁷See https://www.paraview.org/Wiki/The_ParaView_Tutorial for "Paraview self-directed tutorial" (accessed: July 01, 2023).
- ⁵⁸J. Schulman, F. Wolski, P. Dhariwal, A. Radford, and O. Klimov, "Proximal policy optimization algorithms," [arXiv:1707.06347](https://arxiv.org/abs/1707.06347) (2017).
- ⁵⁹R. Paris, S. Bennedine, and J. Dandois, "Robust flow control and optimal sensor placement using deep reinforcement learning," *J. Fluid Mech.* **913**, A25 (2021).
- ⁶⁰L. Wu, M. Tsutahara, L. S. Kim, and M. Ha, "Three-dimensional lattice Boltzmann simulations of droplet formation in a cross-junction microchannel," *Int. J. Multiphase Flow* **34**, 852–864 (2008).
- ⁶¹S. G. Sontti and A. Atta, "CFD analysis of microfluidic droplet formation in non-Newtonian liquid," *Chem. Eng. J.* **330**, 245–261 (2017).
- ⁶²X. Li, L. He, Y. He, H. Gu, and M. Liu, "Numerical study of droplet formation in the ordinary and modified t-junctions," *Phys. Fluids* **31**, 082101 (2019).
- ⁶³P. Zhu, X. Tang, and L. Wang, "Droplet generation in co-flow microfluidic channels with vibration," *Microfluid. Nanofluid.* **20**, 1–10 (2016).
- ⁶⁴P. Dhananchezhian and S. S. Hiremath, "Optimization of multiple micro pumps to maximize the flow rate and minimize the flow pulsation," *Procedia Technol.* **25**, 1226–1233 (2016).
- ⁶⁵M. Nabavi and L. Mongeau, "Numerical analysis of high frequency pulsating flows through a diffuser-nozzle element in valveless acoustic micropumps," *Microfluid. Nanofluid.* **7**, 669–681 (2009).
- ⁶⁶S. M. Recktenwald, C. Wagner, and T. John, "Optimizing pressure-driven pulsatile flows in microfluidic devices," *Lab Chip* **21**, 2605–2613 (2021).

Curriculum Vitae

1. Personal data

Name	Nafisat Gyimah
Date and place of birth	09 June 1990 Accra, Ghana
Nationality	Ghana

2. Contact information

Address	Akadeemia tee 5a-31 Tallinn, Estonia
Phone	+37253672893
E-mail	nafisat.gyimah@ttu.ee

3. Education

2021–Present	Tallinn University of Technology, PhD studies
2018–2020	Tallinn University of Technology, School of Information Technology Communicative Electronics, MSc
2009–2013	Kwame Nkrumah University of Science and Technology, Department of Electrical Engineering Electical/Electronics Engineering, BSc

4. Language competence

English	Fluent
Twi	Fluent
Arabic	Basic

5. Professional employment

2018–2019	Tallinn University of Technology, Tallinn, Estonia , Microfluidics Simulations Engineer
2021–2022	Selfdiagnostics Deutchland GmbH, Leipzig Germany, Software Testing Engineer
2014–2018	Vodafone Telecommunications Limited, Accra, Ghana, International Roaming Specialist

Elulookirjeldus

1. Isikuandmed

Nimi	Nafisat Gyimah
Sünniaeg ja -koht	09.06.1990, Accra, Ghana
Kodakondsus	Ghana

2. Kontaktandmed

Address	Akadeemia tee 5a-31 Tallinn, Estonia
Telefon	+37253672893
E-post	nafisat.gyimah@ttu.ee

3. Hariduskäik

2021–Present	Tallinna Tehnikaülikool- PhD
2018–2020	Tallinna Tehnikaülikool, Infotehnoloogia kool, Kommunikatiivne elektroonika, MSc
2009–2013	Kwame Nkrumah'i teadus- ja tehnoloogiaülikool, Elektriosakond Elektri-/elektroonikatehnika, BSc

4. Keelteoskus

inglise keel	kõrgtase
Twi	kõrgtase
araabia keel	algata

5. Teenistuskäik

2018–2019	Tallinna Tehnikaülikool, Tallinn, Eesti, Mikrofluidika simulatsiooni-insener
2021–2022	Selfdiagnostics Deutschland GmbH, Leipzig Saksamaa, Tarkvara testimise insener
2014–2018	Vodafone Telecommunications Limited, Accra, Ghana, Rahvusvahelise rändluse spetsialist

ISSN 2585-6901 (PDF)
ISBN 978-9916-80-189-5 (PDF)